UNIVERSIDADE D
COIMBRA

Carlos Fernando Morgado Ribeiro

ANALYSIS OF THE INTERACTION BETWEEN FIRE FRONTS IN COMPLEX TOPOGRAPHY

Doctoral Thesis in Mechanical Engineering - Aerodynamics, Natural and Technological Risks, supervised by Professor Domingos Xavier Filomeno Carlos Viegas and Professor Jorge Rafael Nogueira Raposo, submitted to the Department of Mechanical Engineering, Faculty of Sciences and Technology of the University of Coimbra

September de 2023

Analysis of the Interaction Between Fire Fronts in Complex Topography

Thesis in Mechanical Engineering submitted to the Department of Mechanical Engineering of the University of Coimbra to the requirements for degree of Doctor of Philosophy in Mechanical Engineering.

Carlos Fernando Morgado Ribeiro

Scientific advisors:

Prof. Domingos Xavier Filomeno Carlos Viegas, University of Coimbra, Portugal

Prof. Jorge Rafael Nogueira Raposo, University of Coimbra, Portugal

Department of Mechanical Engineering

Faculty of Sciences and Technology

University of Coimbra

Coimbra, September 2023

FACULDADE DE CIÊNCIAS E TECNOLOGIA
UNIVERSIDADE D COIMBRA

To my wife Diana and my family.

In memory of all the people who died in forest fires
and all the fallen firefighters while fighting the fires.
To them all, my respectful salute.

Acknowledgements

The research presented in this thesis has been conducted over the last five years at the Forest Fire Research Center (CEIF) of the Association for the Development of Industrial Aerodynamics (ADAI). These five years of research have been a very productive time for both my academic training and personal development. The freedom in studying forest fires, the analyse of real large fires, prescribed and suppression burnings allowed me to improve my knowledge in the field of forest fire behaviour, especially the dynamics of fire behaviour, the convective forest fire process and merging fires.

My special thanks go to my scientific advisors Professor Domingos Xavier Filomeno Carlos Viegas and Doctor Jorge Rafael Nogueira Raposo for their valuable assistance, support, and constant encouragement throughout my PhD program. During my work in the laboratory, in the field and in the analysis of the results, I greatly appreciate their scientific knowledge and experience, as well as their trust and constant effort to provide me with the best possible working conditions. Your pursuit of scientific rigour was indispensable to the successful completion of this work and at the same time a great source of inspiration to me. I would also like to express my appreciation for the effort invested in this work and for the critical and stimulating reading of the text.

My thanks go to Professor Jason Sharples for the fruitful discussions and critical comments during the writing of the academic papers, which were crucial to the finishing of this thesis.

I thank my colleague André Rodrigues and Abderahman Abouali for his insights into laboratory research, measurement techniques and for his friendship.

I am grateful for the excellent support I received from ADAI members, which enabled me to further develop my research. I would also like to thank all the members of CEIF for the friendly and scientifically stimulating atmosphere at the research centre. My special thanks go to my colleagues who collaborated with me in CEIF, Eng. Teresa Viegas, Luís Mário Ribeiro, Miguel Almeida, Carlos Viegas, Daniela Alves, Thiago Barbosa, Tiago Rodrigues, Sérgio Lopes, Nuno Luís, Fátima Guedes, Ana Rosa, Joana Cardoso, António Cardoso, João Carvalho, Luís Reis (until 2022) and Gonçalo Rosa (until 2021).

I would like to thank all my friends for their encouragement.

My wife Diana Almeida for her love, dreams, tenderness and happiness that she always gives me and for her patience; my all family for the affection and support they have given me, especially my dear parents (Carlos de Sousa Ribeiro and Filomena Morgado Afonso de Sousa) who have always supported me, and my brothers (Bruno Miguel Morgado Ribeiro and Vitor Morgado Ribeiro) who encouraged me. My grandmother (Maria de Lurdes Jorge), passed away in 2022. I would like to thank them all for the reasons already mentioned and for their encouragement, personal sacrifices and understanding during these years. Without them, it would not have been possible to complete this work.

The financial support for this work was provided by the Portuguese Foundation for Science and Technology (FCT) through the PhD grant FRH/BD/140923/2018, for which I express my sincere gratitude.

Coimbra, September 2023

Abstract

Forest fires often exhibit complex and dynamic fire behaviour resulting from interactions between the various parts of a fire and the surrounding environment. These interactions can cause rapid fire progression and lead to loss of containment and critical fire safety problems.

A conceptual model based on the dynamic interaction between the fire, the fuel bed and the surrounding flow is proposed to explain the non-monotonic or intermittent fire behaviour. According to the model, the fire-induced flow changes the flame geometry and its propagation velocity even under nominally permanent and uniform boundary conditions. After an initial acceleration, there is a deceleration in the Rate of Spread (ROS) and it is followed by one or more cycles. Carefully controlled experiments were made with fires in slopes and canyons and the results show that the evolution of fire properties, particularly flame angle and ROS, exhibits high-frequency oscillations superimposed on the low-frequency fire growth cycle described. Based on the analysis of the interaction between a spreading fire and its environment under nominally constant and uniform boundary conditions, it is found that the evolution of the fire front is characterised by fluctuations in its properties, in particular its ROS. Using a database of a large number of fires of different temporal and spatial extent, it is shown that the amplitude of the oscillations of ROS is proportional to the average value of ROS and that the frequency of the oscillation varies according to the type of fire and increases with the

average value of ROS for a given fuel. In the case of rapid spread, the large amplitude of the ROS rise and the sudden fall favour the intermittent behaviour of the fire. In general, the amplitude and period required for the rise of ROS are greater than those of the fall. However, the acceleration and deceleration phases in Junction fires do not follow this rule, indicating different convective processes of interaction between the flow and the fire. This oscillation explains the variability of many fires at all scales and challenges the current interpretation based on the square factors that influence fire spread and classification of wind- or topography-driven fires.

Two fires that ignited in Pedrógão Grande, Portugal, on 17th June 2017 spread very quickly due to unusual physical processes related to the interaction between a thunderstorm and the merging of these two fires, killing 66 people within two hours. In Quiaios, Portugal, on 15th October 2017, two flanks spread for at least 7km and staying 200m apart before finally merging. In this work, the merging fire lines are analysed and show that in the process of merging, the phenomena of heat transfer by radiation and convection are extremely amplified due to the concentration of energy during the interaction. The energy concentration and consequently the development of a strong heat transfer mechanism led to an extremely high and sudden increase of ROS during the interaction until it reaches a maximum value, after which the ROS starts to decrease.

A series of laboratory experiments and the reconstruction of some real fires during the merging process was intended to explain the fire spread conditions and verify that the merging fire lines were responsible for the very intense fire development. The results of the analysis of the Pedrógão Grande fire show that the spread and merging of the two fires in the tests correspond very well with the observations in the field, especially the periods of increase and decrease of ROS, the peaks of ROS and the area growth using the scaling laws. Their physical simulation at a laboratory scale has shown the importance of the mechanisms of two merging fire lines for the development of very important convective processes in a fire. The results of the analysis of the Quiaios fire show that the pyro convective interaction between the two parallel fire lines and the ambient wind changes the ROS of the approaching fire lines and the associated fire spread properties, with the same tendency being independent of the distance between the fire lines. A

physical interpretation of fire development based on the dynamic interaction between two parallel fire lines under wind influence is proposed. A dimensionless physical parameter, the Froude number, defined by the ratio between the inertial force due to the wind flow and the buoyancy forces due to the fire, was used.

Keywords: Forest fires; Dynamic fire behaviour; Extreme fire behaviour; Fire acceleration; Fire modelling; Oscillatory fire behaviour; Intermittent fire behaviour; Merging fires; Junction fires.

Resumo

Os incêndios florestais apresentam um comportamento complexo e dinâmico do fogo resultante das interações entre as várias partes de um incêndio e o ambiente envolvente. Essas interações podem causar uma rápida progressão do incêndio e levar ao seu descontrolo e, consequentemente, graves problemas de segurança durante o combate.

Neste trabalho, um modelo conceptual baseado na interação dinâmica entre o fogo, o leito de combustível e o fluxo envolvente é proposto para explicar o comportamento não monotónico ou intermitente do fogo. De acordo com o modelo, o fluxo induzido pelo fogo altera a geometria da chama e a sua velocidade de propagação mesmo sob condições de contorno permanentes e uniformes. Após uma aceleração inicial, ocorre uma desaceleração da velocidade de propagação e é seguida por um ou mais ciclos. Os ensaios laboratoriais controlados com um foco pontual na encosta e num desfiladeiro mostram que a evolução das propriedades do fogo, particularmente o ângulo da chama e a velocidade de propagação, apresentam oscilações de alta frequência sobrepostas ao ciclo de crescimento do incêndio de baixa frequência. Com base na análise da interação entre o fogo e o ambiente sob condições de contorno constantes e uniformes, verifica-se que a evolução da frente de incêndio é caracterizada por flutuações, em particular afeta a velocidade de propagação. Usando um conjunto alargado de um grande número de incêndios com diferentes extensões temporais e espaciais, mostra-se que a amplitude das oscilações da velocidade de propagação é proporcional ao valor médio da

velocidade e que a frequência da oscilação varia de acordo com o tipo de incêndio e aumenta com o valor médio da velocidade para um determinado combustível. No caso de uma propagação rápida, a grande amplitude da velocidade de propagação e a queda brusca da velocidade de propagação favorecem o comportamento intermitente do fogo. Em geral, a amplitude e o período são maiores durante o aumento da velocidade de propagação do que durante a fase de desaceleração. No entanto, as fases de aceleração e desaceleração nos incêndios de junção não seguem esta regra, indicando diferentes processos convectivos de interação entre o escoamento e o fogo. Essa oscilação explica a variabilidade de muitos incêndios em todas as escalas e desafia a interpretação atual baseada nos quatro fatores que influenciam a propagação do fogo e a classificação dos incêndios causados pelo vento ou pela topografia.

Dois incêndios que deflagraram em Pedrógão Grande, Portugal, a 17 de junho de 2017, alastraram-se muito rapidamente devido a processos físicos invulgares relacionados com a interação entre uma trovoada e a junção dos incêndios, matando 66 pessoas em duas horas. Em Quiaios, Portugal, no dia 15 de outubro de 2017, dois flancos propagaram-se pelo menos 7km, ficando separados por 200m antes de finalmente interagirem. Neste trabalho, as interações de incêndios são analisadas. Durante a interação, os fenômenos de transferência de calor por radiação e convecção são extremamente amplificados devido à concentração de energia durante a interação. A concentração de energia e consequentemente o desenvolvimento de um forte mecanismo de transferência de calor levaram a um aumento extremamente alto e repentino da velocidade de propagação durante a interação até atingir um valor máximo, após o qual a velocidade de propagação começa a diminuir.

Uma série de ensaios laboratoriais e a reconstrução dos incêndios reais durante o processo de interação pretendem explicar as condições de propagação do fogo e verificar que a interação dos incêndios foram os responsáveis pelo desenvolvimento muito intenso do fogo. Os resultados da análise do incêndio de Pedrógão Grande mostram que a propagação e junção dos dois incêndios nos testes laboratoriais correspondem muito bem com as observações de campo, principalmente os períodos de aumento e diminuição da velocidade de propagação e o crescimento de área usando as leis à escala. A simulação

física na escala laboratorial mostrou a importância dos mecanismos durante a interação dos dois incêndios para o desenvolvimento de processos convectivos muito intensos. Os resultados da análise do incêndio de Quiaios mostram que a interação piro convectiva entre as duas linhas de fogo paralelas e o vento ambiente alterou a velocidade de propagação das linhas de fogo que se aproximavam. Assim, foi proposta uma interpretação física do desenvolvimento do fogo baseada na interação dinâmica entre duas linhas de fogo paralelas sob a influência do vento. Foi utilizado um parâmetro físico adimensional, o número de Froude, definido pelo rácio entre a força de inércia devido ao fluxo de vento e as forças de impulsão devido ao fogo.

Palavras Chave: Incêndios florestais; Comportamento do fogo Dinâmico; Comportamento extremo do fogo; Aceleração do fogo; Modelação do fogo; Comportamento do fogo oscilatório; Comportamento do fogo intermitente; Convergência de fogos; Fogo de Junção.

Contents

List of Figures

List of Tables

Acronyms and Symbology

Acronyms

Acr.	Description
ADAI	Association for Development of Industrial Aerodynamics
CEIF	Forest Fire Research Center
CT	Combustion Tunnel of the Forest Fire Research Laboratory
DEP	Point ignition fire in a canyon
EF	Escalos Fundeiros
EFB	Extreme Fire Behaviour
EWE	Extreme Wildfire Event
FCT	Portuguese Foundation for Science and Technology
FMC	Fuel Moisture Content
IR	Infrared camera
JF	Junction Fire
LEIF	Forest Fire Research Laboratory
MCS	Mesoscale Convective System
NFB	Normal Fire Behaviour
PG	Pedrógão Grande

PIV	Particle Imaging Velocimetry
PP	Fuel bed of *Pinus pinaster* dead needles
RE	Regadas
ROS	Rate of Spread
SH	Fuel bed of dead shrubs
SP	Point ignition fire in a slope
ST	Fuel bed of straw
TCO	Oblique Combustion Tunnel of the Forest Fire Research Laboratory
UTC	Universal Time Coordinated
WUI	Wildland-Urban Interface

Symbology

Latin Symbols

Symbol	Units	Description
A	-	Intersection point A of the two non-symmetric fire lines
$A_1, A_2, ..., C_2$	-	Idealized evolution of R during a period in which a complete cycle of oscillations
A_o and C_o	-	Two local minima idealized evolution of R during a period
B_o	-	Local maximum idealized evolution of R during a period
d	m	Predetermined distance between the two parallel fire lines
d_{ig}	cm	Distance at which the fire in point ignition fire in a slope and in a canyon is ignited
d_f	m	Minimum particle size
dx_1	m	Fire front displacement in domain S_1
dx_2	m	Fire front displacement in domain S_2
dA_1	m^2	Burned area in domain S_1

dA_2	m^2	Burned area in domain S_2
dV_i	volt	Potential difference produced by the flow pressure, where i represent the number of the pitot tube
F_r	-	Froude number
F^+ and F^-	s^{-1}	Frequency of oscillation (Hz)
g	$m.s^{-2}$	Gravity acceleration
h_f	m	Height of the fuel bed
h	$W.m^{-2}.K^{-1}$	Convection of heat transfer coefficient
k	$W.m^{-1}.K^{-1}$	Thermal conductivity
k_R	-	Coefficient for the linear fitting Amplitude of fluctuations of the ROS as a function of the average value of R_m
k_F	m^{-1} or cm^{-1}	Coefficients for the linear fitting of frequency of fluctuations of the ROS as a function of the average value of R_m
k_f	-	Ratio between fire spread functions of each domain
k_1	-	Slope of the respective fitted line between γ and δ_{JF}
$k_{f_{ref}}$	-	Physical similarity parameter between domain S_1 and S_2. It is assumed that quasi-complete similarity if this ratio is of the order of 1.
L	m	Length characterising the size of the combustion area generating the lift
$\mathscr{L}$	m	Typical total size of the fire assuming that it spreads as a coherent convective cell
ℓ_1	m	Length in system S_1
ℓ_2	m	Length in system S_2
L_{fl}	m	Flame length (also expressed in cm)
L_{max}	m	Maximum flame length (also expressed in cm)
m_f	%	Fuel moisture content
m_c	$g.m^{-2}$	Fuel load on dry basis (also expressed in $kg.m^{-2}$)

M_c	g.m^{-2}	Fuel load consumed by the fire (also expressed in kg.m^{-2})
$O_oX_oY_oZ_o$	-	Absolute reference frame
$O_oX_oY_o$	-	Horizontal datum plane
O_oZ_o	-	Perpendicular to the ground
P	-	Generic point of coordinates (x, y, z) on the surface on which the fire is spreading
P_i and P_{i+1}	-	Positions of the firing line along the reference line
q_x	W.m^{-2}	Density of heat flux transfer by conduction
q	W.m^{-2}	Density of the heat flux transferred by convection
q_r	W.m^{-2}	Radiation flux per unit area
R	m.s^{-1}	Rate of Spread (also expressed in cm.s^{-1})
R_o	m.s^{-1}	Basic Rate of Spread (also expressed in cm.s^{-1})
R_1	m.s^{-1}	Rate of spread in domain S_1 (also expressed in cm.s^{-1})
R_2	m.s^{-1}	Rate of spread in domain S_2 (also expressed in cm.s^{-1})
R_{or}	m.s^{-1}	Basic ROS for the Pedrógão Grande real fire (also expressed in cm.s^{-1})
R_{o1}	m.s^{-1}	Basic rate of spread in domain S_1 (also expressed in cm.s^{-1})
R_{o2}	m.s^{-1}	Basic rate of spread in domain S_2 (also expressed in cm.s^{-1})
R_{ref1}	m.s^{-1}	Reference value ROS at a certain point in area S_1
R_{ref2}	m.s^{-1}	Reference value ROS at a certain point in area S_2
R_j	m.s^{-1}	Instantaneous value of ROS (also expressed in cm.s^{-1})
R_{MAX}	m.s^{-1}	Maximum value ROS
R_A	m.s^{-1}	Rate of spread (ROS) of Point A (also expressed in cm.s^{-1})
$R_{MAX}{}^*$	m.s^{-1}	Maximum value ROS of the test used as a reference (also expressed in cm.s^{-1})
R_{MAXk}	m.s^{-1}	Maximum value ROS analysed (also expressed in cm.s^{-1})
R'	-	Non-Dimensional Rate of Spread
R'_A	-	Non-dimensional Rate of spread (ROS) of Point A

R'_{ave}	-	Average local Non-dimensional ROS values for the three lines a, b and c.
$R'_{\ell\, ave}$	-	Non-dimensional ROS average for $\ell =$ a (line a), b (line b) and c (line c)
$\bar{R}'_{ave}$	-	Average values estimated for each reference line (a, b, and c) and for each distance ($d = 1$ and 2m)
R'_{max}	-	Maximum non-dimensional ROS of the main fire after the merging of the two fires (also expressed in cm.s^{-1})
S_1	-	Domain system 1 – Real fire
S_2	-	Domain system 2 – Laboratorial analysis
S'	-	Non-dimensional distance
sd	-	Standard deviation
S_i and S_{i+1}	-	Distances travelled by the firing line since the origin
S_j	m	Average of distances travelled between two consecutive measurements
S_i	m	Distances of measurement
t_r	s	Residence time
t'	s	Difference between elapsed since the flame passed this point
t_j	s	Average time between two consecutive measurements
t	s	Time of measurement
t_p	s	Arrival time of the flame at each pitot position
t_o^*	s	Coefficient to correct for errors due to differences in the initial timing Δt_i
t_k	s	Time of the test to be analysed
T_x	K	Temperature distribution
T_s	K	Temperature of the surface
T_∞	K	Temperature of the fluid

T_i	K	Flow temperature inside of the flame, where i represent the number of the pitot tube
T_a	K	Ambient temperature
t_o	UTC	Time in real Pedrógão Grande Fire - 18:30h
t_{rj}	UTC	Teal time at scale 1:1
t_{ij}	UTC	Fictitious ignition time to account for the delay time in the ignition in the experiment
t_j	UTC	Time since the ignition of the fire in experiment j
t^*	-	Reduced time
U_0	m.s^{-1}	Ambient wind speed and reference wind velocity
U_w	m.s^{-1}	Windward flow velocities
U_ℓ	m.s^{-1}	Leeward flow velocities
U	m.s^{-1}	Flow velocity
U_i	m.s^{-1}	Flow velocity of Each pitot i=1 to 5
U'	m.s^{-1}	Difference between flow velocity parallel to the fuel bed at a point P and ambient wind speed
U'_{max}	m.s^{-1}	Maximum difference between flow velocity parallel to the fuel bed at a point P and ambient wind speed
U'_{min}	m.s^{-1}	Minimum difference between flow velocity parallel to the fuel bed at a point P and ambient wind speed
x_A	m	Coordinate along the fire spread (also expressed in cm)

Greek Symbols

Symbol	Units	Description
α	º	Slope of the water line in the canyon fires Slope of the fuel bed in the slope fires
α_{TCO}	º	Pitch angle of pitot tube during the calibration in TCO tunnel

β_o	º	Flame angle between the flame and the horizontal surface
β_{fl}	º	Flame angle
β_f	-	Compactness or packing ratio
γ	º	Angle between the bisector of the fire lines and the maximum ROS
δ	º	Slope of the faces of the canyon
δ_{JF}	º	Angle between the bisector of the fire lines and the line with the highest slope
Δt^+	s	Half period of ROS increase: given by the difference of time at B_o and at A_o
Δt^-	s	Half period of ROS decrease: given by the difference of time at C_o and at B_o
Δt_1	s	Time interval in S_1
Δt_2	s	Time interval in S_2
ΔR^+	m.s^{-1}	Amplitude of ROS increase: given by the difference of ROS at B_o and at A_o
ΔR^-	m.s^{-1}	Amplitude of ROS decrease: given by the difference of ROS at B_o and at C_o
ε	-	Surface emissivity
ε_ℓ	-	Length scale factor
θ_0	º	Initial angle between the fire fronts
θ_1	º	Angle between the Escalos Fundeiros fire line and OY axis
θ_2	º	Angle between the Regadas fire line and OY axis
ρ_b	kg.m^{-3}	Fuel bed bulk density
ρ_p	kg.m^{-3}	Fuel particle density
σ	W.m^{-2}. K^{-4}	Stefan-Boltzmann constant
σ_f	m^{-1} or cm^{-1}	Surface-to-volume ratio
τ	-	Time scale factor for distances

τ_A	-	Time scale factor for the areas burnt

Chapter 1. Introduction

This chapter presents the overall framework of the study on fire behaviour and two forest fires that occurred in Portugal in 2017, namely the Pedrógão Grande (PG) and Quiaios fires, which were considered as study cases. The objectives of this work are presented and defined here, considering the approach to the problem from awareness to understanding of the physical processes and modelling of two real forest fires with laboratory experiments. To facilitate the readability and understanding of the thesis, the structure and main topics of each chapter are also presented.

1.1. Background and Motivation

Forest fires are a complex phenomenon that occurs in different regions of the world, sometimes due to natural causes, but in many situations also due to human activities. Fire is a natural phenomenon and belongs to the ecosystems that intervene in the renewal of landscapes and forest models, but also influence the development of different species. Fire should not disappear completely from the ecosystem and prescribed fires need to be used more to control the spread of forest fires in Portugal and to manage the forest fuel load in the landscape.

Forest fires in Mediterranean areas and in fire-prone zones cause significant socio-economic impacts and high negative consequences for society (Alcasena *et al.*

2019). In southern Europe, the annual average number of burnt areas is about 500k hectares and the number of fires is about 50k (Moreira *et al.* 2011; Alcasena *et al.* 2019). The biggest risks and problems caused by large and devastating fires are the loss of human lives, which is unacceptable in a modern society (Schemel *et al.* 2008; Cardil *et al.* 2017). Climate change in recent decades and the increasing availability of fuel in forest areas is one of the main causes of these types of "large fires" (Barrera-Escoda 2011; Moreira *et al.* 2011; Cardil *et al.* 2014). The Portuguese Forest has been characterised for many years by environmental conditions such as lack of water availability, physical and chemical soil properties, but besides all these conditions, human interventions with anthropogenic spread also contribute to most of the changes in the Portuguese forest (Darouich *et al.* 2022; Soares and Lima 2022). These interventions are usually due to human needs, such as socio-economic factors, technological developments, new raw materials and the increase of agricultural and/or grazing areas. The biggest problem in Portuguese Forests and of the entire agro-forestry system today is the impact of forest fires. The Portuguese climate is described as Mediterranean, with wet winters and dry summers (Tedim *et al.* 2013; Louro *et al.* 2014; Amraoui *et al.* 2018; Nunes *et al.* 2019a; b; Skulska *et al.* 2021).

The largest forest fires in Portugal in the last two decades have destroyed many buildings (e.g., houses and production facilities). The year 2017 was particularly severe in terms of forest fires in Portugal, not only because of the large area burned in only two phases of the year (June and October), which were outside the period considered critical in Portugal, but mainly because of the recurrent accidents, the high number of civilian fatalities and the high socio-economic losses. More than five hundred buildings were destroyed by the forest fires in June and October 2017 in the central regions of Portugal. Most of these destroyed buildings could have been saved if the buildings had been properly designed and the forest prevention around them had been properly implemented and firefighting resources were available (Manzello *et al.* 2012; Viegas *et al.* 2017). Regardless of prevention efforts at the landscape level, wildfires will continue to impact people and their assets and tend to be increasingly destructive, costly and socially threatening (Valente *et al.* 2015; Abrams *et al.* 2015). The number of destroyed buildings is also increasing and the trend is upwards, either due to climate change or urban growth

in Wildland-Urban Interface (WUI) areas. Fuel management is very important to reduce the likelihood of damage to infrastructure from wildfires (Ribeiro *et al.* 2019).

Forest fires are the only natural hazard that humans can intervene in and modify their effects (Viegas *et al.* 2011). It is important to improve knowledge about forest fires, especially about their behaviour. Accidents related to forest fires are often associated to insufficient knowledge about fire behaviour, both among firefighters during firefighting operations and in civil society to mitigate the associated risks. It is therefore important to understand the difference between the concepts of Normal Fire Behaviour (NFB) and Extreme Fire Behaviour (EFB). This knowledge is possibly the most important tool available to persons that have to deal with this complex problem. Fires can be characterised by the Rate of Spread (ROS) and fire intensity. Some fire events have low ROS and fire intensity and do not pose a major hazard. According to Viegas *et al.* 2011, these fires scan be classified as NFB. However, several authors point out that under certain conditions forest fires behave in a surprising way, suddenly changing from a moderate or normal behaviour to an explosive spread with a very high ROS and fire intensity with a large energy release. These events show a pronounced dynamic fire behaviour and can be classified and evaluated as EFB. In Viegas *et al.* 2012, the following definition of EFB is proposed: *"EFB is defined as a set of characteristics and properties of wildfire spread that make it impossible to control safely with currently available technologies and knowledge"*. Tedim *et al.* 2018 proposed the term Extreme Wildfire Event (EWE) to designate what is currently referred in the literature as large fires, megafires, or similar terms, based on different metrics to assess the fire behaviour, fire size or duration or the fire impacts of events that are out of normal and therefore cause concern to the society and to fire managers. In Tedim *et al.* 2018, the following definition of EWE is proposed: *"A pyro-convective phenomenon overwhelming the capacity of control (fireline intensity currently assumed* $\geq 10{,}000 kW.m^{-1}$*; rate of spread* $>50 m.min^{-1}$*), exhibiting spotting distance* $> 1 km$*, and erratic and unpredictable fire behaviour and spread. It represents a heightened threat to crews, population, assets, and natural values, and likely causes relevant negative socio-economic and environmental impacts"*.

Examples of EFB include, but are not limited to, conflagrations, eruptive fires, crown fires, patch fires, vortex structures (vertical or horizontal), junction fires, merging fire lines, fire coalescence, etc. This list is not definitive or complete, as it may be modified as other processes become known.

The dynamic fire behaviour is characterised by sudden changes in properties according to Viegas 2004, 2006 and Viegas and Simeoni 2011 and does not correspond to the classical approach of Rothermel 1972, which supports the existence of a unique value of ROS for a given set of boundary conditions. Dynamic fire episodes and EFB events are of particular interest as they are usually associated with personal accidents and significant property damage.

The present work focuses on the specific EFB mechanism caused by canonical cases defined by point fire in a slope, point fire in a canyon and the intersection of two fires, as well as the merging fire lines defined by the merging of two non-symmetrical linear fire fronts (related to the Pedrógão Grande fire) and the merging of two parallel fire lines (related to the Quiaios fire). Research on this topic was motivated by the fire events that occurred in Portugal in 2017, in particular the Pedrógão Grande fire on 17th June, which spread to the Pedrógão Grande communities, and the Quiaios fire, which occurred on 15th October 2017. On 17th June, at 19:30 and for about three hours, the interaction and convergence of the two fire fronts Escalos Fundeiros (EF) and Regadas (RE) in Pedrógão Grande caused a firestorm and a very rapid development of fire spread, destroying more than twenty-four thousand hectares of forest and killing 66 people. This forest fire was considered one of the worst fires in Portugal and in Europe (Viegas *et al.* 2017). On 15th October 2017, two flanks spread in Quiaios, influenced by the strong winds. One flank of the main fire and the other flank caused by the spot fire spread for at least 7km and remained 200m apart before finally growing together (Viegas *et al.* 2019).

1.2. Objectives and Achievements

The present work focuses on the specific Extreme Fire behaviour (EFB) mechanism observed in a series of canonical cases, i.e., (i) point ignition fire in a slope, (ii) point ignition fire in a canyon and (iii) the merging of two fire lines with one intersection point – Junction fires. However, according to two real fires other experimental laboratory tests were made to analyse the merging of two non-symmetrical linear fire fronts (related to the Pedrógão Grande fire) and the merging of two parallel fire lines (related to the Quiaios fire).

The canonical cases were studied with laboratory experiments:

(i) Point ignition fire in a slope (SP) with a slope angle α equal to 20°, 30° and 40°;

(ii) Point ignition fire in a canyon (DEP) with a slope angle α equal to 20°, 30° and 40° and slope of the faces of the canyon δ equal to 40°;

(iii) Symmetric Junction fire in a slope (JF) with a slope angle α equal to 20°, 30° and 40°.

This work aimed to develop a novel concept of wildfire spread integrating the fire's non-monotonic or intermittent growth. Data from the canonical cases made with laboratory and field experiments, and the real forest fires were used to develop this novel concept of fire spread. These aspects were studied exploring the time as a factor, besides the classical factors of slope, wind and fuel properties on fire spread. These interactions change the fire spread properties, namely producing the oscillations that have an amplitude proportional to the ROS and a frequency that depends on the type of fire and its ROS. In fast-spreading fires large amplitude oscillations produce quick changes in the ROS. The amplitude and frequency of these oscillations were also analysed in the present work.

These aspects were associated with real fires (Pedrógão Grande in June 2017 and Quiaios fire in October 2017), aiming for an improved integration with laboratory

experiments. Regarding Pedrógão Grande fire, the two ignitions that started near Pedrógão Grande in June 2017 were affected by the presence of a thunderstorm in the region. This factor caused a rapid-fire spread, above suppression capacity. The two fires merged causing a very fast and intense fire spread. The merging of two real fires, that occurred in Portugal in 2017, were analysed and studied in detail, namely through laboratory experiments carried out with different fuel bed types and wind flow conditions. These experiments were crucial to explain the fire spread conditions and confirm that the junction of the two fires was responsible for the very intense fire development.

The wildfires that occurred in Quiaios, Portugal in October 2017, spread parallel to the main fire potentiated by strong wind conditions on flat ground. In this thesis, the interaction of two parallel fire lines at a certain distance and having different wind flow conditions, which affected the approaching ROS of the fire lines was also studied. The results showed that the interaction between two parallel fire lines has the same tendency independent of the initial distance between the fire lines.

1.3. Thesis Outline

The contents of the thesis are organized into six chapters. In order to facilitate its readability and comprehension this section presents a brief summary of the topics covered in each chapter.

Chapter 2 aims to familiarise the reader with some of the concepts associated to extreme fire behaviour that are studied in the thesis, namely the non-monotonic fire behaviour and intermittent fire spread, and to introduce a conceptual model that can be used to describe these phenomena. A novel concept of fire growth is proposed to describe and interpret the non-monotonic or intermittent growth of a fire over time due to the interaction between the fire, the fuel and the environment. The interaction between the fire and its environment results in oscillations of the propagation features with an amplitude proportional to the ROS and a frequency that depends on the type of fire and

its ROS. In fast-spreading fires, oscillations with a large amplitude led to rapid changes in ROS.

Chapter 3 aims to familiarise the reader with the merging of fires that can occur when two linear fire fronts interacted between them, or two flank approach each other. The merging of two fire fronts that intersect at a small angle result in very high values of ROS. The fire intensity at their intersection and the ROS decrease with time and the angle between the fire fronts increases. Two real fires, Pedrógão Grande and Quiaios in Portugal, where such intersecting fires occur, were the reason for studying this phenomenon.

Chapter 4 aims to present the methodology used and the initial parameters considered for the experimental program. The different studies presented were supported by experimental work at laboratory, field and real forest fire scale. The experimental work carried out in the PhD programme was important to better understand the phenomena of "extreme forest fire behaviour" and "merging fire lines". The description of the test rigs, the equipment used, and the physical problems considered are presented in this chapter.

Chapter 5 aims to present the results and discussions were supported by experimental work at laboratory and field scales, as well as by real forest fires. This chapter is divided into two sections, presenting the results and discussion of the non-monotonic and intermittent fire behaviour, as well as the analysis of the merging fire lines - the analysis of the Pedrógão Grande fire, non-symmetric junction fire and parallel fire fronts under wind flow conditions.

Chapter 6 summarises the main issues addressed in this work and highlights the main contributions made by this work. Some recommendations are made for future work in experimental work at different scales (laboratory, field, and real fire scale). Some topics on computational simulation of the fire behaviour are suggested.

Part of the work presented in this thesis was published in a peer reviewed journal (Viegas *et al.* 2021, 2022, 2023; Ribeiro *et al.* 2022, 2023):

- Viegas DXFC, Raposo JRN, **Ribeiro CFM**, Reis LCD, Abouali A, Viegas CXP (2021) On the non-monotonic behaviour of fire spread. *International Journal of*

Wildland Fire **30**, 702–719. doi:10.1071/WF21016. – A novel concept of fire growth to describe and interpret the non-monotonic or intermittent growth of a fire in the course of time due to the interaction between the fire, the fuel and the surrounding environment is proposed. Experimental fires in slopes and canyons are used to support the concept, see Chapter 2. The contribution for each paper by the author of this thesis was: Data curation; Formal analysis; Methodology; Experimental tests and Writing - review & editing.

- Viegas DXFC, Raposo JRN, **Ribeiro CFM**, Reis L, Abouali A, Ribeiro LM, Viegas CXP (2022) On the intermittent nature of forest fire spread – Part 2. *International Journal of Wildland Fire* **31**, 967–981. doi:10.1071/WF21098. – Interaction between a fire and its surrounding induces spread properties oscillations with an amplitude proportional to the rate of spread and a frequency that depends on the type of fire and its rate of spread. In fast spreading fires large amplitude oscillations produce quick changes of the rate of spread, see Chapter 2. The contribution for each paper by the author of this thesis was: Data curation; Formal analysis; Methodology; Experimental tests and Writing - review & editing.

- **Ribeiro C**, Reis L, Raposo J, Rodrigues A, Viegas DX, Sharples J (2022) Interaction between two parallel fire fronts under different wind conditions. *International Journal of Wildland Fire* **31**, 492–506. doi:10.1071/WF21120. – The interaction of two parallel fire lines under wind flow conditions in laboratory experiments was studied. The two fire lines were separated by a certain distance and the fire spread on a uniform fuel bed without slope was analysed, see Chapter 3. The contribution for each paper by the author of this thesis was: Conceptualization; Data curation; Formal analysis; Methodology; Experimental test; Writing - original draft and Writing - review & editing.

- **Ribeiro C**, Xavier Viegas D, Raposo J, Reis L, Sharples J (2023) Slope effect on junction fire with two non-symmetric fire fronts. *International Journal of Wildland Fire* **32**, 328–335. doi:10.1071/WF22152. – In Pedrógão Grande on the 17th June 2017, two-fire fronts merged and the propagation of the fire was influenced by the interaction of these non-symmetric fire fronts. We found that the ROS for small rotation depends on the slope angle and the initial angle between fire fronts, see Chapter 3. The contribution for each paper by the author of this thesis was: Conceptualization; Data

curation; Formal analysis; Methodology; Experimental test; Writing - original draft and Writing - review & editing.

- Viegas DX, **Ribeiro C**, Almeida M, Pinto P, Ribeiro LM, Silva Á (2023) Field and laboratory analysis of the junction fire process in the catastrophic fire of Pedrógão Grande in June 2017. *International Journal of Wildland Fire*. doi:10.1071/WF22161. – Two fires that started near Pedrógão Grande in June 2017 were affected by the presence of a thunderstorm in the region, spread out of control and merged producing a very fast spreading fire. A laboratory scale study of this fire showed good qualitative and quantitative agreement with the full-scale observations, see Chapter 3. The contribution for each paper by the author of this thesis was: Conceptualization; Data curation; Formal analysis; Methodology; Experimental test and Writing - review & editing.

Chapter 2. Non-monotonic and Intermittent Fire Behaviour

The purpose of this chapter is to introduce the concepts of non-monotonic fire behaviour, the intermittent nature of forest fire spread and to introduce a conceptual model that allows the phenomena to be described. A novel concept of fire growth will be proposed to describe and interpret the non-monotonic or intermittent growth of a fire over time due to the interaction between the fire, the fuel and the environment. The interaction between fire and its environment results in oscillations of the propagation characteristics with an amplitude proportional to the propagation velocity and a frequency that depends on the type of fire and its Rate of Spread (ROS). In fast-spreading fires, oscillations with a large amplitude led to rapid changes in ROS. Laboratorial experimental tests in slope, canyon and junction fire, field experiments or real fires are used to support this concept.

2.1. Fundamental Concepts

The spread of forest fires is a complex process that is not fully understood despite the variety of approaches that have been used in research in recent decades, from purely empirical to fully theoretical approaches that aim to model and predict fire behaviour. Pastor *et al.* 2003 and Sullivan 2009 provide an overview of the state of the art in fire

behaviour research and provide a variety of references that illustrate the complexity of the problem and the difficulty in finding a general and complete solution. Currently, it is only able to predict fire behaviour under very limited conditions (Thomas *et al.* 2017). This does not consider some of the cases that could be of greater practical importance, such as very intense or fast-moving fires, which are of great concern to fire managers and put people's lives at risk (Bowman *et al.* 2017).

The spread of forest fires is often analysed as a static process that depends on several factors - wind speed, slope gradient and fuel - which, according to some formulations, should be sufficient to determine a well-defined value for the ROS of a fire front (Rothermel 1972, 1983). This concept is due to the fact that in the past little attention was paid to the role of convection induced by the presence of fire and its interaction with the surrounding flow (Viegas 2002, 2004; Finney *et al.* 2015).

It is interesting to find in the classic work by Byram 1959 already an idea of the variability of fire behaviour. Drawing on an excellent scientific background, great intuition, and observation of many real situations, Byram states that *"a high intensity fire has a tendency to pulsate or burn in surges, which can produce a rather wide fluctuation in flame length"*; and later *"the fire that remains small or at low intensity is entirely controlled by its environment. It increases in its state of energy production with time, when fuels and burning conditions combine to produce a very high rate of energy release, the fire interacts with its environment and may modify it drastically."* Quoting experienced firefighters, he says that *"it begins to write its own ticket"*. Few lines below *"a going fire tends to take on a personality of its own and its dynamics easily equate with the behaviour of a living thing in the mind of a firefighter"*. Commenting on the role of wind and topography, Byram says the following: *"the rate of build-up of fire spread in heavy fuel, in level country, and under the influence of a brisk wind is slowed down when the fire's intensity becomes high enough to produce a strong indraft opposite the direction of fire spread"*. Then Byram says that *"this self-regulating process does not occur when a fire builds up intensity when spreading upslope"*, which, according to Viegas *et al.* 2021, is incorrect when analysing fires in slopes and canyons. When it comes to the concept of "blow-up", Byram speaks of a reinforcement cycle to describe the transition

from a low energy to a high-energy state in fire intensity, which he says is *"is seldom a gradual process"* which means that it increases in spurts triggered by factors such as an increase in wind speed, local crowning, or numerous spots. It is interesting to note that these are all external factors and not necessarily due to the fire itself and its dynamics.

A fundamental step in fire modelling is to understand how fires change their properties over time due to the dynamic interaction between the fire and its environment. In 1959, Berlad and Yang questioned the conditions for the existence of a steady state in flame propagation based on the law of conservation of energy (Berlad and Yang 1959). In an earlier work developed by Viegas 2004, he stated that fire behaviour in general is a dynamic process in the sense that even if the boundary conditions are permanent, the properties of fire behaviour depend explicitly on time or distance. In Viegas 2002, it has already been shown that transverse convection along the fire line changes the ROS of the fire and causes its rotational movement. In Viegas and Pita 2004, research on the dynamic behaviour of fires was extended to fires in canyons. In Viegas 2005, 2006 it was shown that the convection caused by the fire causes an acceleration of the fire, called eruption, which is often observed in canyons or on steep slopes. According to the proposed mathematical model, the ROS increases after a relatively short period of time and reaches very high values tending towards infinity, although it was realised that this is not possible under real conditions. In the model, the residence time (t_r) of the combustion in the fuel bed plays an important role. It was used to characterise the dynamic response of the fuel to changes in environmental conditions (namely wind or slope changes) caused either by external conditions or by the fire itself. In Viegas 2005, the concept of the *"square fire factors"* was introduced, which proposes "time" as an explicit factor for fire spread characteristics to account for the dynamic nature of combustion. Dold *et al.* 2006 also addressed this problem.

When analysing the intersection of two linear fires (Viegas *et al.* 2012; Viegas, Raposo, *et al.* 2013; Raposo *et al.* 2014, 2018; Xiaodong *et al.* 2014; Raposo 2016; Ribeiro *et al.* 2023), a non-monotonic evolution of the ROS of the head fire was observed, with a very rapid increase in ROS followed by a decrease. In Raposo *et al.* 2018, this fact

was interpreted as the effect of an opposing flow caused by the very fast spreading fire, which is consistent with the statement of Byram 1959, showing that this flow could limit the growth of the fire and provide a solution to the problem of an infinite ROS predicted by the mathematical model. Thomas *et al.* 2017 also studied this problem. In Ribeiro *et al.* 2023, the interaction of two non-symmetric fire fronts was analysed and they found that the ROS for a small rotation of the Junction Fire depends on the slope angle and the initial angle between the fire fronts. It was also reported that in the interaction of non-symmetrical fire fronts, the convection mechanism is dominant and changes the fire behaviour when the slope angle is high. However, for lower slope angles the radiation becomes more important and influences the fire behaviour.

Albini 1982 studied the variability of wind-assisted fires and found that ROS fires in natural fuels are very sensitive to wind speed, but in many cases, the ROS can also vary considerably with time, even though the fuels and meteorological conditions remain essentially constant. Based on the spectral density of wind fluctuations at frequencies below 0.1Hz, Albini predicted that the fire's response would be oscillatory, with a spectral response that depends on the type of fuel and on the average value of the wind speed. According to this model, there is a dominant oscillatory amplitude of the ROS for a frequency between 0.01 and 0.02Hz, but the average value of the ROS does not seem to change. Although this study captured some of the characteristics of dynamic fire behaviour, it did not consider the natural fluctuations that occur even when there is no wind and the large amplitude fluctuations of the ROS. Finney *et al.* 2015, 2019 and Silvani *et al.* 2018 also addressed the problem of variations in fire properties due to turbulence in fire-induced convection.

Silvani *et al.* 2012 analysed the effect of slope on fire spread in laboratory experiments using video images and heat measurements. Using spectral analysis of gas temperature and total heat flux density, they found an increase in the frequency of fluctuations when the slope was increased from 0 to 30°.

Several authors have studied the spread of a point or linear fire in a slope, namely Mendes-Lopes *et al.* 2003; Dupuy *et al.* 2011 and Silvani *et al.* 2018. Although they

acknowledge the variability of fire spread, they assume that the fire spreads in a steady state and essentially give average values for the fire spread characteristics.

2.2. Fire Dynamics

It is considered a fire spreading with a flaming fire front on a fuel bed at or near the ground surface. The balance of energy exchange between the combustion regions in and above the fuel, the surrounding environment, and the unburned fuel in front of the fire front, considering conduction, convection and radiation, yields as a result the ROS of the fire front in the fuel bed (cf. Albini 1981, 1982; Weber 1989). This ROS of the fire front is a critical parameter in the analysis of fire behaviour because many other properties of fire spread, such as the intensity of the fire line, fuel consumption, smoke production, possibility of extinction, and growth of perimeter or burned area, are related to it.

Each point P on the area where the fire spreads can be associated with the following parameters $P(x, y, t)$, where x and y represent the coordinates that define the position of the point, and t is the time of arrival of the fire at the point. Although the ROS can be defined at any point on the fire line, the head ROS of the most advanced or rapidly spreading section of the fire is of particular importance. Knowledge of this ROS and the ability to estimate its temporal and spatial evolution is of great practical importance because it gives an indication of where the fire is spreading, how fast it is growing, and what can be done to prevent or suppress it.

The oscillatory processes considered occur throughout the fire area because they have a three-dimensional character, as noted by Finney *et al.* 2015. It is concerned with the analysis of fire propagation and its oscillations along the main propagation direction which is characterized by a curved or quasi-linear coordinate x, considering that the fire head trajectory is not necessarily a straight line. Along this line, which contains the fire origin, each point is characterized by $P(x, t)$. Alternatively, it can be used the Rate of Spread (ROS) R, which is defined as follows:

$$R = \lim_{dt \to 0} \frac{dx}{dt} \quad (1)$$

If $R(t)$ is known, it can be determined x by integrating equation 1 into the time from the fire source to t, and therefore each point can be characterized by either $P(R,t)$ or by $P(R,x)$. This means that x, R, or t can be used as independent variables, as needed for fire spread analysis. At each point in this trajectory, the fire will have a particular value $R(x)$. Since each point is reached at a specific time t, the time is used alternatively to describe the evolution of ROS during fire spread $R(t)$.

2.2.1. Square Fire Factors

It is well known that fire spread characteristics depend on the following group of factors, referred to as the *"square fire factors"* (Viegas 2005): (i) topography, (ii) fuel, (iii) meteorology, and (iv) time. In the literature, there is ample evidence of the role and relevance of these factors acting individually or together (Chandler *et al.* 1983). Some key parameters that characterize each one of these factors will be briefly reviewed to provide the basis for the following analysis of the non-monotonic fire behaviour and the intermittent nature of forest fire spread.

Topography

Of the various parameters required to define the terrain topology around the site of fire spread, two remain: (i) the slope angle of the terrain α (º) or simply the inclination; and (ii) the curvature of the terrain that characterizes its convex or concave shape. In this context, concave-shaped terrain, such as ravines or canyons, is of particular importance because they are prone to very rapid eruptive fires (Viegas 2004, 2005). Over the years, many accidents involving firefighters have been recorded in this terrain configuration, due to the rapid and sudden evolution of the fire (Rodrigues *et al.* 2019).

Fuels

A surface fuel bed is characterized by a number of parameters (Rothermel 1972, 1983), namely the fuel load m_c (g.m^{-2}), the height of the fuel bed h_f (m), the compactness

or packing ratio β_f (-), that is given by the ratio of the fuel bed bulk density (ρ_b) by the fuel particle density (ρ_p), the minimum particle size d_f (cm) or its equivalent surface-to-volume ratio σ_f (cm^{-1}), and the moisture content m_f (%) of the particles. For simple fuel beds consisting of uniform particles, as found in many laboratory experiments, these parameters can be easily estimated. However, for real fuel beds consisting of a mixture of particles of different sizes, shapes, and properties, averaging methods such as those proposed by Rothermel 1983; Viegas *et al.* 2013 or Weise *et al.* 2022 must be used to estimate representative values of these parameters. Therefore, for the present work, three parameters: M_c (the typical fuel load consumed by the fire), m_f and σ_f will be kept, or, as an alternative, the minimum dimension d_f (m) of the fuel particles, knowing that in general $\sigma_f \approx 1/d_f$.

Meteorology

Among the various meteorological parameters relevant to fire spread, it is considered those related to changes in fuel moisture content, fire spread, especially wind speed and direction and atmospheric stability. It is assumed that the fuel moisture content, which depends primarily on solar radiation, precipitation, air temperature, relative humidity and ambient wind speed is included in the fuel bed properties. However, it will retain ambient wind speed U_0 (m.s^{-1}) and consider the only meteorological parameter affecting ROS.

Time

Most studies consider average values of fire spread properties and do not consider explicitly time as a parameter or factor in fire behaviour analysis. Time was proposed as an explicit factor by Viegas 2005, in recognition of the dynamic nature of fire behaviour, meaning that in cases where all the above parameters (topography, fuels and meteorology) remain constant in space or time, fire spread properties may change

due to the interaction between the fire and its environment. Examples of this are the spread of a point fire in a slope or a canyon (see Viegas and Pita 2004).

2.2.2. Heat and Mass Transfer Mechanisms

In this section, the most important types of heat transfer mechanisms (conduction, convection and radiation) and mass transfer in connection with the spread of fires are presented. Some basic equations about the process of the heat transfer mechanism are presented. However, they were not directly applied during the present work.

Conduction

Conduction is the mode of heat transfer within the material itself by temperature gradients and the thermal energy is transmitted from the molecules. The density of heat flux transfer by conduction q_x (W.m^{-2}) in a one-dimensional plane with a temperature distribution T_x can be quantified by Fourier's law of one-dimensional heat conduction (Incropera *et al.* 2011):

$$q_x = -k\frac{\partial T}{\partial x} \qquad 2$$

where k (W.m^{-1}.K^{-1}) represents the thermal conductivity and is a material specific property. For plant/wood materials such as forest fuels, the value of k is very low (0.12W.m^{-1}.K^{-1} for softwoods) compared to other materials such as Aluminium (239W.m^{-1}.K^{-1}) (Carvill 1993). Therefore, the mechanism of heat transfer by conduction in forest fires is commonly considered too slow to be significant for heat transfer through a porous fuel bed (Chandler *et al.* 1983).

Convection

The convection process is considered a critical heat transfer mechanism during forest fires because is responsible for the heating and ignition of the fuel elements by

contact with the hot gas freedom by the combustion and flames. Heat transfer by convection is characterised by the transport of heat through a fluid in motion and can be classified into two categories according to the type of flow of fluid driven. In general, when the movement of a gas or liquid is caused by the buoyancy forces due to the density differences caused by the temperature difference is considered natural convection – for example, the rising of hot air and the sinking of cold air. Forced convection corresponds to heat transfer due to the movement of a gas or liquid caused by external influences such as wind or pressure differences. Natural and forced convection often play a combined role during wildfires and this can be called mixed convection. Convection can be expressed by Newton's cooling law (Incropera *et al.* 2011):

$$q = h(T_s - T_\infty) \qquad 3$$

where q (W.m^{-2}) represents the density of the heat flux transferred by convection, h (W.m^{-2}.K^{-1}) represents the convection of heat transfer coefficient, T_s (K) represents the temperature of the surface and T_∞ (K) represents the temperature of the fluid.

The role of fire-induced convection, possibly enhanced by the terrain configuration and its interaction with the combustion process and the shape of the fire front, is sometimes overlooked, making it difficult to explain some features observed in wildfire spread in complex terrain (Viegas and Pita 2004).

For small-area fires, it is true that convection is usually associated with surface atmospheric winds or buoyancy-induced flows. For large fires, these convective currents interact with the upper layers of the atmosphere and create a feedback process (Huang *et al.* 2020). These convective flows are a source of extremely high ROS and sudden changes in their value. This highlights the importance of the heat transfer mechanism of convection to the phenomena of EFB.

The convectively induced flows can further increase the ROS in situations where these flows are aligned with the main direction of fire propagation, either by the effect of the slope or by the angle formed between the flow and the terrain. In this way, a greater amount of heat is released in the upstream fuel, increasing the rate of combustion of the fuel and, consequently, the ROS of the fire front.

Convection is an important factor considered for the experimental laboratory configuration tests made in this work. The fire configuration generates very strong currents that develop within the burning area due to the concentration of energy created by the canyon, slope, or merging of the fire fronts, which favours the propagation of the main fire. These induced flows increase the fire ROS more effectively with a greater angle of slope that causes the generated flow to approach the fire source.

The deceleration phase also depends on convective activity, as the flame configuration gradually changes and a counter-current begins to reduce the ROS of these fires, after which radiation is the main mechanism of this fire propagation phase.

Radiation

The energy emitted by matter at a given temperature above absolute zero is considered as thermal radiation. Radiation heat transfer is the transmission of thermal energy through electromagnetic waves, and it is considered an important heat transfer mechanism during forest fires because hot flames radiate thermal energy to the nearby fuel particles and influence the firefighter's safety. The radiation flux per unit area q_r (W.m^{-2}) is given by the Stefan-Boltzman law (Incropera *et al.* 2011):

$$q_r = \varepsilon \, \sigma \, T_s^4 \qquad 4$$

where ε is the surface emissivity, σ is the Stefan-Boltzmann constant (W.m^{-2}. K^{-4}), and T_s (K) is the absolute temperature of the surface. However, when two different objects at different temperatures face each other, they exchange radiation. The hotter object emits more radiation than it absorbs from the cooler object and the resulting in a net transfer of energy from hotter to cooler. According to several authors, namely Chandler *et al.* 1983; Viegas 2002 and Frankman *et al.* 2013, thermal radiation is an important mechanism in the ROS because very high temperatures are reached in the reaction zones of the fire. At the fire front, there are two main combustion zones: one inside the solid porous fuel bed and the other in the gas phase, in the flame above the fuel bed. The radiation from the solid phase inside the fuel bed has a relatively short range due to the attenuation by the solid fuel particles, so its heat flux causes a relatively slow propagation of the fire front.

The radiation from the flame surface depends essentially on the size and shape of the flame, especially on its angle of slope with respect to the unburned fuel.

When the flame is inclined in the direction of the fuel already burned, e.g., fire spread goes downhill or against wind, the contribution of the flame to the spread of the fire is relatively small and the ROS will be very low and practically constant. The shape of the reaction zone is not very much affected in this case. However, if the fire front spreads in a favourable wind or slope, the flame will be inclined toward the unburned fuel, its distance from the fuel bed will be smaller, and its shape factor in relation to the fuel bed will be much larger, which will significantly increase the rate of spread. Sometimes it is not easy to distinguish between convection and radiation effects since both acts together.

Mass Transport

The mechanism of mass transport is the process of removal, transport, and release of burning particles from the fire front that are stirred up by the convection column and fall at a considerable distance from the main fire (Sardoy *et al.* 2007). When these embers, transported by convection and wind, fall on ignitable material, new fires or spot fires can start, with attendant hazards to firefighters (Ellis 2000; Almeida 2011; Storey *et al.* 2021). These spot fires are particularly common and dangerous in large fires with strong convective activity and can endanger the safety of firefighters (Tarifa *et al.* 1965). Because of its complexity, this is still an open problem in wildfire research. Despite its importance, the mechanism of mass transport was not considered in the present work.

2.2.3. Combustion

The combustion reaction can be most simply described by the reaction of a hydrocarbon fuel with air and is given by:

$$Fuel + air \rightarrow H_2O + CO_2 + \cdots \qquad 5$$

Fuel and air are the reactants in this reaction and water, carbon dioxide and other elements ⋯ are the primary reaction products. The combustion of fuels in the wild during

a fire is even more complex, as it consists of hundreds of thousands or even millions of intermediate reactions. To simplify this analysis, the combustion of cellulose was considered, as it is of great importance for fuels in the wild (Byram 1959; Rothermel 1972, 1983; Sullivan and Ball 2012).

Cellulose consists of long sequences of glucose and the chemical formula is $(C_6H_{10}O_5)_j$, where j is any integer. On average, air consists of 21% oxygen (O_2), 78% nitrogen (N_2), and 1% other gases, mainly argon (Ar), carbon dioxide (CO_2) and water vapour (H_2O) (Shi *et al.* 2013). The combustion reaction of a glucose is given by (Yang *et al.* 2007; Sullivan and Ball 2012):

$$C_6H_{10}O_5 + 6(O_2 + 3.76N_2) \rightarrow 6CO_2 + 5H_2O + 22.56N_2 \qquad 6$$

In the analysis of the chemical reaction, the number of molecules or molecular moles on either side of the equation is equal to the number of atoms of each element. The atoms of carbon, hydrogen, oxygen and nitrogen are neither created nor destroyed in a chemical reaction, but only rearranged. The stochiometric combustion process requires much more air than fuel (Côté 1968).

2.2.4. Ignition

The ignition process is an essential step in fire spread. Forest fuels are different from liquid or gaseous fuels because they (forest fuels) are not uniform or continuous. Ignition is considered the beginning of the combustion process. The flames seen in the combustion of solid fuels are the result of the combustion of flammable gases produced by the thermal decomposition, i.e., pyrolysis, of solid fuels. The first step is to heat the fuel to the point where gaseous fuel begins to form. This is considered one of the most important steps in the combustion process. Heating can occur by thermal radiation from the approaching flames, by convection when in contact with the flames, by the rise in temperature around the fuel or by direct contact with a burning ember. During this process, the temperature of the fuel increases and some of the fuel moisture is vaporised when the temperature of the fuel reaches 100ºC. The evaporation rate is highest for dead

fuels compared to live fuels (Babrauskas 2002; Safdari *et al.* 2019; Amini *et al.* 2019; Weise *et al.* 2022).

As the fuel is heated in continuous mode, the temperature continues to rise, and the pyrolysis process begins. Pyrolysis is a chemical reaction and the gaseous fuels produced are sometimes referred to as pyrolysis states. The process for a low temperature is different compared with the higher temperature, because for lower temperature the molecules are larger compared with the higher temperature (Finney *et al.* 2013, 2015; McAllister and Finney 2014). In this fact, for the higher temperature, those molecules are more ready to react chemically, and the rate of pyrolysis is strongly dependent of the temperature. However, the pyrolysis process for the solid fuels is very complex. It is not really known what the gaseous fuel in forest fires are produced and only a global approach with a simplification of hundreds of thousands of individual chemical reactions is made.

The pyrolysis temperature depends on the molecular structure of the solid fuel because some structures are more stable compared with others that are more likely to break apart, e.g., hemicellulose begins at $\sim 260°C$, cellulose at $\sim 355°C$ (Yang *et al.* 2007) and lignin intermittently between 350 and $600°C$ (Kawamoto 2017). This temperature indicated when the thermal breakdown begins, not when the combustion process occurred. So, it can be considered a pyrolysis temperature around 300ºC and at this temperature the fuel gases (pyrolysates) may be visible, and the smoke is white or grey (Finney *et al.* 2013; McAllister and Finney 2014; Safdari *et al.* 2019; Amini *et al.* 2019; Weise *et al.* 2022).

2.3. Fire Evolution

2.3.1. Conceptual Model

The present conceptual model of fire evolution assumes that a head fire is created by a flaming fire front on a flat surface with a homogeneous fuel bed and with a uniform and permanent ambient flow over the surface of the fuel bed characterised by a reference

velocity U_0. Alternatively, it is assumed that the fire propagates along a slope or canyon with constant slope α with respect to a horizontal reference datum.

It is recognised that fires are always 3D processes, and the variations in fire and flow properties along the *OX* axis described also occur along the *OY* axis and form a convection cell as observed by Finney *et al.* 2015. In the present work, it is addressed the phenomena along the main fire propagation direction that are relevant to practical applications in the case of fires driven by slope or wind.

In Figure 1 a), it is presented the conceptual evolution of fire spread characteristics, namely flame length (L_{fl}), flame angle (β_{fl}) as a function of time and the diagram of characteristic windward U_w and leeward U_ℓ flow velocities, see Figure 1 b). At the beginning of the fire (stage 1 in Figure 1), the flame angle (β_{fl}) is nearly vertical ($\beta_{fl} = 90°$) and the natural convection flow is symmetrical on both sides of the fire. The presence of a constant wind flow, a constant slope, or a topographic effect, inclines the flame towards the fuel, decreasing its angle ($\beta_{fl} < 90°$) and increasing the ROS (stage 2). The growth of the fire due to the flame and the prevailing wind is described and explained by the feedback effect in Viegas 2005 for the process of fire growth in a canyon.

The larger value of ROS, the greater the depth of flame and thus the amount of fuel burning will increase simultaneously. For this reason, the flame thickens and begins to become vertical, increasing the value of β_{fl} due to the greater amount of fuel burning and increased buoyancy (Stage 5). As the fire accelerates, the local flow on both sides of the flame also increases. The increase in ROS and flame length with local flow velocity and the decrease in slope angle with wind or slope are described in detail in the literature (cf. Dupuy 1995) and are documented below.

The increased modulus of the flow velocity on the lee side of the flame contributes to its deceleration, and after reaching a value of $\beta_{fl} \approx 90°$ (stage 7), the ROS decreases and reaches a local minimum, so a new acceleration cycle begins (stage 8), but with a larger and deeper flame front than in stage 1. This cycle can be repeated several times if the boundary conditions persist.

To analyse the asymmetric flow near the flame, two characteristic reference values U_w and U_ℓ are considered for the flow velocity on the windward and leeward sides of the flame, respectively (Figure 1 b)). The flame is assumed to be sufficiently thick to prevent flow through it and to act as an impermeable or solid surface separating the leeward and windward flows.

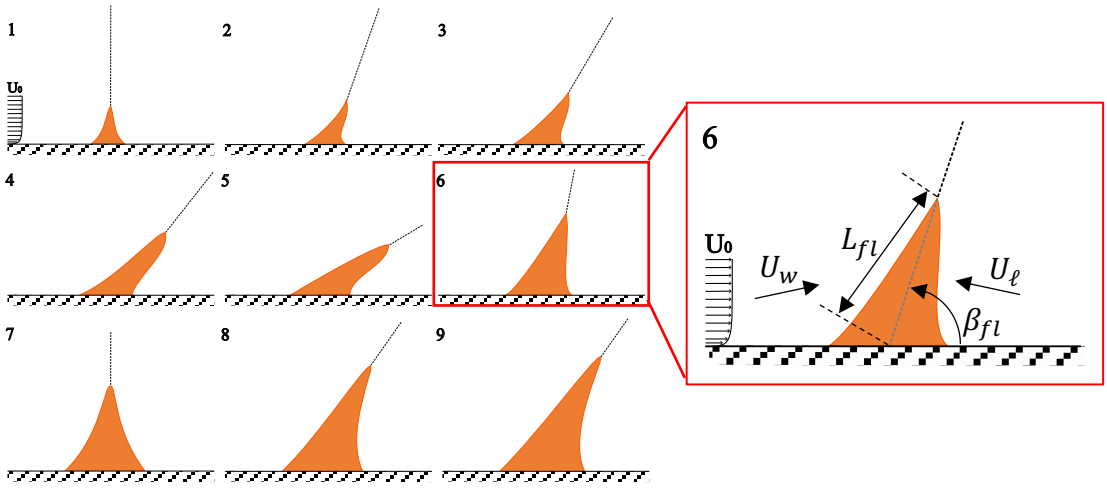

a) b)

Figure 1: a) Conceptual temporal evolution of a 2D flame front on a plane surface with a constant wind flow characterized by the reference velocity U_0. b) Diagram of characteristic windward U_w and leeward U_ℓ flow velocities and definition of the flame length (L_{fl}.) and flame angle β_{fl}.

According to Viegas 2005, the presence of the flame alters the ambient flow over time. During the time period dt, the amount of air and oxygen introduced by the ambient flow at the characteristic velocity U_0 will enhance the combustion process, leading to an increase in the energy released during combustion at the fire front. As a result, the flame length increases, and the value of the wind flow velocity U_w also increases and becomes equal to $U_0 + dU$. Due to the higher energy flow, the ROS of the fire increases and the flame angle β_{fl} becomes smaller. The increasing heat release of the fire during its growth changes the inflow from the lee side, so the velocity U_ℓ also gradually increases.

In the time from t_1 to t_2, the previous processes continue in infinitesimal steps until stage 2 is reached at time t_2, when the flame length and the evolution of the fire - represented, for example, by the Rate of Spread (ROS) or by the flame length - increase

and the value of β_{fl} decreases. This evolution goes from stage 2 to 3 and further to 4 and 5. At this stage, the increase in U_ℓ will cause the fire front to slow down and β_{fl} to increase until it again reaches a value close to 90º (stages 6 and 7).

It is assumed that the flow velocities are measured relative to the fire front, in a reference frame where the flame is static (see Figure 1 b)). In the case of a fire front moving with a ROS R that is of the same order of magnitude as the horizontal component U_x of U_w or U_ℓ, a correction should be made in defining these relative velocities. If $R \ll U_x$ this correction is not important, but in the case of fast-moving fires it should be considered.

2.3.2. Rate of Spread Evolution

To analyse the evolution of the fire front, it is followed many authors, namely Byram 1959; Rothermel 1972, 1983; Albini 1981, 1982; Sharples 2009; Alexander and Cruz 2017, the concept of the ROS of the head fire is used, as it gives a very important indication of the evolution and intensity of the fire. Various fire properties related such as fire line intensity, flame length, energy release rate, residence time, heat impact on the ground, gas emissions, and others can be inferred from knowledge of the local ROS (see (Freeborn *et al.* 2008; Canfield *et al.* 2014; Moinuddin *et al.* 2018). Accurate knowledge of the evolution of the main fire in conjunction with other information about the terrain, fuel cover, and topography, can also provide an overall assessment of fire spread and the extent or evolution of the burned area over time.

As a result of the process described above, according to the present model, the ROS of the fire front will exhibit the temporal evolution shown in Figure 2 with a sort of looping effect. There is an initial increase in ROS Stage 1 to Stage 7, then a decrease to Stage 8, followed by another cycle. At the beginning of this second cycle, the fire usually has a higher ROS than in Stage 1 as the flame grows to Stage 6. Eventually, the cycle may repeat one or more times, as shown in Figure 2 and observed in the fire tests shown below and in some real fires (see Anderson 1968; Wade and Ward 1973). Superimposed on the general cycle of development of ROS are a process of higher frequency during a

short period of time and low amplitude fluctuations resulting from the dynamic interactions between the fire and the surrounding turbulent flow. These fluctuations are not shown in Figure 2 for clarity but are clearly demonstrated in subsequent laboratory experiments.

The conceptual evolution of the angle β_{fl} with time is also plotted in Figure 2 with the same time scale, but with an arbitrary vertical scale. At the beginning of the fire, the value of β_{fl} is close to 90º, then decreases to a value of the order of 30º and increases, while ROS continues to increase and reaches a local maximum close to 90º, after which another cycle begins. As shown in Figure 2, the growth of R is gradual and then followed by a sudden decrease, as confirmed in the experiments, giving the fire behaviour the characteristic oscillatory or intermittent pattern. This sudden decrease, caused by the overall fire dynamics triggered by the fire, explains why an eruptive fire in a canyon does not reach infinite values of R after a finite time, as predicted by the mathematical model of Viegas 2005, 2006, because the changes in flame and flow properties during this phase reduce the value of R significantly.

The present model is mainly concerned with the kinematic properties of the fire and the surrounding flow, but it must be considered that the flow-induced changes in the flame geometry are associated with a change in the combustion processes as well as in the force balance and heat transfer processes of the flame system, leading to a change in ROS over time. This time dependence on the fire properties induced by the fire itself leads to defining this process as dynamic, in contrast to other approaches that mainly consider average values of the fire properties (Viegas 2005, 2006; Viegas *et al.* 2021, 2022).

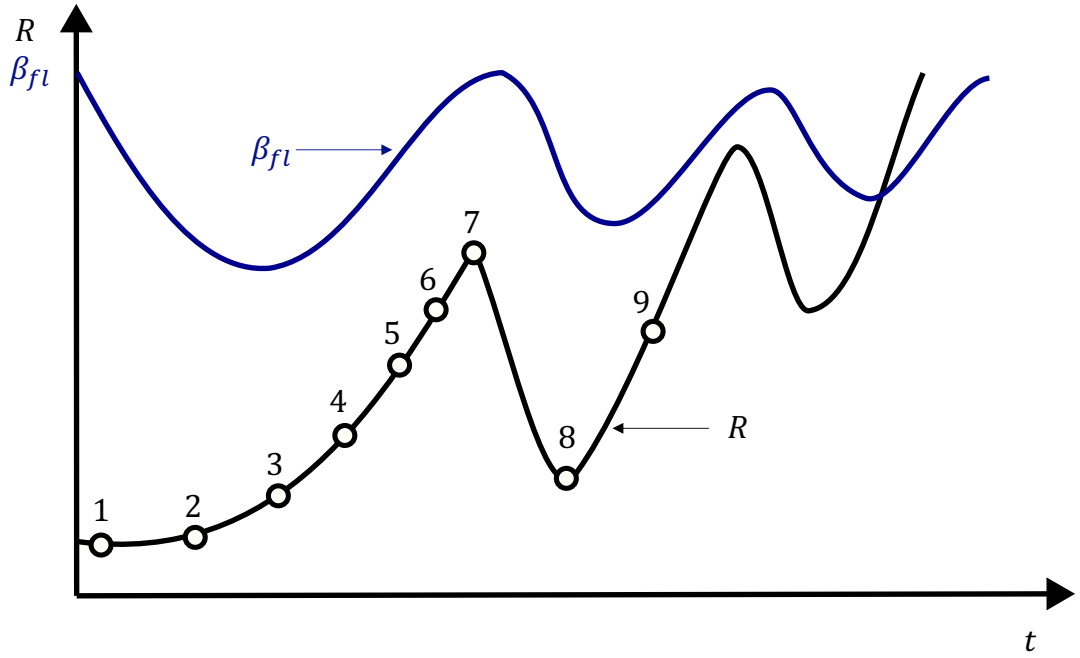

Figure 2: Conceptual time evolution of the flame angle β_{fl} and of the ROS R of a head fire with constant wind flow or slope. An arbitrary scale was considered for each value of β_{fl} and R.

2.3.3. Reference Flow Velocities

To analyse the flow near the fire front, it is considered the time evolution of the component of the flow velocity $U' = U_x - U_0$ parallel to the fuel bed at a point P located at a certain distance above it, as a function of the time $t' = t_p - t$ elapsed since the flame passed this point. If the flow induced by the fire has opposite directions on either side of the flame, it is considered the time t_p at which the relative velocity U' changes sign as the time of arrival of the fire at P. As shown in the laboratory experiments, the flow velocity increases on the windward side U_w of the flame due to the draft generated by the fire and reaches a maximum value U'_{max}. Then the flow velocity decreases and is zero at the trailing edge of the flame becomes negative on the leeward side U_ℓ of the flame and reaches a minimum value U'_{min} in front of the leading edge of the flame. It will be used these values of U'_{max} and U'_{min} as reference flow velocities for the upwind and leeward flows, respectively, near the flame.

The conceptual curve was validated with the experimental results when the no wind conditions ($U_0 = 0$), in this case, the value of $U' = U_x$. When the process of fire propagation is unsteady, knowing the evolution of the propagation velocity $R(t)$, it is possible to estimate the distance $x_f(t)$ of the flame to the point *P* as follows:

$$x_f = \int_{t_P}^{t} R(t_P - t).dt \qquad 7$$

Negative and positive values of x_f correspond to the windward and leeward sides of the fire, respectively.

2.4. Intermittent Fire Spread

In this work, the temporal evolution of ROS in fires that ideally spread on a uniform fuel bed, on terrain with a uniform configuration (constant slope or curvature), and with a constant and permanent wind flow is considered. It is easy to see that such conditions exist only in very controlled laboratory experiments. In field experiments or real fires, even if one factor (such as wind or slope) is dominant, some parameters, such as fuel coverage, may change, leading to uncertainties in the analysis.

2.4.1. Oscillatory Fire Behaviour

There is evidence in the literature and in the analysis of fire spread at various scales that ROS does not remain constant even under nominally permanent and uniform boundary conditions but evolves with oscillations that can reach quite high values and drop suddenly in intermittent form, as in eruptive fires (Wade and Ward 1973; Simard *et al.* 1983; Rothermel and Mutch 1986). These can be observed over a wide range of space and time, as illustrated by the three examples shown in Figure 3.

In Figure 3 a) it can be seen the evolution of *R* as a function of time or distance travelled by the source of the fire in a laboratory experiment with a point fire in a canyon (test DE301). Figure 3 b) shows the results of a field experiment with a linear fire

spreading upslope (Test 807), and Figure 3 c) shows the estimated values of R, also as a function of time or distance, in the case of the Sundance fire (Anderson 1968). It is used the same units in all plots to illustrate the variation in the parameters involved and the predominant oscillatory behaviour of fire spread in all cases.

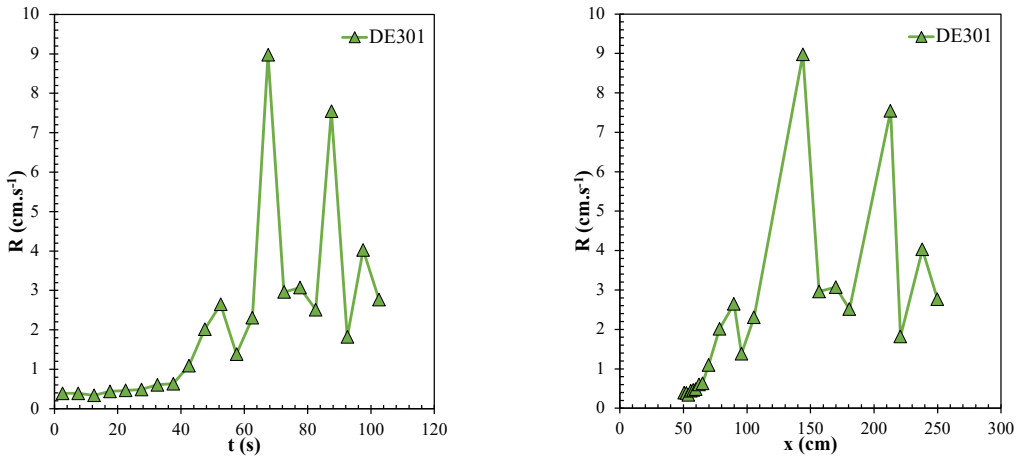

a)

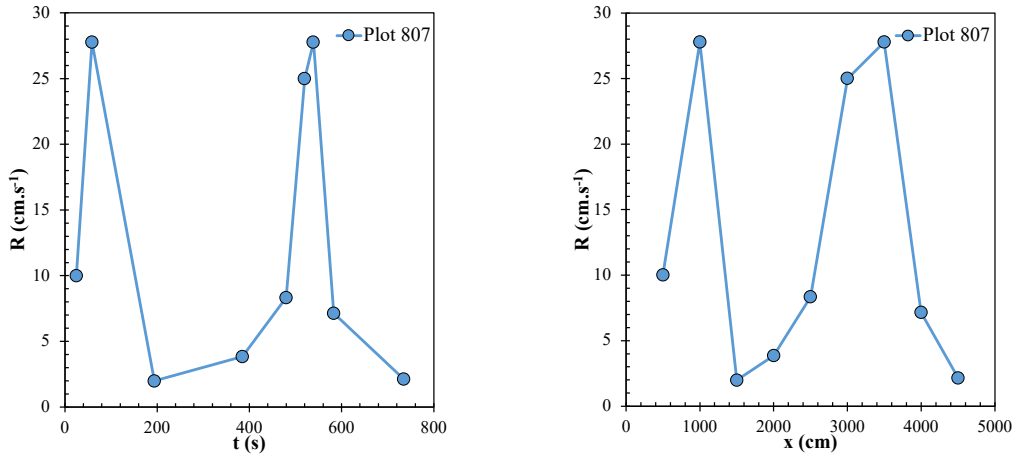

b)

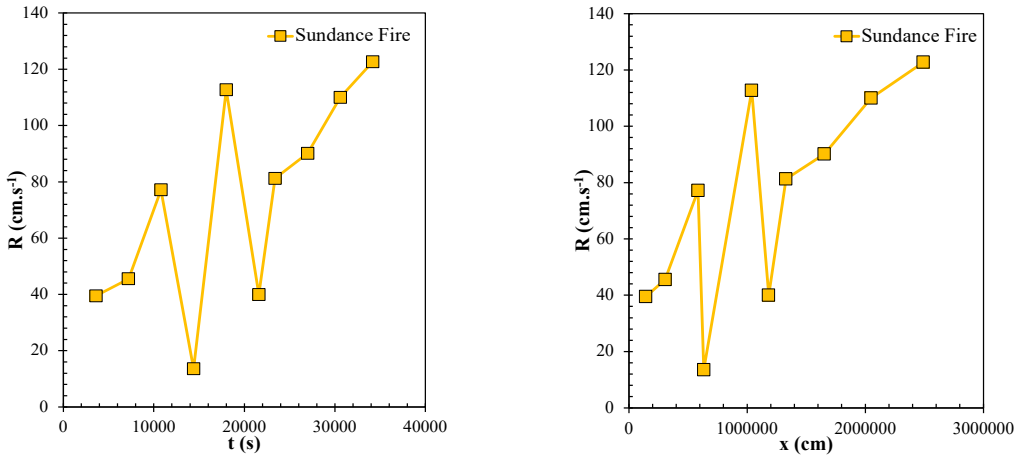

c)

Figure 3: Examples of R evolution at various scales as a function of time and distance: a) Laboratory experiment; b) Field experiment; c) Sundance Fire – head fire.

2.4.2. Amplitude and Period of Oscillations

To characterize the properties of the oscillatory fire behaviour propagation, it will be estimated the amplitude and period or frequency of these oscillations. As the previous cases have shown, it can be used either time or distance to describe the evolution of fire propagation in each direction. From this analysis, it is considered the domain (R, t), as shown in Figure 4, where each point $P(R,t)$ is a vector that characterized the pair of values of ROS R and time t. The line defined by points A_1, A_2, ..., C_2 represents the idealized evolution of R during a period in which a complete cycle of oscillations between A_o and C_o can be observed. The points A_o and C_o are two local minimum and B_o is a local maximum. The cycle is not symmetric, so it can be considered two separate half-periods, one with an increase in R between A_o and B_o and another with a decrease in R between B_o and C_o. It is introduced the following definitions:

- Amplitude of ROS increase: ΔR^+ given by the difference of ROS at B_o and at A_o;
- Amplitude of ROS decrease: ΔR^- given by the difference of ROS at B_o and at C_o;

- Half period of ROS increase: Δt^+ given by the difference of time at B_o and at A_o;
- Half period of ROS decrease: Δt^- given by the difference of time at C_o and at B_o.

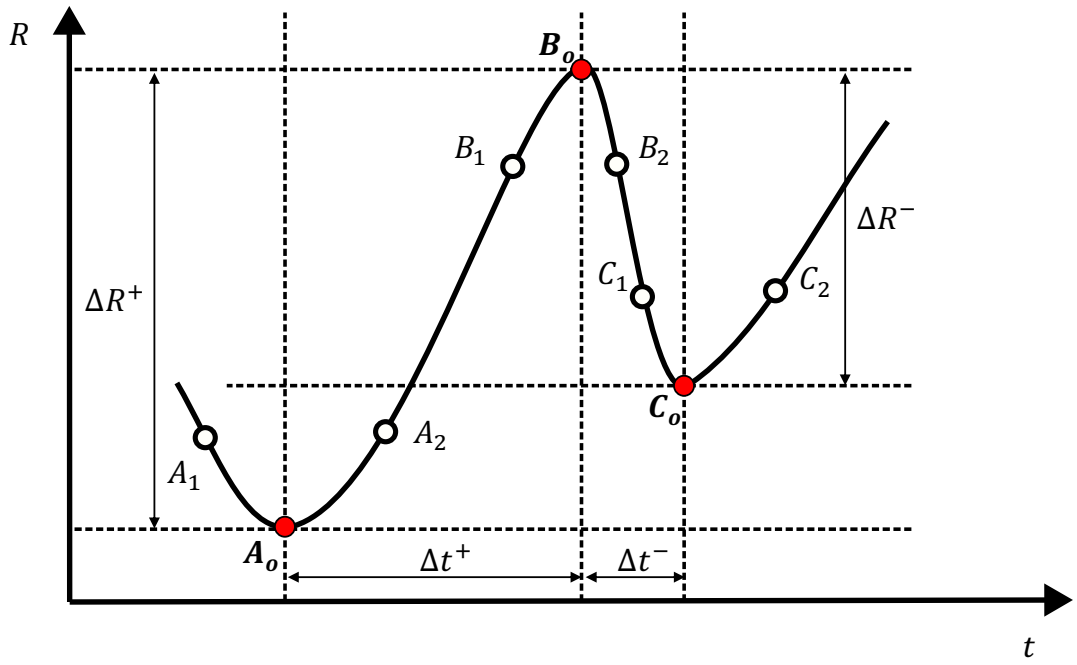

Figure 4: Idealized evolution of the function $R(t)$ during two half-period variations of the ROS defined by many points.

Given the limitations of data collection in real fires, in experimental fires in the field, and even in laboratory experiments, in many cases it does not have a complete trace of $R(t)$, but only a series of discrete points as shown in Figure 5. In the absence of more precise data, it must equate the points A_i, B_i, and C_i with A_o, $B_o$and C_o, respectively.

Since each of these points may not correspond to the actual local extreme values, this assumption is a source of error in the evaluation of Δt and ΔR. For example, instead of A_o, A_i can be either A_1 or A_2 (see Figure 4), and the same can happen with the other two points. Depending on the temporal resolution of the data from ROS, the error in estimating Δt and ΔR can be as high as 100%, which means that the actual value of these parameters estimated from incomplete data can be either half or twice the estimated value.

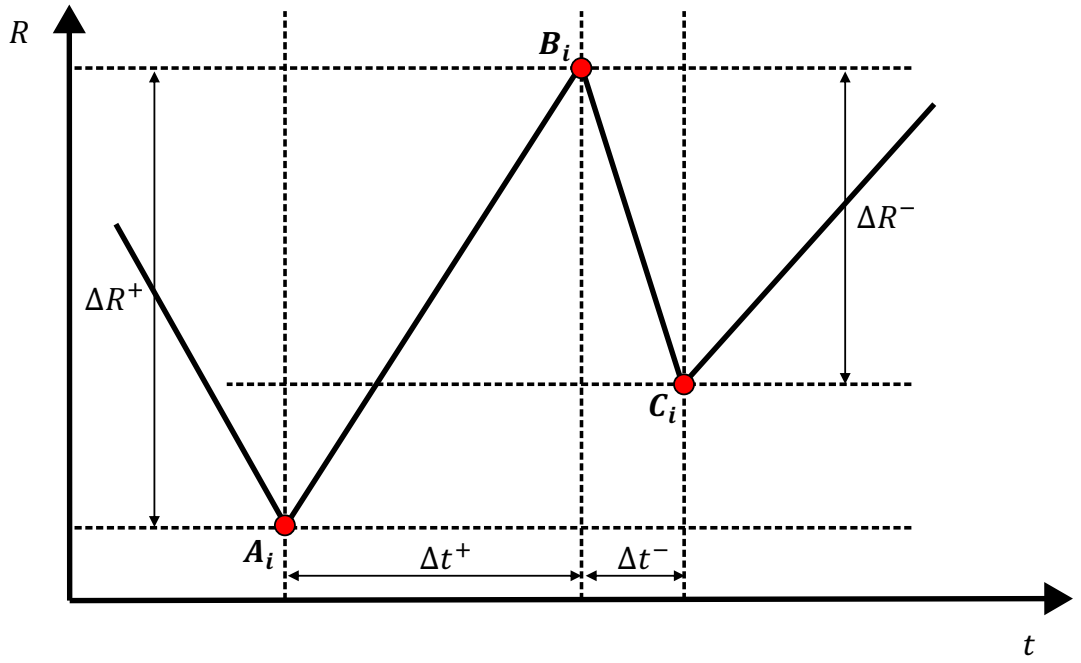

Figure 5: Partial trace of the function $R(t)$ defined by a finite number of discrete points.

The present analysis is based on experimental data collected at different scales and from different sources, it can be argued that the observed variations may be related to measurement errors, as described by Fujioka 2002. Only in some laboratory experiments with $R < 0.1$cm.s^{-1} the measurement error can be of the same order as ΔR, but in all other cases, including real fires, the amplitude of the oscillations is much larger than the estimated measurement error.

2.4.3. Analysis of Amplitude of Oscillations

Considering three points P_1, P_2 and P_3 of the space (R, t) and $P_1 \equiv A_o$, $P_2 \equiv B_o$ and $P_3 \equiv C_o$ and the ROS for each point is $R_1<R_2$ and $R_2>R_3$. The amplitude of ROS $\Delta R^+$and ΔR^- are defined by:

$$\Delta R^+ = R_2 - R_1 \qquad 8$$

and

$$\Delta R^- = R_2 - R_3 \quad (9)$$

The average of the ROS is defined by:

$$R_m = \frac{R_i + R_{i+1}}{2} \quad (10)$$

where i is given by $i = 1, 2, \ldots \mathbb{N}$. It is used this definition to obtain essentially positive values for the amplitude of the oscillation. It has been defined two values for the amplitude of the oscillation, one for the increasing phase and the other for the decreasing phase. It is assumed that the positive and negative amplitudes are different. This is generally confirmed by the available data, which show that $\Delta R^+ > \Delta R^-$. However, it will be also referred to as the oscillation amplitude ΔR, whether it is one or the other.

In estimating the arithmetic mean R_m to characterize the oscillation represented by the pair of ROS values R_i and R_{i+1}, the use of the arithmetic mean was chosen instead of the geometric or harmonic mean (cf. Fujioka 1985; Weise and Biging 1994) because does not intend to give the "mean ROS" of the fire between the two points P_1 and P_2, since this would require information that does not have in many cases. Moreover, the arithmetic mean, unlike the harmonic mean that gives a higher weight to the lowest value, is equidistant from both values.

2.4.1. Analysis of Frequency of Oscillations

To each of the half-periods Δt^+ and Δt^- defined above, it can be assigned an oscillation frequency F^+ and F^-, which is obtained as follows:

$$F^+ = \frac{1}{2.\Delta t^+} \quad (11)$$

and

$$F^- = \frac{1}{2.\Delta t^-} \quad (12)$$

The physical unit for these frequencies is Hertz (s^{-1}). The available data suggest that $F^+ < F^-$ because the time required for the fire to grow is greater than for it to decrease the ROS. It has also been defined as a single value for the oscillation frequency F, which is given as either F^+ or F^-.

It could have been defined the frequency with a single equation without distinguishing between F^+ and F^- but, as in the case of the amplitude for the accelerating and decelerating half-cycles, it has been chosen to keep these definitions to illustrate the different behaviour of the fire observed in each half-cycle.

Chapter 3. Merging Fire Lines

The aim of this chapter is to introduce the problem of the merging fires lines that can occur when two fire fronts or two flank fires approach between them. The merging of two fire fronts that intersect at a small angle result in very high values Rate of Spread (ROS). Fire intensity at their point of intersection and the ROS over time decrease and the angle between the fire fronts increases. Two real fires, Pedrógão Grande and Quiaios in Portugal, where such merging fire lines occur, were the reason for studying this phenomenon. Near Pedrógão Grande, on 17th June 2017, two fires were influenced by a thunderstorm in the region, spread uncontrollably, and merged into a very fast-spreading fire, resulting in a Junction Fire. In Quiaios on 15th October 2017, a fire spread parallel to the main fire under high wind conditions in flat terrain, and the flanks of these fires spread for at least 7km and staying 200m apart before finally merging.

3.1. Fundamental Concepts

The interaction of fires has been observed and studied by several authors. Brown and Davis 1973 noted that in prescribed burning, fire fronts or even some parts of the fire near the edges of the property are dangerous because runs with the highest ROS can develop against one side of the property and the fire can jump out and / or create a spot fire. Johansen 1984 noted that in prescribed fires, the pooling of spot fires leads to rapid

fire spread and an increase in flame length, while Pyne 1984 noted that large fires attract small fires and multiple fires can burn out and pool the intervening fuels. Clark *et al.* 1996 emphasised the importance and utility of developing a coupled atmosphere-fire model based on the fundamental equations of motion and thermodynamics and showed the convergence pattern near linear fire lines because of air entrainment into the hot air column of the fire. In the absence of ambient wind and gradient, a vertically oriented convection cell draws low-level air uniformly from all sides. In the presence of wind, this dynamic is modified in a way that leads to a parabolic or conical shape of the fire line.

Morvan 2007 developed a numerical study to analyse flame geometry and crown fire potential in forest fires propagated by bush fuels and introduced a dimensionless physical parameter, the Froude number (F_r), which can be defined by the ratio between the inertial force due to wind flow and buoyancy. He found that the flame length increases when the wind flow is less than 6m.s^{-1}, but that after this value, a sharp reduction in flame length is observed as the wind speed increases. He explains that this phenomenon can be related to the buoyancy flow due to the vertical expansion of the hot gases above the combustion zone and the inertial flow induced by the wind, and that the relationship between these two forces can be represented by the dimensionless physical parameter, designated as the Froude number.

Sullivan 2007 used a series of experimental field tests conducted in July and August 1986 in the Northern Territory, Australia, and analysed the role of the convective Froude number and Byram's energy criterion. He found that Byram's energy criterion can be calculated as the inverse cubic number of the convective Froude number. Byram's energy criterion (or Byram number) is another dimensionless physical parameter that relates the horizontal dynamic force generated by the wind flow and the vertical buoyancy forces of the fire. However, Clark *et al.* 1996; Morvan 2007 and Sullivan 2007 only consider a linear fire line propagating perpendicular to the wind.

Morvan *et al.* 2011 analysed numerically the interaction between two parallel fire fronts using a flat, grassy fuel bed and a wind direction perpendicular to the fire lines such that fire spread occurred in opposite directions (one fire spread as a head fire and the other as a “back fire”). This analysis was intended to replicate the behaviour that can

occur during fire suppression operations (i.e. “back fire”). They concluded that the interaction is only felt at a relatively short distance.

Viegas *et al.* 2012 studied the interaction and merging of two oblique and symmetrical fire fronts that intersect at a point (forming a “V-shaped” fire line) and developed a conceptual analytical model for the speed of propagation of the vertex of the “V”. Initially, Viegas *et al.* 2012 described this phenomenon as a “Jump Fire” due to the sudden increase of the head fire ROS, but after more analysis they changed that designation to “Junction fire”. The coincidence of two fire fronts intersecting at a single point has been analysed by several authors over the last decade, and this phenomenon has been referred to as “Junction Fire” (Viegas *et al.* 2013; Sharples *et al.* 2013; Raposo *et al.* 2015; Hilton *et al.* 2016; Thomas *et al.* 2017; Sullivan and Gould 2019; Filkov *et al.* 2020; Ribeiro *et al.* 2023). The fire fronts were always symmetrical with respect to the vertex “V”, and there was no fuel bed burning outside the linear, straight fire lines. The results showed that the fronts and that the ROS suddenly increased from zero to values of the order of a hundred times the basic ROS. Recently, Filkov *et al.* 2020 developed a simple, fast, and accurate method to track the spread of fire fronts and quantify the behaviour of coalescing fires at field scales. Ribeiro *et al.* 2023 studied the slope effect of JF with two non-symmetric fire fronts.

3.2. Pedrógão Grande Fire

The fires that broke out in the early afternoon of 17th June 2017 near Pedrógão Grande (PG) will go down in history as the worst fires in Portugal, destroying some 45k hectares, but above all because they caused the deaths of 66 people. Several authors have analysed this fire and written reports examining different aspects of this very complex event (Guerreiro *et al.* 2017; Viegas *et al.* 2017; Ribeiro *et al.* 2020, 2023; San-Miguel-Ayanz *et al.* 2021; Pinto *et al.* 2022; Viegas *et al.* 2023).

The fire was initiated by a 15kV electrical line at two locations separated by 3km (Figure 6). The interaction between the thunderstorm, organized as a Mesoscale Convective System (MCS) and the two fires was extensively analysed in Pinto *et al.* 2022 using weather stations, satellite and radar observation data. As a result of this interaction the two insufficiently manned fires began to spread out of control. The very unusual conditions that resulted from that interaction produced the merging of the two fires during the late evening of that day are described here in detail. The process of this interaction is designated as a Junction Fire (Viegas *et al.* 2012; Viegas, Raposo, *et al.* 2013; Xiaodong *et al.* 2014; Raposo *et al.* 2018; Ribeiro *et al.* 2023) and is accompanied by very strong convective processes resulting in a very fast ROS of the fire which in this case caused the death of 66 persons in a period of two hours.

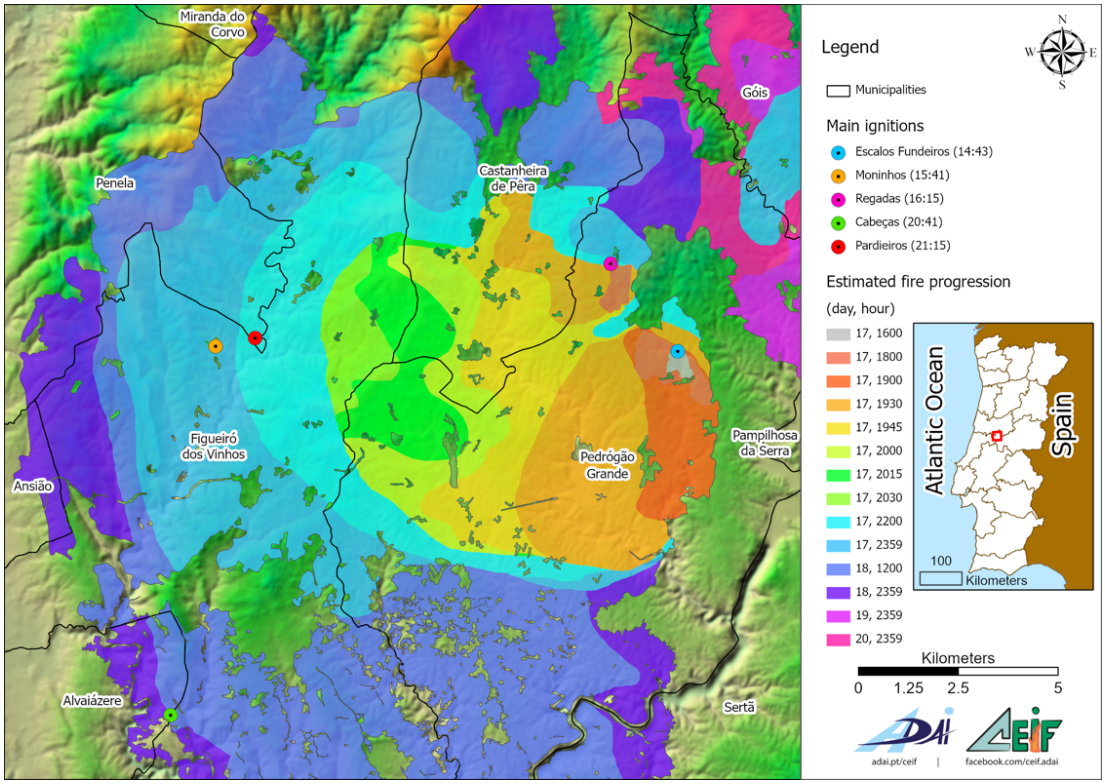

Figure 6: Map of Portugal and of the Pedrógão Grande fire area, showing the sources and spread of the fire.

The spread of the fire was reconstructed by Viegas *et al.* 2017 from extensive field data. A physical laboratory simulation of the fire spread (Viegas *et al.* 2023) was performed using modelling and scaling laws that provided a good agreement with the fire phenomena observations including the development of the very tall smoke column and the violent convective processes that were reported in Viegas *et al.* 2017. Artés *et al.* 2021 based on the analysis of the vertical profiles of the atmosphere above wildfires proposed an alternative to the use of traditional fire danger indices and they take as an example the Pedrógão Grande Fire.

The main objective of this analysis was to show the relevance of the merging processes of the two separate ignitions on the PG fire development, namely, to show that the fire development would have been quite different if only one of the fire ignitions had occurred, and to assess the capacity of simulating complex fire phenomena using laboratory scale experiments and adequate scaling laws.

3.2.1. Fire Ignition and Spread

The fire of PG occurred in the district of Leiria in central Portugal (Figure 6) during a period of drought with air temperatures above 40°C and very low relative humidity. The wind flow in the region was from the Northwest and not very strong. A large MCS developed over the central-western Iberian Peninsula and moved West-northwest, causing several fires by lightning, but at 14h30 (all times are local time, i.e. UTC plus one hour) when the fire broke out at PG, the more active part of this system was still almost 100km away, and electrical impacts were recorded in the area of the fire only at 18h00 (Pinto *et al.* 2022).

The PG fire was caused by two ignitions near Escalos Fundeiros (EF) at 14h30 and near Regadas (RE) at 15h40 (Figure 6). Both fires were caused by the contact of a power line with the foliage of trees located below and in the immediate vicinity of the lines, see Figure 7. The two sites are 3.2km apart, but the access road from EF to RE was difficult for heavy vehicles to access.

a)

b)

Figure 7: Aerial view of the location of the ignition points of a) Escalos Fundeiros (EF) and b) Regadas (RE).

As there were other sources of fire in the area, firefighting resources were scattered and there were not enough ground and air resources available to control the very difficult spread of the EF fire, which began to spread at 15h30 and threatened houses in the village of EF. When the fire was discovered by RE, there were no emergency personnel there either and the fire practically spread by itself. Between 18h00 and 18h15, a downdraft from the MSC, which was not yet over the fire area, tilted the fire column towards Southwest, causing the flames to spread over a large area and making it virtually impossible to control the fire from that point on. This process was continuously recorded by video cameras installed in the Pedrógão Grande fire station. Two images taken at 18h00 and 18h15 by the north-facing camera can be seen in Figure 8. The process of this downburst flow was carefully studied, using different methods, especially radar and ground sensors, to analyse the very complex flow generated by the thunderstorm and fire in Pinto *et al.* 2022.

The fire EF spread towards the town of Pedrógão Grande, covering many villages. At the same time, the smaller fire of RE got completely out of control and spread towards the Northwest, where it formed the right side of a large pincer that now spread like a curved fire front with a length of more than 20km, threatening an approximately circular area with a diameter of 10km, where hundreds of people lived and felt their existence threatened by this very violent and raging fire (see Figure 6).

a) b)

Figure 8: Views of the column of the fire of Escalos Fundeiros at a) 18h00 and at b) 18h15, showing the interaction with the down flow produced by the mesoscale convective flow.

3.2.2. Merging of EF and RE Fires

There is evidence that after 19h30 both fires were very close to each other with their inner flanks forming a small angle between them, i.e., they had the ideal conditions to merge into a crossing fire studied by Viegas *et al.* 2012, Raposo *et al.* 2018 and Ribeiro *et al.* 2023. Between 19h30 and 20h30, the merging fires lines process resulted in very strong winds in the area in front of the fire. The ROS of the fire head was of the order of 14km.h^{-1}. The rapid burning of a very large amount of vegetation produced a convection column that reached 12km at 20h10 and remained at this height for several hours. Flames in the order of 50 to 100m in length were recorded, which broke away from the vegetation and created a blast furnace-like environment near the ground. There are reports of stands

of trees that began to burn from their tops to the ground (see Figure 9). People who were near the fire were in pitch darkness and reported that the air was full of fireballs. Pieces of wood, branches and bark were also flying around, sometimes starting new fires. In at least two highly confined areas, numerous trees more than 20cm in diameter were twisted and broken by wind tornadoes, making them look like toothpicks. The wind speed required to cause this effect is estimated at around 200km.h^{-1} (Doogan 2006). Similar phenomena were observed in the merging of the McIntyre and Bendora fires near Canberra on 18th January 2003, when the fire spread very rapidly (27km.h^{-1}) and a tornado broke trees over 30cm in diameter (Doogan 2006).

The perception of the fire's violence, caused by the noise of the very high and roaring flames that threatened to destroy everything in their path, caused many citizens to flee their homes. Some of them made this decision even though they knew that their houses would normally survive a fire, which was the case for most of them. While fleeing in their cars, many people, sometimes whole families, were caught in the smoke, poor visibility and flames and lost their lives. The situation was particularly dramatic on a 200m stretches of the N326-1 road between Figueiró dos Vinhos and Castanheira de Pêra (see Figure 9), where 30 people died in or near their cars.

The lack of maintenance of vegetation - including trees - near the main roads contributed to the citizens lack of chances of survival. It was identified that one pine tree that was very close to the roadside and with the very strong wind triggered by the fire, it fell onto the road and crossed it from side to side. This tree and a group of cars bumping into each other formed a trap from which the cars could not drive out. Based on the testimonies of survivors and people who passed by this road before or during the accident, it was able to identify at least 16 people whose deaths can be directly attributed to this tree.

The main fire was brought under control at 23h50 on 22nd June, after a total burnt area of 45328ha, with the deployment of more than 1400 firefighters and other forces.

Figure 9: Some images of fire phenomena during its spread in the late afternoon of the 17th of June 2017.

3.2.3. Scaling Laws

This section presents a methodology for modelling fire spread in the case of Pedrógão Grande, based on physical laboratory experiments. Considering the need to conduct these experiments at a relatively small scale and to make approximations in terms of several physical processes and parameters that govern the phenomena at both scales, it will be described the modelling laws that were developed, and the assumptions made for the scaling distance, fire spread and area.

The problem of transferring the results of fire spread in two areas S_1 and S_2 covered with a superficial fuel bed, possibly with different properties, with different dimensions, but assuming that there is a geometric similarity between the two areas and a physical similarity between the fire spread processes. This means that the laws of fire propagation at a given location and time in system S_1 are the same as those occurring at the corresponding location and time in system S_2. In the general case, the fuel coverage in both systems can be arbitrary, subject to geometric similarity, provided that the local fire spread properties are known to be similar at each pair of corresponding points. In the present work, for simplicity, it is assumed that the fuel cover in both systems is homogeneous.

Under the above conditions of geometric similarity, it will be developed scaling laws to transfer the conditions of fire spread properties from a given point P_1 in region S_1 to the corresponding point P_2 in region S_2. At the two corresponding points in both domains, the local ROS is respectively given by:

$$R_1 = f_1 . R_{o1} \quad 13$$

and

$$R_2 = f_2 . R_{o2} \quad 14$$

In these equations, it is used as reference values of the basic ROS R_{oi}, where *i* correspond to system S_1 or S_2, (Viegas and Pita 2004; Raposo *et al.* 2014, 2018; Xiaodong *et al.* 2014; Rodrigues *et al.* 2019, 2023; Viegas *et al.* 2021, 2022; Ribeiro *et al.* 2022, 2023), which corresponds to a linear fire propagation in the same fuel under no-wind and no-slope conditions.

The value of R_o characterises the combustibility properties of the fuel bed, i.e., its composition, fuel load, compactness, and fuel moisture content. The dimensionless function f_i characterises the physical properties of the spreading fire, i.e., the role of wind, topography and induced convection on the heat transfer processes and combustion of the fuel bed particles, for each system S_1 or S_2.

If it has a reference value ROS R_{ref1} at a certain point in area S_1, then the value of the reference value in area S_2 is R_{ref2}. The physical similarity parameter can be defined by:

$$k_{f_{ref}} = \frac{f_{1_{ref}}}{f_{2_{ref}}} \quad 15$$

A complete physical similarity between the fire propagation conditions would be achieved given by:

$$k_{f_{ref}} = 1 \quad 16$$

This means that both physical processes are similar. It is assumed that quasi-complete similarity is achieved when the ratio $k_{f_{ref}}$ between the two functions is of the order of 1.

If a given line has length ℓ_1 in system S_1 and length ℓ_2 in the system S_2, it can be defined the length scale factor ε_ℓ as follows:

$$\varepsilon_\ell = \frac{\ell_1}{\ell_2} \quad 17$$

If a section of the fire front in a given time step in system S_1 is transformed by:

$$dx_1 = f_1 . R_{o1} . dt_1 \quad 18$$

The corresponding distance in the other system is:

$$dx_2 = f_2 . R_{o2} . dt_2 \quad 19$$

Using the length scale factor ($\boldsymbol{\varepsilon_\ell}$), it can be seen that:

$$\varepsilon_\ell = \frac{dx_1}{dx_2} = \frac{f_1 . R_{o1} . dt_1}{f_2 . R_{o2} . dt_2} = k_f . \frac{R_{o1} . dt_1}{R_{o2} . dt_2} \quad 20$$

From this equation it can derive the time scale factor τ:

$$\tau = \frac{dt_1}{dt_2} = \frac{\varepsilon_\ell}{k_f} . \left(\frac{R_{o2}}{R_{o1}}\right) = \varepsilon_\ell . \frac{R_2}{R_1} \quad 21$$

The time scale factor shows that in the analysis of the linear displacements of the fire front a certain time interval Δt_1 in S_1 corresponds to a time lapse of Δt_2 in S_2 multiplied by the length scale factor and the ratio of the reference ROS values.

If it is considered an elementary growth of area in the two systems, they are each given by:

$$dA_1 = dx_1 . dy_1 . = f_{x_1} R_{o1} dt_1 . f_{y_1} R_{o1} dt_1 \quad 22$$

and

$$dA_2 = dx_2.dy_2. = f_{x_2} R_{o2} dt_2 . f_{y_2} R_{o2} dt_2 \quad 23$$

In these equations, f_{x_i} and f_{y_i} are the factors of the function ROS for the component along the axis OX or OY and i = 1 or 2. It is assumed that the ratio of the dimensionless functions is the same at both scales:

$$\frac{f_{x_1}}{f_{x_2}} = \frac{f_{y_1}}{f_{y_2}} = k_f \quad 24$$

Considering $dA_1 = \varepsilon_\ell{}^2 dA_2$, it can be determined the time scale factor τ_A for the areas burnt in both systems in the corresponding time periods:

$$\tau_A = \left(\frac{dt_1}{dt_2}\right)_A = \left(\frac{\boldsymbol{\varepsilon_\ell}}{k_f}\right).\left(\frac{R_{o2}}{R_{o1}}\right) = \boldsymbol{\varepsilon_\ell}.\frac{R_2}{R_1} = \tau \quad 25$$

As can be seen, the time scale factor for areas is the same as that for distances.

3.3. Quiaios Fire

The complex fire of Quiaios on 15th October 2017 (Viegas *et al.* 2019) was originated from the occurrence of the Cova da Serpe ignition and consists of several new fire ignition oriented according to the wind direction, see Figure 10. Some of these fires are clearly spot fires of the original event, while others have an undetermined origin. The fire in Cova da Serpe at 14h36 was the one that stands out the most among the extreme forest fire events (Tedim *et al.* 2018) that day, both because of the extent of the area burnt and the fire spread. The fire in Quintã in Vagos at 13h34 was the one that started earlier. As it is flanked on the left by the N109 (national road) and on the right by a wet agricultural marsh, this event was of little importance in the first hours of this complex fire, although it became more significant when it was reactivated after 18h00. Another event in this complex fire was Águas Boas fire, deserves to be highlighted, not only because of the large burned area it caused but also because it was crucial for the fire front coming from Cova da Serpe to interrupt its fire progression when it reached the burned area of this event, which started shortly before 16h00.

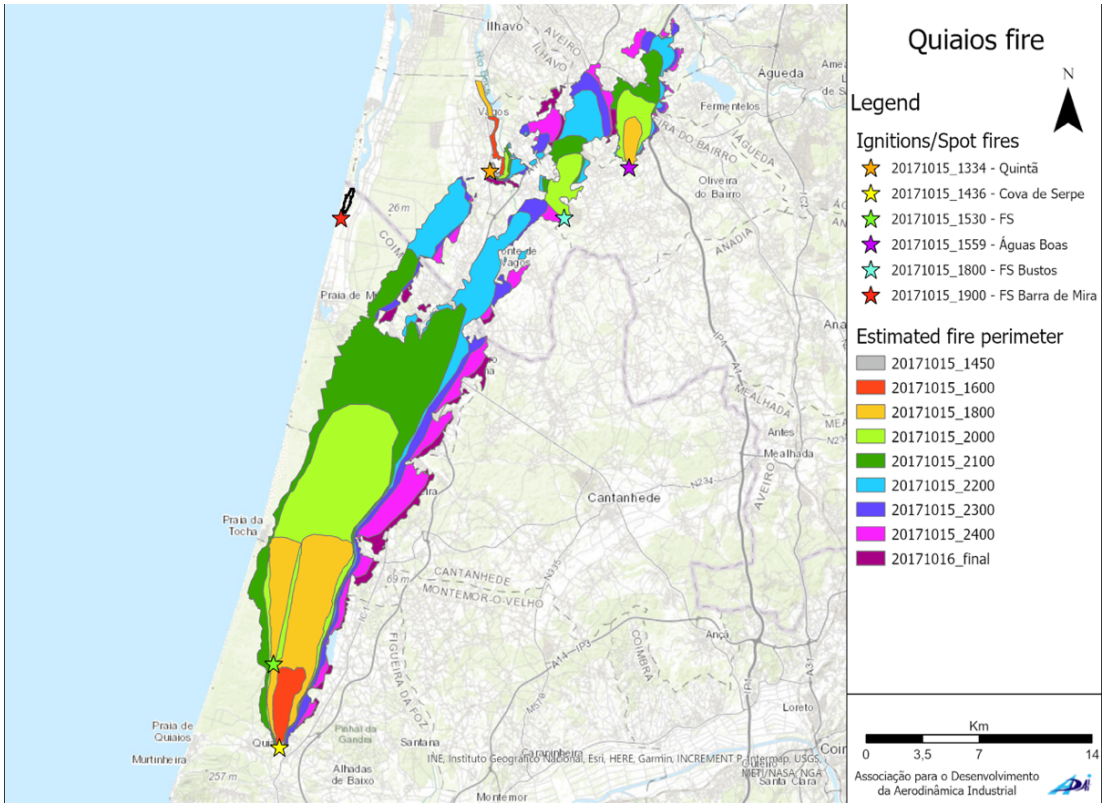

Figure 10: Estimated fire burnt area of the Quiaios forest fires on 15th October 2017. The stars and coloured areas represent the ignitions/spot fires that occurred in this complex Quiaios forest fire and the estimated fire extent during this period, respectively. The yellow star represents the approximate position of the main ignition in Cova de Serpe - Quiaios at 14h36. The green star represents the spot fire at 15h30. The orange area is the estimated area burnt between 16h00 and 18h00, with the main fire and the spot fire spreading in parallel over a length of about 7km.

Since a large part of the burnt area of this complex fire can be attributed to the Cova da Serpe fire and there were no obvious interactions during the three events mentioned, apart from the limitation of the fire course of the largest event when it reached the burnt area of the two events to the north, the following description will mainly focus on the Cova da Serpe fire.

Figure 10 shows the estimated fire extent of the forest fires that occurred in Quiaios, Portugal, on 15th October 2017. The first fire occurred at 13h34 in Quintã, see the orange star in Figure 10, and the main fire occurred one hour later in Cova de Serpe, with the yellow star in Figure 10, representing the approximate location of this fire. The

ignition in Cova de Serpe resulted in a spot fire that spread on flat ground parallel to the main fire under strong wind conditions (cf. Viegas *et al.* 2019). In Figure 10 the green star represents the approximate location of this spot fire. According to the ground and aerial imagery, the flanks of these fires spread for at least 7km, remaining 200m apart before finally merging - the orange area with reference number 20171015_1800 in Figure 10, represents the estimated position of this fire edge between 16h00 and 18h00. This work aims to describe the process of two fire lines merging under a wind blowing parallel to the fire lines, which has not been well understood or even studied.

3.3.1. Evaluation of the ROS of the Approaching Fires

The evaluation of the instantaneous ROS of the approaching lines is measured along three reference lines in the direction OY axis. Figure 11 shows the evaluation of the ROS of the approaching two parallel fire lines.

If P_i and P_{i+1} are the positions of the firing line along the reference line and S_i and S_{i+1} are the distances travelled by the firing line since the origin, the instantaneous value R_j of ROS can be calculated by:

$$R_j = \frac{\Delta S_i}{\Delta t_i} = \frac{s_{i+1} - s_i}{t_{i+1} - t_i} \quad 26$$

These values were calculated for the time t_j and at distance S_j given by:

$$t_j = \frac{t_i + t_{i+1}}{2} \quad 27$$

$$S_j = \frac{S_i + S_{i+1}}{2} \quad 28$$

To compare the results obtained for different values of the initial distance d between the parallel fire lines, a non-dimensional distance (S') defined by:

$$S' = \frac{S_j}{d} \quad 29$$

was introduced, where d is the predetermined distance between the two firing lines. This analysis was carried out in both positive and negative directions OY. Assuming that the fire spreads symmetrically, the average of the two values was used to characterise each time step.

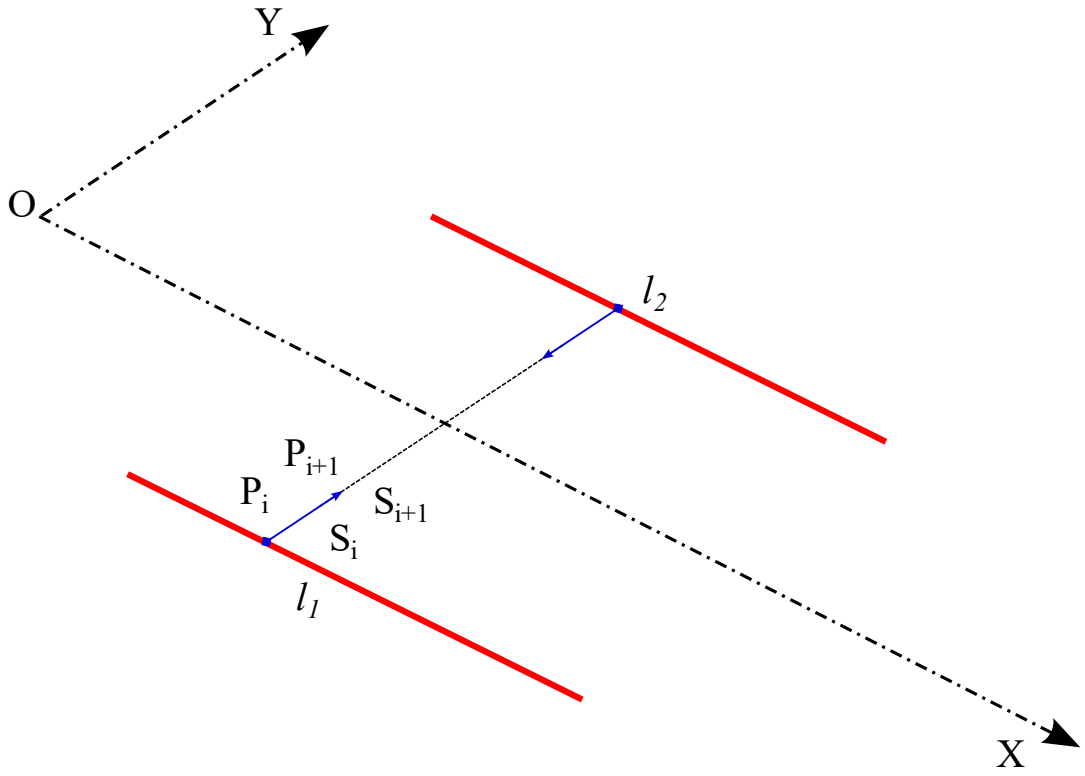

Figure 11: Evaluation of the ROS of the approaching two parallel fires lines.

3.3.2. Balance Between Horizontal and Vertical Forces

The physical problem analysed concerns the balance between the horizontal force emanating from the wind flow and the vertical forces related to the fire-induced buoyancy. The dimensionless convective Froude number (F_r) was used to describe the relationship between these two forces, which is defined by:

$$Fr = \sqrt{\frac{{U_0}^2}{g \times L}} \qquad 30$$

where U_0 is the reference wind speed (m.s^{-1}), g is the acceleration due to gravity (9.81m.s^{-2}) and L (m) is a length characterising the size of the combustion area generating the lift. Two possibilities were considered to estimate this dimension: (i) the average length $L(t_j)$

of the two fire lines measured along the axis OX at each time step; (ii) the square root of the burnt area $A(t_j)$ of each fire line at each time step.

The average of the two fire line lengths (l_1 and l_2) along the axis OX is defined by:

$$L(t_j) = \frac{L_{l1}(t_j) + L_{l2}(t_j)}{2} \qquad 31$$

where t_j is the time step defined in equation 27. The square root of the mean of two fire line areas is defined by:

$$L^*(t_j) = \sqrt{\frac{A_{l1}(t_j) + A_{l2}(t_j)}{2}} = \sqrt{\frac{c_1.L_{l1}(t_j).B_{l1}(t_j).+c_2.L_{l2}(t_j)B_{l1}(t_j).}{2}} \qquad 32$$

In this equation, B_{li} is the width of each area burnt and c_i is a shape coefficient equal to 1, considering that the shape of the fire is a rectangle.

The vertical forces associated with the Froude number were analysed using two approaches: the fire length L and the square root of the burnt area L^*. The values determined did not differ significantly from each other, so it will be used L because it is easier to determine.

Chapter 4. Methodology

4.1. Experimental Analysis

The work presented was extensively supported by experimental work at the laboratory and field scale, and the real forest fires. The experimental work carried out in the PhD programme was important to better understand the phenomena of "Extreme Wildfire Behaviour" and "merging fire lines". This chapter presents the methodology used and the initial parameters considered for each test. The description of the test rigs, equipment used and developed in the research work is the subject of this chapter.

4.1.1. Laboratory Experiments

The laboratory experiments were conducted at the Forest Fire Research Laboratory (LEIF) of the University of Coimbra in Lousã, which is one of the largest laboratories existing in Europe for forest fire research. One of the reasons for this was the possibility of collecting valid, reliable, and controlled data on the phenomena throughout the year and at any time of the day, simulating the conditions observed in real cases of occurrence of the phenomena. In the laboratory, it is possible to set the values of several parameters, such as fuel load, bulk density and slope, change each one of them and repeat

the experiments to assess measurement errors. In this form, it is easier to draw conclusions about the effect of the selected parameter being studied.

Physical Problem for Non-monotonic and Intermittent Fire Behaviour

To validate the conceptual model, a series of laboratory experiments were conducted with point fire ignition (slope and canyon) and merging of two fire lines as a Junction Fire (JF) under controlled and permanent conditions. However, field scale tests and some real forest fires were used as well. Since it is physically difficult to generate a flow with uniform velocity over a large area, the laboratorial experiments were carried out under the influence of a constant slope with no wind. Using the analogy between slope and wind influence on fire spread, the above considerations on fire development under constant wind can be extended to the case of fire on a constant slope (Viegas 2004). The following study cases were used:

- Laboratory Experiments:
  - Point ignition fire in a slope (SP) with a slope angle α equal to 20°, 30° and 40°;
  - Point ignition fire in a canyon (DEP) with a slope angle α equal to 20°, 30° and 40° and slope of the faces of the canyon δ equal to 40°;
  - Symmetric Junction fire (JF) with a slope angle α equal to 20°, 30° and 40°;
- Field Experiments will be presented in Section 4.1.2;
- Large Fires will be presented in Section 4.1.3.

All laboratory experiments were carried out with a standard fuel bed that consists of dead needles of *Pinus pinaster* (PP) with a fuel load of $600 g.m^2$ (dry basis), which has been used by CEIF research group in a large number of experiments over the years (cf. Raposo 2016; Raposo *et al.* 2018; Rodrigues *et al.* 2019, 2023; Viegas *et al.* 2021, 2022, 2023; Ribeiro *et al.* 2022, 2023).

The laboratory experiments with a point ignition fire in a slope were conducted on the Canyon Table DE4 of the Forest Fire Research Laboratory of the University of Coimbra. Figure 12 a) shows a schematic of the experimental setup and Figure 12 b) a photo of the experimental setup taken during experiment SP303.

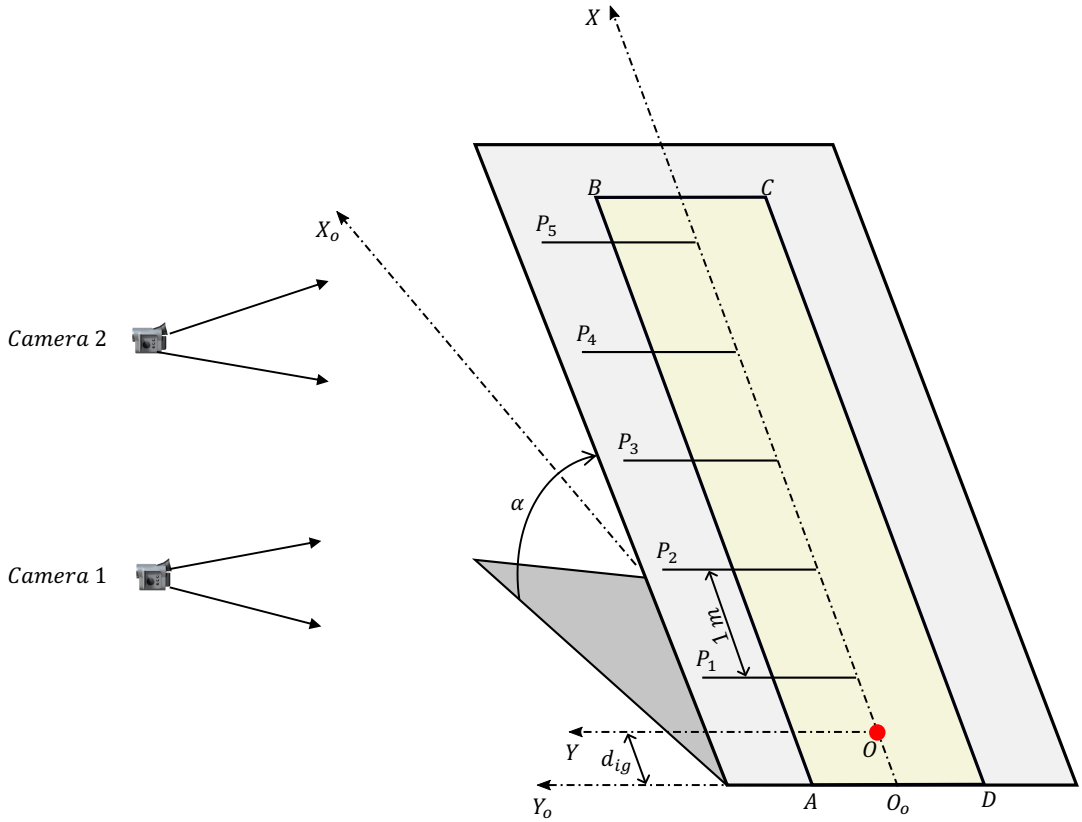

a)

b)

Figure 12: a) Geometry of a point ignition fire in a slope. P_1 to P_5 stand for the position of the pitot tubes, α for the slope angle, d_{ig} for the distance of 50*cm at which the fire was ignited, cameras 1 and 2 for the side cameras measuring the flame angle and length, and the yellow area (ABCD) for the area of the fuel bed. b) View of the Canyon Table DE4 of the Forest Fire Research Laboratory of the University of Coimbra.*

The table has a size of $6x8\text{m}^2$, but only half of it was used in the present experiments. Further details of this experimental setup can be found in Viegas and Rossa 2009. The area of the fuel bed $ABCD$ was a rectangle of $5.5x2\text{m}^2$ (in some experiments the dimensions were $5x2\text{m}^2$), and the ignition was placed in the centre $d_{ig} = 50\text{cm}$ above the bottom of the fuel. Five S-pitot tubes placed 15cm above the surface of the table and measured the U_x component of the flow. The pitot tubes will be presented in Section 4.5. The slope angle α of the table was set to 20°, 30° and 40° and four replicates were performed for each configuration. The parameters of the experiments are listed in Table 1, with the fuel moisture (m_f) for each experiment, the basic ROS (R_o), the maximum non-dimensional ROS (R'_{max}) and the maximum flame length ($L_{fl\,max}$).

Table 1: Parameters of slope tests.

Ref.	α (º)	Test	Test Dim. (m^2)	m_f (%)	R_o ($cm.s^{-1}$)	R'_{max}	$L_{fl\,max}$ (cm)
1	20	SP201	5x2	12.5	0.31	2.88	86.23
2		SP202	5x2	13.8	0.26	2.68	77.63
3		SP203	5.5x2	17.9	0.21	3.92	98.32
4		SP204	5.5x2	17.1	0.21	3.02	80.58
5	30	SP301	5x2	12.5	0.31	5.85	109.25
6		SP302	5x2	13.8	0.26	6.49	132.40
7		SP303	5.5x2	17.0	0.21	8.21	74.76
8		SP304	5.5x2	18.2	0.21	5.65	79.30
9	40	SP401	5x2	12.5	0.31	11.34	96.39
10		SP402	5x2	13.8	0.26	10.92	78.57
11		SP403	5.5x2	16.4	0.21	8.95	101.90
12		SP404	5.5x2	17.1	0.21	9.44	96.56

Fire in canyons can “blow up” or exhibit eruptive behaviour, with the ROS increasing continuously over time (see Viegas and Pita 2004; Viegas 2005, 2006; Dold and Zinoviev 2009; Viegas and Simeoni 2011; Xie *et al.* 2020). A canyon consists of two lateral surfaces that form an angle δ (slope of the faces of the canyon) with a horizontal reference plane, and whose intersection - the waterline - forms an angle α with the horizontal reference point (see Figure 13).

Experiments reported in Viegas and Pita 2004, conducted in a $3x3\text{m}^2$ canyon using Pine needles of *Pinus pinaster* (PP) as a fuel bed, showed a tendency for a non-monotonic change in ROS. The mathematical model proposed in Viegas 2005 estimates that the ROS of the head fire along the waterline of the canyon will reach very high values after a finite time.

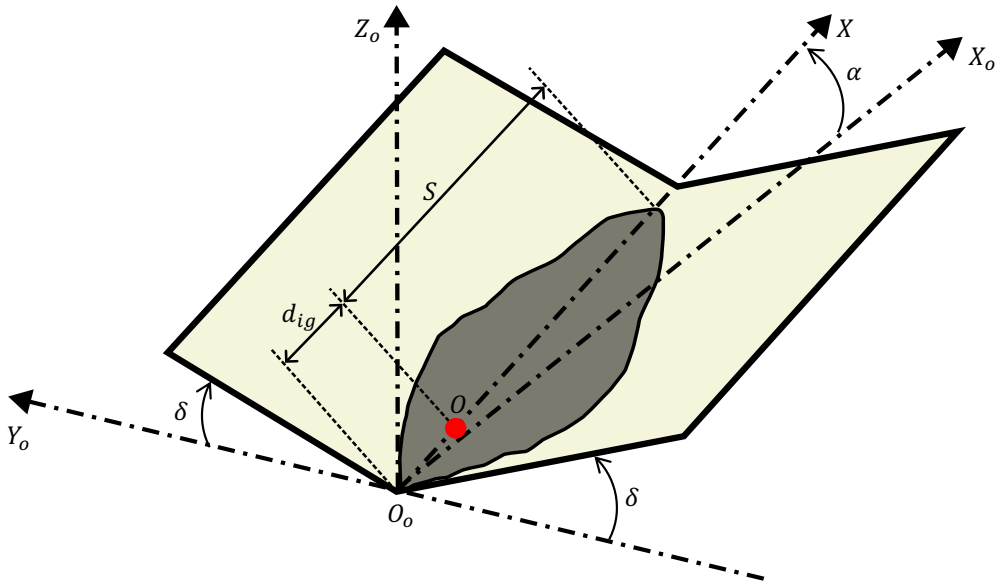

a)

b)

Figure 13: a) Geometry of a symmetrical canyon, where δ represents the slope of the faces of the canyon, α the slope angle of the waterline, d_{ig} the distance of 50*cm at which the fire was ignited and S the fire spread distance in the waterline of the canyon. b) View of the Canyon Table of the Forest Fire Research Laboratory of the University of Coimbra during a training of the Portuguese firefighters performed by the author of this work. The laboratorial experiment during a training was made with* $\alpha = 30°$ *and* $\delta = 40°$.

In the present work, a series of experiments with $\delta = 40°$ (measured when $\alpha = 0°$) were conducted for different values of the slope angle α of the waterline in this experimental setup. Five replicates were performed for each configuration and the parameters of these tests are listed in Table 2 with, for each test, the fuel moisture (m_f), the basic ROS (R_o) and the maximum non-dimensional ROS (R'_{max}). Further details on the experimental methodology can be found in Viegas and Pita 2004.

Table 2: Parameters of canyon tests.

Ref.	$\boldsymbol{\delta}$ (º)	$\boldsymbol{\alpha}$ (º)	***Test***	$\boldsymbol{m_f}$ **(%)**	$\boldsymbol{R_o}$ **($cm.s^{-1}$)**	$\boldsymbol{R'_{max}}$
1	*40*	*20*	DEP201	10.98	0.29	---
2			DEP202	10.98	0.29	8.33
3			DEP203	11.98	0.29	10.86
4			DEP204	10.50	0.29	8.99
5			DEP205	10.30	0.29	---
6		*30*	DEP301	10.30	0.28	32.05
7			DEP302	8.51	0.28	36.48
8			DEP303	13.01	0.28	26.45
9			DEP304	10.70	0.27	---
10			DEP305	10.30	0.29	---
11		*40*	DEP401	7.60	0.30	39.56
12			DEP402	8.10	0.28	33.02
13			DEP403	9.00	0.28	39.02
14			DEP404	13.00	0.21	---
15			DEP405	10.70	0.27	---

Physical Problem for Merging Fires Lines

To analyse the merging fire lines, a series a laboratory experiments were conducted with the interaction of fire line ignition under controlled boundary conditions. It was used the following study cases with laboratory scale experiments:

- Field and laboratory analysis of the junction fire process in the catastrophic fire of Pedrógão Grande in June 2017;
- Slope effect on junction fire with two non-symmetric fire fronts;
- Interaction between two parallel fire fronts under different wind conditions.

Analysis of the Junction Fire Process in the Catastrophic Fire of Pedrógão Grande in June 2017

The presented work was conducted with laboratory experiments in the Combustion Tunnel (CT) of the Forest Fire Research Laboratory of the University of Coimbra to simulate the evolution of the two fire fronts.

The physical problem is shown schematically in Figure 14 a). It was considered an absolute reference system $O_oX_oY_oZ_o$ in which the horizontal reference plane is defined by the axis $O_oX_oY_o$. The system $OXYZ$ is consistent with the absolute reference system. The test of the surface of the fuel bed is a rectangle defined by $ABDE$ with a dimension AB of 5m and BD of 4m. The straight line OC represents the centre of the fuel bed in the axis OY and the wind currents generated by two fans run parallel to the axis OX (shown as black arrows in Figure 14 a)).

In order to simulate the propagation of the two fires of Escalos Fundeiros (EF) and Regadas (RE) after 18h30 and their merging, it was drawn two straight lines FG and HI representing at this time the fire of EF and RE, respectively. From now on, these lines will be labelled L_{EF} (Escalos Fundeiros) and L_{RE} (Regadas). The angles between these fire lines and the axis OY are $\theta_1 = 25°$ (EF) and $\theta_2 = 48°$ (RE), as shown in Figure 14 a).

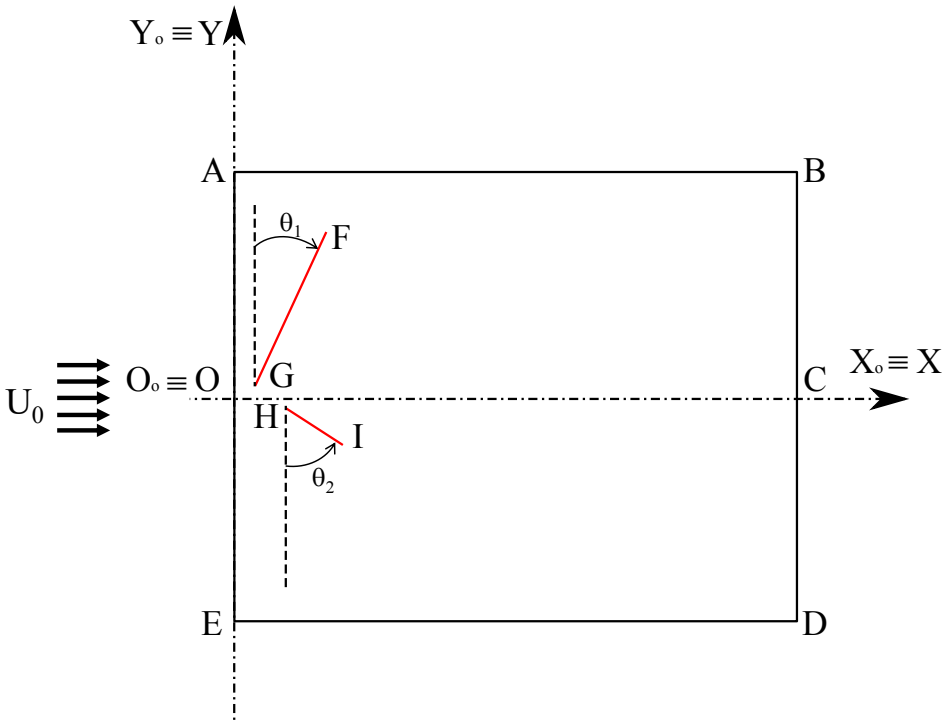

a)

b)

Figure 14: a) Schematic layout of the fuel bed and the ignition lines; b) General view of the Combustion Tunnel of the Forest Fire Research Laboratory of the University of Coimbra during test PG 42.

Given the geometric similarity between the position, orientation, and length of each fire line in the laboratory and in the field, it was able to determine the length scale parameter. Using the ratio of the linear dimensions of the EF fire length in both systems at the nominal time t_i, it can be concluded that:

$$\varepsilon_\ell = \frac{\ell_1}{\ell_2} = \frac{\ell_r}{\ell_m} \approx \frac{4400}{1.5} = 2933 \qquad 33$$

In the experiments, the test area of $4x5\text{m}^2$ was covered with a uniform fuel bed consisting of either dead needles of *Pinus pinaster* (PP), Straw (ST) or fine twigs and leaves of Shrubs (SH), with a fuel load of 600g.m^{-2} (dry basis).

As shown in Table 3, initial experiments were made with different fuels and wind speeds to test the role of this parameter and found that the processes were similar in all cases, although they were enhanced at larger values of U_0. In this work it will be only used the results of the experiments marked with an (*) in Table 3.

Table 3: Parameters of the tests that were performed to analyse the Junction Fire Process in the Catastrophic Fire of Pedrógão Grande in June 2017.

Ref.	***Fuel***	U_0 ***[m.s^{-1}]***	***Designation***	m_f ***[%]***	R_o ***[cm.s^{-1}]***	R'_{max}
1	*PP*	*0*	PG 10	*11.73*	*0.36*	*1.27*
2	*PP*	*2*	PG 12*	*11.34*	*0.34*	*47.05*
3	*PP*	*3*	PG 13*	*11.34*	*0.35*	*95.70*
4	*PP*	*4*	PG 14*	*12.87*	*0.35*	*112.82*
5	*ST*	*2*	PG 22*	*10.50*	*0.71*	*45.00*
6	*SH*	*2*	PG 32*	*10.38*	*1.35*	*23.10*
7	*PP*	*2*	PG E 12	*11.24*	*0.43*	*50.05*
8	*ST*	*2*	PG E 22	*12.11*	*0.80*	*45.00*
9	*SH*	*2*	PG E 32	*9.89*	*1.34*	*23.10*
10	*PP*	*2*	PG EF 12*	*12.11*	*0.37*	*34.48*
11	*PP*	*2*	PG RE 12*	*11.36*	*0.33*	*18.29*
12	*ST*	*2*	PG 22A	*11.34*	*0.34*	*93.97*
13	*PP*	*2*	PG 42*	*11.40*	*0.24*	*41.28*

Junction Fire with Two Non-Symmetric Fire Fronts

In the present work, the fire is assumed to start from two straight lines i_1 and i_2 that intersect at point A with an initial angle θ_0 (see Figure 15 a)) and propagate in a uniform fuel bed layer on a flat surface OXY, forming an slope angle α with the horizontal reference point $O_oX_oY_o$. The Cartesian coordinate system $O_oX_oY_oZ_o$ is considered, in which O_oZ_o is perpendicular to the ground. Point A initially coincides with the origin of the Cartesian reference system, with the axis OX parallel to the slope. The axis OX_1 represents the line of symmetry of the crossing fire and can be defined by the angle δ_{JF}, which is the angle between the bisector of the fire lines and the line of greatest slope. For any combination of the angles α and δ_{JF}, the maximum ROS is on the axis OX_m, and this axis is rotated by a certain angle γ, which represents the angle between the bisector of the fire lines and the maximum ROS. The fire area is defined by ABC and is covered by a uniform, forest fuel bed layer that can support the spread of a fire. The merging of two linear fire fronts is shown schematically in Figure 15 a).

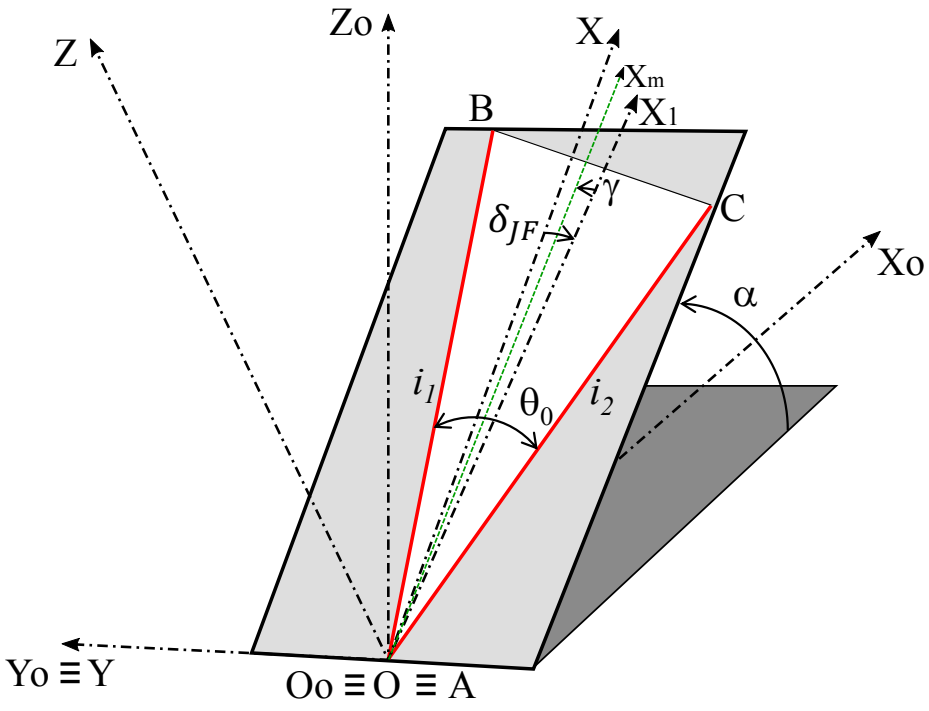

a)

b)

Figure 15: a) Schematic layout of the merging of two non-symmetric straight fire lines making an initial angle θ_0 between them. The axis OX is parallel to the slope gradient, the axis OX_1 represents the symmetry line of the fire configuration and the axis OX_m, defined by the green dashed line, represents the maximum ROS happened. b) View of the Canyon Table DE4 of the Forest Fire Research Laboratory of the University of Coimbra during the test 1-JF1030..

It is considered that the two linear fire fronts defined by two straight lines (AB and AC) that are not symmetrical in the axis OX as shown in Figure 15 a). It is assumed that at time $t_0 = 0$s and throughout the experiment, there are no ambient winds in the laboratory and the fire lines are straight and ignited simultaneously and immediately.

The experimental study was carried out at Canyon Table DE4 (see Figure 15 b)) of the Forest Fire Research Laboratory of the University of Coimbra in Lousã (Portugal). The area of the fuel bed was defined by a fixed angle between the fire fronts $\theta_0 = 30°$ and a fixed length of 5.5m, i.e., 8.73m^2. The fuel bed for the experiments was composed of dry particles of pine needles of *Pinus pinaster* with a constant load of *600g.m^{-2}* (dry basis) (Viegas and Pita 2004; Xie *et al.* 2014; Raposo 2016; Raposo *et al.* 2018; Rodrigues *et al.* 2019; Viegas *et al.* 2021, 2022). The chosen value of $\theta_0 = 30°$ was a good compromise for conducting this study. After an extensive testing programme with values of θ_0 between 10° and 90°, it was found that for smaller values of θ_0 the test was very fast and it was difficult to measure the fire spread characteristics, while for large values

of θ_0 the fire acceleration was not very important and the process characterising the interaction between the two fire lines was not very relevant. This is in line with previous work carried out on converging fronts (cf. Viegas *et al.* 2012, 2013; Raposo *et al.* 2018).

To reduce uncertainty, three replicate tests (T1, T2 and T3) were performed for each set of parameters, as shown in Table 4. For the symmetric condition ($\delta_{JF} = 0°$), it was performed only one test and validated our results with previous work by Raposo 2016; Raposo *et al.* 2018.

The evaluation of the merging process of the two fire lines shows a change in the angle θ between them. The angle between the fire lines increases during the burning of the fuel bed and tends towards 180°, which corresponds to a straight line. According to Raposo *et al.* 2018, ROS R_A shows a functional dependence near the intersection of two fire lines (point *A*) described by:

$$R_A = f(\theta_0, \alpha, \delta_{JF}, m_f, \dots, t) \qquad 34$$

where θ_0 is the initial angle between two linear fire fronts, α is the slope angle, δ_{JF} is the angle between the bisector of the fire lines and the line with the greatest slope, m_f is the moisture content of the fuel, the points represent a variety of parameters required to define the properties of the fuel bed, and t is the time each test has taken since ignition. It is considered time as an explicit variable because fire behaviour changes over time as it is a dynamic process (Viegas 2005; Viegas *et al.* 2021, 2022). However, the distance x_A travelled from point A and the time t are not independent, and the distance x_A at a given time t is given by:

$$x_A = \int_0^t R_A . dt \qquad 35$$

and equation 34 can be replaced by:

$$R_A = f(\theta_o, \alpha, \delta_{JF}, m_f, \dots, x) \qquad 36$$

The role of the initial angle θ_0 has been extensively studied by several authors, where it was found to be a relevant parameter for the evolution of the crossing fires

(Viegas *et al.* 2012; Sharples *et al.* 2013; Thomas *et al.* 2015). In the present work, a constant value for $\theta_0 = 30°$ is assumed for all experimental laboratory tests.

The slope angle (α) had the following values: $\alpha = 10°$, $20°$, $30°$ and $40°$, and for each set of these parameters the angle δ_{JF} of the linear fire fronts was $\delta_{JF} = 0°$, $5°$, $10°$ and $15°$, see Figure 16. It is assumed that the angle δ_{JF} of the linear fire fronts is of the same order of magnitude as the angles between the studied fire fronts $\theta_0 = 30°$. It was chosen this angle because it wants to determine the smallest angle that would trigger a change in fire behaviour.

Table 4: Parameters of the non-symmetric junction fires cases considered in the present work.

Ref.	α	δ_{JF}	Designation			m_f (%)			R_o (cm.s^{-1})		
	(º)	(º)	T1	T2	T3	T1	T2	T3	T1	T2	T3
1	10	0	1-JF010	-	-	10.99	-	-	0.352	-	-
2		5	1-JF510	2-JF510	3-JF510	13.89	10.99	12.32	0.228	0.328	0.290
3		10	1-JF1010	2-JF1010	3-JF1010	13.25	10.99	12.30	0.276	0.328	0.298
4		15	1-JF1510	2-JF1510	3-JF1510	13.25	10.99	11.01	0.226	0.328	0.310
5	20	0	1-JF020	-	-	13.90	-	-	0,235	-	-
6		5	1-JF520	2-JF520	3-JF520	13.25	12.10	10.99	0.267	0.247	0.340
7		10	1-JF1020	2-JF1020	3-JF1020	13.25	13.28	13,51	0.221	0.221	0.221
8		15	1-JF1520	2-JF1520	3-JF1520	13.25	12.15	11,99	0.289	0.241	0.265
9	30	0	1-JF030	-	-	13.64	-	-	0.209	-	-
10		5	1-JF530	2-JF530	3-JF530	14.03	14.29	10.99	0.247	0.221	0.340
11		10	1-JF1030	2-JF1030	3-JF1030	12.49	14.29	11.50	0.245	0.218	0.294
12		15	1-JF1530	2-JF1530	3-JF1530	12.49	13.90	11.50	0.245	0.203	0.294
13	40	0	1-JF040	-	-	11.86	-	-	0.255	-	-
14		5	1-JF540	2-JF540	3-JF540	13.61	12.23	12.24	0.221	0.282	0.282
15		10	1-JF1040	2-JF1040	3-JF1040	13.64	12.36	12.37	0.263	0.249	0.249
16		15	1-JF1540	2-JF1540	3-JF1540	14.88	12.38	12.39	0.197	0.243	0.243

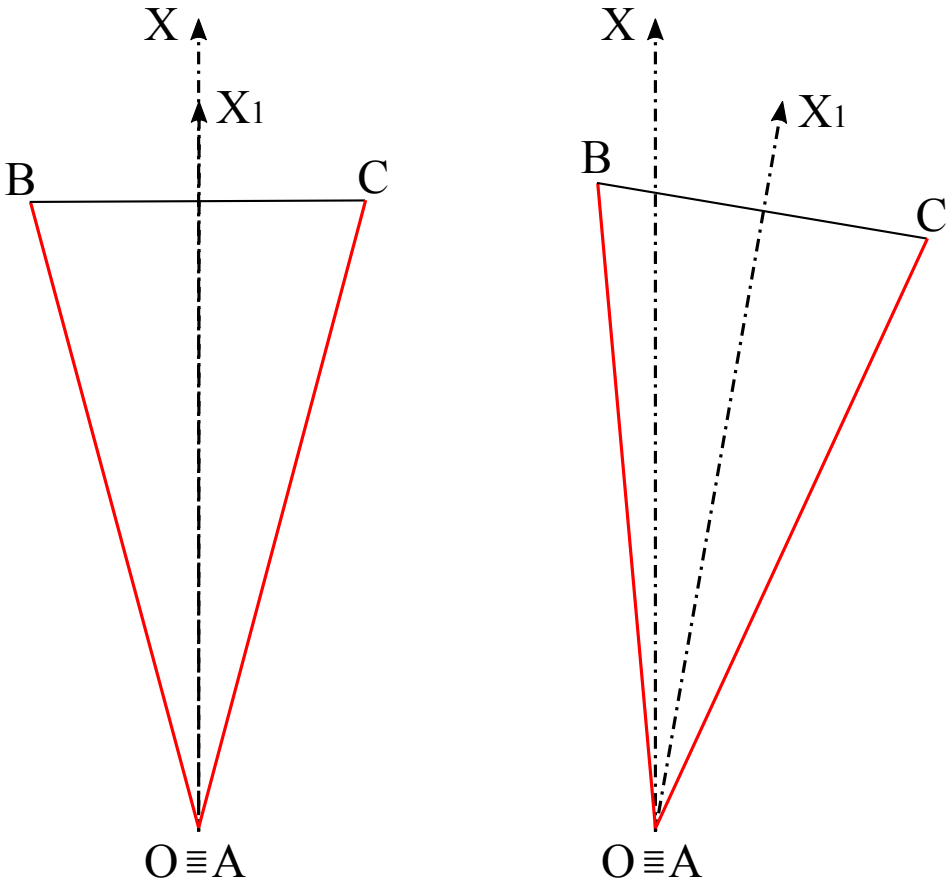

a) b)

Figure 16: Angle δ_{JF} of linear fire fronts changes between δ_{JF} =0° to δ_{JF} =15°. This Figure show a) δ_{JF} =0° and b) δ_{JF}=10°

The problem to be analysed can be formulated either as a function of time or distance:

$$R_A = f_1(\alpha, \delta_{JF}, R_o, t) = f_2(\alpha, \delta_{JF}, R_o, x) \quad 37$$

The rate of displacement of the intersection point A of the two fire lines over time from its original position O was analysed. The angle of rotation δ_{JF} changes the symmetry of the boundary conditions of the fire fronts with respect to the maximum angle of inclination and the intersection point. For each set of values of α and δ_{JF} the maximum ROS occurs along the OX_m axis. In order to compare the results with other types of fuel beds - although the same type of fuel bed was always used in the present experimental

programme - and to minimise the effect of m_f on R_A in the experiments conducted under different conditions, it was used the following non-dimensional ROS of the intersection point defined by:

$$R'_A = \frac{R_A}{R_o} \quad 38$$

where R_o represents the basic value ROS (cm.s^{-1}) under no-slope and no-wind conditions.

Parallel Fire Fronts

It is assumed that two parallel fire lines can spread on flat terrain and interact with each other under the influence of wind flow. The two fire lines are initially separated by a certain distance (d) on a uniform fuel bed, as shown schematically in Figure 17 a). The Cartesian coordinate system $O_oX_oY_oZ_o$ is considered, where O_oZ_o is perpendicular to the ground. The study area is defined by $ABCD$ and the area of the fuel bed by $EFGH$. The line EF has a displacement (1m) in the axis O_oX_o. The fuel bed is covered by a uniform layer of forest fuel, which may favour the spread of a surface fire. The fuel bed for the experiments consisted of dry straw (ST) particles (*Avena sativa*) with a constant load of 600g.m^{-2} (dry matter).

It was considered two linear fire fronts, each 2m long, defined by two straight lines symmetrical in the OXZ plane (IJ and KL) with a distance d between them, as shown in Figure 17 a). In the following, the straight fire lines IJ and KL are referred to as l_1 and l_2, respectively. Parallel to the OX_o axis, a uniform boundary layer flow blows with a characteristic velocity (U_0), which is shown by black arrows in Figure 17 a). At time $t_0 =$ 0s, the fire lines are ignited and can spread freely in all directions.

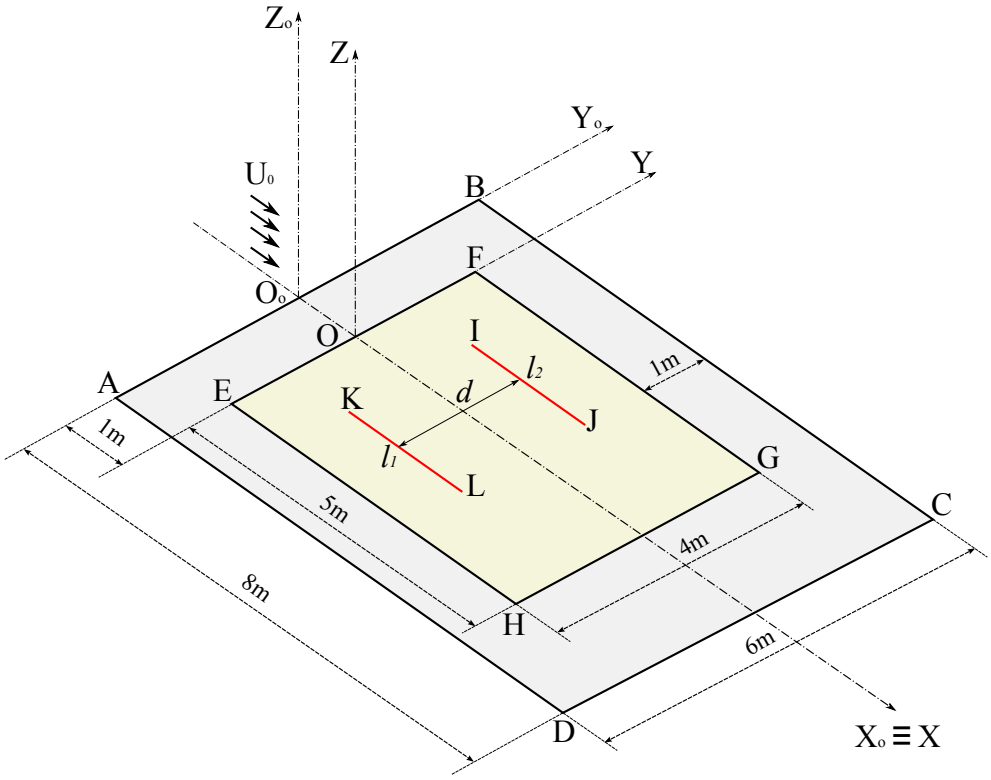

a)

b)

c)

Figure 17: a) Geometry of two parallel fire lines in symmetrical conditions. b) General view of the combustion tunnel of the Forest Fire Research Laboratory of the University of Coimbra. The length of the working section is 8m and the width is 6m. The maximum flow velocity is 8m.s^{-1}. The position of the infrared camera and of the visible camera can be seen on the top left of the image, placed in the lifting platform. c) View of the Combustion Tunnel (CT) of the Forest Fire Research Laboratory of the University of Coimbra during the test 2-D2U2.

The experimental study was conducted in the Combustion Tunnel (CT) of the Forest Fire Research Laboratory of the University of Coimbra in Lousã (Portugal). The CT has a working area of $6x8$m^2, defined by $ABCD$ according to Figure 17 a). The fuel bed area was $4x5$m^2, with side dimensions EF and GH 4m and the other sides FG and EH 5m. To avoid the edge effect inside the wind combustion channel, a distance of 1m was left between the vertical walls of the combustion channel and the edges of the fuel bed (EF and GH). The wind flow was generated by two fans with a maximum power and flow velocity of 70kW and 8m.s^{-1}, respectively. The tests were carried out with reference wind speeds of $U_0 = 0,\ 1,\ 2,\ 3,\ 4$ and 5m.s^{-1}. The reference wind speed (U_0) was measured in the OX axis with a KimoAMI 300 hot-wire probe (Kimo Instruments,

Montpon-Ménestérol, France) 22cm above the ground CT. Further details can be found in Appendix A1.

In order to reduce uncertainty, three replication tests (T1, T2 and T3) were performed for each set of parameters, the fuel moisture content and the basic ROS, shown in Table 5.

Table 5: Parameters of the parallel fire fronts under wind condition.

Ref.	d (m)	U_0 ($m.s^{-1}$)	Designation			m_f (%)			R_o ($cm.s^{-1}$)		
			T1	T2	T3	T1	T2	T3	T1	T2	T3
1	1	0	1-D_1U_0	2-D_1U_0	3-D_1U_0	9.1	9.0	9.3	0.83	0.85	0.81
2		1	1-D_1U_1	2-D_1U_1	3-D_1U_1	10.2	10.4	10.7	0.70	0.75	0.72
3		2	1-D_1U_2	2-D_1U_2	3-D_1U_2	9.5	9.5	9.5	0.85	0.85	0.85
4		3	1-D_1U_3	2-D_1U_3	3-D_1U_3	10.4	10.2	10.7	0.75	0.70	0.74
5		4	1-D_1U_4	2-D_1U_4	3-D_1U_4	10.8	10.9	10.9	0.71	0.72	0.72
6		5	1-D_1U_5	2-D_1U_5	3-D_1U_5	11.2	11.1	11.3	0.60	0.61	0.64
7	2	0	1-D_2U_0	2-D_2U_0	3-D_2U_0	10.0	9.5	9.7	0.76	0.80	0.76
8		1	1-D_2U_1	2-D_2U_1	3-D_2U_1	10.0	10.2	10.1	0.77	0.75	0.77
9		2	1-D_2U_2	2-D_2U_2	3-D_2U_2	10.0	10.2	10.1	0.77	0.75	0.77
10		3	1-D_2U_3	2-D_2U_3	3-D_2U_3	9.5	9.4	9.5	0.80	0.83	0.80
11		4	1-D_2U_4	2-D_2U_4	3-D_2U_4	11.2	11.1	11.3	0.65	0.67	0.65
12		5	1-D_2U_5	2-D_2U_5	3-D_2U_5	10.8	10.9	10.9	0.71	0.70	0.71

4.1.2. Field Experiments

The field experiments fires were conducted in the Lousã Mountains in central Portugal in three sets of experiments. Table 6 shows the resume of the main characteristics of the test plots. This area, the Gestosa test plot, offers similar conditions in terms of fuel and topography in a region characterised by a warm, temperate climate with dry summers, following the Koeppen-Geiger climate classification (Kottek *et al.* 2006).

In the plots used, the minimum elevation is 702m in plot 13_04 and the maximum elevation is 1100m in plot 804. Most of the plots face southwest (between 209 and 256 degrees from north), one faces west (plot 808), another faces northwest (plot 809) and three face northeast (Tests 2011).

*Table 6: Resume of the main characteristics of the test plots. * V-shaped plots. The width refers to the top of the plot.*

Ref	Year	Plot	Dimensions (WxL) *(m)*		Slope (º)	Orientation Degrees from North (º)	Fuel height *(m)*	Fuel Load *(g.m^{-2})*	Ignition
1	2000	40	90	155	13.9	219	0.75	1925	Linear
2		41	95	140	19.0	238	0.69	2356	Linear
3		42	90	160	16.7	220	0.55	1556	Linear
4		43	110	150	21.7	232	0.87	2062	Linear
5		44	90	130	27.1	219	1.06	2631	Linear
6		45	90	130	24.0	209	0.64	1904	Linear
7	2006	804	40	56	10.4	215	0.43	2610	Linear
8		807	43	56	16.4	256	0.39	2500	Linear
9		808	35	40	17.8	270	0.42	2760	Linear
10		809	28	40	18.0	299	0.52	4140	Linear
11	2011*	13_01	27	46	17.5	48	0.77	3792	Linear (2 Laterals)
12		13_04	27	45	20.7	45	0.73	3855	Linear (2 Laterals)
13		13_02	42	94	18.6	40	1.23	4344	Linear (2 Laterals)

The typical vegetation of the area consists of a continuous, homogeneous mixture of shrubs and, in some areas, isolated maritime pines (*Pinus pinaster*). The predominant shrub species are *Erica umbellate, Erica australis, Chamaespartium tridentatum, Ulex sp. and Halimium ocymoides.*

The arrangement of the plots was determined each year according to the specific objectives of the tests. Firebreaks were created either manually with hand tools or, in some cases, mechanically when vegetation was taller. Firebreaks were also created to provide larger safety zones. The width of the firebreaks varied between 5 and 20m, depending on the location. In 2002 and 2006, the plots were rectangular, but triangular plots were tested in 2011. In Raposo *et al.* 2018, tests 13_01, 13_02 and 13_04 were named CF57, CF78 and CF79, respectively. In 2000 and 2006, pyrotechnic flares were used to create linear ignitions at the bottom of the plots. In 2011, pyrotechnic ignitions were used to achieve simultaneous ignition on both sides of the triangular plots. The course of the fire was determined after processing the images taken with infrared cameras.

4.1.3. Large Fires

From a large amount of data available in the literature on the spread of large fires, it was selected eight cases where the oscillatory behaviour of the fire head is evident at different scales. These cases were chosen because during their spread one main factor - usually the wind - remained practically constant in terms of speed and direction, so that the justification of the fluctuations of ROS due to changes in the environmental factors is not convincing. Further details of these eight large fire cases can be found in Anderson 1968; Finklin 1973; Wade and Ward 1973; Simard *et al.* 1983; Rothermel and Mutch 1986; Doogan 2006; Viegas 2010; Kutiel 2012; Sharples *et al.* 2012; Shavit *et al.* 2013. Viegas *et al.* 2022 in Supplementary Appendix S3 show each of these cases.

Table 7: Large fire cases (LF)

Ref.	Year	Case	Country	Ref.	Year	Case	Country
1	1968	Sundance	USA	*5*	2003	Canberra	Australia
2	1971	Air Force	USA	*6*	2003	Vidauban	France
3	1980	Mack Lake	USA	*7*	2004	Amodôvar	Portugal
4	1985	Butte Fire	USA	*8*	2010	Carmel	Israel

4.2. Fuels

During the preparation of each laboratorial experiments fuel loading and bulk density conditions were controlled and air temperature (ºC), relative humidity (%) and fuel moisture (m_f) were monitored.

In this work, the laboratory experiments were conducted with three different fuels consisting of dead needles of *Pinus pinaster* (PP), Straw of *Avena sativa* (ST) and Shrubs (SH), a mixture of twigs and foliage of *Erica umbellate, Erica australis, Chamaespartium tridentatum and Ulex minor*. The fuel is spread uniformly on the tables and the fuel bed height (h_f) was measured at several points, usually in five aleatory positions. The characteristic properties of these different fuels are listed in Table 8. The packing ratio (b_f) is given by the ratio of the fuel bed bulk density (ρ_b) by the fuel particle density (ρ_p) (Viegas and Pita 2004; Xiaodong *et al.* 2014; Raposo 2016; Raposo *et al.* 2018; Rodrigues *et al.* 2019, 2023; Viegas *et al.* 2021, 2022, 2023; Ribeiro *et al.* 2022, 2023).

Table 8: Characteristic Properties of the different fuels.

Fuel	Fuel Bed Height	Packing Ratio	Particle Surface-Area-to-Volume Ratio	Bulk Density	Fuel Particle Density	High Heat of Combustion
	(h_f)	**(b_f)**	**(σ_f)**	**(ρ_b)**	**(ρ_p)**	**HHC**
	[m]	**[-]**	**[m^{-1}]**	**[$kg.m^{-3}$]**	**[$kg.m^{-3}$]**	**($MJ.kg^{-1}$)**
Straw	0.07	0.029	4734	7.5	258	18
Pine needles	0.04	0.027	4100	14.50	530	19.57 to 21.61
Shrubs	0.15	0.007	69.0	3.92	500	13.9

The fuel load m_c in all experiments was $600 g.m^{-2}$ (dry basis) as in the experiment described in Byram 1959; Van Wagner 1968; Chandler *et al.* 1983 and Pyne 1984.

The shape, size, density, chemical composition, fuel moisture content (FMC) and other characteristics are important properties of fuel layers that affect fire behaviour. The FMC (m_f) is one of the properties of fuels that has a great influence on fire behaviour, especially on the ROS. According to Byram 1959; Chandler *et al.* 1983 and Pyne 1984, m_f determines the possibility of a forest fuel igniting and how much of it is available for the combustion process (Viegas *et al.* 2013). The moisture content of the fuel was measured twice during each test using an A&D ML50 moisture analyser: during fuel bed preparation and before ignition of each test. This device can determine the amount of water in the fuel within ten minutes, and before each test this value is determined, and the amount of fuel used is corrected to compensate for the amount of water in the fuel. This ensured that the amount of fuel used in each test remained constant throughout the work programme. To ensure that the moisture content of the fuel did not change when in contact with the ambient air, the time between the preparation of the fuel bed and the start of the burning test was no more than ten minutes.

The basic ROS R_o (cm.s^{-1}) is a property of a given fuel bed when a linear fire front burns that fuel under no-slope and no-wind conditions and it depends principally on the fuel moisture (m_f). The basic ROS R_o of a linear fire front in a fuel bed with the same properties was measured for each test series with a horizontal fuel bed of $1x1$m^2, see Figure 18.

Figure 18: Determination of the basic Rate of Spread R_o in a combustion table with $1x1m^2$ with a fuel bed of pine needles. The white cotton lines are separated by 10cm of distance and are used to determine the ROS at each distance. The fuel bed load is the same that was used in the experimental tests. This analysis was made for each experimental test.

4.3. Ignition Procedure

The ignition procedure was different according to the laboratorial experiments. For the point ignition fire in the slope and in a canyon the ignitions were made by only one person and the ignition was started with a small cotton ball soaked in a mixture of petrol (50%) and diesel fuel (50%). However, for the laboratory analysis of the junction fire process in the catastrophic fire of Pedrógão Grande, slope effect on junction fire and interaction between two parallel fire fronts, the ignitions were made by two persons to assure that the lines started burning simultaneously. For this purpose, two wool threads soaked in a mixture of petrol (50%) and diesel fuel (50%) were used.

During the tests performed in Combustion Tunnel, the flow velocity in the wind tunnel was turned on only after the two persons had left the test chamber, for safety reasons. This time delay led to uncertainty in determining the start of the experiment. In

the laboratorial tests performed for analysis of Pedrógão Grande Fire, it was wanted to simulate the spread of the fire after the time t_o (18h30 under real conditions), but due to this delay, this time did not match the time of ignition, which corresponded to the start of data registration.

4.4. ROS Measurements with Infrared Images

All tests were monitored and recorded in continuous mode with an infrared camera (IR) (FLIR SC660) and a video camera in the visible range mounted on top of a lifting platform. To avoid parallax errors, the angle between the optical axis of the infrared camera and the ground surface of the different combustion tables used was approximately 90°. The parameters considered for the camera IR were a temperature range between 300°C and 1500°C, an emissivity of 0.98 (Dlugogorski *et al.* 2014) and an acquisition rate of 15 Hz. A threshold of 350°C was used to avoid obstruction of vision by the smoke and flame cloud (Xiaodong *et al.* 2014; Liu *et al.* 2015). Videos from IR were used to obtain the contour perimeter of the fire with predefined times adjusted for each test performed. To determine the evolution of the fire front, the cartesian coordinates of the image points were used to calculate the instantaneous values of ROS at each point on the fire line. More details on this methodology can be found in Raposo 2016; Raposo *et al.* 2018; Viegas *et al.* 2021, 2023; Ribeiro *et al.* 2022 and 2023.

For the point ignition fire in the slope and in a canyon the positions of fire progress along the OX axis (see Figure 12 and Figure 13) of the combustion tables and the positions $P_i(x_i, t_i)$ and $P_{i+1}(x_{i+1}, t_{i+1})$ were determined at predefined times. In the slope tests, these points coincided with the top of the fire. However, in some configurations of the canyon fires, there was a branching of the fire with two heads, one on each slope canyon faces, but the analysis was always performed on the intersection of the two sides of the canyon, corresponding to the axis OX (see Figure 13). For the parallel

fire lines under a wind condition, in Section 3.3.1 the analysis of the approaching fires was explained.

Using this data, it can be determined the instantaneous ROS $R_i(x_i, t_i)$:

$$R_i = \frac{x_{i+1} - x_i}{t_{i+1} - t_i} \quad 39$$

It was calculated this value for time t_j as follows:

$$t_j = \frac{t_i + t_{i+1}}{2} \quad 40$$

To minimise the influence of fuel moisture m_f on R_i, it was used the non-dimensional ROS (Viegas 2006) in this work, which is calculated as follows:

$$R' = \frac{R_i}{R_o} \quad 41$$

where R_o represents the basic ROS (cm.s^{-1}) under no-slope and no-wind conditions.

4.5. Flow Velocity

S-type pitot tubes locally built according to standard specifications and calibrated in a wind tunnel at ambient temperature with high-precision pressure sensors that were used in the experimental program. S-type pitot tubes allow the determination of the local flow velocity by measuring the differential pressure based on Bernoulli's equation. The calibration coefficient of the Pitot tube $C_{P,S}$ is used to calculate the flow velocity U using the following equation:

$$U = C_{P,S} \cdot \sqrt[2]{\frac{2 \cdot \Delta P}{\rho}} \quad 42$$

where ΔP is the differential pressure between windward side and leeward side and ρ is the density of the fluid, in this case air. The coefficient $C_{P,S}$ was determined during previous calibration S-type pitot with $C_{P,S} = 0.69$, this value being similar to what is found for this type of sensors (Pinto *et al.* 2020).

The calibration tests were performed on the Oblique Combustion Tunnel (TCO) of the Forest Fire Research Laboratory of the University of Coimbra, see Figure 19. This wind tunnel is an open circuit type with a closed test chamber with a square cross-section of $0.4 \times 0.4 m^2$. The flow is generated with variable rotational velocity to control the reference flow velocity. The flow is relatively uniform inside the test chamber, and the maximum flow velocity is near $30 m.s^{-1}$. The fan rotation speed is controlled with a manual potentiometer and, this provides a frequency value (Hz) that is proportional to the fan rotation. To determine the TCO tunnel calibration constant, the relationship between the frequency value (Hz) of the fan rotation speed and the flow speed in the rectangular section, where the tests are carried out, was measured. For this calibration, a hot film anemometer (KIMO AMI 300) was used to measure the flow velocity (U) for different fan rotation speeds (frequency - Hz). Three replications were performed, and the hot film anemometer recorded the flow velocity during the 60s and calculated the average flow velocity to reduce uncertainty. It is considered that the flow velocity can be determined by applying the equation:

$$U = 0.613 \times Freq \qquad 43$$

where U represents the flow velocity ($m.s^{-1}$) and $Freq$ (Hz) represents the different fan rotation speeds. The correlation coefficients of the linear regression R^2 was 0.999. Further details can be found in Appendix A2.

a)

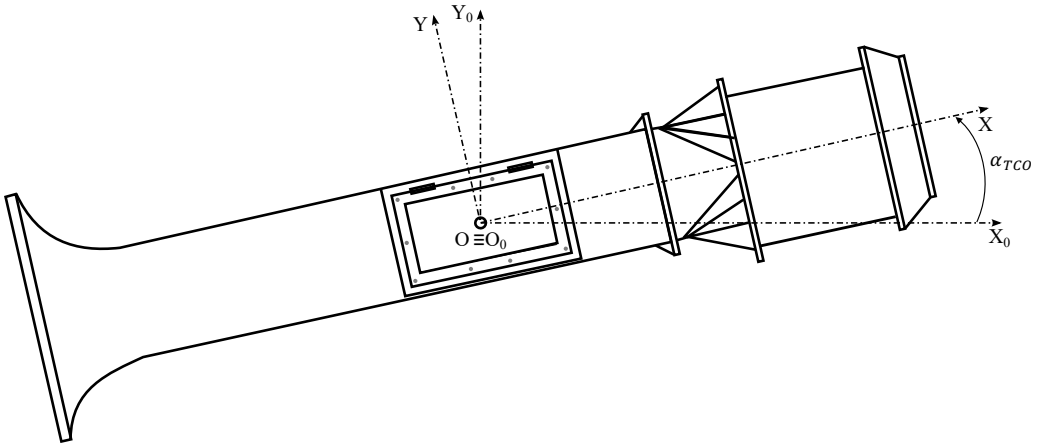

b) b1)

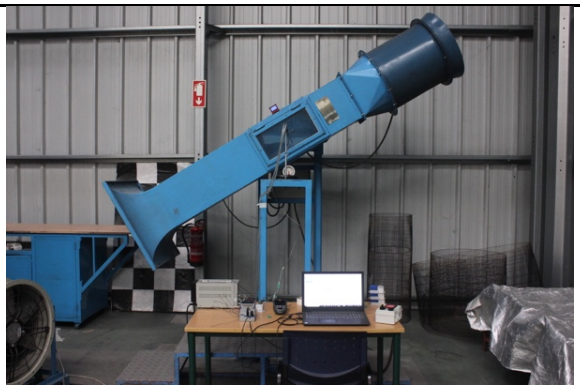

b2)

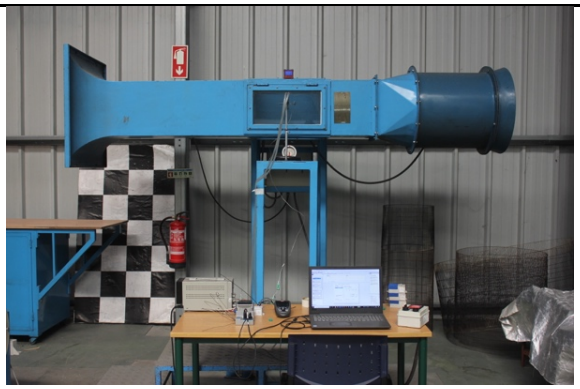

b3)

Figure 19: a) Experimental setup scheme (top view) of the S-type Pitot tube in the TCO. b) View the TCO of the Forest Fire Laboratory of the University of Coimbra with three different pitch angles: b1) $\alpha_{TCO} = +30°$. *b2)* $\alpha_{TCO} = 0°$ *and b3)* $\alpha_{TCO} = -30°$.

The value of the flow velocity U as a function of the square root of the signal (in voltage dV (Volt)) coming from the pressure transducers gives an almost linear relationship (cf. Figure 20). The flow velocity during the experimental programme was measured at various points along the axis OX with S-type pitot tubes, which are specially designed for measuring pressure differences in high-temperature flows, i.e., in flames. To

compensate for the difference due to the temperature increase near the flames in relation to the ambient temperature, the following equation was used:

$$U_i = 4.66 \times \left(\left(\frac{T_i}{T_a} \right) . \sqrt{dV_i} \right) \quad 44$$

where U_i represents the flow velocity (m.s^{-1}), T_i and T_a represent the flow temperature measured by the thermocouple K-type thermocouples (K) inside of the flame and the ambient temperature, respectively and dV_i represents the potential difference produced by the flow pressure. In this equation, it was assumed that the ambient pressure is the same in the calibration tests and in the fire experiments. The correlation coefficients of the linear regression R^2 was 0.998. From the temperature recording at each pitot position at an acquisition rate of 1Hz using K-type nickel-chromium/nickel-aluminium thermocouples, metal-shielded, with a diameter of 0.5mm, connected to a NI cDAQ-9174 with a TC module NI 9213, which allows synchronous data recording, it was possible to determine the arrival time t_p of the flame at each pitot position, which was determined by the fact that the temperature reached a value of 350ºC.

The pitot tubes were placed along the centre line, aligned with the OX axis, 15cm above the surface of the table, so that the tube was always above the fuel bed but within the flame zone. During the tests performed by the point ignition fire in the slope tests, five tubes were used at 1, 2, 3, 4 and 5m along OX axis from the its origin, with the pitot tubes designated P_1, P_2, P_3, P_4 and P_5, respectively, see Figure 12 (a). Each pitot measured the flow temperature T_i and velocity U_i ($i = 1$ to 5) parallel to the fuel bed at every second. Each Pitot tube was connected via pipes to a Gems 5266-50L Very Low Range Differential Pressure Transducer (0 to 100Pa). These transducers were connected to the NI cDAQ-9174 with a voltage module NI 9205, which also performs the data recording of the signal at a frequency of 1Hz. The transducers are bidirectional, so the signal is positive when the flow is oriented towards the positive OX axis and negative when it is opposite. Using the data collected by this method and the values of the synchronous temperature measurements, it was possible to estimate the flow velocity caused by the

fire phenomena by applying a calibration. It is noted that sometimes the flow is not aligned with the Pitot tube axis, but if this deviation of the flow with respect to the Pitot tube axis is less than 30º, the measurement error is very small and can be neglected (Pinto *et al.* 2020). Further details on the use and calibration of S-Pitot tubes can be found in Kang *et al.* 2015 and Pinto *et al.* 2020. Pinto *et al.* 2020 found that the error due to misalignment between the flow velocity and the probe axis is negligible at an angle below 6°. However, during this calibration it was found that if the misalignment is in the range between 0 to 30°, the error is less than 2%. During the calibration tests it is performed hysteresis test to analyse the response time. The response time is on average around 2s, thus being in the same order of magnitude as the signal acquisition. Further details can be found in Appendix A2.

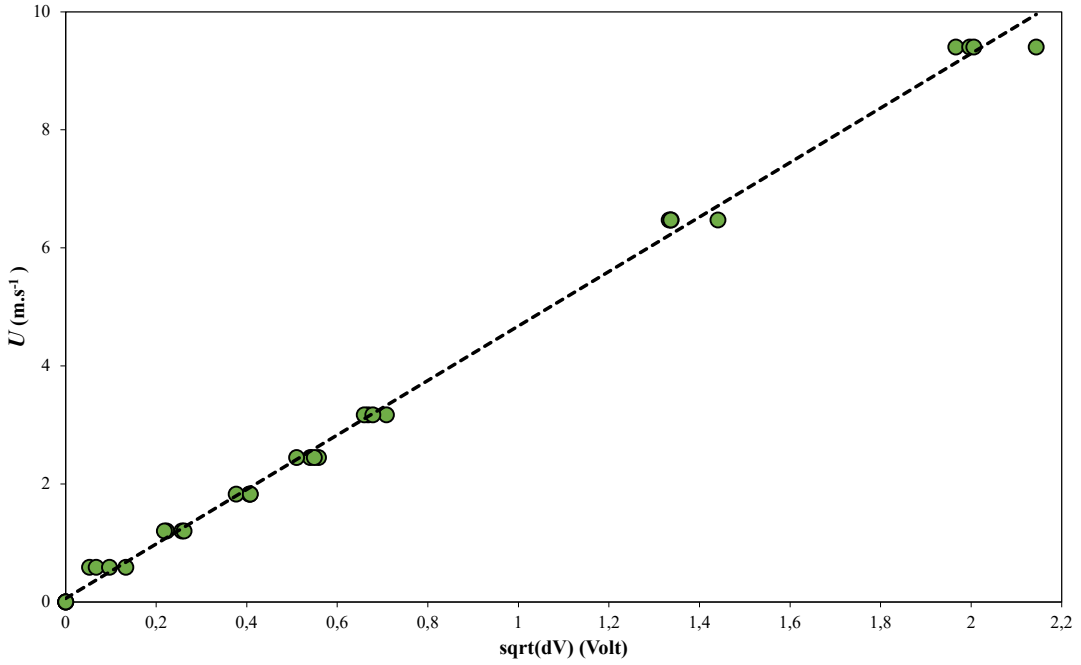

Figure 20: Linear relation between the value of the flow speed and the squared rout of the signal, in voltage, of the pressure transducers. The correlation coefficients of the linear regression R^2 *was* 0.998.

4.6. Flame Geometry

During the point ignition fire in a slope (SP), two video cameras were placed on the side of the burn table surface to record the spread of the head burn during each test (see Figure 12). The two cameras were Sony AVCHD MPEG2 SD and Sony HD DCR-SR87, recording 20 frames per second. Although each camera was able to capture the entire length of the fire spread, to minimise parallax errors it was used the camera 1 to analyse the fire spread in the first half of the table and camera 2 for the remaining part. Reference directions and scale markings were used to estimate the flame angle and length. It is estimated that the errors of angle and length measurement are less than 1º and 2 cm respectively in the whole field of view of each camera.

The flame length L_{fl} was defined by the length of a line connecting the tip of the continuous flame to the centre of the base of the flame (see Figure 21). The flame angle β_{fl} is the angle between the base of the fuel bed and the above-mentioned line, as shown in Figure 21.

To estimate L_{fl} and β_{fl} at a given time t_j, three images taken 1 second apart were used, at time $t_j - 1$s, t_j and $t_j + 1$s. The properties of the flame were the average of these three values.

The experiments used in this work are controlled by the slope terrain α, it was considered the possibility of using a different flame angle $\boldsymbol{\beta_0}$ defined by:

$$\beta_o = \beta_{fl} + \alpha \qquad 45$$

when analysing the flame angle following Cruz and Alexander 2019. The angle β_0 between the flame and the horizontal surface would be more meaningful in describing the role of gravity or buoyancy in flame development and fire spread. However, it has been found that this is especially true in the initial stages of fire development, as fire-induced convection soon becomes the dominant mechanism controlling flame geometry and fire spread.

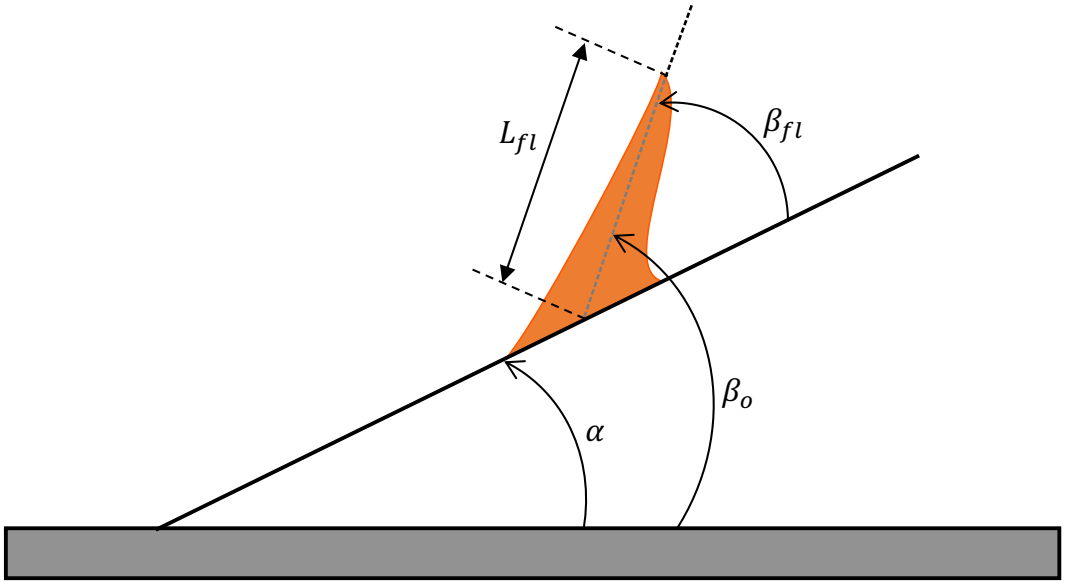

Figure 21: Schematic view of the flame geometry where: α is the slope angle, β_o is the angle between the flame and the horizontal surface, β_{fl} is the flame angle and L_{fl} is the flame lengths.

Chapter 5. Results and Discussion

In this chapter, the results and discussion have been supported by experimental work at laboratory and field scale, as well as by the real forest fires. This chapter has been divided into two sections, presenting the results and discussion of the non-monotonic and intermittent fire behaviour and the analysis of the merging fire lines - the Pedrógão Grande fire, non-symmetric junction fire and parallel fire fronts under wind flow conditions.

5.1. Main Results of Non-monotonic and Intermittent Fire Behaviour

5.1.1. Fire Spread in Slopes

This section presents the results of the experiments of point ignition fire in a slope (SP) with a slope angle α of 20°, 30° and 40°. The results of the ROS of the main fire front developed by the spot ignition of the fire, the flame characteristics of the fire head with the lateral video cameras (flame angle and flame length), the temporal evolution ROS and the flame angles corresponding to the conceptual model, and the reference flow velocities measured by the pitot tubes are shown.

Rate of Spread

The results of the non-dimensional ROS R' as a function of the time elapsed since the origin of the four tests carried out for each configuration for the slope angles $\alpha = 20°$, $30°$, and $40°$, are shown in Figure 22 a), b) and c), respectively. Despite the random nature of the variations in R', good repeatability can be observed for the tests performed in each configuration. For $\alpha = 20°$ (see Figure 22 a)), it can be seen that R' increases on average from an initial value close to 1.5 to about 2.5 and then slightly decreases. For $\alpha = 30°$ (see Figure 22 b)) it can be seen that R' increases on average to values close to 5 and then decreases with two or more cycles. For $\alpha = 40°$ (see Figure 22 c)) it can be seen that R' increases on average to values close to 8, although there is an indication of a decreasing phase of R', however, the length of the fuel bed considered was not sufficient to observe the fully deceleration phase.

The relationship between the relatively high frequency, low amplitude fluctuations and the low frequency, high amplitude oscillations will be analysed in sections 5.1.3 and 5.1.4. It appears that high amplitude oscillations occur mainly at values of $R' > 4$, because for this fuel the amount of energy involved in the combustion process is sufficient to cause larger deflections of the $R'(t)$ curve.

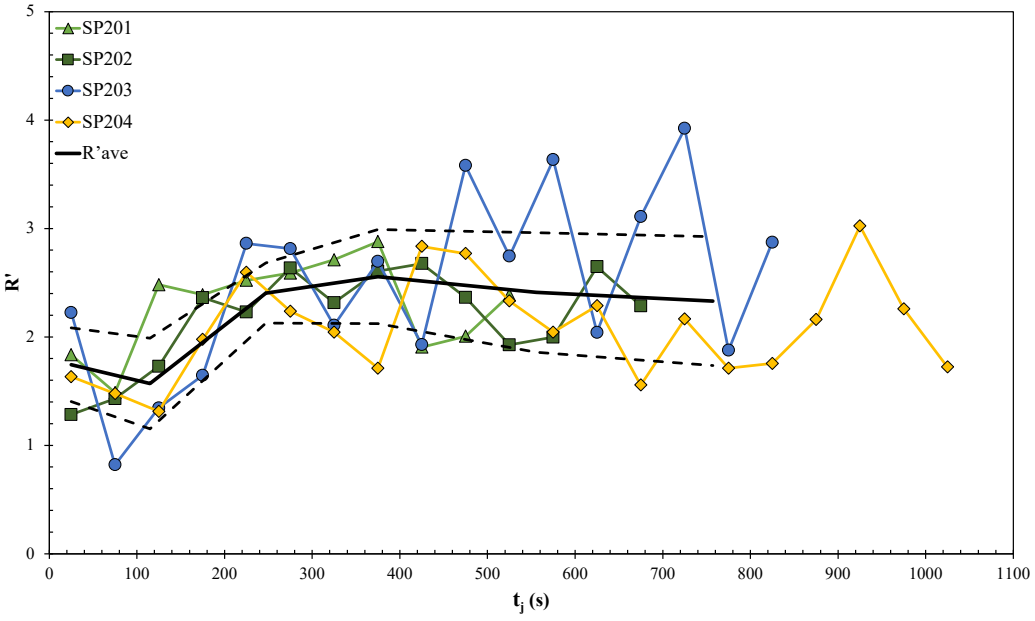

a)

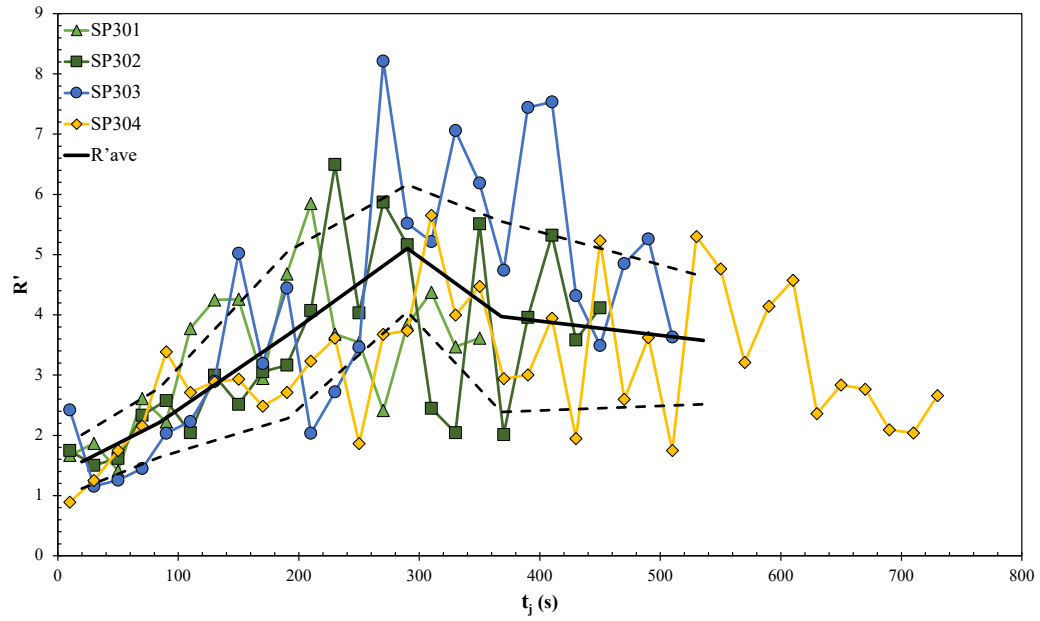

b)

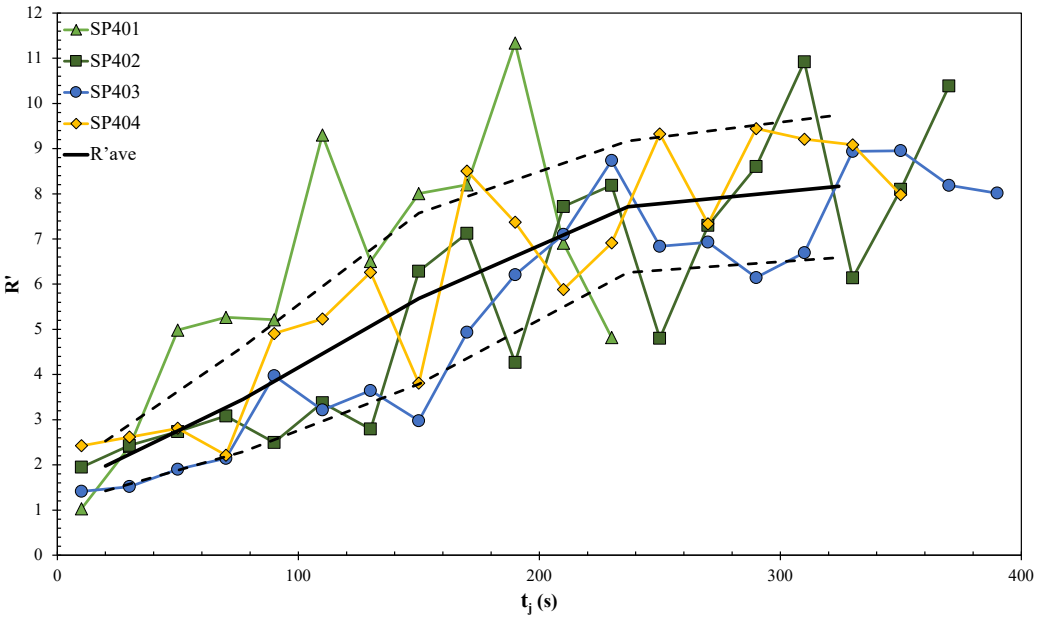

c)

Figure 22: Plots of non-dimensional ROS R' as a function of time t_j in all tests of each configuration: a) $\alpha = 20°$; b) $\alpha = 30°$; c) $\alpha = 40°$. The curves with R'_{ave} and the dashed line curves $R'_{ave} \pm \Delta R'$ are shown in each case.

Flame Properties

The results of the flame angle β_{fl} and the flame length L_{fl} as a function of time for all the experiments carried out for each configuration, $\alpha = 20°$, $30°$, and $40°$ are shown in Figure 23 a), b) and c), respectively. The good repeatability of the experiments is evident in the four tests performed for each configuration for both parameters. Following the pattern of variation of R', the flame angle for $\alpha = 20°$ (Figure 23 a)) decreases from the initial value of $70°$ (corresponding to $\beta_0 \approx 90°$) to about $50°$ at the end of the experiment. For $\alpha = 30°$ (Figure 23 b)), the initial values of β_{fl} are around $60°$ (corresponding to $\beta_0 \approx 90°$), then drop to around $40°$, remain constant and then tend to increase, at least in some tests. For $\alpha = 40°$ (Figure 23 c)), the flame angle β_{fl} starts with values of the order of $50°$ (corresponding to $\beta_0 \approx 90°$) and then increases to $60°$ or even $70°$.

Silvani *et al.* 2018 experimentally investigated the propagation of a linear fire front in a $3x6\text{m}^2$ tiltable bench for two tilt angles of $0°$ and $30°$ and for three values of fuel load. For the $30°$ tilt angle, they refer to oscillations in the flame geometry, which they describe as spherical ("fireball") or elongated in shape, which is consistent with the variations observed for both L_{fl} and β_{fl}, but they do not provide detailed data on the temporal evolution of the fire properties.

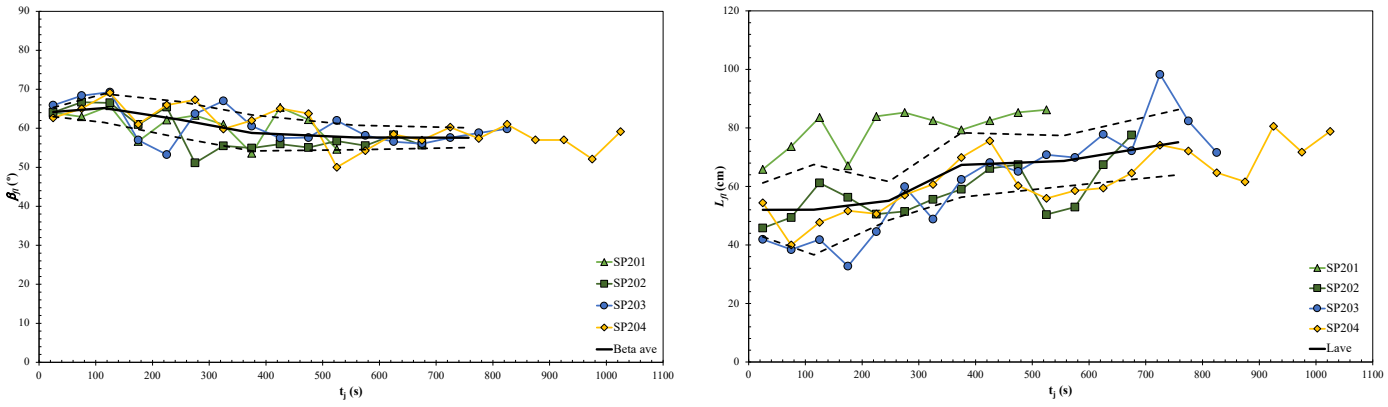

a)

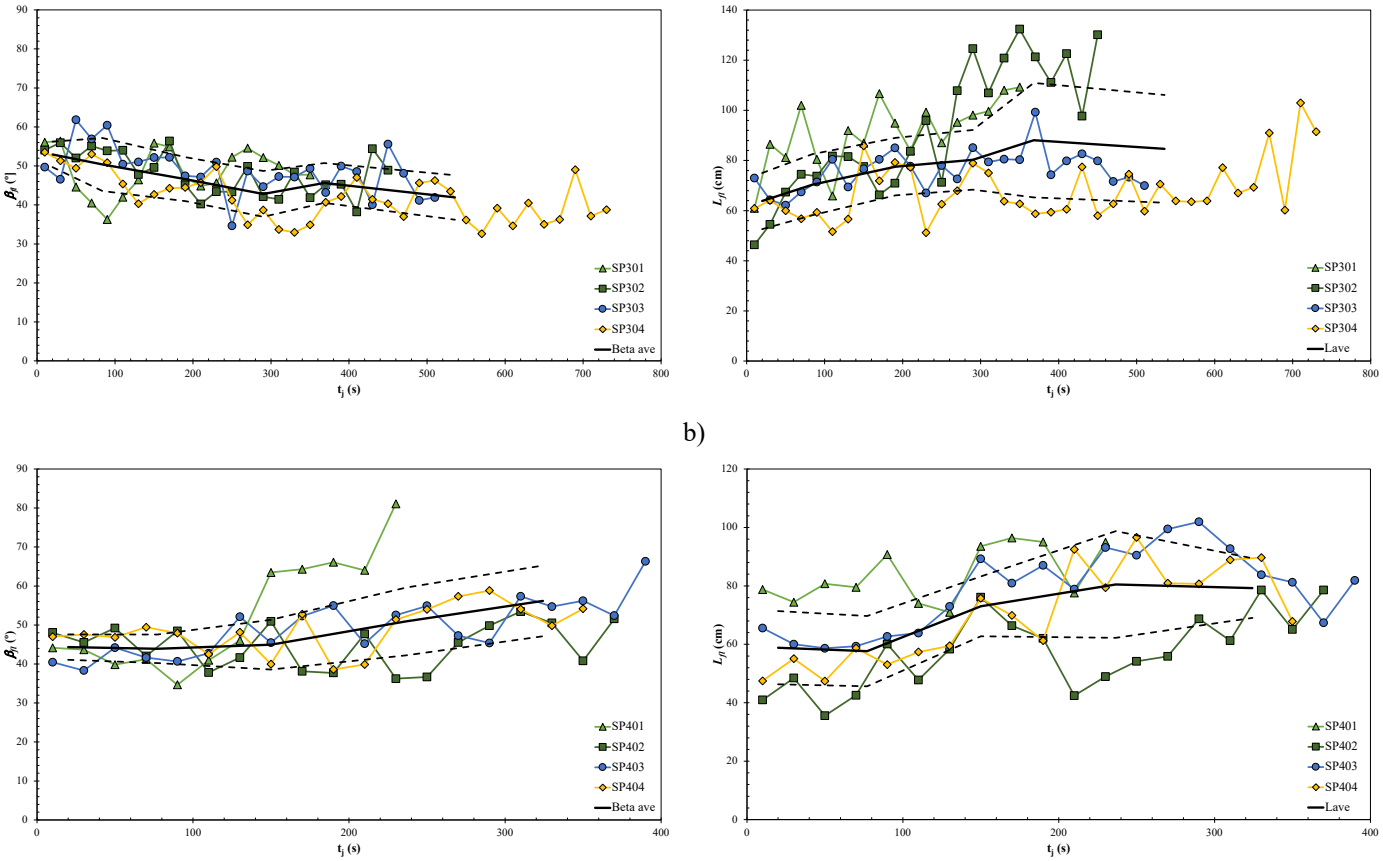

Figure 23: Plots of flame angle β_{fl} and flame length L_{fl}, as a function of time t_j in all tests of each configuration: a) $\alpha = 20°$; b) $\alpha = 30°$; c) $\alpha = 40°$. The dashed line curves corresponding to the average values ±STDEV.

Mendes-Lopes *et al.* 2003 experimentally investigated the spread of a linear fire on a $2x0.7m^2$ fuel bed of pine needles of *Pinus pinaster* with a fuel load of $500g.m^{-2}$ under different slope conditions and wind speeds. The moisture content of the fuel was controlled during the experiments and two values of moisture content, 10% and 18%, were used. The slope was varied between $\pm 15°$ and the wind speed between $\pm 3m.s^{-1}$. Although not all combinations of slope and wind were tested for practical reasons, 192 tests were conducted for different combinations of the three control parameters. The authors give the results of the variation of the flame angle over time for two cases without

slope. In the case without wind, the value of β_{fl} oscillates around 90° with small variations, but with 1m.s^{-1} wind, the flame angle varies between 40° and 90° with an average value of 70°. With a flow of 3m.s^{-1}, the flame height increases from 15 to 45cm in the first 120s, with some fluctuations, and then decreases to values close to 20cm after 20s.

Time Evolution of ROS and Flame Angle

To illustrate the processes described in the conceptual model, it was used some samples of slope tests for each configuration to analyse the evolution of R' and β_{fl} as a function of time t_j. The results are shown in Figure 24, 25 and 26, which include video image frames of each test at selected time points. Despite the accuracy and detail of the experiments, it was recognised that there are some high-frequency oscillations of both parameters that are not easy to interpret or explain due to the discrete nature of our data set, which means that it cannot observe the extreme values of R' or β_{fl} as they may not occur exactly at the observation times.

In test SP202 (Figure 24) for $\alpha = 20°$, the ROS increases and the flame angle decreases, corresponding to points 1, 2 and 3 in Figure 2. There is an acceleration period between 25s and 275s with an oscillation of R' and β_{fl}. In this period R' varies between 1.28 and 2.64 and β_{fl} oscillates around 65°. Between 275s and 325s, β_{fl} decreases to 51°, while R' drops from 2.68 to 2.32. From this point until the end of the test, β_{fl} rises again while R' goes through a complete cycle of rise and fall. The three photos on the top of Figure 24 correspond to video frames taken at 325s, 425s and 525s, corresponding to a period of increasing values of β_{fl}, while R' rises to 2.65 and then falls to 1.93.

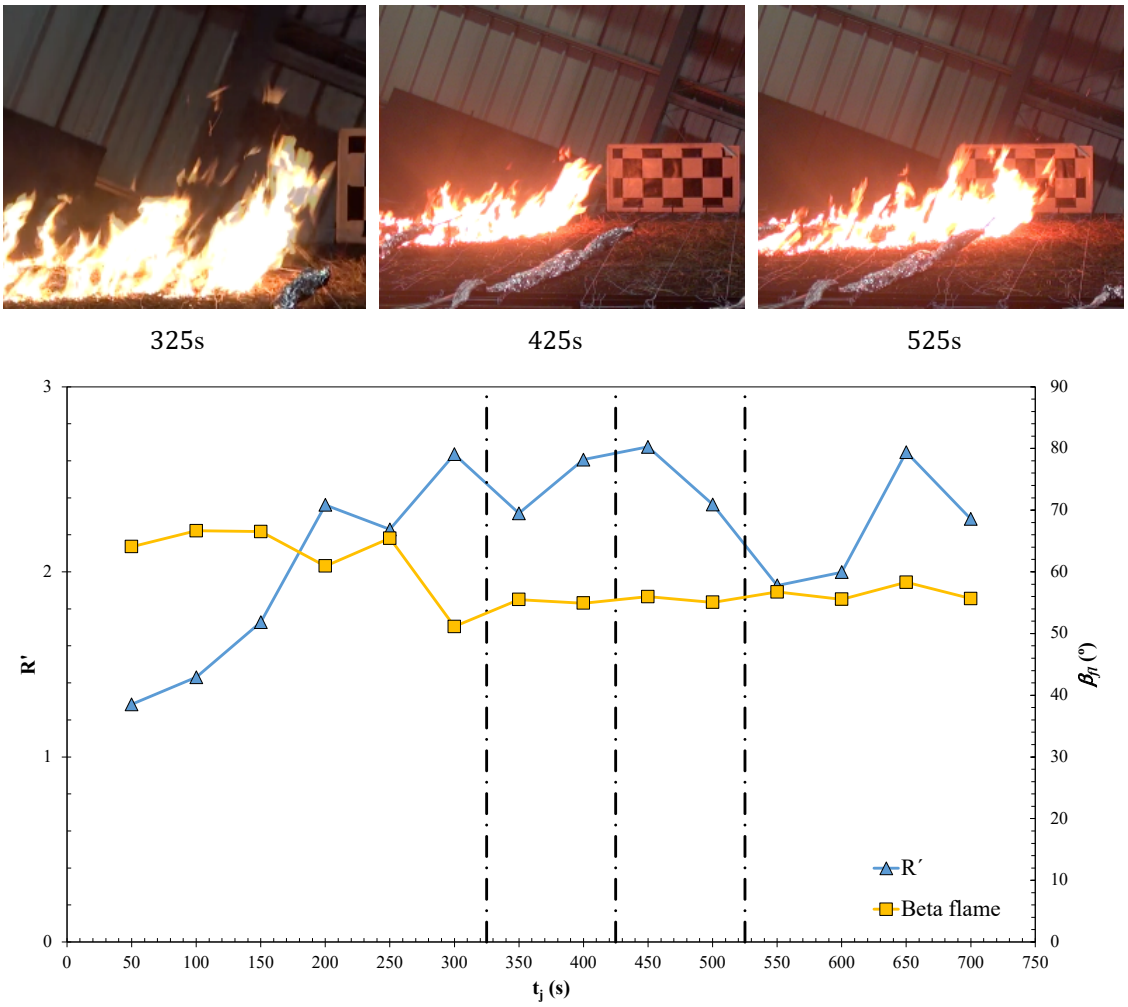

Figure 24: Evolution of R' and β_{fl} as a function of time for the test SP 202 – $\alpha = 20°$. The photos above the figure show the flame in the time steps indicated next to each image. The vertical dotted lines in the diagram correspond to the individual photos. The same applies to Figure 25 and 26.

In the SP 302 test (Figure 25) for $\alpha = 30°$, the ROS and the change in flame angle correspond to essentially the same phase as in the previous case. There is a period during which R' increases overall until it reaches a value of 6.49 at 230s. During this period, two oscillations of R' and β_{fl} are observed. Between 230s and 330s there is a period in which R' drops from 6.49 to 2.04, also with two oscillations. Then two peaks of R' occur at 350s and 410s with oscillations in between. From this point to 450s, R'

drops to 4.12 with an overall increase of β_{fl} with at least two oscillations. The three photos on top in Figure 25 correspond to video images taken at 170s, 210s and 270s. They illustrate the decrease of β_{fl} and the increase of R' between 170s and 210s and the opposite trend in the second period.

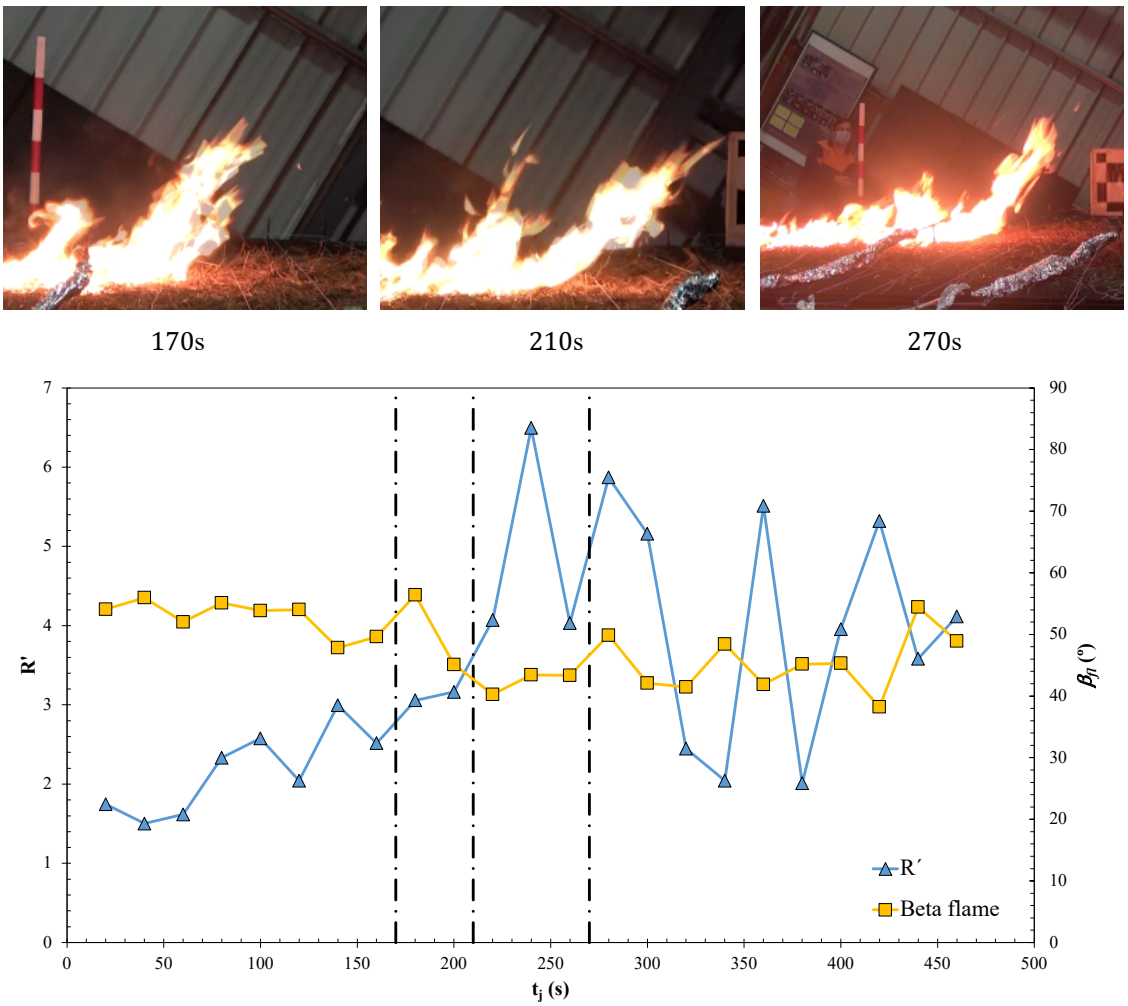

Figure 25: Evolution of R' and β_{fl} as a function of time for test SP 302 – $\alpha = 30°$.

The SP 403 test (Figure 26) for $\alpha = 40°$ may be easier to interpret as the value of R' increases from 1.2 at the beginning to 8.74 at 230s. The ROS and the flame angle increase according to points 4, 5, 6 and 7 in Figure 2. There are several fluctuations of both R' and β_{fl} during this period. Throughout the test, β_{fl} increases with fluctuations, some of which are in phase with the fluctuations of R'. Between 230s and 390s, R' and

β_{fl} have two oscillations. The photographs from this test taken at 130s, 250s and 330s show a period of a general increase in β_{fl} and R' with two pronounced oscillations.

130s 250s 330s

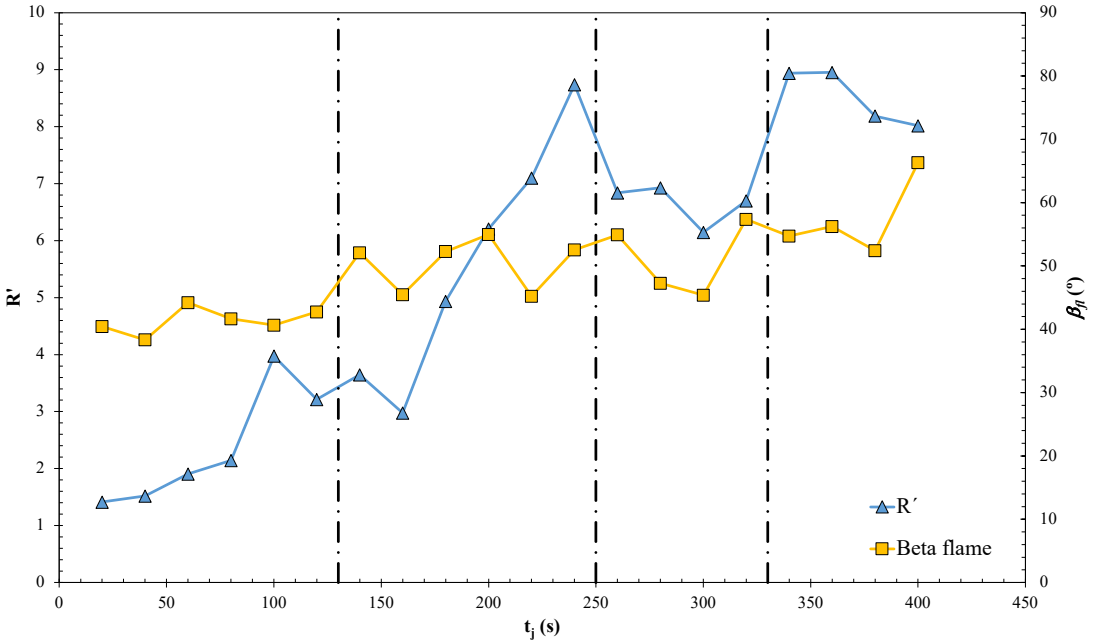

Figure 26: Evolution of R' and β_{fl} as a function of time for test SP 403 – $\alpha = 40°$.

Flame Angle and Flame Length

The distribution of the values of the flame angle β_{fl} for all tests as a function of R' is shown in Figure 27. In the initial phase of fire propagation, when $R' < 2$, β_0 would possibly better describe the evolution of the flame angle, as previously suggested, but the

fire-induced flow velocity increases rapidly with R', and the fire is dominated by convective flow and is less dependent on terrain slope, as shown in Figure 27.

Despite the scatter of the data, it is possible to see the trend of reduction of β_{fl} from $90°$ for $R' = 0$ to a minimum value between $30°$ and $40°$ for $R' \approx 4$. For $R' > 5$, β_{fl} increases to values close to $70°$.

This trend can also be seen in the line from $\beta_{ave}(\mathrm{R}')$ in Figure 27. The lines corresponding to $\beta_{ave} \pm \Delta\beta$, where $\Delta\beta$ is the standard deviation calculated in each interval of R', are also shown. Note that in this figure the values of β_{fl} correspond to periods of fire acceleration (increase in R') or deceleration (decrease in R'), which may contribute to the scatter in the data.

The distribution of the values of the flame length L_{fl} for all experiments as a function of R' is shown in Figure 28. The scatter of the data is greater than for β_{fl}, but a trend can be seen from the test points and the L_{ave} line that L_{fl} increases for $1.5 < R' < 3$. Possibly there is a local maximum value of L_{fl} for $R' \approx 4$ which corresponds to the minimum of β_{fl}. For $R' > 5$, there seems to be a second stage of increase in L_{fl}, but the available data are insufficient to support this claim in this range of tests.

The results show that for a given fuel bed, there is a unique relationship between ROS and the flame angle and flame length, but this relationship is not bi-univocal as many fires spread models assumed. For a given fire spread condition - in this case, the slope of the terrain - some values of β_{fl} or L_{fl} may correspond to different values of R'. As shown in the present analysis, this fact is due to the oscillatory behaviour of fire spread caused by the interaction between fire induced convection and the combustion process.

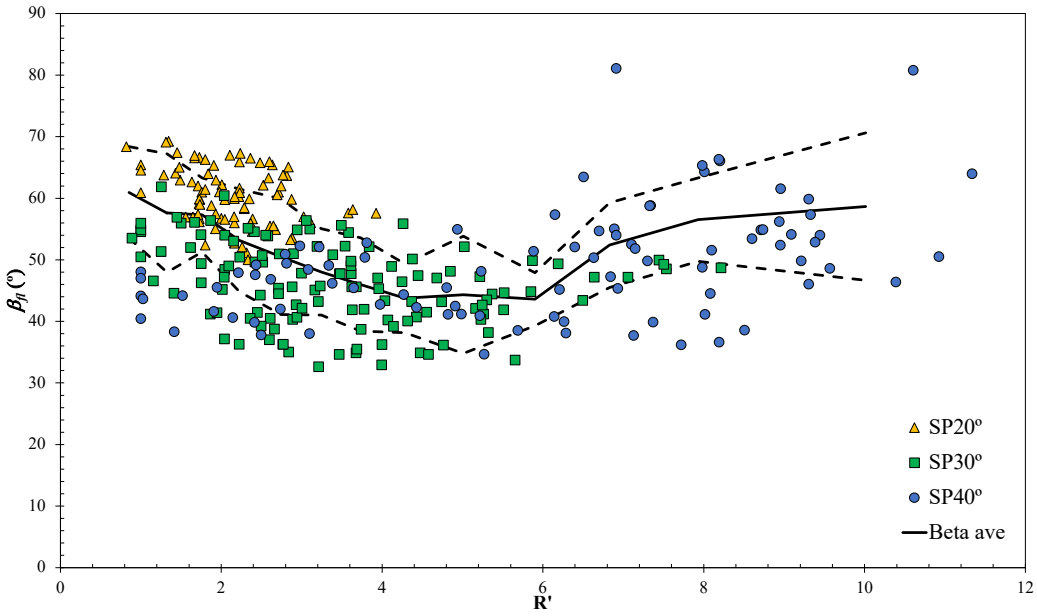

Figure 27: Distribution of $\beta_{fl}(R')$ for all tests. A line of "Beta Ave" – β_{ave} values is shown, and a dashed lines correspond to $\beta_{ave} \pm \Delta\beta_{fl}$, where $\Delta\beta_{fl}$ is the standard deviation calculated in each interval of R'.

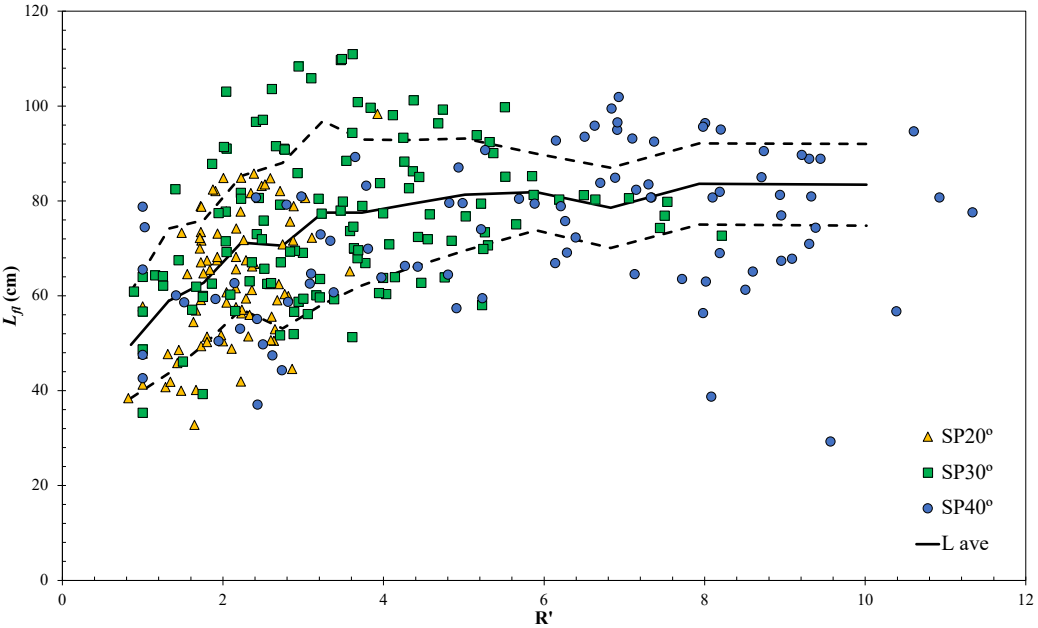

Figure 28: Distribution of $L_{fl}(R')$ for all tests. A line of "L ave" – L_{ave} values is shown, and dashed lines correspond to $L_{ave} \pm \Delta L_{fl}$, where ΔL_{fl} is the standard deviation calculated in each interval of R'.

Reference Flow Velocities

The flow velocity was measured at five points 15cm above the ground in all experiments with S-pitot tubes, as described in methodology section 4.5. Using the average values of flow velocity every 5 seconds, the time t_P of the passage of the flame at each pitot tube position was estimated from the curve of $U'(t)$ when the flow velocity changed its signal from essentially positive to essentially negative values of U'. The results obtained for each configuration were very consistent, and the results of an example experiment for each configuration are shown in Figure 29.

To simplify the analysis, it was assumed that the flame is static at the position of the pitot tube ($x = x_P$). As the flow approaches the leeward side of the flame (negative values of $x_P - x$ and $t_P - t$), the value of U' increases to a maximum value as envisaged in the conceptual model and then decreases due to the presence of the flame acting like a solid, leading to a stagnation point under the present test conditions. On the lee side of the flame, the flow velocity U' becomes negative and has a clearly defined minimum value. Very similar results can be found in Liu *et al.* 2015 and Yang and Chen 2018.

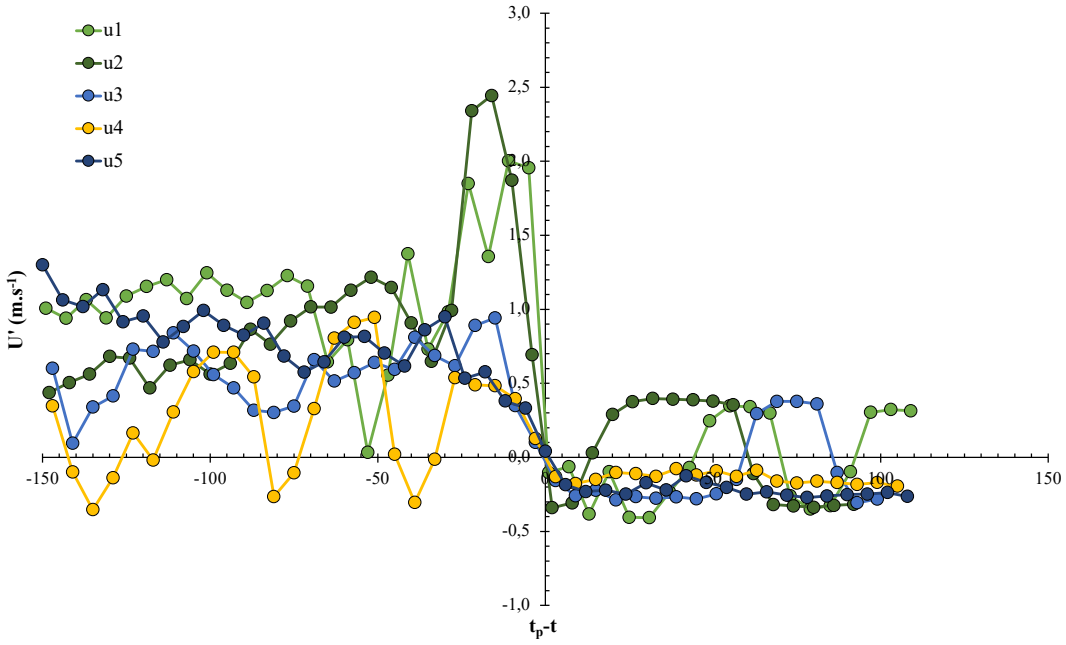

a)

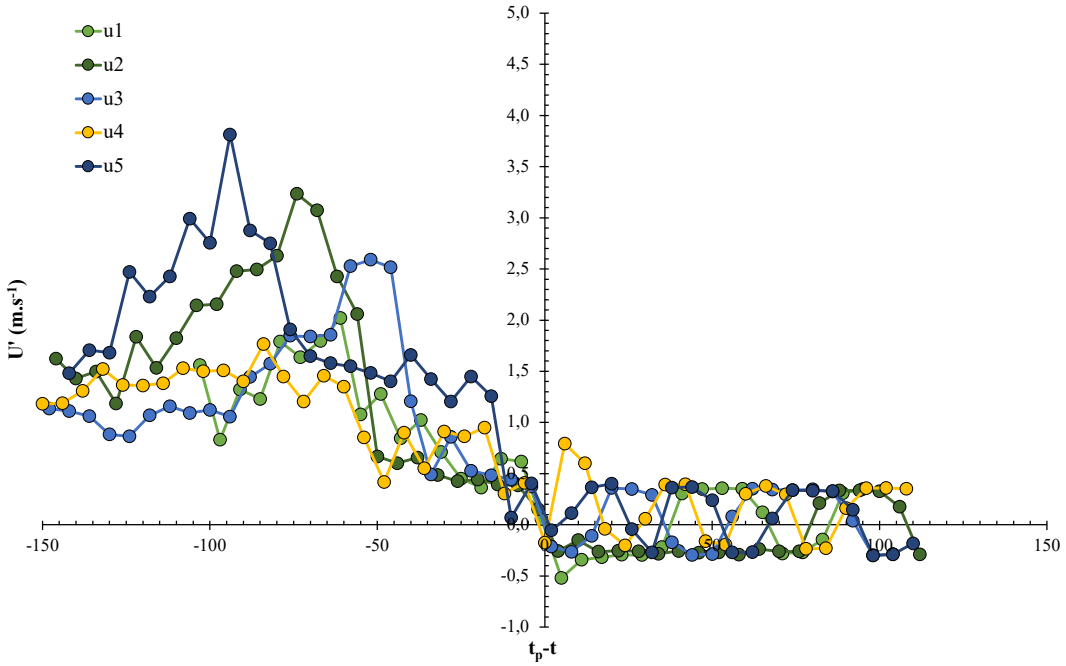

b)

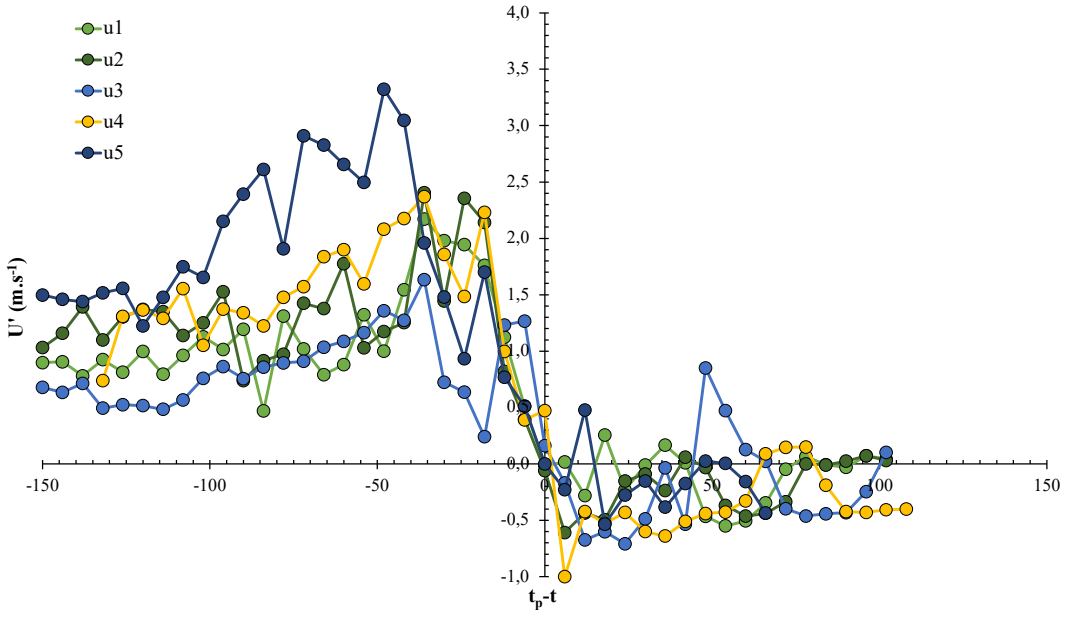

c)

Figure 29: Plots of U' as a function of $t_p - t$ for one sample test of each configuration: a) SP201 – $\alpha = 20°$; b) SP301 – $\alpha = 30°$; c) SP401 – $\alpha = 40°$.

The values of U'_{max} and U'_{min} obtained in each test as a function of the local value of R' are shown in Figure 30 and 31, respectively. As can be seen in Figure 31, U'_{max} increases with R' as expected, although the present data suggest that this increase is not monotonic. For the fuel bed at hand, there appears to be a local peak of U'_{max} for $R' \approx 4$. The distribution of U'_{min} also shows a tendency to decrease with R', as shown in Figure 31, but may also not be monotonic.

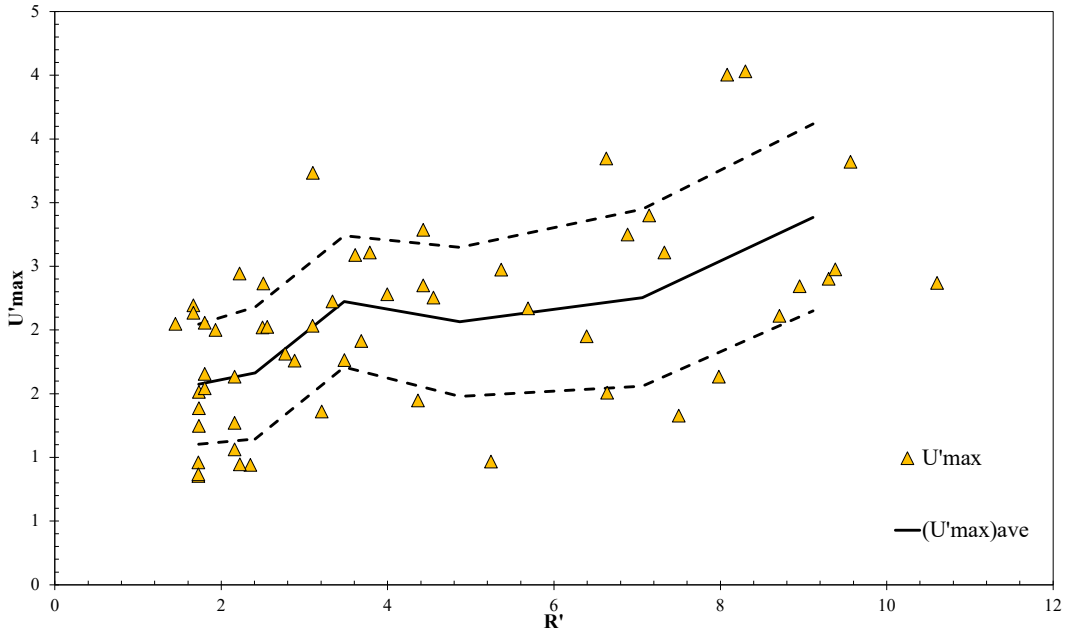

Figure 30: Distribution of U'_{max} as a function of R' for all tests. Lines with $(U'_{max})_{ave}$ and $(U'_{max})_{ave} \pm \Delta U'_{max}$ (dashed line curves) are shown as well.

Silvani *et al.* 2018 used an innovative technique with Particle Imaging Velocimetry (PIV) to analyse the flow field in a vertical plane. Their flow visualisation and measurement techniques confirm the presence of a positive fire-induced wind on the windward side of the flame and a negative flow towards the flame on its windward side.

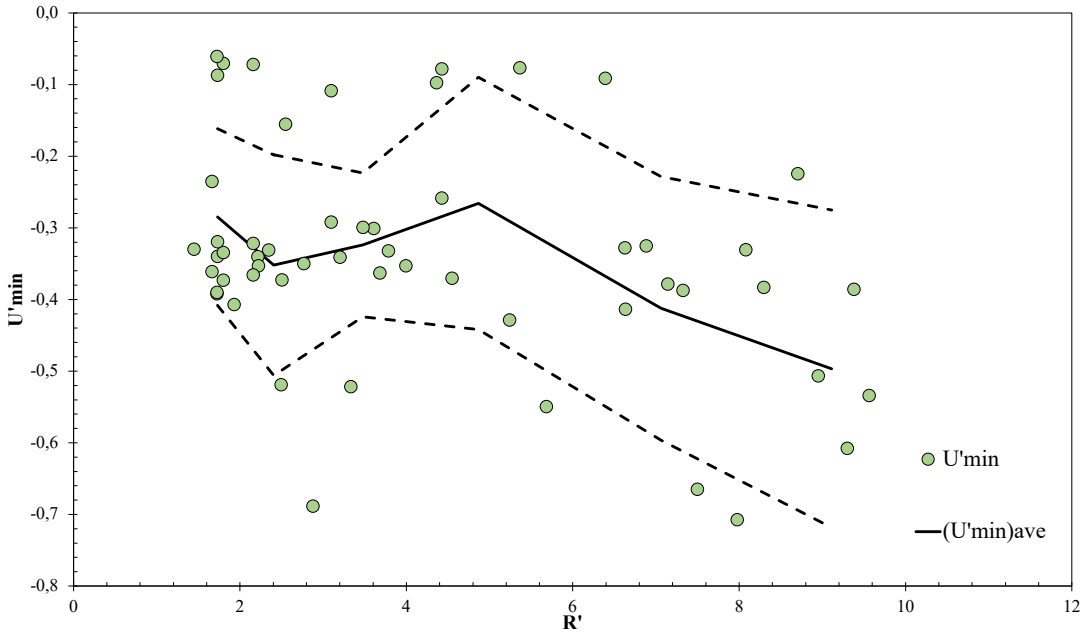

Figure 31: Distribution of U'_{min} as a function of R' for all tests. Lines with $(U'_{min})_{ave}$ and $(U'_{min})_{ave} \pm \Delta U'_{min}$ (dashed line curves) are shown as well.

5.1.2. Fire Spread in Canyon

This section presents the results of the ROS of the head fire in a canyon along its OX axis, which cover a wider range of values of R' and therefore better illustrate the non-monotonic behaviour of fire propagation predicted by the conceptual model. Due to practical difficulties, the flow and flame properties were not analysed in this experimental configuration.

Figure 32 a), b) and c) plot the non-dimensional ROS R' values of the head fire along the centreline of the canyon every five seconds as a function of time for the three experiments with $\alpha = 20°$, 30° and 40° along with the curves of R'_{ave} and $R'_{ave} \pm \Delta R'$. Considering the relatively high temporal resolution of the fire spread analysis, the existence of fluctuations in the ROS values over time can be clearly seen.

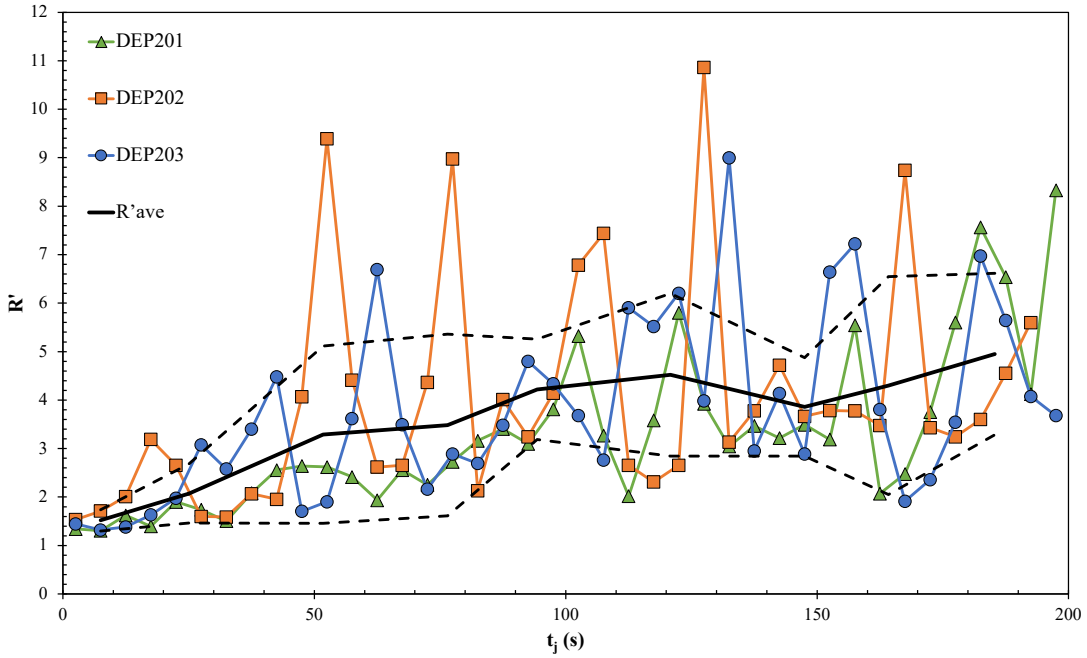
DEP201
DEP202
DEP203
R'ave
R'
t_j (s)

a)

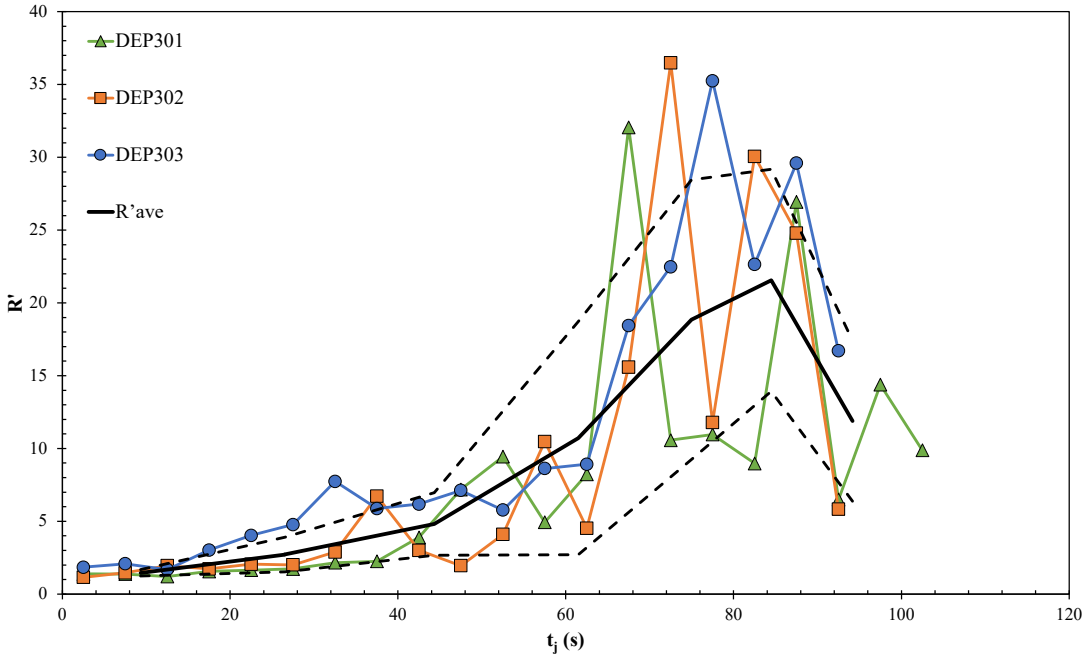
DEP301
DEP302
DEP303
R'ave
R'
t_j (s)

b)

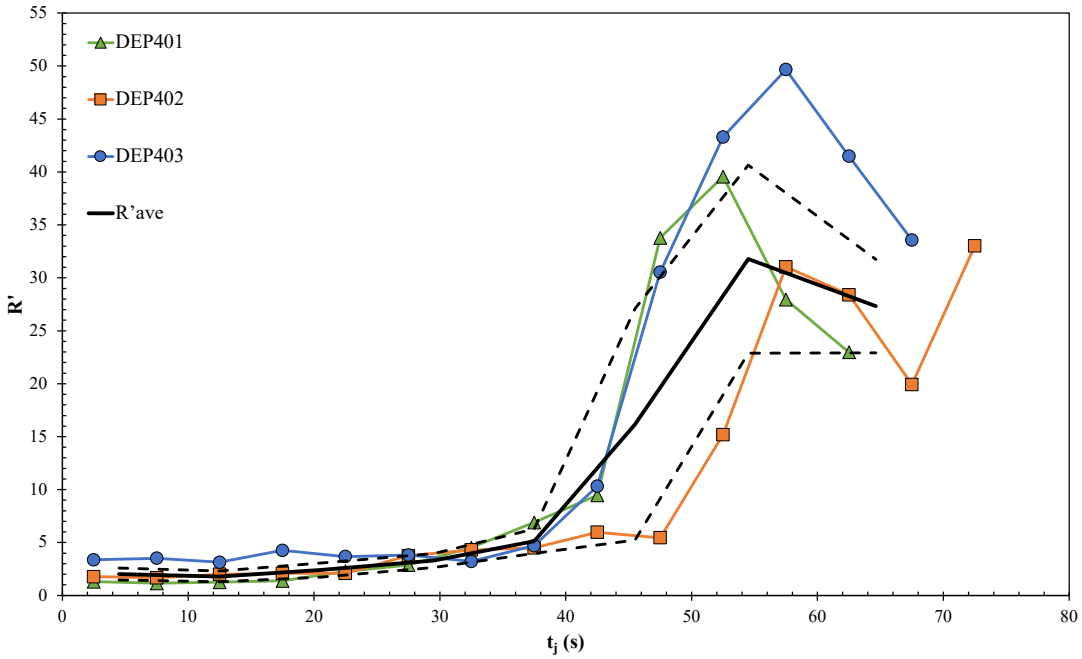

c)

Figure 32: Non-dimensional ROS R' of the head of fire in the water line of a canyon ($\delta = 40°$) for three values of the slope angle α as a function of the time t_j. The average value R'_{ave} and the $R'_{ave} \pm \Delta R'$ dashed line curves are shown in each case. a) $\alpha = 20°$; b) $\alpha = 30°$ and c) $\alpha = 40°$.

The fluctuations of ROS can be considered as an instability or disturbance of the equilibrium state in the fire (cf. Finney *et al.* 2015). In some cases, the amplitude of this oscillation is sufficient to cause a relatively large increase in ROS, resulting in an "eruption" or "blow-up", but in other cases, these oscillations are damped by the fire environment system and the ROS value returns almost to its initial value, as predicted by the conceptual model. This can be clearly seen in Figure 32 a) for the experiment with $\alpha = 20°$, where the average value of R' steadily increases from about 1.5 at the beginning to 4 at the end of the experiment. Given the random nature of the turbulent flow fluctuations, each test differs from the others, and the scatter of the ROS values is not necessarily due to a lack of accuracy or other systematic measurement errors, but to the random nature of the fire fluctuations. Therefore, the averaging process only provides an indication of the general trend of the evolution of $R'(t)$.

In the case of $\alpha = 30°$ (Figure 32 b)), the fluctuations persist, but when the value of R' is $R' > 7$, the amplitude of the fluctuations becomes very large, and a sudden fire acceleration occurs. As predicted by the model of Viegas 2005, the value of R' increases very rapidly and reaches about 35. After reaching this maximum value there are one or more fluctuations with a general tendency to decrease ROS. The same happens for $\alpha = 40°$ (Figure 32 c)) with an increase of R' to about 40, although in this case the reduction phase is not completed due to the limited size of the fuel bed.

5.1.3. Amplitude of Oscillations

From the analysis of the cases mentioned in sections 4.1.1, 4.1.2 and 4.1.3, the values of ΔR and R_m were estimated, which are shown in Figure 33. As can be seen in this figure, the data points cover a range of more than three orders of magnitude, from 0.22 to 514cm.s^{-1} for R_m and a similar range also for ΔR. Given a linear relationship between the amplitude ΔR of the oscillations and the mean R_m of the ROS, it can be expressed by:

$$\Delta R = k_R R_m \qquad 46$$

Figure 33 shows a straight line covering the entire data set and the corresponding value of k_R is equal to 1.276. The two dashed lines shown in the figure correspond to k_R values of 2.0 for the upper line and 0.2 for the lower line. A line that passes through the origin has been chosen because it was assumed that there should be no oscillations for $R_m = 0$ and therefore it should also be $\Delta R = 0$.

It has been analysed the fit of equation 46 to partial data sets for each of the five cases studied. For each case, it was considered ΔR^+, ΔR^- and ΔR and obtained the respective values of k_R, which are given in Table 9 with the corresponding R^2 values.

The relevance of the data in Figure 33 is that it shows the existence of a relationship between ΔR and R_m, i.e., a monotonically increasing function over the entire data range. By using the arithmetic mean, this function is well represented by a linear function. Other methods of calculating the mean of R_m have been tested, such as using

the harmonic mean, which also gives a monotonic increase of ΔR with R_m, but with a large scatter.

The two-way analysis ANOVA without replication for the values presented in Table 9 showed that the k_R values for positive, negative and all data were significantly different (p-value<0.05) for all scales used, see Andrade 2019.

To analyse the significance of the coefficient k_R for the change in ROS during an oscillation, it was assumed that $R_2 > R_1$, thus:

$$\Delta R = k_R \frac{R_1 + R_2}{2} \tag{47}$$

From this it is easy to conclude that:

$$\frac{R_2}{R_1} = \frac{2 + k_R}{2 - k_R} \tag{48}$$

The evolution of the ratio between R_2/R_1 as a function of k_R according to equation 48 is shown in Figure 34.

The ratio k_R^+/k_R^- between the two coefficients is usually greater than one, indicating that the amplitude of the fire growth oscillations is on average greater than that of the fire spread decrease, as assumed above.

As shown in Figure 33 and Table 9 the value, of k_R estimated for partial data sets shows three typical values: between 0.4 and 0.8 for laboratory experiments, 0.9 for field experiments and 1.3 for large-scale fires. This means that the ratio R_2/R_1 between the local maximum and minimum values of ROS during a period of oscillation increases with the extent of the fire and can reach values of 4 or 5 for large fires.

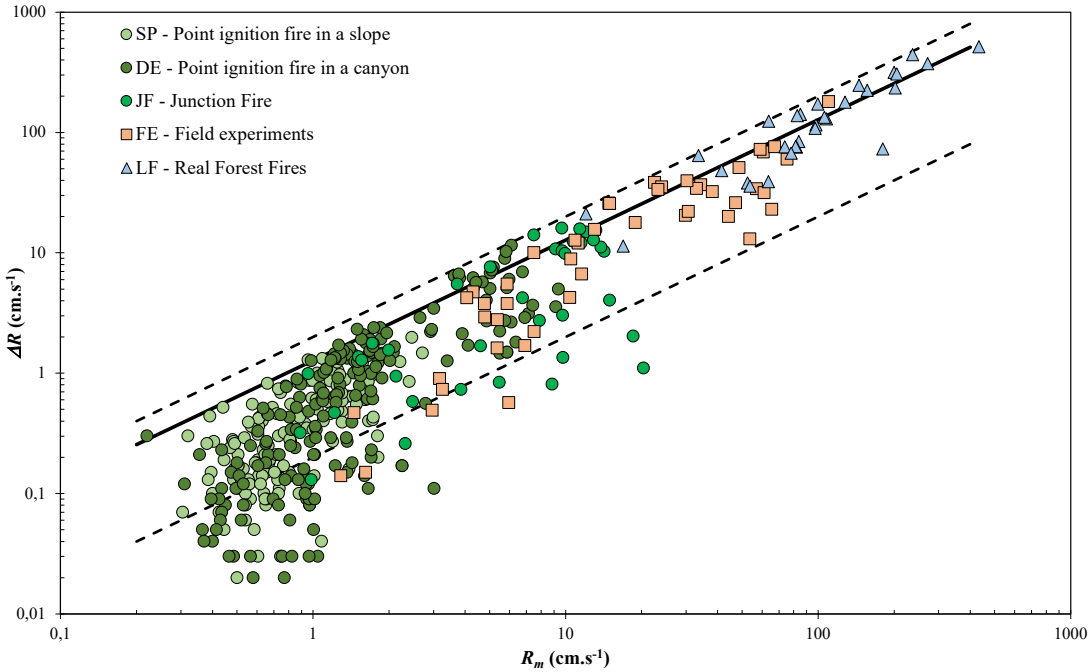

Figure 33: Amplitude of fluctuations of the ROS as a function of the average value of R_m for all cases. The black line is a linear fitting to the entire data with k_R=1.276; the dashed lines correspond to k_R equal to 0.2 (lower line) and to 2.0 (upper line).

Table 9: Coefficients k_R for the various types of fires studied and the correlation coefficients of the linear regression R^2 for each k_R coefficient.

Ref.	ΔR			k_R^+/k_R^-	R^2 (ΔR)		
	k_R^+	k_R^-	k_R		k_R^+	k_R^-	k_R
SP	0.287	0.225	0.482	*1.28*	0.415	0.408	0.767
DE	0.452	0.318	0.770	*1.42*	0.351	0.401	0.711
JF	0.612	0.484	0.683	*1.26*	0.642	0.268	0.633
FE	0.784	0.398	0.984	*1.97*	0.590	0.424	0.821
LF	0.879	0.530	1.307	*1.66*	0.661	0.356	0.949
All Cases	0.871	0.520	1.276	*1.67*	0.655	0.357	0.927

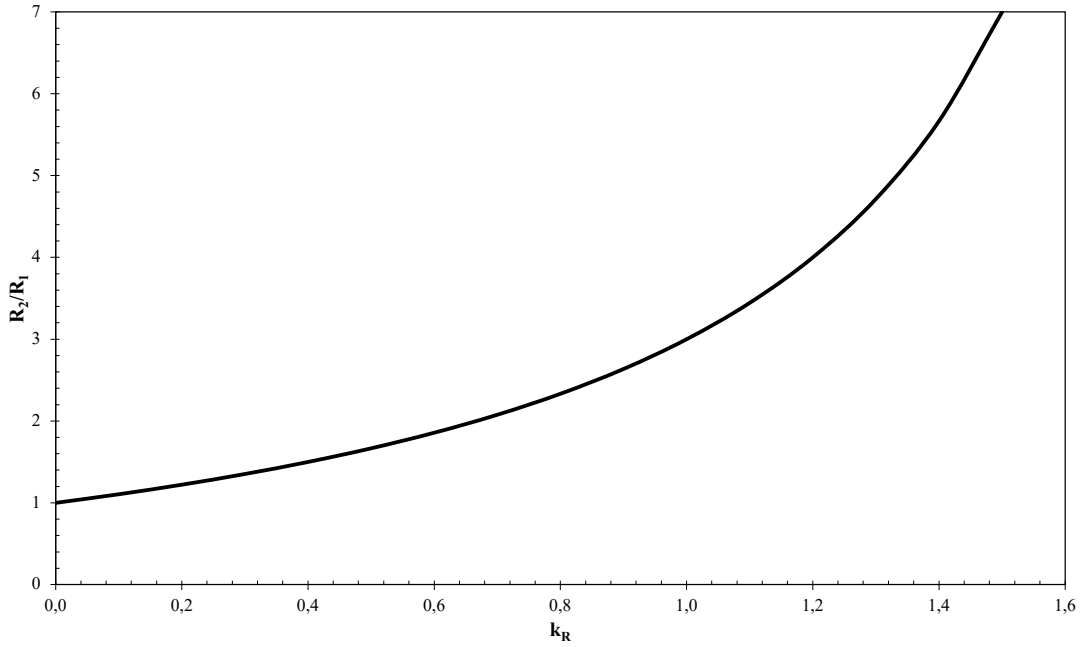

Figure 34: Evolution of the ratio of maximum to minimum value of R in a fluctuation cycle as a function of coefficient k_R, according to equation 48.

The data show that k_R varies according to the type of fire. Despite the limited amount of data, it will try to establish correlations between k_R and three proposed parameters: (i) the typical size d_f (cm) of the largest fuel particles consumed by the fire during its spread; (ii) the typical fuel load consumed by the fire M_c (kg.m^{-2}); and (iii) the typical total size $\mathscr{L}$ (m) of the fire assuming that it spreads as a coherent convective cell. In very large fires, there may be different fire cells or fire sections along the perimeter of the fire, possibly with different heads. In such cases, each cell must be treated separately.

The analyses of each large fire do not intend to provide very precise data on the characteristics of each fire, i.e., an average value for each of the proposed parameters, such as Weise *et al.* 2022, but rather to give typical values representative of the magnitude of each parameter in the range of cases studied. In the laboratory experiments, d_f and M_c can be defined with great accuracy as 0.06cm and 0.6kg.m^{-2}, respectively, as they were kept constant in all the series of experiments used in this work. The size $\mathscr{L}$ of the fire can

be fixed at 3m, which corresponded to the typical size of the fuel beds used in the experiments, see Table 10. For the field tests, it was assumed that the largest particles consumed by the fire had a thickness of up to 2cm and that the fuel load averaged 4kg.m^{-2}. The extent of the fire was assumed a value of 40m, which corresponded to the typical width of the experimental plots (cf. Table 6), see Table 10. For the real fires, it is more difficult to estimate average values for these parameters, and was assumed, somewhat arbitrarily, the following indicative values: $d_f = 10$cm, $M_c = 20$kg.m^{-2} and $\mathscr{L} = 4000$m, see Table 10.

Figure 35 shows k_R as a function of the three characteristic parameters considered, d_f, M_c and $\mathscr{L}$. In each case, a power law adjustment can be performed by:

$$k_R = a_R . X^{b_R} \qquad 49$$

Table 10: Proposed parameters of the fires: the typical size of the largest fuel particles consumed d_f, the typical fuel load consumed by the fire M_c and the typical total size $\mathscr{L}$.

Ref.	d_f (cm)	M_c (kg.m^{-2})	$\mathscr{L}$ (m)
SP	0.06	0.6	3
DE	0.06	0.6	3
JF	0.06	0.6	3
FE	2	4	40
LF	10	20	4000

In equation 49, the parameter X is either d_f, M_c or $\mathscr{L}$, and the corresponding coefficients of the equation are given in Table 11. Despite the imprecision of this analysis, it can be seen that k_R has a relatively small variation with each of these parameters, as indicated by the exponent in the order of 0.1 to 0.2 in the power law fit. Now, it does not have a physical interpretation for this power law function, but simply note that the parameters a_R and b_R are always of the same order of magnitude and that the modulus of b_R is quite small.

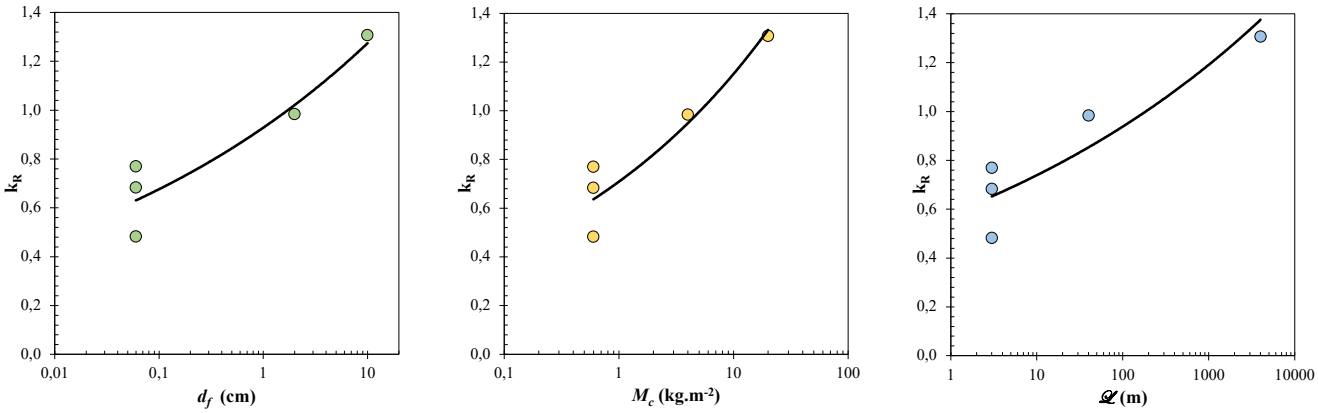

a) b) c)

Figure 35: Plot of coefficients k_R estimated for each series of tests as a function of: a) Fuel particle size d_f; b) Fuel Load consumed by the fire M_c, and c) Overall dimension of the fire $\mathscr{L}$.

Table 11: Parameters of equations 49.

X	k_R		
	a_R	b_R	R^2
d	0.929	0.138	0.883
M_c	0.709	0.211	0.887
$\mathscr{L}$	0.582	0.104	0.842

5.1.4. Frequency of Oscillations

From the analysis of the cases described in section 4.1.1, 4.1.2 and 4.1.3, the values for the frequency of the oscillations of the ROS was estimated and are shown in Figure 36. The frequency of the oscillations varies in a range of five orders of magnitude, from 6×10^{-6}Hz (corresponding to a period of about 46 hours) to 0.1Hz (corresponding to a period of ten seconds). Despite the scatter of the data, three main groups of results can be identified, corresponding to the three scales of experimental data: Laboratory (SP, DE and JF), Field (FE) and Large Fires (LF).

For a given fuel type, an approximately linear relationship between F and R for given data sets can be expressed as follows:

$$F = k_F R_m \quad (50)$$

As in the previous case where it was tested a correlation between ΔR and R_m, in this case, a linear function with zero origin to the distribution of F and R_m for given ranges of values was fitted. According to equation 50, the coefficient k_F has the unit (cm^{-1}), which also applies to σ_f. Following the methodology described above, the values of k_F^+, k_F^- and k_F for each data set were estimated and the results are shown in Table 12 with the corresponding R^2 values. Unlike k_R, the coefficient k_F has a wide range of variation - four orders of magnitude - between fuels, so it is not possible to establish a general average value for k_F for the entire data set. The two-way analysis ANOVA without replication shows that the results were significantly different for the k_F values for each type of scale analysed (p-value < 0.05), but not significantly different (p-value > 0.05) for another analysis of the k_F values (positive, negative and all data). For more information on the p-value, see Andrade 2019.

As can be seen from Table 12, the ratio between k_F^+/k_F^- is essentially less than one, which means that on average $\Delta t^+ > \Delta t^-$, as indicated above in the definition of the half periods of oscillation. This means that on average the process of fire acceleration takes more time than the decreasing phase, suggesting that the mechanisms controlling each half-cycle are different. However, it will be analysed these differences in more detail in future work. Experiments with compound fires show a different trend, with $k_F^+/k_F^- > 1$, which means that in this type of fire, the convective processes play a different role during the acceleration and deceleration phases. These processes have already been studied by Viegas *et al.* 2012; Raposo 2016 and Raposo *et al.* 2018, but need further investigation.

Following the analysis carried out above, the variation of k_F with each parameter describing the conditions of fire propagation, namely d_f, M_c and $\mathscr{L}$ were plotted in Figure 37. The power law was fitted by:

$$k_F = a_F . X^{b_F} \quad (51)$$

and the coefficients a_F and b_F are given in Table 13.

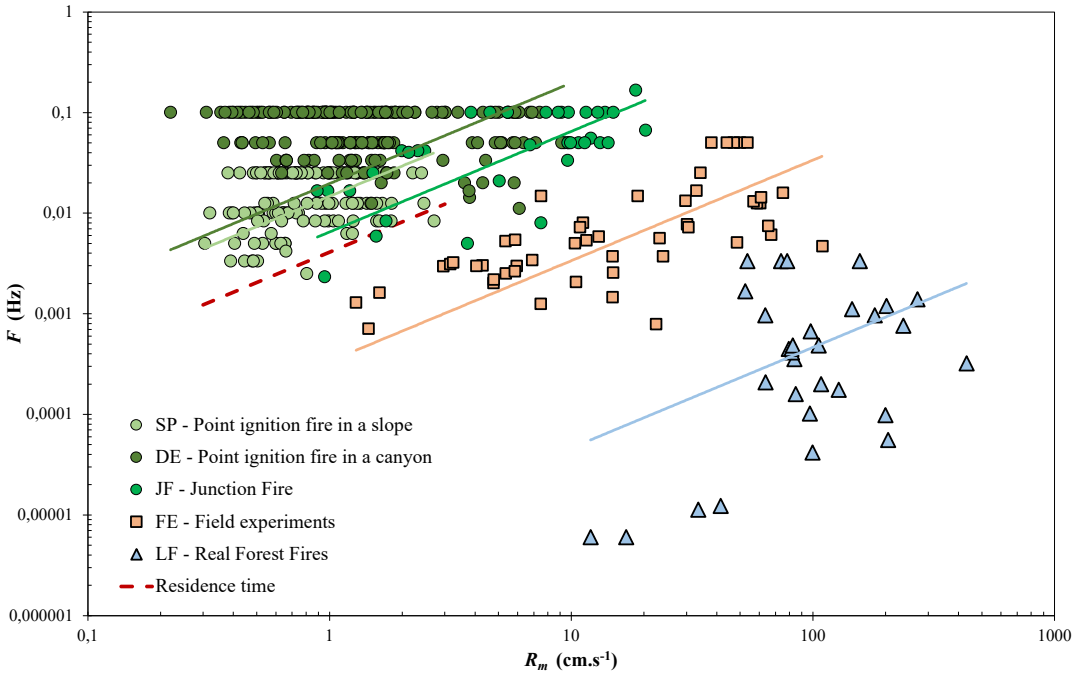

Figure 36: Frequency of oscillations of R_m as a function of the average value R_m of the ROS. The five groups of data correspond to: SP - Slope tests; DE - Canyon tests; JF - Junction fires; FE - Field experiments and LF - Large fires (real forest fires). The colour lines correspond to equation 49 for each group of data with the same colour. The dashed line (resid time) corresponds to the estimation of F for experimental fires using the inverse of the residence time $1/t_r$ given by equation 54.

Table 12: Coefficients k_F for the various types of fires studied and the correlation coefficients of the linear regression R^2 for each k_F coefficient.

Ref.	F			k_F^+/k_F^-	$R^2(F)$		
	k_F^+	k_F^-	k_F		k_F^+	k_F^-	k_F
SP	1.30E-02	1.64E-02	1.47E-02	*0.79*	0.657	0.698	0.678
DE	1.90E-02	2.01E-02	1.97E-02	*0.95*	0.432	0.408	0.413
JF	7.26E-03	5.85E-03	6.50E-03	*1.24*	0.821	0.721	0.766
FE	2.62E-04	3.77E-04	3.37E-04	*0.69*	0.379	0.529	0.457
LF	3.79E-06	6.00E-06	4.63E-06	*0.63*	0.213	0.314	0.251

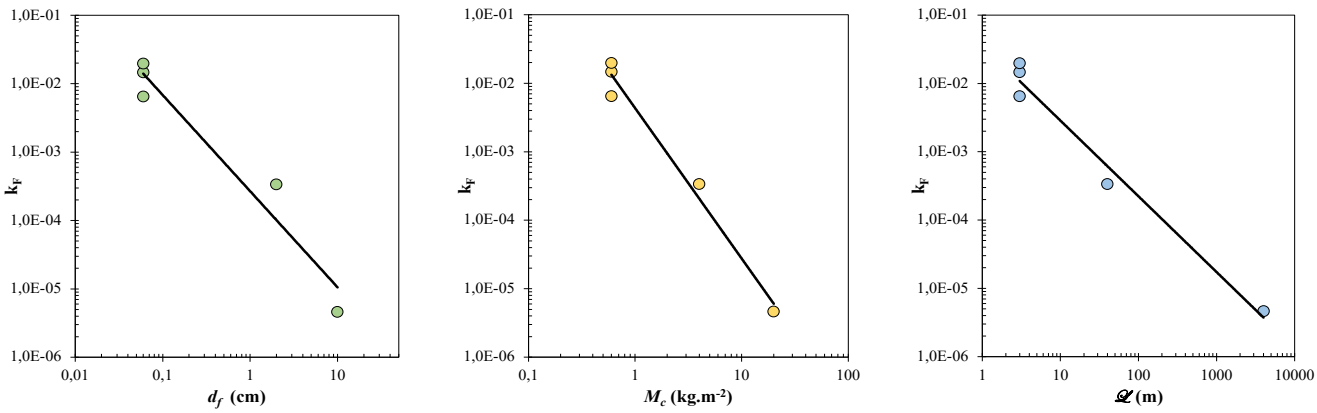

a) b) c)

Figure 37: Plot of coefficients k_F estimated for each series of tests as a function of: a) Fuel particle size d_f; b) Fuel load consumed by the fire M_c, and c) Overall dimension of the fire $\mathscr{L}$

Given the very rough approximations made in estimating these parameters, it cannot be drawing many conclusions or physical interpretations from these relationships. However, it is interesting to note that the coefficient a_F varies by two orders of magnitude and the exponent b_F varies between 1.1 and 2.1, indicating a much stronger dependence of the oscillation frequency on the chosen parameters. It is needing more data to draw more definitive conclusions about the role and relationship of the parameters identified.

Table 13: Parameters of equations 51.

X	k_F		
	a_F	b_F	R^2
d	0.0003	-1.406	0.710
M_c	0.0043	-2.195	0.710
$\mathscr{L}$	0.0367	-1.109	0.709

5.1.5. Residence Time

The duration of the natural oscillations of the fire is physically related to the duration of the combustion process in the fuel bed or the residence time of the flame (t_r). Following Nelson 2003, it was assumed that the residence time of the flame is equal to

the reaction time (travel time of the fire front over a distance equal to the flame depth). For a given fuel bed it should have:

$$\Delta t \propto t_r \rightarrow F \propto \frac{1}{t_r} \qquad 52$$

The residence time t_r of the flame can be measured experimentally or estimated using models from the properties of the fuel bed. Vaz *et al.* 2004 investigated different empirical models for estimating the residence time of fuel beds based on their physical properties. They report a model proposed by Fons 1946, given for relatively thick particles ($d_f >$ 4mm), which suggests $t_r \propto d_f^{1.5}$. Referring equation 52, it can be state that this law is very close to the present finding $k_F \propto d_f^{1.4}$. In contrast, another model by Anderson 1982 proposes a linear relationship between t_r and d_f.

In Vaz *et al.* 2004, the effect of the ROS of fire on t_r is not directly addressed, although some stated results on the effect of moisture content m_f may include this effect. In several experiments with cot fires, it is observed that t_r increases with m_f. Since ROS decreases with m_f, it can be inferred that t_r decreases with ROS. In experiments in a slope with pine needles as a fuel bed, was found this relation. The air temperature was measured 15 cm above the ground inside the flames with a K-type thermocouple and it was assumed that the duration of the temperature trace above 350ºC corresponds to the residence time of the flame. The obtained values of t_r are plotted in Figure 38 as a function of the local value of ROS. The data show a large scatter, but a linear fit shows a negative slope, confirming the decreasing trend of t_r (s) with R (cm.s^{-1}). The linear fit is defined by:

$$t_r \approx 56.31 - 10.79R \qquad 53$$

Using the equation 53 to calculate $1/t_r$ in the interval $0.3 < R <$ 3cm.s^{-1}, the values obtained can be adjusted by:

$$\frac{1}{t_r} \approx 0.015 + 0.0082R \qquad 54$$

A line corresponding to equation 54 in the range of values of R_m has been drawn in Figure 36.

In Viegas 2004, the residence time was considered as a relevant parameter for the dynamics of fire behaviour in each fuel bed. In the differential equation of the eruptive fire model, it was assumed that this value is constant for a given fuel bed. The present results show that this assumption must be revised.

In Viegas 2006, typical values of residence time were proposed for different types of fuels, with indication of the estimated minimum, maximum and average values of t_r for each of them. These values are given in Table 14, where litter, shrubs and ash wood correspond respectively to pine litter, field tests and heavy surface fuels, as they occur in high intensity fires. Calculating the corresponding oscillation frequency using the equation 11 gives the values presented in the Table 14. It can be noted that these values follow the trend found in this work for the range of variation of the oscillation frequency.

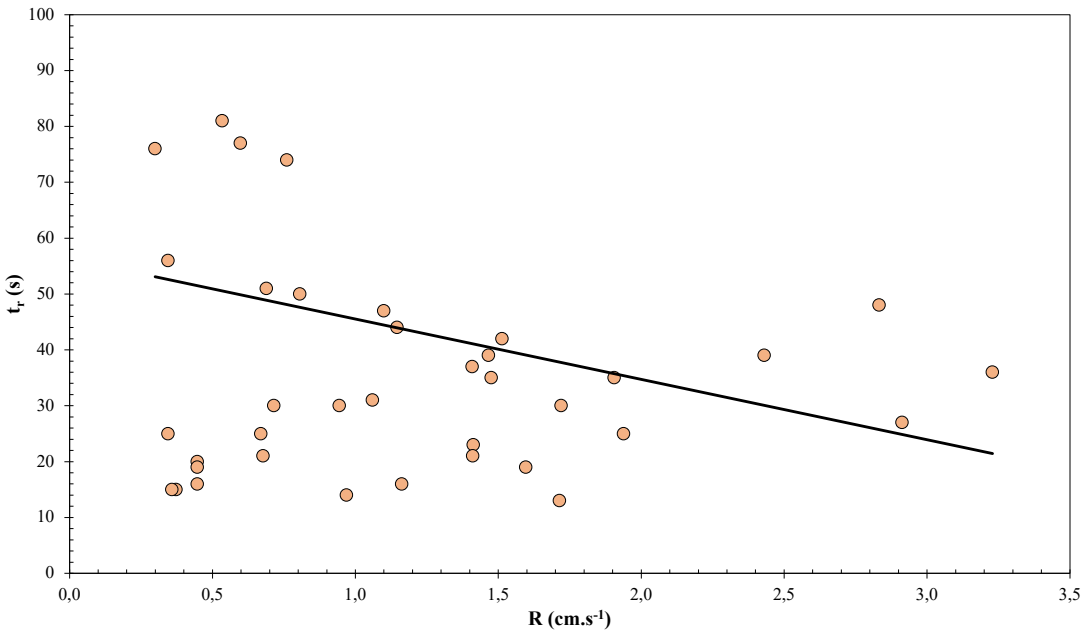

Figure 38: Residence time t_r measured with a thermocouple in pine needles laboratory tests of point ignition fires in a slope.

Table 14: Residence time (Viegas 2006) *of flaming combustion of typical fuels and associated characteristic frequencies.*

Type of fuel	t_r (s)			F (Hz)		
	Min	**Max**	**Average**	**Min**	**Max**	**Average**
Herbaceous	10	50	30	0.05	0.01	0.0167
Litter	30	100	80	0.017	0.005	0.00625
Shrubs	100	1000	1000	0.005	0.0005	0.0005
Slash	1000	10000	5000	0.0005	0.00005	0.0001

5.2. Main Results of Merging Fire Lines

5.2.1. Junction Fire Process in the Catastrophic Fire of Pedrógão Grande

This section presents the results of field and laboratory analysis of the junction fire process in the catastrophic fire of Pedrógão Grande in June 2017. Two fires that started near Pedrógão Grande in June 2017 were influenced by a thunderstorm in the region, spreading uncontrollably and merging into a very fast-spreading fire. The tests were carried out with different wind flow velocities U_0 and different fuel beds. A laboratory-scale investigation of this fire showed good qualitative and quantitative agreement with the large-scale observations.

Evaluation of the Similarity

One of the conditions for the physical similarity of the processes at both scales is the geometric similarity of the terrain and the location where the fire was ignited at the beginning of the fire. The Pedrógão Grande fire area considered in this work has a slope of 6° (10.5%), which can be considered negligible to allow the simulation of the fire on a horizontal surface at a laboratory scale (Ihsan *et al.* 2023). The full-scale terrain consists

of hilly ground with elevation differences of the order of 100m and a maximum slope of 19.8° (36%). The terrain roughness caused by these topography elements over a length of 8 km can be considered negligible compared to the vertical evolution of the fire (Pinto *et al.* 2022) and the overwhelming role of fire-induced convection, allowing to use of a flat surface to represent the laboratory-scale terrain. Figure 39 represents the topography of the area along a 8km section of the terrain along the main fire spread direction.

The fuel cover in the full scale is mainly a mixture of eucalyptus and pine trees with shrubs in the understory. Some areas had acacia and broad leave trees, as well as agricultural cultures, but the predominant fuel was unmanaged and mature eucalypt plantations (Viegas *et al.* 2017; Pinto *et al.* 2022).

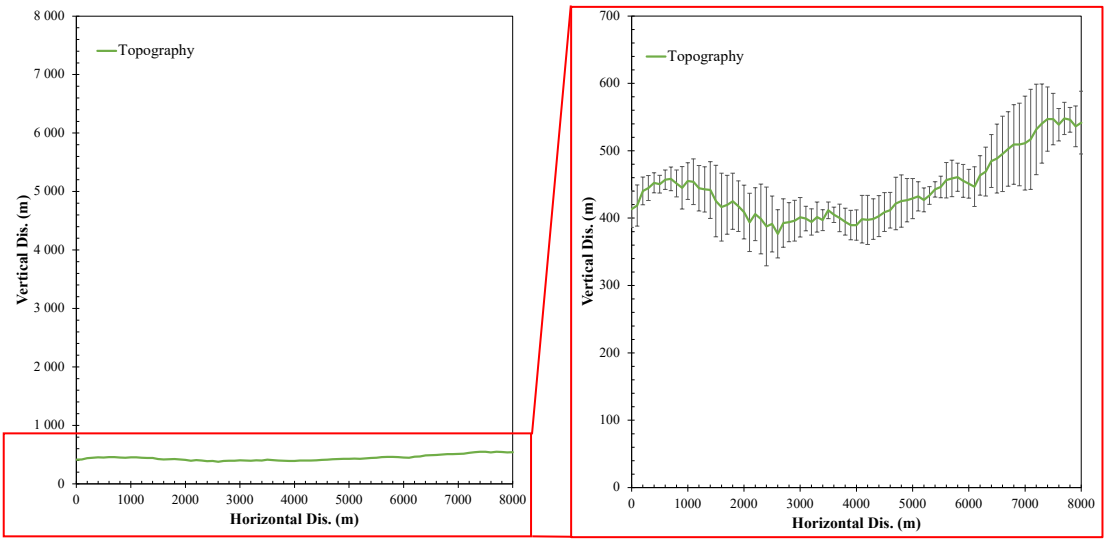

Figure 39: The roughness of the terrain in which a transept of the terrain from the origin of the fire along the main fire spread direction. The line representing the terrain profile can be well represented by a straight line, this justifying our approach of using a flat surface to model the area of the fire.

The fuel bed structure can generally be considered constant for the duration of a single fire behaviour simulation (Scott 2012). When spatially describing a landscape for fire behaviour simulation, the vegetation is usually physically characterised using fuel models (Anderson 1982; Scott and Burgan 2005; Heinsch 2020). These models are used to describe surface fire behaviour (Rothermel 1972), i.e., to estimate windward and upslope spread (Sullivan 2009). This estimation also includes an indication of Byram

1959 fire intensity, which usually determines which fuels are burned during a fire (Cruz *et al.* 2014), such as large woody fuels during glowing combustion (Hollis, Anderson, *et al.* 2011; Hollis, Matthews, *et al.* 2011) or fine fuels in low intensity fires (e.g. Mccarthy 2003).

In the case of Pedrógão Grande, given the very high intensity of fire spread, the differences between fuel types and species were very much attenuated, so it can be assumed that the behaviour of the fire corresponded to a homogeneous fuel bed with the average characteristics of real vegetation. Therefore, a homogeneous fuel bed in the laboratory scale is also used.

For the fire of PG there is a characteristic value of ROS, namely the maximum value R_{MAX} of the main fire after the merging of the two fires. If it is choosing this value as the reference velocity, to achieve physical similarity, it must have been the same or very similar values for R'_{MAX} on both scales.

In the laboratory experiments, the incident wind velocity U_0 is considered a variable parameter. Looking at the series of experiments PG12, PG13 and PG14 carried out with pine needles at velocities of 2, 3 and 4m.s^{-1} respectively, it can be seen that the corresponding values of R'_{MAX}, given in Table 3, are of the same order of magnitude as the value of 72.3 for the real fire. Calculating the $k_{f_{ref}}$ values for each case, it was found that the $k_{f_{ref}}$ values for PG12, PG13 and PG14 are 1.54, 0.757 and 0.642, respectively, close to one. Therefore, it was assumed that the physical similarity of the fire spread conditions is largely fulfilled in the present test series.

Rate of Spread Analysis of the Pedrógão Grande Fire

The isochrones of fire spread under what is called "real" conditions are shown as shaded areas in Figure 6 and are explained in more detail in Figure 40. In Figure 40 a) the trajectories of the three main fires EF, RE and JF are shown, while in Figure 40 b) some trajectories of the back fires and flank fires are shown. These lines were used to

estimate the main fires ROS and the flank fires ROS, which was equated with the basic ROS R_{or} for the real fire.

The isochrones of fire spread obtained for the test with Ref. 2: PG 12 with both ignitions with pine needles at a time step of 20s is shown in Figure 41. The corresponding lines for the tests with Ref. 10: PG EF 12 and Ref. 11: PG RE 12, with only one ignition each, for EF and RE, respectively, are shown in Figure 42.

As is usual when analysing the values of ROS at different scales, a non-dimensional ROS R' is used and is defined by equation 41. In this equation, R_i is the actual value of the modulus of ROS at a given point for each fuel bed and R_o is a reference value ROS, which is a characteristic property of the fuel bed. As mentioned above, this property was systematically measured in the laboratory for each test condition, and the corresponding value of R_o is given in Table 3.

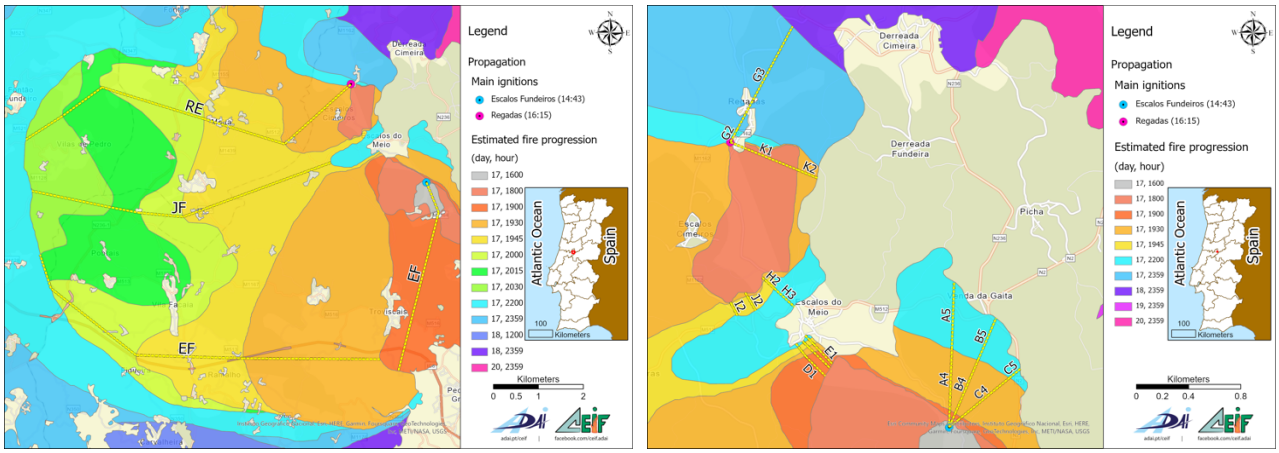

a) b)

Figure 40: a) Isochrones of the PG fire based on the reconstruction of the fire evolution with the trajectories of the three head fires. b) Some trajectories of back and flank fires of the PG fire.

However, for the field conditions, given the heterogeneity and diversity of the fuel bed properties, the reference ROS was estimated using the backing and flanking sections of the fire perimeter. It is known that the ROS is very close to R_o in these cases (cf. Viegas 2004; Sharples *et al.* 2010; Liu *et al.* 2015; Raposo *et al.* 2015; Rossa *et al.* 2015; Rossa and Fernandes 2018).

Using the trajectories of the back and flank fires shown in Figure 40 b), the local values of ROS along these lines were estimated and their arithmetic mean $R_{or} = 5.37 \text{cm.s}^{-1}$ was calculated. This value was used as a reference for determining the dimensionless values for the field scale.

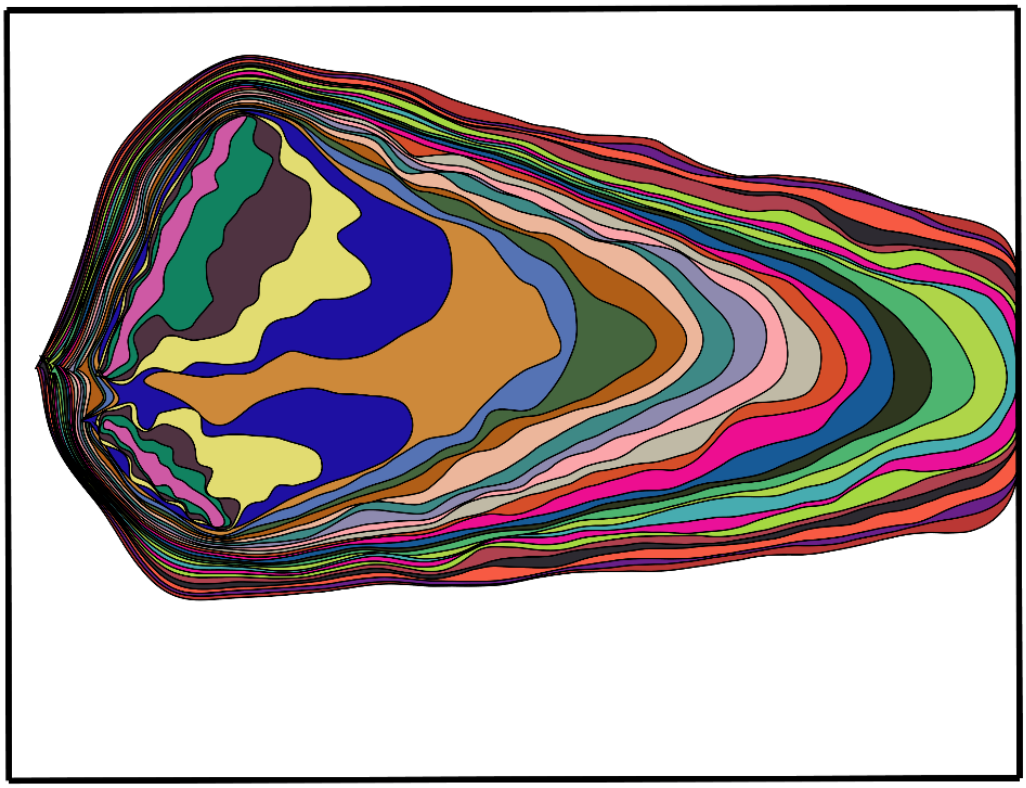

Figure 41:Map with the isochrones of fire spread of the physical simulation of the two fires in the Combustion Tunnel of the University of Coimbra. The initial position of the fires (pink areas) corresponds at the situation at around 18h30-19h30. The time lapse between the lines is 20s.

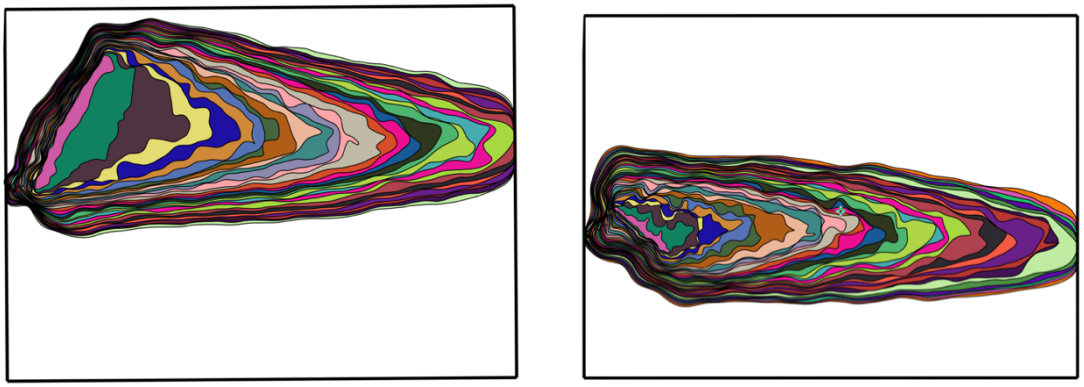

a) b)

Figure 42: a) Map with the isochrones of fire spread of the physical simulation of the fire of EF (Ref. 10: PG EF 12) in the Combustion Tunnel of the University of Coimbra. b) Isochrones for fire spread of RE fire line (Ref. 11: PG RE 12). The time lapse between the lines is 20s in both cases.

Scale Factors for Field and Laboratory System

In the present work, the evolution of scale factors for two situations was considered: (i) transfer of results from full-scale fire to model laboratory experiments; and (ii) transfer of results from laboratory experiments conducted at the same scale with different fuels.

(i) Field and laboratory results:

In this case, the system $S_1 \equiv S_r$ is the field or real fire domain and $S_2 \equiv S_m$ is the model laboratory domain. Using equations 21 and 25 and the values of R_i given for each case, the time scale factors for linear dimensions and for area evaluation in each case can be estimated. The corresponding values are given in Table 15.

(ii) Laboratory tests with different fuels:

When comparing the time-dependent results of laboratory experiments conducted with different fuels, the following definition of reduced time t^* to convert the time scale to a common reference was used:

$$t^* = t^*_o + \frac{R_{MAXk}}{R_{MAX}^*}.t_k \qquad 55$$

where R_{MAX}^* is the maximum value ROS of the test used as a reference, R_{MAXk} and t_k are the maximum value ROS and time of the test to be analysed, respectively. The

parameter t^*_o was introduced to correct for errors due to differences in the initial timing Δt_i.

Table 15: Time scale factors for the transposition of linear and area measurements from laboratory experiments and the real fire.

Test Ref.	***Fuel bed***	R_o ***(cm.s^{-1})***	τ_A	***Ignition time***
PG 12	PP	0.34	120.68	18.30h
PG 13	PP	0.35	252.68	18.30h
PG 14	PP	0.35	297.89	18.23h
PG 22	ST	0.71	241.03	18.03h
PG 32	SH	1.35	235.26	17.21h
PG 42	PP	0.23	71.63	17.54h
Field	Forest	5.37	1	19:30

Note that equation 54 with $\varepsilon_\ell = 1$ is equivalent to equation 21 since it will compare laboratory experiments conducted on the same linear scale. In the present work, the data from test PG 12 was used as a reference, so the reduced time t^* refers to this particular test.

Comparison Between Tests Performed with Different Fuels

Equation 55 was used to estimate the reduced time t^* for the experiments PG 12, PG 22 and PG 32, which were carried out with pine needles, straw and shrubs, respectively. The evolution of the head burns of EF, RE and JF as a function of t^* is shown in Figure 43 a), b) and c). In all cases it has been assumed that $t^*_o = 0$.

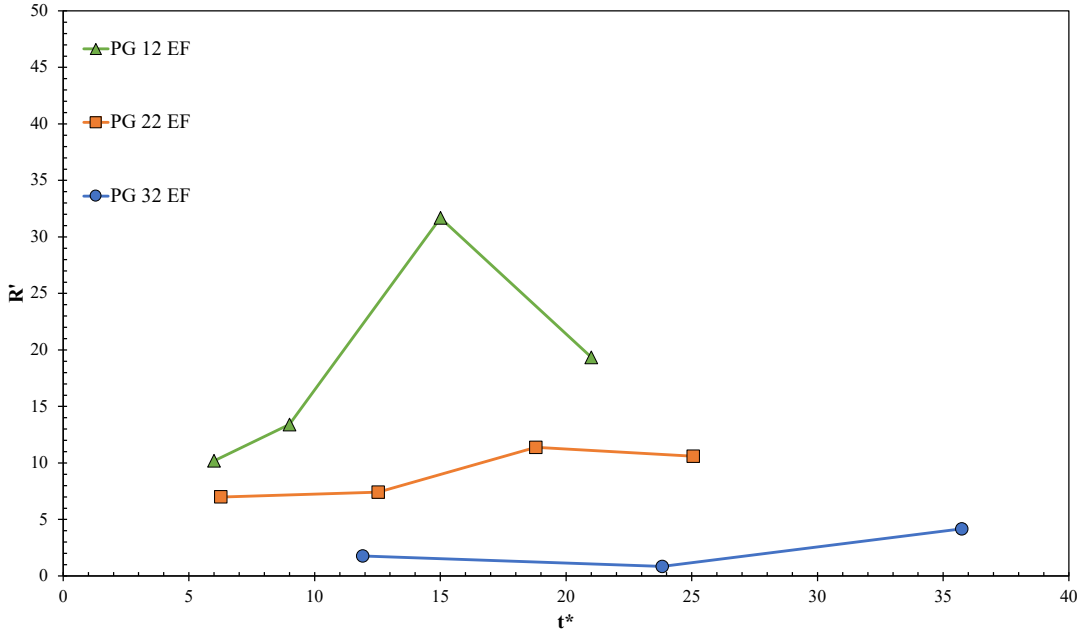
PG 12 EF
PG 22 EF
PG 32 EF
R'
t*
0
5
10
15
20
25
30
35
40
45
50

a)

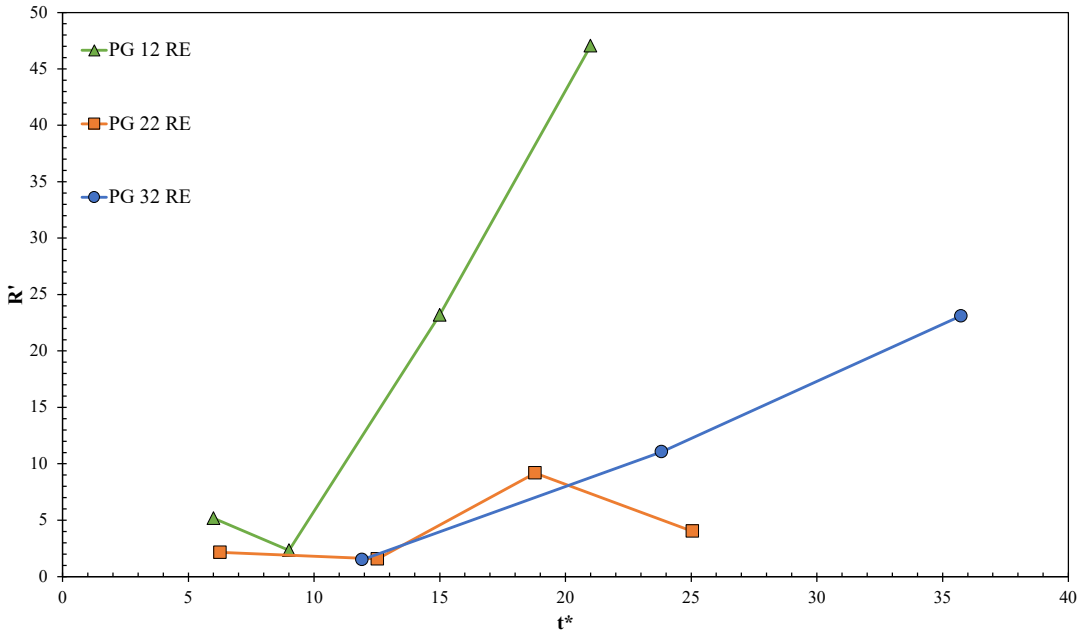
PG 12 RE
PG 22 RE
PG 32 RE
R'
t*
0
5
10
15
20
25
30
35
40
45
50

b)

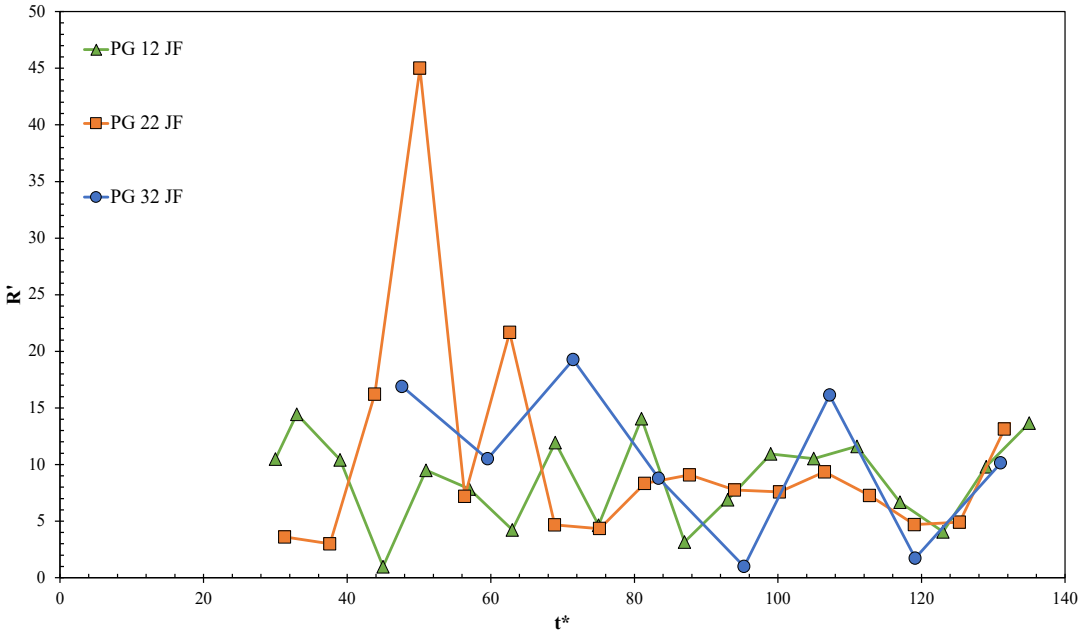

c)

Figure 43: Comparison between non-dimensional ROS from tests with different fuels as a function of reduced time (t^*). The fuels used are Pine needles (PP): PG 12, Straw (ST): PG 22 and Shrubs (SH): PG 32. a) EF; b) RE and c) JF.

As can be seen in these figures, the evolution of each head fire follows the same trend in all cases, but with some differences due to the different ignition conditions and reaction time of the combustion process in each fuel combined with the residence time of the flames (Viegas 2006; Raposo 2016). The maximum value of R' of 45 is reached in the test PG 12 with the RE head fire, while it is reached in PG 22 with straw from the JF. In the PG 32 test with shrub, the ROS increase is much slower due to the higher residence time, and the maximum R' value reached in this test is 22, much lower than in the other fuels and in the field (cf. Figure 45).

Comparison Between Single and Joint Ignitions

One of the aims of the experimental study was to show the difference in the conditions of fire spread between the actual situation with two fires developing

simultaneously and the situation with only one of them. To this end, two experiments similar to PG 12 were conducted: PG EF 12, with only EF ignited, as shown in Figure 42 a), and PG RE 12, with only RE ignited, Figure 42 b).

Analysis of these figures clearly shows that the areas burnt by the individual fires are much smaller than those burnt by the joint fires (Figure 41), as was to be expected. This was one reason why the residents of the area affected by the JF tried to flee from the very fast spreading fire that was approaching their residential area, not knowing that they were in the middle of a very large fire generated by these two large fire fronts. Many survivors told the CEIF team that no matter where they tried to go, they were always surrounded by fire.

To illustrate the large acceleration created at the top of the merging fires lines, in Figure 44 the values of R' of the head fires of the two isolated fires with those of the joint fires in the test PG 12 were compared.

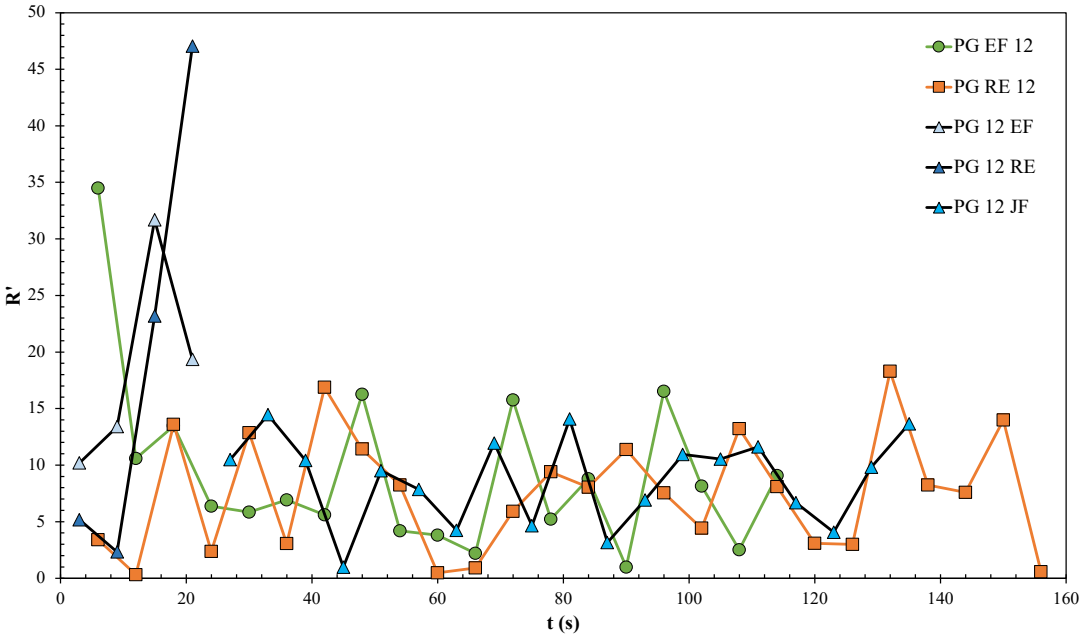

Figure 44: Comparison between the non-dimensional ROS of the EF and RE head fires of the tests PG 12 where both ignitions were performed with the results of the same head fires in isolated ignitions.

As can be seen in this figure (Figure 44), the fire EF in the test PG EF 12 reaches a rather high value of $R' = 34$ at the beginning of the spread, while this fire in the test PG 12 reaches a much higher value of $R' = 48$; the corresponding values for the fire RE are $R' = 32$ in the test PG 12 and $R' = 13$ in the test PG RE 12, respectively.

These results confirm the intensification of fire spread in the merging fires lines, which leads to much higher values of burnt area, higher values of ROS and the presence of the very strong convective processes observed and described above.

Comparison Between Model and Real Scale

The results of the tests PG 12, PG 13 and PG 14, conducted with pine needles but with three different flow rates, are plotted in Figure 45 using the real time scale of the fire according to the proposed model. As can be seen in this figure, the peak R' values reach 72.4 for the JF fire and values close to 50 for both the EF and RE fires.

Using the time scaling equations, it can be used the following equation to translate the time of the model experiments into the time under full scale conditions:

$$t_{rj} = t_{ij} + \tau_j . t_j \qquad 56$$

where t_{rj} is the real time at scale 1:1 corresponding to the results of experiment j, τ_j is the corresponding time scale factor given in Table 15 for each experiment, and t_j is the time since the ignition of the fire in experiment j. The parameter t_{ij} is a fictitious ignition time to account for the delay time in the ignition in the experiment. The values of t_{ij} were adjusted for each test to achieve better overall agreement and the corresponding values are shown in Table 15.

As can be seen in Figure 45, the results of the physical modelling of the Pedrógão Grande fire during its very intense spread in the late afternoon of 17th June 2017, using the scaling laws proposed in the present work, agree quite well with the observed parameters of the real fire. The overall fire growth trend for the different head fires, as well as the magnitude of the non-dimensional ROS and its temporal variation obtained in 1:2933 scale experiments with different flow rates, agree very well with the full-scale

observations, showing that the use of laboratory experiments is a valid tool for modelling the extreme fire behaviour in forest fires.

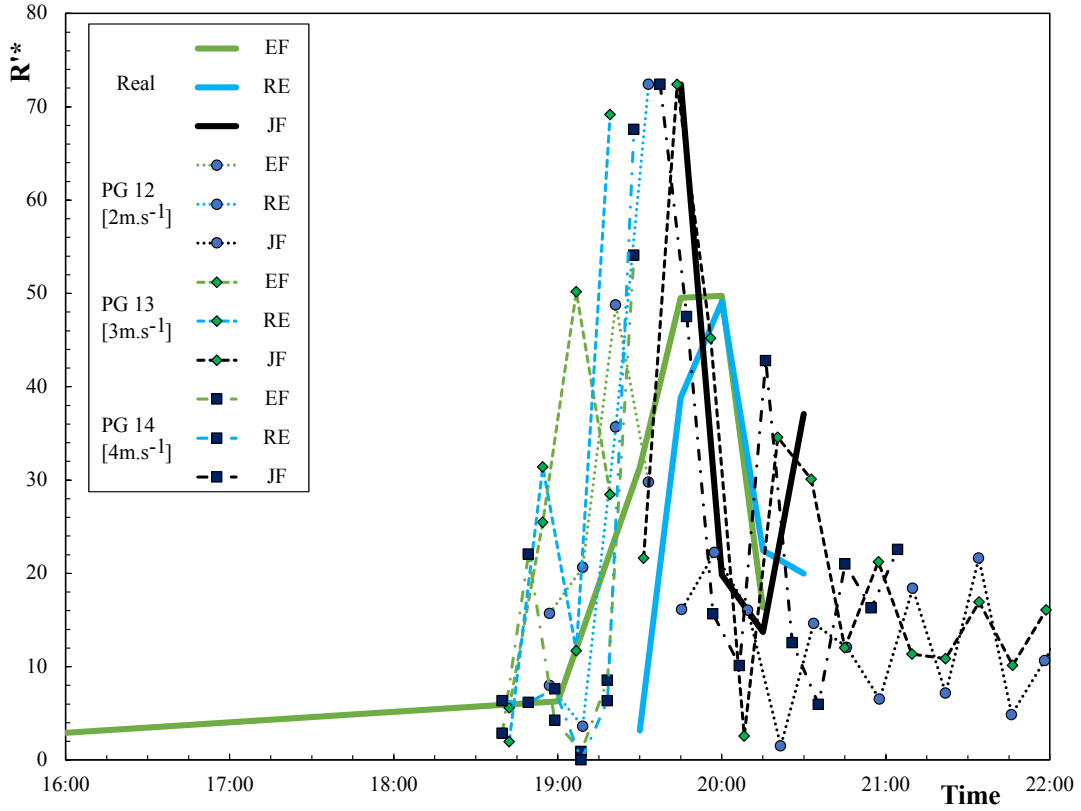

Figure 45: Comparison between non-dimensional normalized ROS of the EF, RE and JF head fires from the real fire and from tests performed with Pine needles (PP) and different wind velocities: PG 12 (2m.s^{-1}), PG 13 (3m.s^{-1}), and PG 14 (4m.s^{-1}).

Area Growth Analysis with Different Fuels

The growth of the burnt area over time is a very important parameter for assessing firefighting capacity or effectiveness and for estimating the release of energy and smoke into the atmosphere (Fernandes *et al.* 2022). In Figure 46 a) the evolution of the burnt area of the fire during the experiments PG 12, PG 22 and PG 32, which were carried out with three different fuels, was compared. In each case, the measurement of the area was stopped when the fire head reached the boundary of the fuel bed.

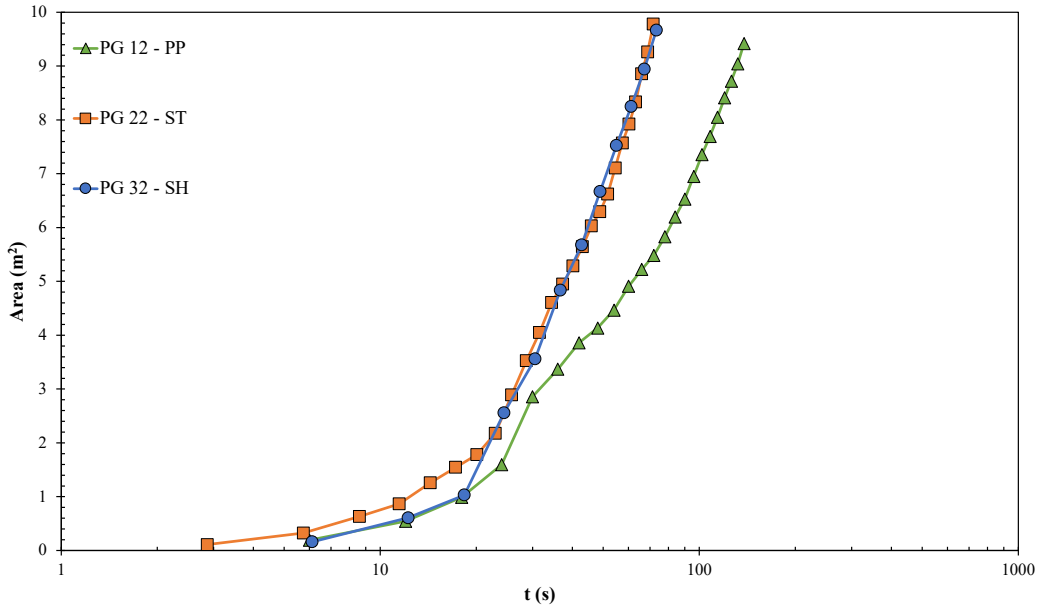

a)

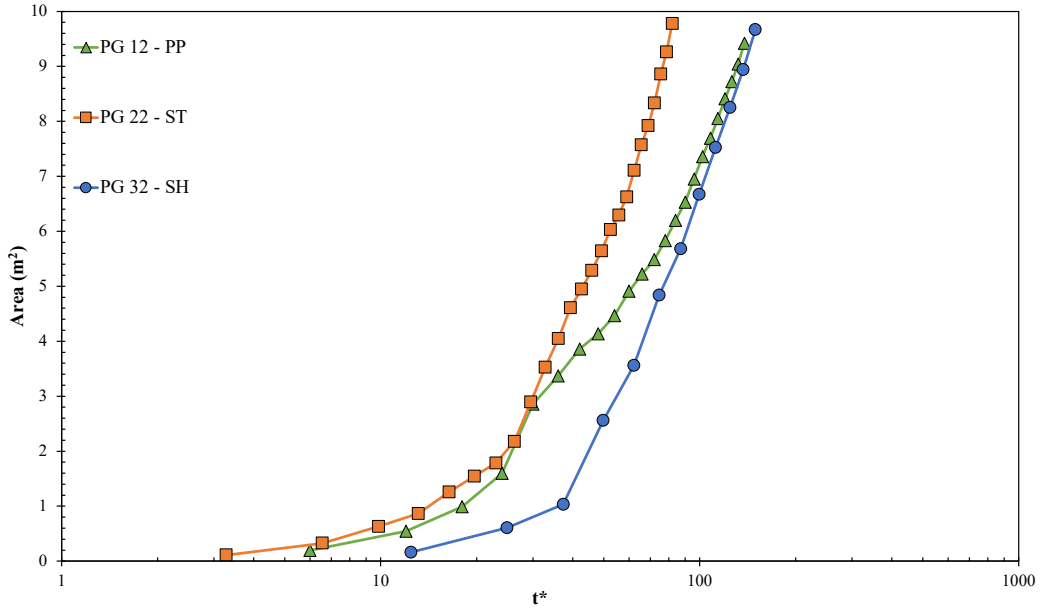

b)

Figure 46: Evolution of the burned area in three tests performed with different fuels: Pine needles PG 12, Straw PG 22 and Shrubs PG 32. a) as a function of physical time; b) as a function of reduce time.

The time course of the three curves is similar, but the time required to burn a given area is, as expected, inversely proportional to the respective value of R_{MAX}. This is evident in Figure 46 b), in which have used the reduced time t^* corresponding to the test PG 12, as the three curves almost merge into one. In these figures, no corrections have been made to account for the ignition delay.

Comparison of the Variation in Burnt Area Between Model and Real Fire

This section will be analysed and compared the area growth under real conditions after 19h30, which nominally corresponds to the start of the laboratory experiments when the two fire lines began to spread freely without any extinguishing efforts. For this, it was used the results of the experiments PG 12, PG 13 and PG 14, are closest to the real conditions of fire spread. For this purpose, the area $A2$ burnt by the three main fires (EF, RE and JF) since 19h30 was used. For this reason, it was assumed in the graph that the area of the fire was zero at this time, while it was already 3154ha in the real fire. For the time scale factor τ_A, the corresponding values from Table 15.

As can be seen in Figure 47, where the four curves are plotted, the experimental results show that the area growth rate was very high at the beginning, but after 20h30 this area growth rate decreased, as was the case with the real fire. Although the overall trend of area growth is reproduced in the experiments, under the modelling assumptions of the present work it was obtained much lower values for the area burnt, which leads to analyse of the possible reasons for this.

The most obvious is the fact that the fire spread processes in the laboratory experiments are very different from those in the full-scale experiments when the fire developed into a very intense firestorm. After 20h00, extensive spot and crown fires occurred in the real fire, which are not replicated in the laboratory scale experiments. Consequently, the actual values of the fire spread parameters from the model experiments, such as the burnt area and its growth rate, do not fully match the scale, but they follow the same temporal trend and are of the same order of magnitude, demonstrating the usefulness and interest of the present method of physical and scale modelling for the

analysis of complex and intense fires that cannot be simulated otherwise with current simulators.

Despite these discrepancies, the high similarity of the overall fire behaviour observed at both scales is worth noting. This is due to the overwhelming effect of the convective flows generated by the fires at the junction fire, which leads to a significant acceleration of the fires even on flat ground.

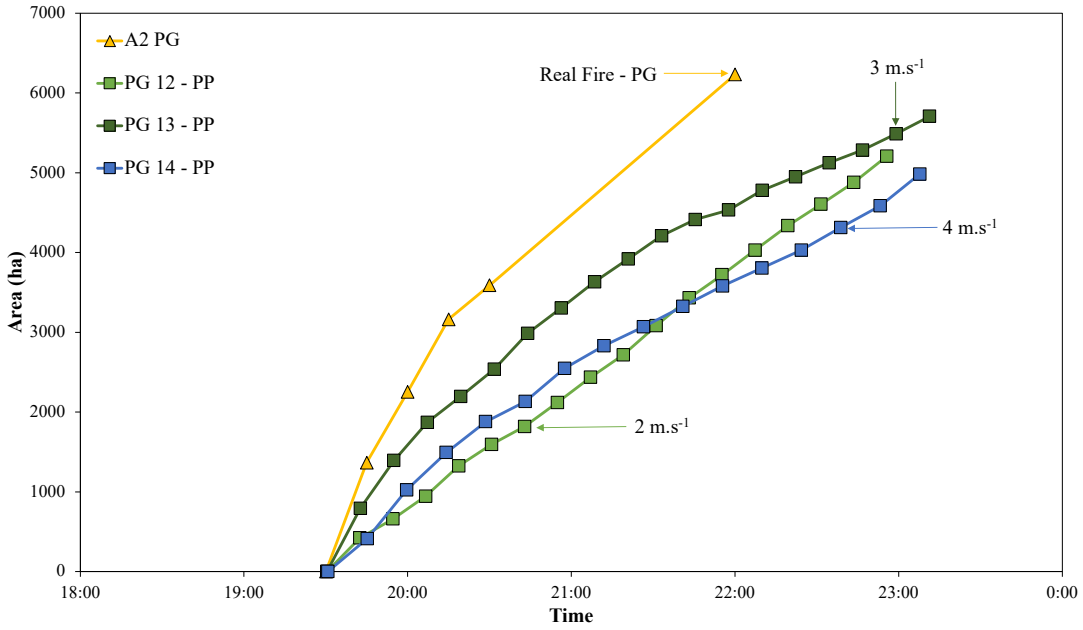

Figure 47: Comparison between the burned area growth in test PG 12, PG 13 and PG 14 with the real fire between 19h30 and 22h00.

5.2.2. Junction Fire with Two Non-Symmetric Fire Fronts

This section presents the results of laboratory tests of junction fire with two non-symmetric fire fronts. The tests were carried out with the constant angle between two fire fronts $\theta_0 = 30°$ and a different slope angle $\alpha = 10°$, $20°$, $30°$ and $40°$. To reduce uncertainty, three replicates were performed for each set of parameters $\delta_{JF} = 5°$, $10°$, and $15°$. The results presented are the average of three replicates for each parameter set, and

the error bars represent the $\pm 95\%$ confidence intervals. It was assumed that the ROS of the intersection point A can be influenced by the slope α, which changes the flame geometry, the convection and radiation process, and by the rotation δ_{JF} of the two fire lines with respect to the maximum slope. To test the combined influence of each variable, an analysis of variance (ANOVA) was performed to test the effects of the slope ($\alpha = 10°$, 20°, 30° and 40°) and the angle δ_{JF} of the linear fire fronts between ($\delta_{JF} = 5°$, 10°, and 15°).

Rate of Spread Analysis of Intersection Point A

In order to analyse the role of the slope α and the rotation δ_{JF} of the fire fronts in relation to the maximum slope, a series of experiments were carried out in the laboratory (see Table 4). Based on general observations of fire behaviour (in loco, IR and visible videos) during the experiments, there was a large change in fire dynamic behaviour when the slope increased compared to the effects of the small rotations δ_{JF} tested in the present work.

To evaluate these dynamic changes, ROS R_A for the intersection A of the two fire fronts in each experiment was estimated. It was used at certain predefined times to record the fire boundaries with the infrared camera depending on the slope angle of each test: $\alpha = 10°$ - $\Delta t = 10$s, $\alpha = 20°$ - $\Delta t = 5$s, $\alpha = 30°$ and 40° - $\Delta t = 2$s. The non-dimensional ROS R'_A was calculated according to equation 38 and the basic ROS (R_o) for each parameter set can be seen in Table 4. The average, minimum, maximum and standard deviation (sd) of the non-dimensional ROS (R'_A) for three experiments (T1, T2 and T3) and for each δ_{JF} rotation angle ($\delta_{JF} = 5°$, 10°, and 15°) were calculated and are shown in Table 16. A total of forty experiments were conducted specifically for this study, and twelve previously conducted tests for symmetrical conditions in Raposo 2016 were used as well.

For all conditions studied and for slope angles considered, the average of non-dimensional ROS values ranged from 13.74 ($\alpha = 10°$ and $\delta_{JF} = 5°$) to 121.27 ($\alpha = 40°$ and $\delta_{JF} = 15°$). The average of the non-dimensional ROS is generally greatest as the

slope or angle of rotation increases (see Table 16). Two-way analysis ANOVA with replication showed that the non-dimensional ROS R'_A was significantly (p-value < 0.05) affected by the slope angles (α), but the considered rotation δ_{JF} of the two fire fronts had no significant effect (p-value > 0.05) on non-dimensional ROS R'_A.

Table 16: Summary of the non-dimensional ROS (R'_A) for experiments at three δ_{JF} rotation angles ($\delta_{JF} =$ 5°, 10° and 15°). Values in the table are composed by - average (min-max, sd). A R'_A of 10, for example, equates to the experiments having 10 times the ROS of the basic ROS R_o: ROS no wind and no slope.

Ref.	$\boldsymbol{\alpha}$	$\boldsymbol{\delta_{JF}}$ **(°)**		
	(°)	**5**	**10**	**15**
1	10	13.74 (3.81 – 43.15, 1.10)	14.19 (3.41 – 51.43, 0.86)	14.66 (2.58 – 46.47, 2.34)
2	20	32.20 (6.14 – 80.89, 6.12)	36.67 (1.48 – 93.35, 1.48)	26.90 (5.47 – 81.18, 2.83)
3	30	75.44 (25.21 – 136.26, 12.17)	81.79 (46.68 – 182.80, 7.81)	77.27 (28.31 – 137.49, 7.69)
4	40	82.12 (25.42 – 121.77, 11.40)	90.60 (34.10 – 147.00, 3.14)	121.27 (78.16 – 156.73, 12.06)

To analyse the influence of the small rotation δ_{JF} in the ROS of intersection point A, the values of the non-dimensional ROS R'_A with the symmetric boundary conditions ($\delta_{JF} = 0°$) developed in the past by Raposo 2016 were compared. However, for clarity, in the following figures, the average results for the three replicates performed under the same conditions were presented with standard deviation bars representing ±95% confidence intervals. Fire spread can be described as a function of either time or space (distance) according to equation 37, and the behaviour of fire spread is non-monotonic (cf. Viegas *et al.* 2021, 2022).

Figure 48 plots the non-dimensional average ROS R'_A values for each slope angle α and each angle of rotation δ_{JF} as a function of time and displacement distance. The R'_A values for $\delta_{JF} = 5°$, 10° and 15° were compared with the non-dimensional ROS R'_A values for the two symmetrical fire fronts ($\delta_{JF} = 0°$). Despite the random nature of the fluctuations of R'_A that occur for each set of parameters used, a good relationship between the tests performed with the rotation condition δ_{JF} ($\delta_{JF} = 5°$, 10° and 15°) and

the symmetric boundary condition ($\delta_{JF} = 0°$) is obtained and the values of R'_A tend to occur with the same natural fluctuations during time and distance travelled by point A.

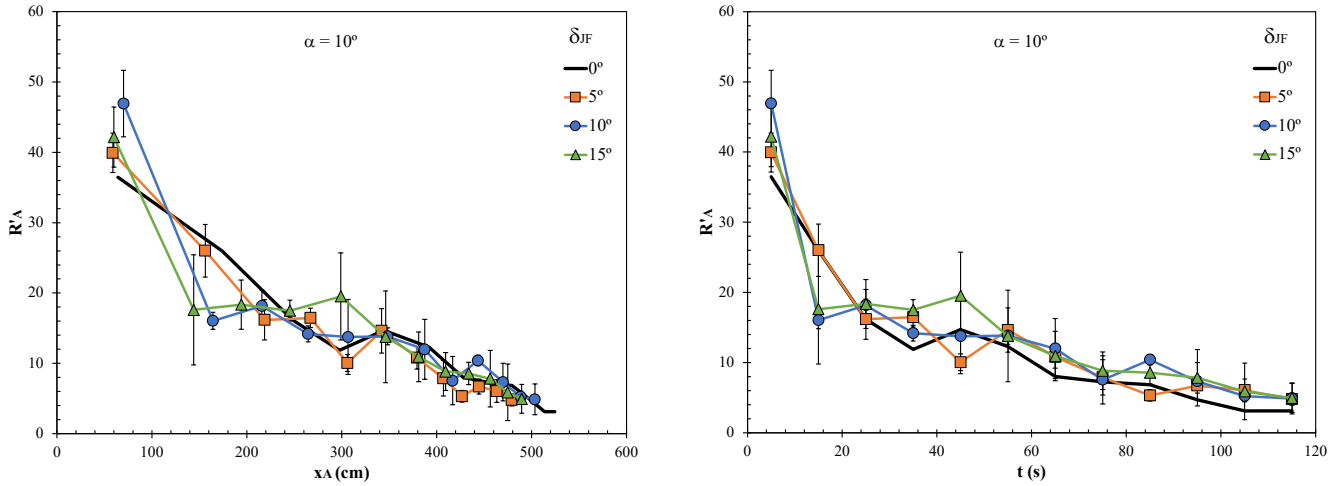

a)

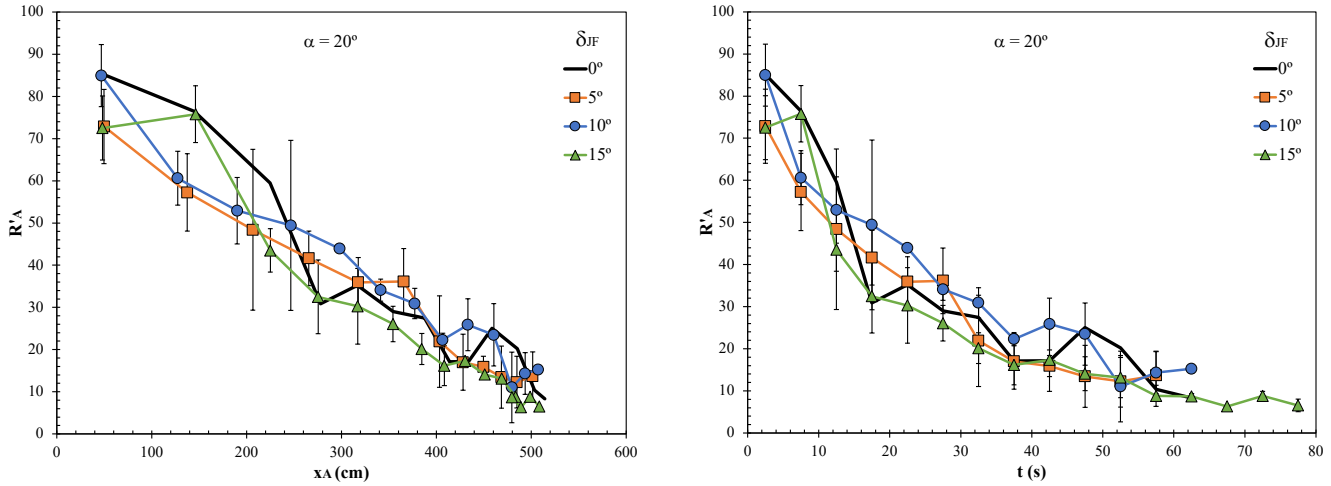

b)

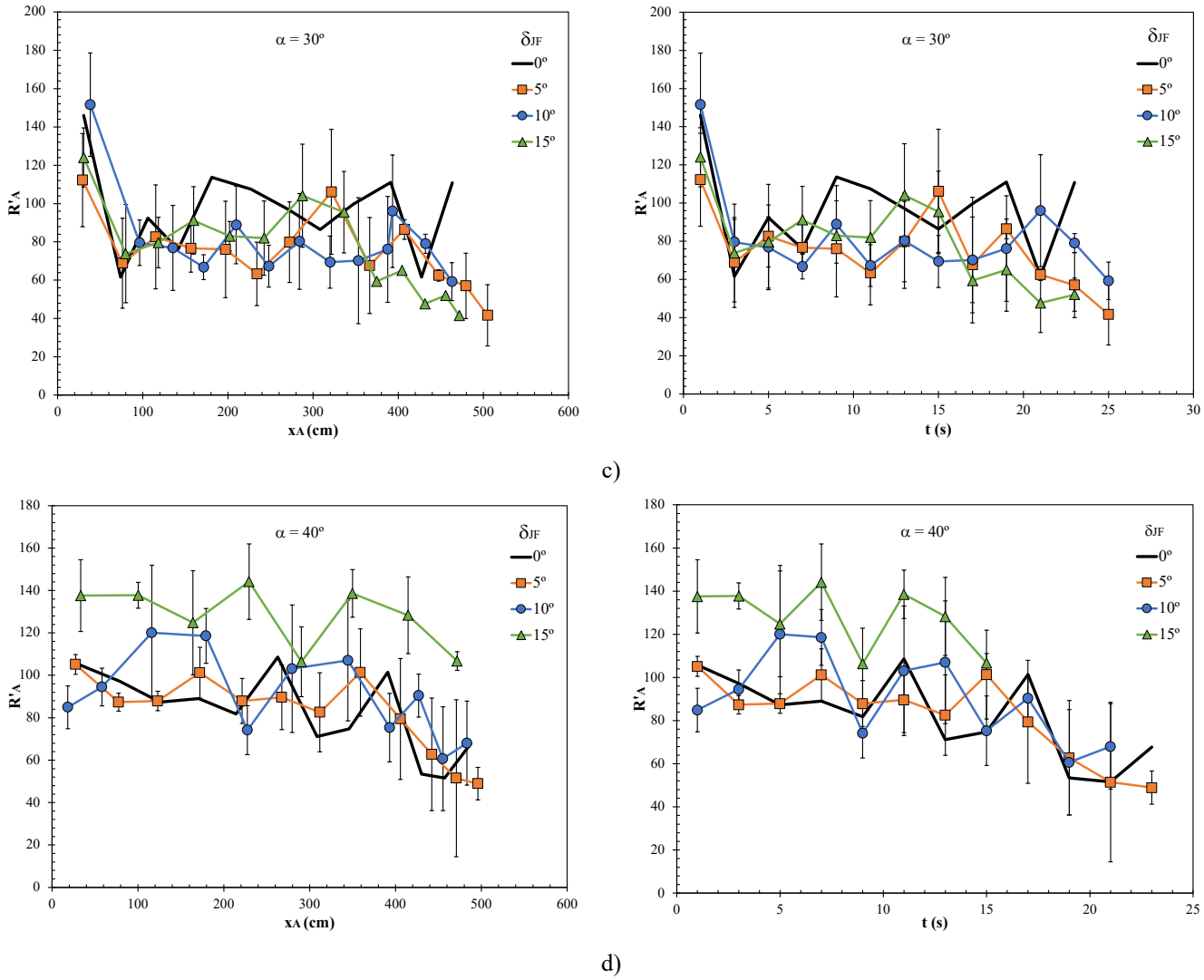

Figure 48: Development of the non-dimensional ROS R'_A as a function of time and distance for different slope angles (α) and different rotations (δ_{JF}) of the fire fronts. The average values R'_A of the three replications with 95% confidence intervals ($\delta_{JF} = 5°$, $10°$ and $15°$) were plotted with the symmetric boundary conditions ($\delta_{JF} = 0°$). a) $\alpha = 10°$, b) $\alpha = 20°$, c) $\alpha = 30°$ and d) $\alpha = 40°$.

The behaviour of the interaction of two linear fire lines is non-monotonic and the oscillations tend to increase with the slope angle because the convection process increases and dominates the interaction of these fire fronts. Junction fires are characterised by two distinct phases: the acceleration phase and the deceleration phase.

In the cases with lower slope angles (see Figure 48 for $\alpha = 10°$ and $20°$), the acceleration phase is very short, while the deceleration phase is more pronounced in these cases. This is due to the fact that at lower slope angles the radiation process becomes more important compared to the convection process. The opposite is true for the largest slope angles (see Figure 48 for $\alpha = 30°$ and $40°$), where the deceleration phase is not as pronounced, and the fire accelerates throughout the combustion table. In some experiments it is possible that the R'_A does not reach its maximum value. At these slope angles, the convection process dominates and the ROS of intersection A develops very quickly with the highest oscillations. Measurements are difficult because point A moves very quickly and in these cases, the standard deviation and error bars tend to increase.

Angle of the Maximum ROS

To assess the general role of the parameters α and δ_{JF}, the angle γ at which the maximum ROS occurs was measured for each set of parameters. The average values of γ with a 95% confidence interval for all tests performed are shown in Figure 49 as a function of the angle between the bisector of the linear fire lines and the line with the largest slope.

As can be seen, the angle γ shows a similar trend for the higher values of the slope ($\alpha = 30°$ and $40°$), and in these cases, the axis on which the maximum ROS occurs is more influenced by the convection process. However, at lower values of slope ($\alpha = 10°$), the angle γ tends to decrease and the maximum ROS occurs near the bisector of the fire lines ($\gamma \approx 1°$). In this case, the radiation process near point A is more relevant compared to the convection process. The fitted lines result from the linear relationship between the angle γ (the angle between the bisector of the fire lines and the maximum ROS) and the angle δ_{JF} (the angle between the bisector of the linear fire lines and the line with the maximum slope) and can be expressed as follows:

$$\gamma = k_1 \delta_{JF} \qquad 57$$

where k_1 is the slope of the respective fitted line. For each case, the respective values of k_1 and the correlation coefficients of the linear regression (R^2) were obtained and can be seen in Table 17.

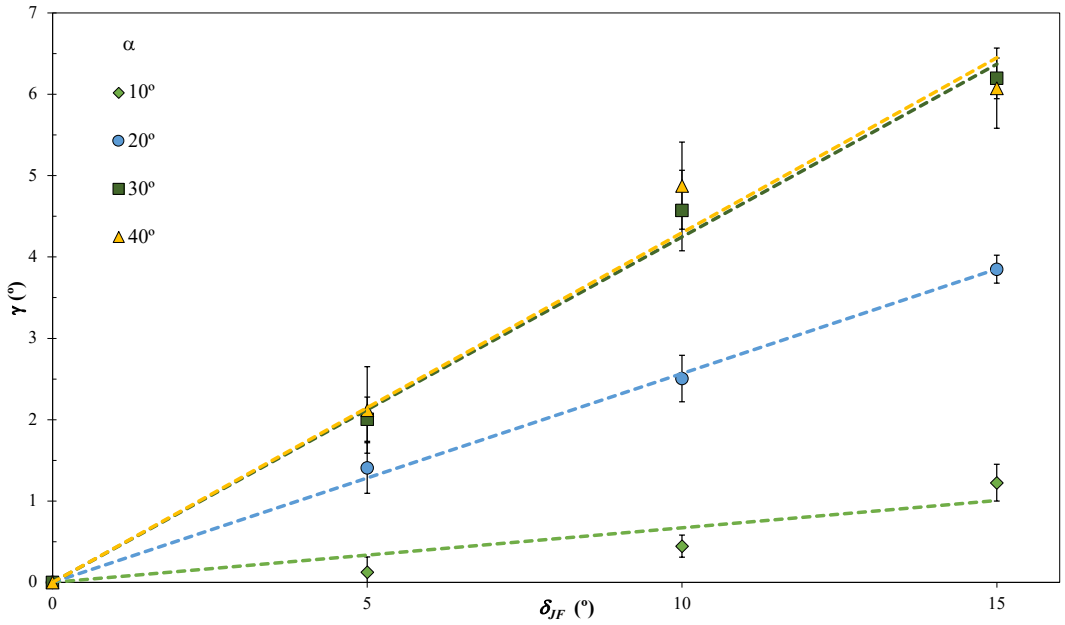

Figure 49: The angle between the bisector of the fire lines and the maximum ROS (γ) as a function of the angle between the bisector of the fire lines and the line with the maximum slope (δ_{JF}). The average values of γ are plotted with 95 % confidence intervals for each case. The dashed lines represent the fitted linear regression of the data values for each slope angle (α).

The two-way analysis ANOVA with replication for all data values of the angle between the bisector of the fire lines and the maximum ROS (γ) showed that γ was significantly (p-value<0.05) affected by the slope angles (α) and by the considered rotation δ_{JF} of the two fire fronts.

Table 17: Coefficients k_1 and correlation coefficients of the linear regression (R^2) for the fitted linear regression of the data values for each slope angle (α) are presented in Figure 49.

Ref.	α (°)	k_1	R^2
1	*10*	0.067	0.917
2	*20*	0.257	0.999
3	*30*	0.425	0.998
4	*40*	0.429	0.993

5.2.3. Parallel Fire Fronts Under Wind Flow Conditions

This section presents the results of laboratory tests with parallel fire fronts under wind flow conditions. The tests were carried out with reference wind speeds of $U_0 = 0$, 1, 2, 3, 4 and 5m.s^{-1}. The distances between the two fire fronts considered were $d = 1$ and 2m. The results of the approach ROS of two fire lines, the average approach ROS under different wind flow conditions and the physical interpretation of the fire development are shown. It was assumed that the convergence ROS of two linear fire lines can be influenced by the wind flow (U_0), which changes the flame geometry, the horizontal and vertical forces emanating from the wind flow and the vertical buoyancy of the fire, respectively, and by the distance (d) between the two fire lines. To test the combined influence of the individual variables, an analysis of variance (ANOVA) was performed to investigate the effects of wind flow velocity and the distance between parallel fire lines.

Approaching Rate of Spread Analysis

When the fire lines are ignited, they are initially segments of a straight line, but as they spread under the influence of wind flow (horizontal forces) and buoyancy flow (vertical forces), they become curved, and the conditions of spread may change as the fire develops along the OX axis. Based on general observations of fire behaviour (in loco, IR

and visible videos) during the experiments, there was a large change in fire dynamics when the wind flow velocity (U_0) was increased compared to the effects of changing the distance between the fire fronts (d).

To assess these dynamic changes, the instantaneous value R'_j for each reference line (lines a, b and c, see Figure 50) was estimated, from the fire history plots taken from the frames of the infrared camera at every five seconds during each test. The non-dimensional instantaneous value or local ROS R'_j was calculated by the ratio between the equation 26 by the basic ROS (R_o). The basic ROS (R_o) for each set of parameters are listed in Table 5. The average, minimum and maximum values as well as the standard deviation (sd) of the non-dimensional ROS (R'_j) for three tests (T1, T2 and T3) and for each reference line (lines a, b and c) were calculated and are listed in Table 18.

For the two fire lines with an initial distance $d = 1$m, the average values of the non-dimensional ROS over all considered wind flow intervals were between 1.76 ($U_0 = 2$m.s^{-1}) and 3.79 ($U_0 = 0$m.s^{-1}). In contrast, the average values for the two fire lines at an initial distance $d = 2$m ranged from 1.81 ($U_0 = 2$m.s^{-1}) to 4.11 ($U_0 = 5$m.s^{-1}) (see Table 18). For each individual set of conditions tested, the non-dimensional ROS was generally highest for wind flow $U_0 = 0$m.s^{-1} and $U_0 = 5$m.s^{-1} and lowest for wind flow $U_0 = 1$m.s^{-1} and $U_0 = 2$m.s^{-1} (see Table 18).

The average of the results for the three replicates carried out under the same conditions was presented in the following figures. The spread of the fire can be described either as a function of time or space (distance) (cf. Viegas *et al.* 2021). From now on, the non-dimensional distance will be used to analyse the evolution of the ROS of the two approaching fires, as this gives a better indication of the behaviour of the fire since the distance between the fire lines is reduced to zero when S' tends towards 0.5.

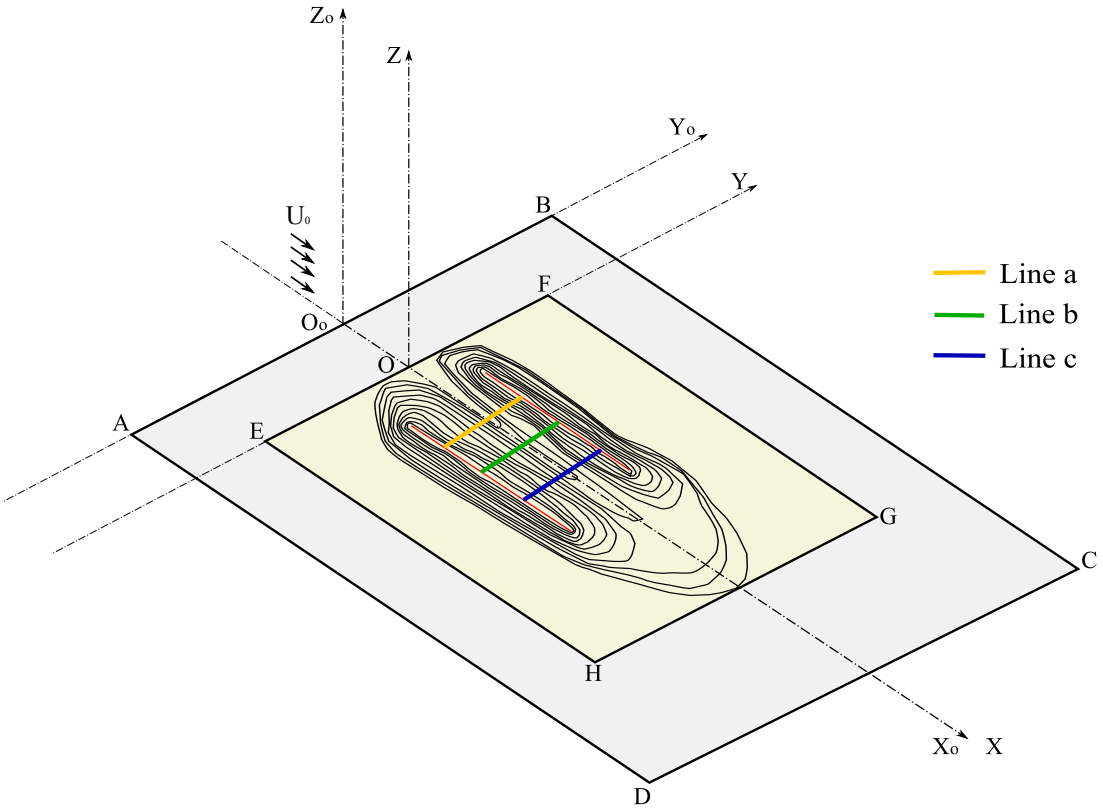

Figure 50: The interaction between the two fire lines was analysed along three reference lines (line a, b and c) at a distance of 1, 1.5 *and* 2*m with respect to the OXYZ reference frame, measured in the axis OX. As an example, this figure shows the isochrones of the tests 1-D1U3 together with the reference lines used to analyse fire spread.*

Figure 51 plots the non-dimensional average ROS $R'_{\ell\ ave}$ values for each reference line a - $R'_{a\ ave}$, b - $R'_{b\ ave}$ or c - $R'_{c\ ave}$ with the same configuration as a function of the non-dimensional distance S'. As can be seen, there is not much difference between the three lines in each test configuration, and the average local ROS R'_{ave} values for the three lines a, b and c can be used to estimate the local behaviour of the approaching fire lines for each set of values of d and U_0.

Table 18: Summary of the non-dimensional ROS (R'_j) for experiments at three reference lines (lines a - R'_a, b - R'_b and c - R'_c). Values in table are composed by - average (min - max, sd). A R'_j of 3, for example, equates to the experiments having 3 times the ROS of the basic ROS R_o: ROS no wind and no slope.

Ref	d (m)	U_0 ($m.s^{-1}$)	R'_j for reference line a, b and c		
			R'_a	R'_b	R'_c
1	1	0	3.60 (2.77 – 4.42, 0.64)	3.64 (2.07 – 5.26, 0.92)	3.79 (2.57 – 4.64, 0.74)
2		1	1.84 (1.16 – 3.24, 0.58)	1.93 (1.15 – 3.12, 0.55)	2.24 (1.06 – 4.27, 0.83)
3		2	1.76 (1.33 – 2.39, 0.34)	2.17 (1.27 – 3.06, 0.54)	2.11 (1.55 – 3.06, 0.55)
4		3	2.16 (1.29 – 2.95, 0.49)	2.41 (1.21 – 4.72, 1.27)	2.38 (1.24 – 4.09, 0,85)
5		4	2.41 (0.73 – 3.80, 0.85)	2.77 (1.86 – 3.83, 0.66)	2.58 (1.49 – 3.73, 0.69)
6		5	3.15 (1.50 – 5.02, 1.10)	3.18 (1.60 – 5.46, 1.33)	3.31 (1.05 – 6.82, 1.54)
7	2	0	3.29 (1.55 – 4.89, 0.98)	3.64 (2.42 – 5.66, 1.04)	3.23 (1.54 – 5.29, 1.00)
8		1	1.95 (1.26 – 3.17, 0.52)	1.99 (0.77 – 3.61, 0.75)	2.41 (1.40 – 3.47, 0.54)
9		2	1.81 (1.21 – 2.87, 0.46)	1.82 (1.13 – 3.47, 0.65)	2.11 (1.52 – 2.77, 0.43)
10		3	2.22 (0.61 – 3.20, 0.70)	2.16 (1.64 – 3.19, 0.47)	1.94 (1.20 – 2.78, 0.42)
11		4	2.46 (1.53 – 4.28, 0.82)	2.76 (1.20 – 3.87, 0.78)	2.88 (0.62 – 4.64, 1.08)
12		5	4.27 (1.30 – 9.21, 2.10)	4.11 (0.94 – 8.04, 1.97)	3.77 (2.42 – 6.23, 1.20)

Figure 52 plots the mean values of the non-dimensional values of the local ROS R'_{ave} with bars of the standard deviation, the bars corresponding to the 95% confidence intervals, as a function of the non-dimensional distance S' for two experiments with $d = 1$ and 2m for each wind speed value $U_0 = 0, 1, 2, 3, 4$ and 5m.s^{-1}.

The behaviour of the approaching fires is intermittent in the sense that it is not constant, but on the contrary, the laterally spreading fire tends to decelerate or accelerate. The results suggest that the behaviour for both values of d considered depends less on the initial distance and more on the surrounding wind speed, as the combination of wind speed and buoyancy flow changes the approaching fires and the dynamic fire behaviour. The results of the approaching fires along the OY axis is now presented and illustrate the changing behaviour of fire spread when the flow velocity is modified.

As can be seen in Figure 52 a) ($U_0 = 0$m.s^{-1}), the value of R'_{ave} has two stages: first, when $S' \approx 0$ to 0.25, R'_{ave} increases because the flames incline towards each other, then the flames become more vertical and their length and height increase. After that, R'_{ave} decreases until $S' \approx 0.5$ because the flames incline towards the burnt area and the length and height of the flames continue to decrease. The ratio of the convective process between two fire lines during the first phase results in an acceleration during the approach of the fire, but when the burnt area increases, this convective process changes and a deceleration phase occurs.

For $U_0 = 1$m.s^{-1} (Figure 52 b)), the value of R'_{ave} has relatively high initial, lower than R'_{ave} for $U_0 = 0$m.s^{-1}, but during the approach to the fire, when S' increases, the R'_{ave} value decreases.

However, for $U_0 = 2$m.s^{-1}, Figure 52 c), the approach velocity is relatively constant in this experimental setup. At this wind flow velocity ($U_0 = 1$ and 2m.s^{-1}), the convection flow is symmetrical on both sides of each fire front. In this case, the wind inhibits the interaction, the flames are almost vertical, and the buoyancy flow increases in this case compared to the flow influenced by the wind. The ratio between vertical and horizontal forces tends to equilibrium and leads to a minimum value of R'_{ave}, Figure 53 and Figure 54, respectively, but the flame height is constant throughout the time and approach, see Figure 55.

For $U_0 = 3$, 4 and 5m.s^{-1} (Figure 52 d), e) and f)), the rate of approach R'_{ave} generally increases with the approach of the flames and with significant variations (Figure 52 f)). At $U_0 = 5$m.s^{-1}, the non-dimensional ROS generally increases because the flame depth and the amount of burning fuel increase under the influence of the wind flow blowing between two fire lines. The higher wind speed increases the turbulence, which is very important, and decreases the flame height, but the combustion process increases.

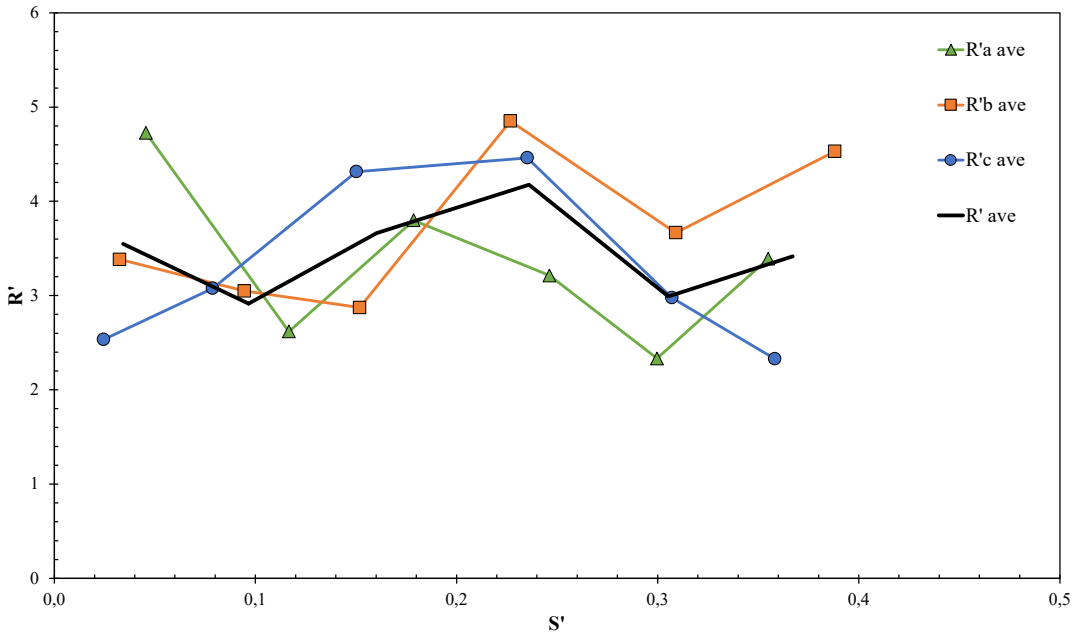
R'a ave
R'b ave
R'c ave
R' ave
R'
S'
0
1
2
3
4
5
6
0,0
0,1
0,2
0,3
0,4
0,5

a)

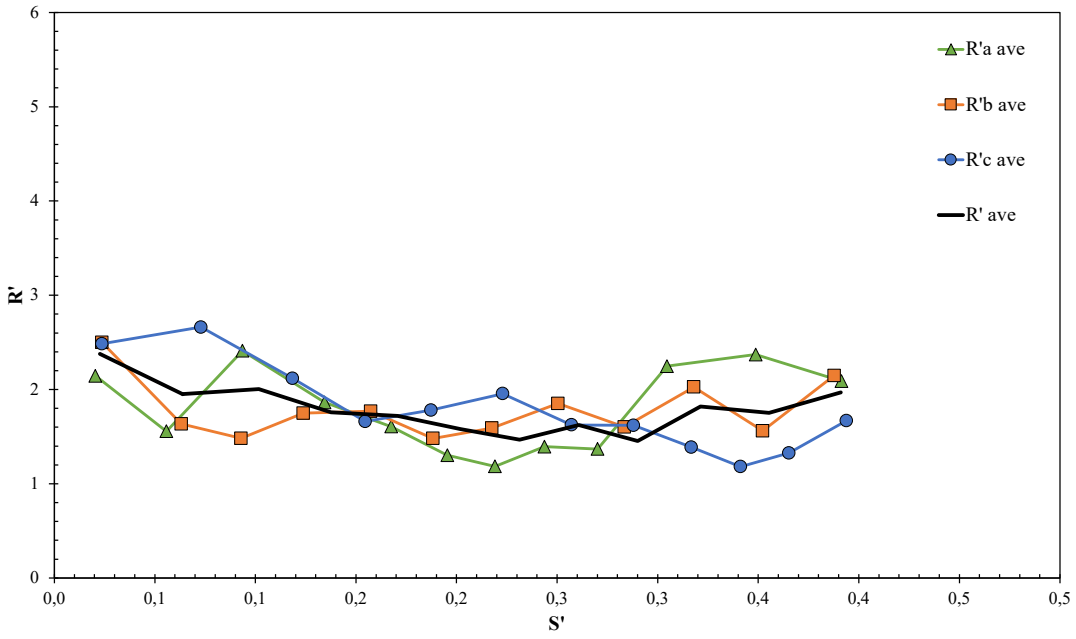
R'a ave
R'b ave
R'c ave
R' ave
R'
S'
0
1
2
3
4
5
6
0,0
0,1
0,1
0,2
0,2
0,3
0,3
0,4
0,4
0,5
0,5

b)

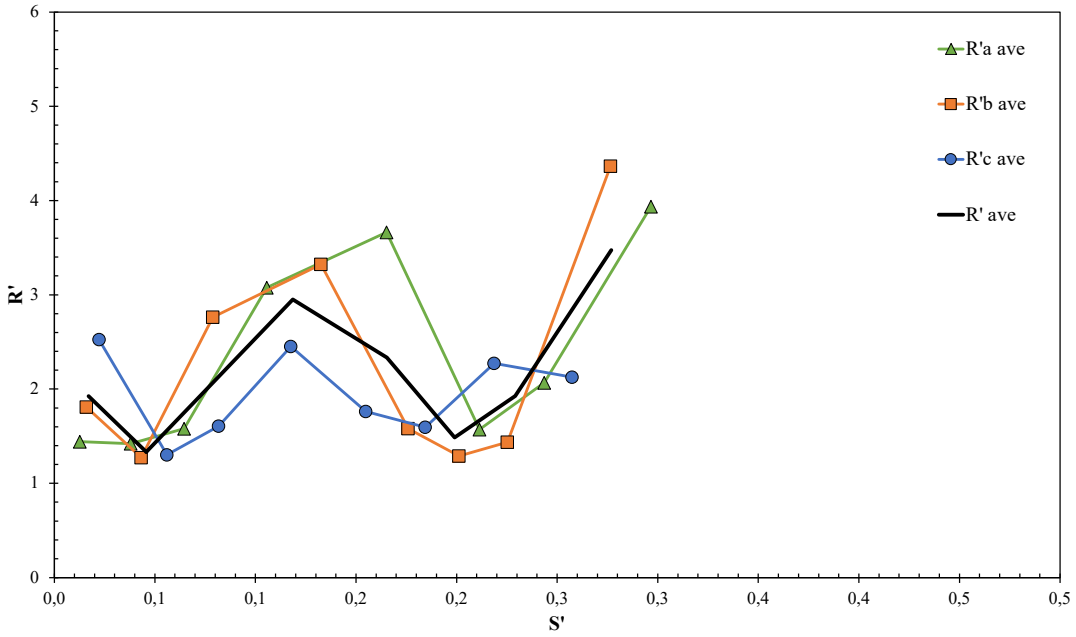

c)

Figure 51: Non-dimensional average ROS $R'_{\ell\ ave}$ values for each reference line a - $R'_{a\ ave}$, b - $R'_{b\ ave}$ or c - $R'_{c\ ave}$ as a function of the non-dimensional distance S', together with the average ROS R'_{ave} values. The fire fronts distance is $d = 2m$. a) $U_0 = 0m.s^{-1}$. b) $U_0 = 2m.s^{-1}$. c) $U_0 = 5m.s^{-1}$.

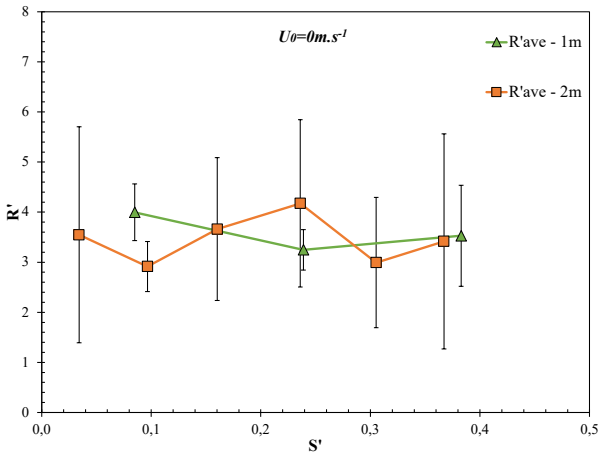

a)

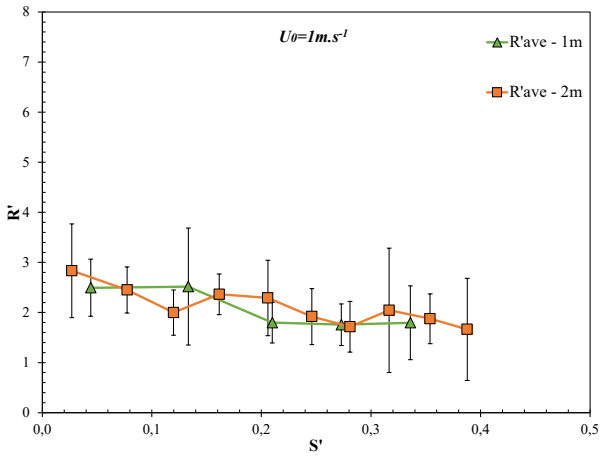

b)

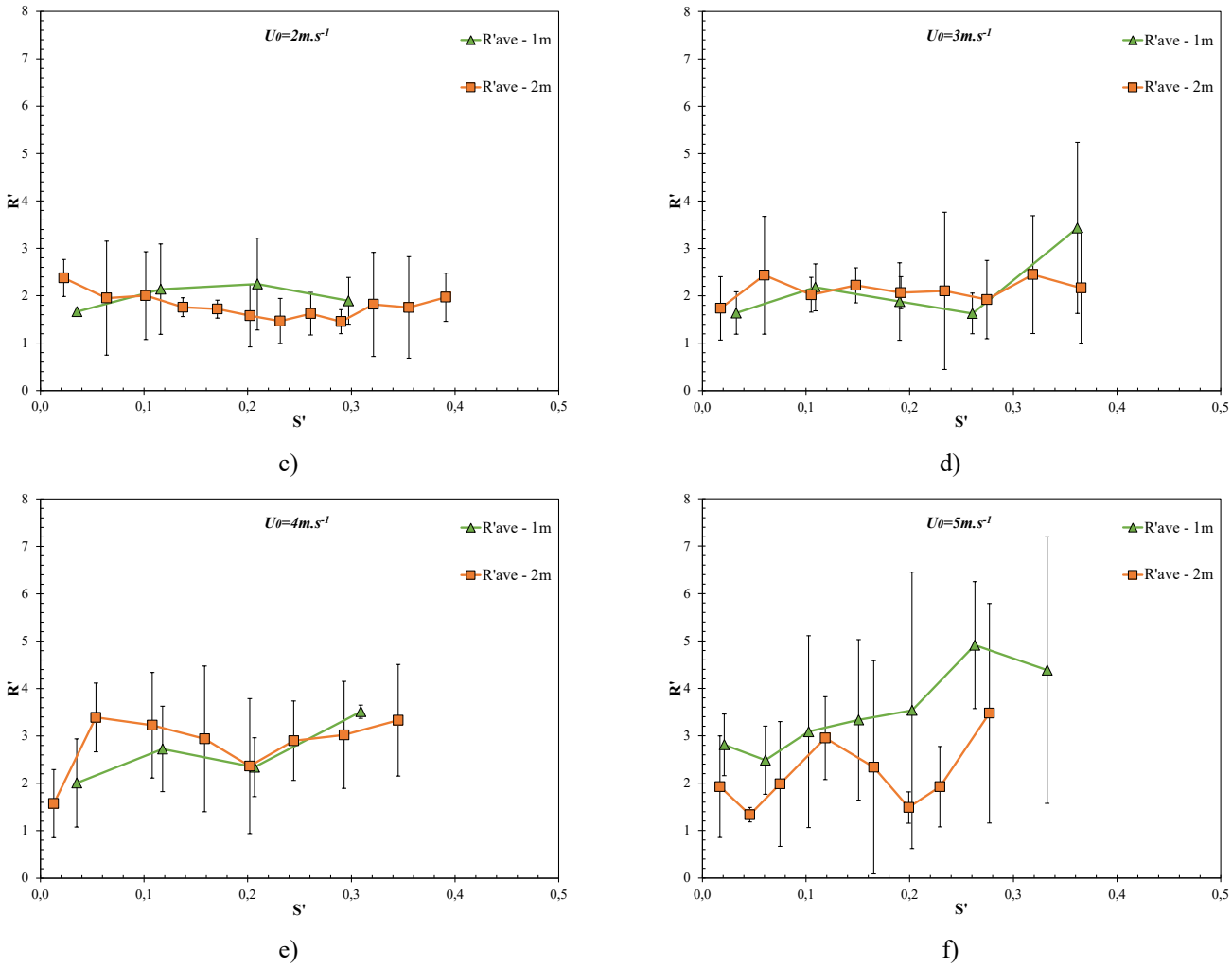

Figure 52: Non-dimensional ROS between two fire fronts under different wind flow velocities (U_0) with two different distances ($d = 1$ and $2m$) as a function of the non-dimensional distance S'. The average values R'_{ave} with the 95% confidence intervals are shown in each case. a) $U_0 = 0m.s^{-1}$; b) $U_0 = 1m.s^{-1}$; c) $U_0 = 2m.s^{-1}$; d) $U_0 = 3m.s^{-1}$; e) $U_0 = 4m.s^{-1}$ and f) $U_0 = 5m.s^{-1}$.

Average Values of Approaching Rate of Spread Analysis

To evaluate the general role of the parameters d and U_0 in the interaction between the two lines, the average $\bar{R}'_{ave}$ values are estimated for each reference line and for each distance ($d = 1$ and 2m). These values are shown in Figure 53 as a function of the wind flow velocity U_0 (0 to 5m.s^{-1}) for all the tests performed. As can be seen, the

values of $\bar{R}'_{ave}$ a similar trend with a clear minimum for wind speeds between $U_0 = 1$ and 2m.s^{-1}.

The set of data points was fitted by a quadratic law given by:

$$\bar{R}'_{ave} = 0.29{U_0}^2 - 1.38U_0 + 3.55 \qquad 58$$

The correlation coefficient R^2 for this fit was 0.891. Therefore, it was assumed that under the present experimental conditions the non-dimensional ROS is independent of the distance between the fire lines and that there is a wind speed value between 1 and 2m.s^{-1} for which the ROS has a minimum value overall. The two-way analysis ANOVA with replication showed that the $\bar{R}'_{ave}$ of the approaching fire is significantly (p-value<0.05) influenced by the wind flow (U_0), but the distance between two fire lines has no significant influence (p-value>0.05) on the $\bar{R}'_{ave}$ for the series of experimental laboratory tests performed.

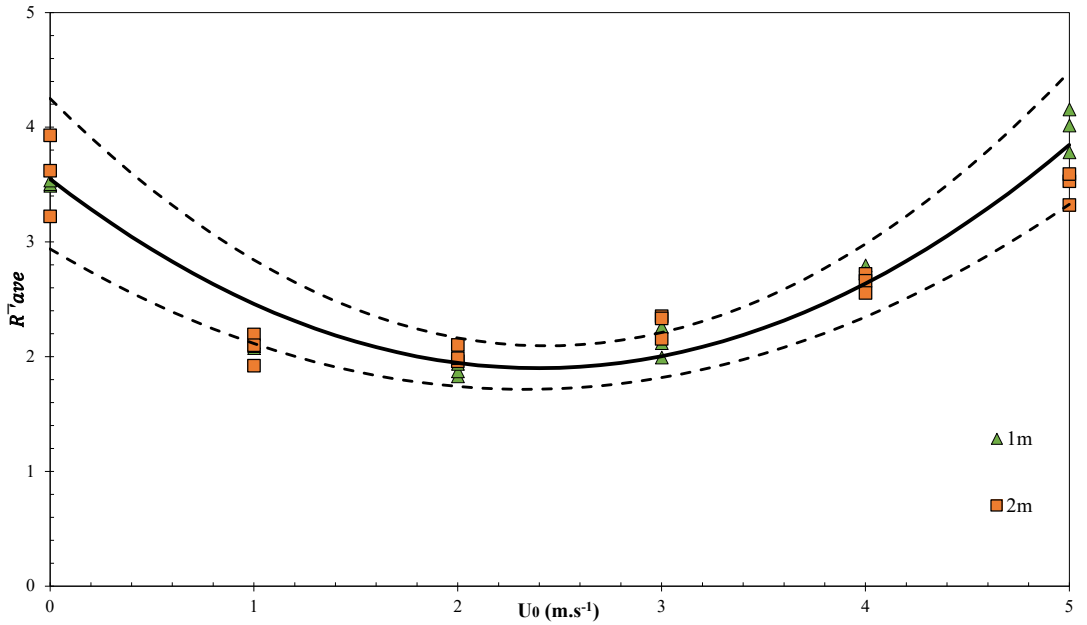

Figure 53: The average $\bar{R}'_{ave}$ values of three replications performed and two distances $d = 1$ and 2m as a function of the wind flow velocity U_0 (0 to 5m.s^{-1}). The black curve represents the predicted $\bar{R}'_{ave}$ as function of the wind flow velocity (U_0) defined by the equation 58 with $R^2 = 0.891$. The dashed-line curves represent the $\bar{R}'_{ave} \pm \Delta\bar{R}'_{ave}$, the standard deviation (sd).

The relationship between the vertical forces generated by the buoyant flow during the ascent of the hot gases and the horizontal forces generated by the wind was calculated according to equation 30 and 31. Figure 54 shows the non-dimensional average value $\bar{R}'_{ave}$ as a function of the Froude number (F_r) for all tests performed. As can be seen in Figure 54, the values of $\bar{R}'_{ave}$ as a function of F_r have a similar trend with a clear minimum for the same $\bar{R}'_{ave}$ occurring for $U_0 = 1$ and 2m.s^{-1}.

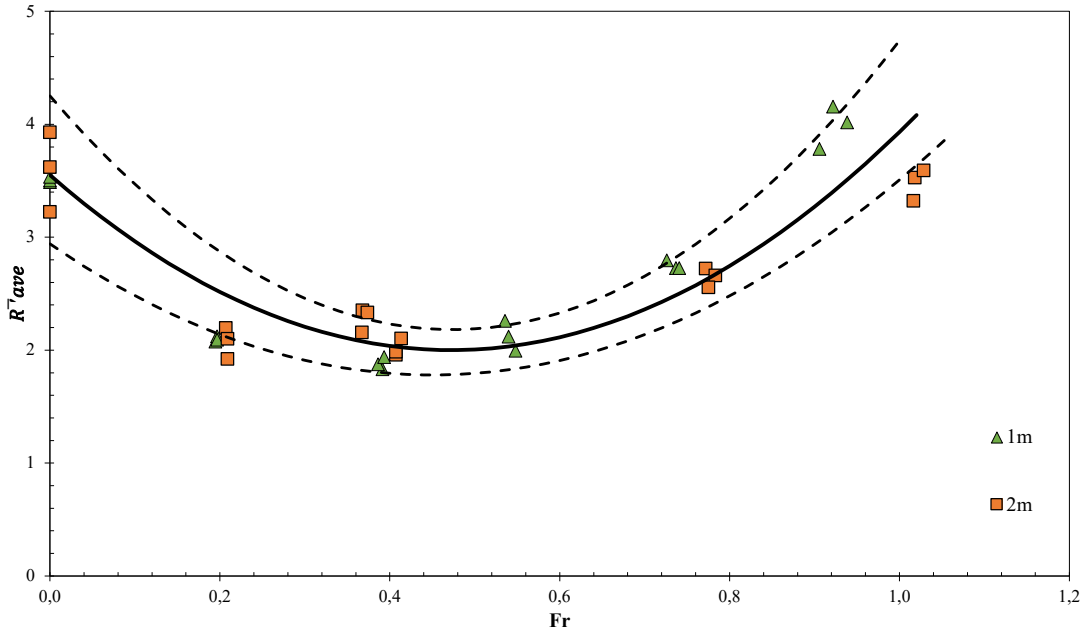

Figure 54: The average $\bar{R}'_{ave}$ values of three replications performed and two distances $d = 1$ and 2m as a function of the Froude number (F_r). The black curve represents the predicted $\bar{R}'_{ave}$ as function of the Froude number defined by the equation 59 with $R^2 = 0.788$. The dashed-line curves represent the $\bar{R}'_{ave} \pm \Delta\bar{R}'_{ave}$, the standard deviation (sd).

The set of data points was fitted by a quadratic law given by:

$$\bar{R}'_{ave} = 6.94{F_r}^2 - 6.56F_r + 3.55 \qquad 59$$

The correlation coefficient R^2 for this fit was 0.788. Therefore, it was assumed that under the present experimental conditions, the relationship between horizontal and vertical forces affecting the rate of spread is independent of the initial distance between the fire.

The two-way analysis ANOVA with replication showed that the Froude number is significantly (p-value<0.05) influenced by the wind flow (U_0), but the distance between two fire lines has no significant influence (p-value>0.05) on the Froude number in the experimental laboratory tests conducted.

The dimensionless Froude number becomes an important parameter to study the similarity of a real phenomenon at a smaller model scale. In this case, two relationships between the vertical forces generated by the buoyant flow during the ascent of the hot gases and the horizontal forces generated by the wind, were considered. The Froude number turns out not to be fully sufficient to explain the phenomenon because, for the same ROS, there are two different Froude values. It is considered that one reason is the dynamic of the fire behaviour and, for this reason, it is considered that this subject should be further investigated in future works.

Physical Interpretation of Fire Evolution

The experiments show that the average of the approaching ROS of two fire lines with a parallel wind varies in a non-monotonic fire behaviour with the wind velocity. To interpret this result, the videos of these and other similar experiments in conjunction with the instantaneous values of ROS were analysed in detail to find an explanation for the existence of a minimum value for ROS.

The fire propagation is always three-dimensional and the variations in fire and flow properties create convection cells (Finney *et al.* 2015). To simplify the interpretation of the dynamic interaction between the fire, the fuel bed and the surrounding flow, and to explain the non-monotonic or intermittent behaviour of the fire (Viegas *et al.* 2021, 2022), will be considered the evolution of the fire and flame properties along a specific reference direction. Since it is concerned with the phenomena that occur when two parallel fire lines interact under the influence of a parallel wind flow, a line parallel to the OY axis between the two fire lines was considered.

Figure 55 presents a physical interpretation of the fire spread characteristics for three values of flow velocity ($U_0 = 0$, 2 and 5m.s^{-1}) corresponding to the three fire spread regimes identified. For each flow velocity, three different stages when the fire fronts

spread toward each other are shown. It is also inset a diagram that shows the typical evolution of the ROS as a function of the local non-dimensional distance S' between the fire lines, as given in Figure 51 and 52.

As shown in each case, the flame geometry and size change as the fire fronts advance in a way that depends on the flow velocity. These changes are related to the role of horizontal and vertical forces that modify the flame geometry (Morvan 2007; Balbi *et al.* 2020; Viegas *et al.* 2021) and consequently the ROS between the two parallel fire lines.

When the wind is still $U_0 = 0\text{m.s}^{-1}$ (Figure 55 a)) there is no horizontal flow and buoyancy is the dominant factor. After the two fire lines begin to burn, the flames incline towards each other (see Figure 55 a1)) and the fire fronts rapidly converge in this initial phase. After the two fire lines increase the burnt area, the residual heat of the burnt area causes an updraft towards the burnt areas and the flames become more vertical and the flame length and height increase (see Figure 55 a2)). Thereafter, the flames incline towards the burnt fuel (see Figure 55 a3)) and ROS decreases (see Figure 55 a4)). Since the initial phase of acceleration is very strong in this case - there is no horizontal wind - the average ROS is relatively high, despite the deceleration during the approach of the two fire lines.

In the case of wind flow $U_0 = 2\text{m.s}^{-1}$ (see Figure 55 b)) in the first stage (Figure 55 b1)), the flame is almost vertical and the convection flow is symmetrical on both sides of each fire front. In this case, the wind inhibits the interaction, and the flames are almost vertical. In the second and third stages (see Figure 55 b2) and b3)), the flames lean towards the burnt area and the flame length and height are constant because the residual heat from the burnt area dominates the heat of the flames. This leads to a stronger flow convergence over the burnt areas. In this case, the fire fronts spread as backfire most of the time, so the value of ROS is relatively low. As a result, the average value of ROS is very low compared to the previous case.

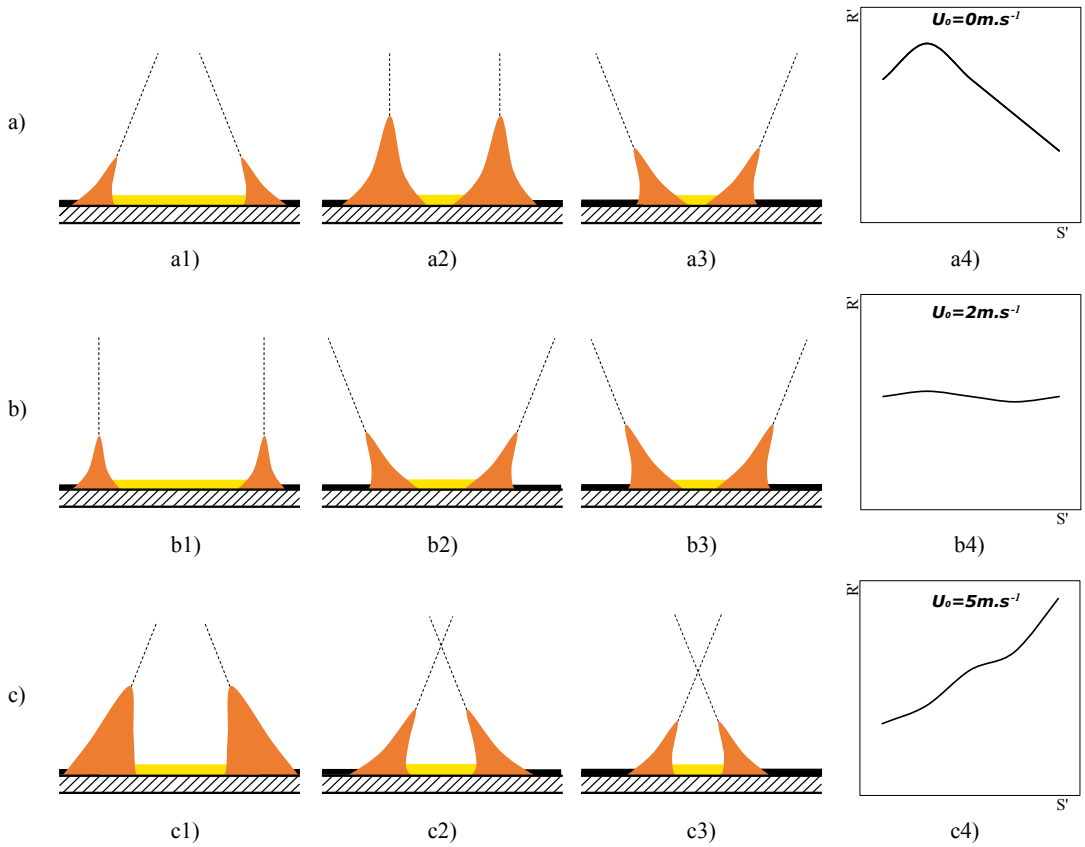

Figure 55: Physical interpretation of fire evolution of a 2D flame during the integration of the two parallel fire lines for three different wind flow velocities. a) b) and c) is considered the wind flow velocity equal to $U_0 = 0m.s^{-1}$, $U_0 = 2m.s^{-1}$ and $U_0 = 5m.s^{-1}$, respectively. For each different wind velocity, it was considered three different stages during the integration of the two parallel fire lines (e.g., stage a1), a2) and a3)). a4), b4) and c4) represent the conceptual evolution of the non-dimensional ROS towards two fire fronts in function of the time for $U_0 = 0m.s^{-1}$, $U_0 = 2m.s^{-1}$ and $U_0 = 5m.s^{-1}$, respectively.

With the wind flow $U_0 = 5\text{m.s}^{-1}$ (see Figure 55 c)), the flames of the individual fire lines incline towards each other, the flame angle decreases and the ROS increases in all phases (see Figure 55 c1), c2) and c3)). As a result of this continuous acceleration, the average value of ROS for this set of boundary conditions is also larger than in the previous case. This can be explained by the fact that the stronger wind has intensified the overall fire behaviour (including the two approaching flanks), allowing the heat from the two approaching flame fronts to overwhelm the residual heat from the burnt area, resulting in stronger flow convergence between the two approaching fire lines. It has been confirmed

that similar fire behaviour associated with flame typology and convective processes occurs in other types of fires. One of these cases corresponds to the well-controlled experiments on junction fires described by Raposo *et al.* 2018. In this work, strong convective effects were observed during the development of fires started by two linear ignition lines intersecting at a 30º angle and propagating along a 30º slope. In particular, near the intersection, there was a strong convective movement towards the unburnt area and a significant acceleration of the fire, while at the other end of the fire line, fire-induced convection tilts the flames towards the burnt fuel, reducing the ROS. At other points along the fire line, the balance between convection conditions and the ROS remains practically constant during propagation.

Chapter 6. Conclusions

In this work, a conceptual model of fire spread based on the interaction between fire-induced convection, the fuel and the surrounding flow, which changes the flame geometry and thus the characteristics of fire spread, is proposed to interpret and justify the non-monotonic growth of a fire. According to this model, there is a process of relatively high frequency fluctuations related to the turbulent flame and flow characteristics, superimposed on a lower frequency evolution related to the fuel bed and its combustion characteristics, namely the flame geometry due to its interaction with the surrounding environment, which produces an oscillatory or intermittent behaviour in fire propagation. This concept was validated in carefully controlled laboratory experiments, without external flow, with point ignition fire in a slope or in a canyon. It was observed that the ROS of the fire head goes through a growth cycle over time, followed by a sudden decrease, especially for fires in canyons, with higher frequency and smaller amplitude fluctuations. A careful analysis of the flow through the flame shows the changes caused by the presence of the flame in the flow on the windward or leeward side of the flame, with two characteristic velocities. For a given fuel bed, these velocities increase with modulus ROS but may not be monotonic. The flame angle with respect to the fuel bed shows a characteristic non-monotonic variation with R', decreasing from a relatively high value - corresponding to an initially vertical flame - to a minimum value of the order of

30°, - for $R' \approx 4$ for this fuel - and then increasing to values close to 70°. The flame length increases with R', but also shows a local maximum near the minimum of the flame angle.

Based on data from virtually all sizes of fires of practical interest, an oscillatory motion characterises the fire spread. This natural oscillation results from combustion and its interaction with the surrounding atmosphere. This oscillation is comparable to the respiration process of a living animal and is an intrinsic property of a spreading fire, with a well-defined frequency and amplitude of oscillation. As a result, the ROS of any section of the fire, namely its head fire or the most advanced section, varies in time and space, with oscillations composed of a half period of R increase followed by a half period of R decrease. The amplitude of these oscillations is proportional to the average value of R, and the constant of proportionality depends slightly on the type of fire, i.e., its size.

The oscillation frequency of the variations of R spans more than five orders of magnitude in the range of fires that were studied. The preliminary data suggest that the oscillation frequency depends on the type of fire and its ROS. For a given fuel bed and type of fire (characterised by its size or fuel mass loading) the oscillation frequency increases linearly with R.

The cases of large fires analysed in the literature illustrate well the reality of the intermittent fire behaviour under continuous and uniform conditions. The difficulty in explaining the rapid changes in fire behaviour - especially the rapid decrease in ROS - due to the “triangle of fire factors” framework and way of thinking became very clear in the review carried out. However, larger fires tend to have relatively higher oscillation amplitudes.

The fire, which occurred on 17th June 2017 near Pedrógão Grande on an area of 45k hectares, destroyed more than 1000 houses and buildings and caused the death of 66 persons. This fire had a very intense spread within a few hours, due to a convergence of unusual circumstances, which was analysed in this work. First, there were two separate fires started by a power line 3km apart. Due to insufficient resources, these fires could not be brought under control when at 18h00 a thunderstorm that passed over the region impacted on the two fires and caused them to grow out of control. The merging of these

fires resulted in what is known as a junction fire, which spread over a very wide area with a very high ROS and very intense convective processes, surprising hundreds of people who were in the area and eventually causing the deaths of 66 people.

Based on extensive field data, it was possible to reconstruct the evolution of the fire and assess the spread of the main fire and flank fires. These results were compared with those from a series of laboratory experiments (at a scale of 1: 2933) conducted under similar geometric conditions. A scale modelling method is proposed to transfer the results of linear displacements or area growth measurements from the laboratory experiments to the real fire scale. The results show that despite the differences in the geometry of the site and in some mechanisms of fire spread, that certainly existed between the real fire and the laboratory scale experiments, the results obtained in the laboratory experiments follow the same trends in terms of fire spread configuration, fire acceleration and burnt area growth observed in the full-scale conditions.

The present work shows that physical modelling of fire spread in laboratory-scale experiments is a useful tool to reproduce and interpret the characteristics of some complex fires, provided that appropriate modelling rules and parameter transformation equations are used.

Analysis of junction fires with non-symmetrical linear fire lines based on laboratory scale experiments was carried out for different slope angles, $\alpha = 10°, 20°, 30°$ and $40°$, and different fire front rotation conditions $\delta_{JF} = 0°$, $5°$, $10°$ and $15°$. The evolution of the fire front consists mainly of the advancement of the intersection point A with an initial angle $\theta_0 = 30°$ between the fire lines. For the tested angles δ_{JF}, the random fluctuations of the non-dimensional ROS R'_A are well related to the tests carried out with the rotation δ_{JF} ($\delta_{JF} = 5°$, $10°$ and $15°$) and the symmetrical boundary condition ($\delta_{JF} = 0°$) during the time and the distance travelled by the point A. For $\alpha = 10°$ and $20°$, the non-dimensional ROS R'_A is quite similar to the symmetrical condition $\delta_{JF} = 0°$. These laboratory tests suggest that the non-dimensional ROS of the intersection point A depends on the slope angle for small angles of rotation, but the angle of rotation has no influence

on the non-dimensional ROS. However, at larger slope angles the convection process dominates and changes the angle γ at which the maximum ROS occurs, but at smaller slope angles the variation of the angle γ is smaller and very close to 0º.

The interaction of two parallel fire fronts initially separated by a certain distance d and propagating laterally in a parallel flow at different wind speeds was investigated. The experimental results, obtained under a range of test conditions, show that the average ROS of the two approaching fires is independent of the initial distance between the lines, but does not vary monotonically with wind speed. In the absence of wind, the average ROS of the two approaching fires has a relatively high value that decreases with increasing wind speed, reaches a minimum value for a range of relatively low values of wind speed, and then increases with wind speed. In the present tests, which were carried out for wind speeds up to $5 m.s^{-1}$, the minimum value of ROS was reached for wind speeds between 1 and $2 m.s^{-1}$.

Based on the analysis of the fire ROS and the flame properties during fire spread, a physical interpretation of the dynamics of fire spread was provided to justify the existence of this minimum value. The equilibrium between the fire-induced buoyancy and the wind flow determines the angle and length of the flames so that in the absence of wind the fire spreads relatively quickly due to the large initial acceleration. At relatively low wind speeds, the spreading speed of the fire lines remains constant and relatively low. As the wind speed increases, the flames incline towards the unburnt fuel between the fire lines, which accelerates their spread and increases the average values of ROS.

As future work, more research must be carried out to explore this important mode of extreme fire behaviour and dynamic fire behaviour. Experimental tests with different fuel bed types at a laboratory scale to better understand the physical processes involved are required. It is important, with a large range of experimental tests (laboratory, field and real fires) and further experimental data, to develop a mathematical model to interpret the present conceptual model (this work is now in progress) and implement this mathematical model to predict the fire behaviour of real fires (this work is now in progress).

The capacity to record and analyse the propagation of a fire front will be necessary to improve other solutions with greater temporal resolution. The analysis of the dynamic evolution of the fire and its interaction with the surrounding flow is important to better continue characterization and estimate the amplitude and frequency of the oscillations. However, the analysis of the centre of convergence of the pyrogenic flow in parallel fire front and comparing it with numerical simulations for a wider range of laboratory experiments with slope influence will be the subject of future work.

To allow a better comparison with forest fires, it is also important to increase the scaling factor (field scale experiments and real fire analysis) in order to extend the range of data points and fill the gap mentioned.

During the present work, the author had some difficulties in developing the experimental work. The study of fire behaviour, in the laboratory or in the field, depends on the meteorological condition and implies that there are acceptable conditions to do scientific work because the humidity of the air affects the humidity of the fuels (live or death) and this affects the fire behaviour. Field experiments depend on the availability of areas for carrying out experimental fires, the availability of suppression teams to provide security during the experimental field tests and depend on better meteorological conditions for carrying them out. Sometimes these conditions only appear close to or during the critical period of the fires in Portugal, which does not allow them to be carried out.

References

Abrams JB, Knapp M, Paveglio TB, Ellison A, Moseley C, Nielsen-Pincus M, Carroll MS (2015) Re-envisioning community-wildfire relations in the U.S. west as adaptive governance. *Ecology and Society* **20**,. doi:10.5751/ES-07848-200334.

Albini F (1981) A model for the wind-blown flame from a line fire☆. *Combustion and Flame* **43**, 155–174. doi:10.1016/0010-2180(81)90014-6.

Albini FA (1982) Response of Free-Burning Fires to Nonsteady Wind. *Combustion Science and Technology* **29**, 225–241. doi:10.1080/00102208208923599.

Alcasena FJ, Ager AA, Bailey JD, Pineda N, Vega-García C (2019) Towards a comprehensive wildfire management strategy for Mediterranean areas: Framework development and implementation in Catalonia, Spain. *Journal of Environmental Management* **231**, 303–320. doi:10.1016/j.jenvman.2018.10.027.

Alexander ME, Cruz MG (2017) Interdependencies between flame length and fireline intensity in predicting crown fire initiation and crown scorch height. *Int J Wildland Fire* **26**, 95–113. doi:10.1071/WF11001.

Almeida M (2011) Propagação de incêndios florestais por focos secundários. Universidade de Coimbra.

Amini E, Safdari MS, Weise DR, Fletcher TH (2019) Pyrolysis kinetics of live and dead wildland vegetation from the Southern United States. *Journal of Analytical and Applied Pyrolysis* **142**,. doi:10.1016/j.jaap.2019.05.002.

Amraoui M, Parente J, Pereira MG (2018) Fire seasons in Portugal: the role of weather and climate. 'Advances in forest fire research 2018'. pp. 472–479. (Imprensa da Universidade de Coimbra) doi:10.14195/978-989-26-16-506_51.

Anderson HE (1968) Fire spread and flame shape. *Fire Technology* **4**, 51–58. doi:10.1007/BF02588606.

Anderson HE (1982) Aids to Determining Fuel Models For Estimating Fire Behavior. (Gen. Tech. Rep. INT-GTR-122. Ogden, Utah: U.S.Department of Agriculture, Forest Service, Intermountain Forest and Range Experiment Station. 22 p.) doi:10.2737/INT-GTR-122.

Andrade C (2019) The P Value and Statistical Significance: Misunderstandings, Explanations, Challenges, and Alternatives. *Indian Journal of Psychological Medicine* **41**, 210–215. doi:10.4103/IJPSYM.IJPSYM_193_19.

Artés T, Castellnou M, Durrant TH, San-Miguel J (2021) Wildfire-Atmosphere Interaction Index for Extreme Fire behaviour. *Natural Hazards and Earth System Sciences*. doi:https://doi.org/10.5194/nhess-2021-122.

Babrauskas V (2002) Ignition of Wood: A Review of the State of the Art. *Journal of Fire Protection Engineering* **12**, 163–189. doi:10.1177/10423910260620482.

Balbi JH, Chatelon FJ, Morvan D, Rossi JL, Marcelli T, Morandini F (2020) A convective-radiative propagation model for wildland fires. *International Journal of Wildland Fire* **29**, 723–738. doi:10.1071/WF19103.

Barrera-Escoda (2011) Climate change projections for Catalonia (NE Iberian Peninsula). Part I: Regional climate modeling. *Tethys, Journal of Weather and Climate of the Western Mediterranean*. doi:10.3369/tethys.2011.8.08.

Berlad AL, Yang CH (1959) On the existence of steady state flames. *Combustion and Flame* **3**, 447–452. doi:10.1016/0010-2180(59)90049-5.

Bowman DMJS, Williamson GJ, Abatzoglou JT, Kolden CA, Cochrane MA, Smith AMS (2017) Human exposure and sensitivity to globally extreme wildfire events. *Nature Ecology and Evolution* **1**,. doi:10.1038/s41559-016-0058.

Brown AA, Davis KP (1973) 'Forest Fire – Control and Use.' (McGraw-Hill: New York)

Byram B (1959) Combustion of forest fuels. In 'Forest Fire: Control and Use'. pp. 61–89. (New York, NY)

Canfield JM, Linn RR, Sauer JA, Finney M, Forthofer J (2014) A numerical investigation of the interplay between fireline length, geometry, and rate of spread. *Agricultural and Forest Meteorology* **189–190**, 48–59. doi:10.1016/j.agrformet.2014.01.007.

Cardil A, Delogu GM, Molina-Terrén DM (2017) Fatalidades em incêndios florestais de 1945 a 2015 na Sardenha (Itália). *Cerne* **23**, 175–184. doi:10.1590/01047760201723022266.

Cardil A, Molina DM, Kobziar LN (2014) Extreme temperature days and their potential impacts on southern Europe. *Natural Hazards and Earth System Sciences* **14**, 3005–3014. doi:10.5194/nhess-14-3005-2014.

Carvill J (1993) Thermodynamics and heat transfer. 'Mechanical Engineer's Data Handbook'. pp. 102–145. (Elsevier) doi:10.1016/B978-0-08-051135-1.50008-X.

Chandler C, Cheney P, Thomas P, Trabaud L, Williams D (1983) 'Fire in forestry. Volume 1. Forest fire behavior and effects.' (John Wiley & Sons, Inc.: New York)

Clark TL, Jenkins MA, Coen J, Packham D (1996) A Coupled Atmosphere - Fire Model: Convective Feedback on Fire-Line Dynamics. *Journal of Applied Meteorology* **35**, 875–901. doi:10.1175/1520-0450(1996)035<0875:ACAMCF>2.0.CO;2.

Côté WA (1968) Chemical Composition of Wood. 'Principles of Wood Science and Technology'. pp. 55–78. (Springer Berlin Heidelberg: Berlin, Heidelberg) doi:10.1007/978-3-642-87928-9_2.

Cruz MG, Alexander ME (2019) Flame Dimensions. 'Encyclopedia of Wildfires and Wildland-Urban Interface (WUI) Fires'. pp. 1–5. (Springer International Publishing: Cham) doi:10.1007/978-3-319-51727-8_54-1.

Cruz MG, Sullivan AL, Leonard R, Malkin S, Matthews S, Gould JS, Mccaw WL, Alexander ME (2014) 'FIRE BEHAVIOUR KNOWLEDGE IN AUSTRALIA A SYNTHESIS OF DISCIPLINARY AND STAKEHOLDER KNOWLEDGE ON FIRE SPREAD PREDICTION CAPABILITY AND APPLICATION.'

Darouich H, Ramos TB, Pereira LS, Rabino D, Bagagiolo G, Capello G, Simionesei L, Cavallo E, Biddoccu M (2022) Water Use and Soil Water Balance of Mediterranean Vineyards under Rainfed and Drip Irrigation Management: Evapotranspiration Partition and Soil Management Modelling for Resource Conservation. *Water* **14**, 554. doi:10.3390/w14040554.

Dlugogorski BZ, Hirunpraditkoon S, Kennedy EM (2014) Ignition temperature and surface emissivity of heterogeneous loosely packed materials from pyrometric measurements. In 'Fire Safety Science', 262–275. (International Association for Fire Safety Science) doi:10.3801/IAFSS.FSS.11-262.

Dold JW, Zinoviev A (2009) Fire eruption through intensity and spread rate interaction mediated by flow attachment. *Combustion Theory and Modelling* **13**, 763–793. doi:10.1080/13647830902977570.

Dold JW, Zinoviev A, Weber (2006) Nonlocal flow effects in bushfire spread rates. http://eprints.maths.manchester.ac.uk/.

Doogan Maria (2006) 'The Canberra firestorm: inquests and inquiry into four deaths and four fires between 8 and 18 January 2003.' (ACT Magistrates Court)

Dupuy J-L (1995) Slope and Fuel Load Effects on Fire Behaviour : Laboratory Experiments in Pine Needles Fuel Beds.

Dupuy JL, Maréchal J, Portier D, Valette JC (2011) The effects of slope and fuel bed width on laboratory fire behaviour. *International Journal of Wildland Fire* **20**, 272–288. doi:10.1071/WF09075.

Ellis PF (2000) The Aerodynamic and Combustion Characteristics of eucalypt bark-a Firebrand study FOR THE DEGREE OF DOCTOR OF PHILOSOPHY.

Fernandes AP, Lopes D, Sorte S, Monteiro A, Gama C, Reis J, Menezes I, Osswald T, Borrego C, Almeida M, Ribeiro LM, Viegas DX, Miranda AI (2022) Smoke emissions from the extreme wildfire events in central Portugal in October 2017. *International Journal of Wildland Fire* **31**, 989–1001. doi:10.1071/WF21097.

Filkov AI, Duff TJ, Penman TD (2020) Frequency of dynamic fire behaviours in australian forest environments. *Fire* **3**, 1–17. doi:10.3390/fire3010001.

Finklin AI (1973) Meteorological Factors in the Sundance Fire run Intermountain Forest and range Experiment Station.

Finney MA, Cohen JD, Forthofer JM, McAllister SS, Gollner MJ, Gorham DJ, Saito K, Akafuah NK, Adam BA, English JD, Dickinson RE (2015) Role of buoyant flame dynamics in wildfire spread. *Proceedings of the National Academy of Sciences of the United States of America* **112**, 9833–9838. doi:10.1073/pnas.1504498112.

Finney MA, Cohen JD, McAllister SS, Jolly WM (2013) On the need for a theory of wildland fire spread. *International Journal of Wildland Fire* **22**, 25–36. doi:10.1071/WF11117.

Finney MA, Smith CT, Maynard TB (2019) United States Department of Agriculture Experiments on Wildfire Ignition by Exploding Targets.

Fons WL (1946) Analysis of fire spread in light forest fuels. *Journal of Agricultural Research* **72**, 93–121.

Frankman D, Webb BW, Butler BW, Jimenez D, Forthofer JM, Sopko P, Shannon KS, Hiers JK, Ottmar RD (2013) Measurements of convective and radiative heating in wildland fires. *International Journal of Wildland Fire* **22**, 157–167. doi:10.1071/WF11097.

Freeborn PH, Wooster MJ, Hao WM, Ryan CA, Nordgren BL, Baker SP, Ichoku C (2008) Relationships between energy release, fuel mass loss, and trace gas an aerosol emissions during laboratory biomass fires. *Journal of Geophysical Research Atmospheres* **113**,. doi:10.1029/2007JD008679.

Fujioka FM (1985) Estimating Wildland Fire Rate of Spread in a Spatially Nonuniform Environment. https://www.fs.usda.gov/psw/publications/fujioka/psw_1985_fujioka001.pdf.

Fujioka FM (2002) A new method for the analysis of fire spread modeling errors. *International Journal of Wildland Fire* **11**, 193. doi:10.1071/WF02004.

Guerreiro J, Fonseca C, Salgueiro A, Fernandes P, Lopez E, de Neufville R, Mateus F, Castellnou M, S. SJ, Moura J, Rego F, Mateus P (2017) Análise e apuramento dos factos relativos aos incêndios que ocorreram em Pedrógão Grande, Castanheira de Pera, Ansião, Alvaiázere, Figueiró dos Vinhos, Arganil, Góis, Penela, Pampilhosa da Serra, Oleiros e Sertã, entre 17 e 24 de junho de 2017. (Lisbon) https://www.parlamento.pt/Documents/2017/Outubro/Relat%C3%B3rioCTI_VF%20.pdf.

Heinsch FA (2020) Fuel Model. 'Encyclopedia of Wildfires and Wildland-Urban Interface (WUI) Fires'. pp. 520–538. (Springer International Publishing: Cham) doi:10.1007/978-3-319-52090-2_178.

Hilton JE, Miller C, Sharples JJ, Sullivan AL (2016) Curvature effects in the dynamic propagation of wildfires. *International Journal of Wildland Fire* **25**, 1238–1251. doi:10.1071/WF16070.

Hollis JJ, Anderson WR, McCaw WL, Cruz MG, Burrows ND, Ward B, Tolhurst KG, Gould JS (2011) The effect of fireline intensity on woody fuel

consumption in southern Australian eucalypt forest fires. *Australian Forestry* **74**, 81–96. doi:10.1080/00049158.2011.10676350.

Hollis JJ, Matthews S, Anderson WR, Cruz MG, Burrows ND (2011) Behind the flaming zone: Predicting woody fuel consumption in eucalypt forest fires in southern Australia. *Forest Ecology and Management* **261**, 2049–2067. doi:10.1016/j.foreco.2011.02.031.

Huang X, Zhuo X, Huang T, Xing C, Cheng C, Chow W (2020) Thermal radiation model for the buoyancy-controlled diffusion plumes from rectangular fire sources. *International Journal of Thermal Sciences* **150**,. doi:10.1016/j.ijthermalsci.2019.106234.

Ihsan Muh, Putra PS, Nasri N, Hamzah AS, Maulany R illa, Ngakan PO (2023) Impact of land slope, tree density and basal area on fire intensity in pinus merkusii plantation forest. *Jurnal Penelitian Kehutanan Wallacea* **12**, 27–33. doi:10.24259/jpkwallacea.v12i1.26707.

Incropera FP, Bergman TL, Lavine AS, Dewitt DP, Bergman TL, Lavine AS (2011) 'Fundamentals of Heat and Mass Transfer.' (FP Incropera and FPFOHAMT Incropera, Eds.). (John Wiley & Sons, Inc.: United States of America) doi:10.1016/j.applthermaleng.2011.03.022.

Johansen RW (1984) Prescribed burning with spot fires in The Georgia Coastal Plain. *Georgia Forest Research* **49**, 1–8. http://www.treesearch.fs.fed.us/pubs/36481.

Kang W, Trang ND, Lee SH, Choi HM, Shim JS, Jang HS, Choi YM (2015) Experimental and numerical investigations of the factors affecting the S-type Pitot tube coefficients. *Flow Measurement and Instrumentation* **44**, 11–18. doi:10.1016/j.flowmeasinst.2014.11.006.

Kawamoto H (2017) Lignin pyrolysis reactions. *Journal of Wood Science* **63**, 117–132. doi:10.1007/s10086-016-1606-z.

Kottek M, Grieser J, Beck C, Rudolf B, Rubel F (2006) World Map of the Köppen-Geiger climate classification updated. *Meteorologische Zeitschrift* **15**, 259–263. doi:10.1127/0941-2948/2006/0130.

Kutiel H (2012) Weather conditions and forest fire propagation-the case of the carmel fire, december 2010. *Israel Journal of Ecology and Evolution* **58**, 113–122. doi:10.1560/IJEE.58.2-3.113.

Liu N, Wu J, Chen H, Zhang L, Deng Z, Satoh K, Viegas DX, Raposo JR (2015) Upslope spread of a linear flame front over a pine needle fuel bed: The role of convection cooling. *Proceedings of the Combustion Institute* **35**, 2691–2698. doi:10.1016/j.proci.2014.05.100.

Louro G, Monteiro M, Constantino L, Rego F (2014) The Portuguese Forest Based Chains: Sector Analyses. pp. 39–65 doi:10.1007/978-3-319-08455-8_2.

Manzello SL, Suzuki S, Hayashi Y (2012) Enabling the study of structure vulnerabilities to ignition from wind driven firebrand showers: A summary of experimental results. In 'Fire Saf J', 181–196 doi:10.1016/j.firesaf.2012.06.012.

McAllister S, Finney M (2014) Convection ignition of live forest fuels. In 'Fire Safety Science', 1312–1325. (International Association for Fire Safety Science) doi:10.3801/IAFSS.FSS.11-1312.

Mccarthy G (2003) Fire Management Drought Factor (fine fuel consumption) prediction from field measurement of Fine Fuel Moisture Content.

Mendes-Lopes JMC, Ventura JMP, Amaral JMP (2003) Flame characteristics, temperature - time curves, and rate of spread in fires propagating in a bed of Pinus pinaster needles. *International Journal of Wildland Fire* **12**, 67. doi:10.1071/WF02063.

Moinuddin KAM, Sutherland D, Mell W (2018) Simulation study of grass fire using a physics-based model: striving towards numerical rigour and the effect of grass height on the rate of spread. *International Journal of Wildland Fire* **27**, 800. doi:10.1071/WF17126.

Moreira F, Viedma O, Arianoutsou M, Curt T, Koutsias N, Rigolot E, Barbati A, Corona P, Vaz P, Xanthopoulos G, Mouillot F, Bilgili E (2011)

Landscape - wildfire interactions in southern Europe: Implications for landscape management. *J Environ Manage* **92**, 2389–2402. doi:10.1016/j.jenvman.2011.06.028.

Morvan D (2007) A numerical study of flame geometry and potential for crown fire initiation for a wildfire propagating through shrub fuel. *International Journal of Wildland Fire* **16**, 511–518. doi:10.1071/WF06010.

Morvan D, Meradji S, Mell W (2011) Numerical Study of the Interaction Between a Head Fire and a Backfire Propagating in Grassland. *Fire Safety Science* **10**, 1415–1424. doi:10.3801/IAFFS.FSS.10-1415.

Nelson Jr, RM (2003) Power of the fire—a thermodynamic analysis. *International Journal of Wildland Fire* **12**, 51. doi:10.1071/WF02032.

Nunes LJR, Meireles CIR, Pinto Gomes CJ, Almeida Ribeiro NMC (2019a) The Evolution of Climate Changes in Portugal: Determination of Trend Series and Its Impact on Forest Development. *Climate* **7**, 78. doi:10.3390/cli7060078.

Nunes LJR, Meireles CIR, Pinto Gomes CJ, Almeida Ribeiro NMC (2019b) Historical Development of the Portuguese Forest: The Introduction of Invasive Species. *Forests* **10**, 974. doi:10.3390/f10110974.

Pastor E, Zárate L, Planas E, Arnaldos J (2003) Mathematical models and calculation systems for the study of wildland fire behaviour. *Prog Energy Combust Sci* **29**, 139–153. doi:10.1016/S0360-1285(03)00017-0.

Pinto C, André J, Viegas DX (2020) Double S-type Pitot Tube for velocity field study of fire whirls. *Flow Measurement and Instrumentation* **76**,. doi:10.1016/j.flowmeasinst.2020.101806.

Pinto P, Silva ÁP, Viegas DX, Almeida M, Raposo J, Ribeiro LM (2022) Influence of Convectively Driven Flows in the Course of a Large Fire in Portugal: The Case of Pedrógão Grande. *Atmosphere* **13**, 414. doi:10.3390/atmos13030414.

Pyne SJ (1984) 'Introduction to wildland fire: Fire Management in the United States.' (John Wiley and Sons: New York)

Raposo J (2016) Extreme Fire Behaviour Associated with the Merging of Two Linear Fire Fronts. University of Coimbra. http://hdl.handle.net/10316/31020.

Raposo JR, Cabiddu S, Viegas DX, Salis M, Sharples J (2015) Experimental analysis of fire spread across a two-dimensional ridge under wind conditions. *International Journal of Wildland Fire* **24**, 1008–1022. doi:10.1071/WF14150.

Raposo JR, Viegas DX, Xie X, Almeida M, Figueiredo AR, Porto L, Sharples J (2018) Analysis of the physical processes associated with junction fires at laboratory and field scales. *International Journal of Wildland Fire* **27**, 52–68. doi:10.1071/WF16173.

Raposo J, Viegas DX, Xie X, Almeida M, Naian L (2014) Analysis of the jump fire produced by the interaction of two oblique fire fronts: comparison between laboratory and field cases. 'Advances in forest fire research'. pp. 88–94. (Imprensa da Universidade de Coimbra) doi:10.14195/978-989-26-0884-6_8.

Ribeiro C, Reis L, Raposo J, Rodrigues A, Viegas DX, Sharples J (2022) Interaction between two parallel fire fronts under different wind conditions. *International Journal of Wildland Fire* **31**, 492–506. doi:10.1071/WF21120.

Ribeiro LM, Rodrigues A, Lucas D, Viegas DX (2020) The Impact on Structures of the Pedrógão Grande Fire Complex in June 2017 (Portugal). *Fire* **3**, 57. doi:10.3390/fire3040057.

Ribeiro C, Viegas X, 12 D, Almeida M, Ribeiro L, Rodrigues A, Alves D (2019) 'Forest Fuel Management in Wildland Urban Interface Areas.'

Ribeiro C, Xavier Viegas D, Raposo J, Reis L, Sharples J (2023) Slope effect on junction fire with two non-symmetric fire fronts. *International Journal of Wildland Fire* **32**, 328–335. doi:10.1071/WF22152.

Rodrigues A, Ribeiro C, Raposo J, Viegas DX, André J (2019) Effect of Canyons on a Fire Propagating Laterally Over Slopes. *Frontiers in Mechanical Engineering* **5**,. doi:10.3389/fmech.2019.00041.

Rodrigues A, Viegas DX, Almeida M, Ribeiro C, Raposo J, André J (2023) Fire propagating laterally over a slope with and without an embedded canyon. *Fire Safety Journal* 103791. doi:10.1016/j.firesaf.2023.103791.

Rossa CG, Davim DA, Viegas DX (2015) Behaviour of slope and wind backing fires. *International Journal of Wildland Fire* **24**, 1085–1097. doi:10.1071/WF14215.

Rossa CG, Fernandes PM (2018) An empirical model for the effect of wind on fire spread rate. *Fire* **1**, 1–19. doi:10.3390/fire1020031.

Rothermel RC (1972) A mathematical model for predicting fire spread in wildland fuels.

Rothermel RC (1983) How to Predict the Spread and Intensity of Forest and Range Fires.

Rothermel R, Mutch R (1986) Behaviour of the Life-Threatening Butte Fire: August 27–29. Alexander M, Thomas D (2003) 'WILDLAND FIRE STUDIES AND ANALYSES: Part 2'' (Washington, DC) Section: Behavior of the Life-Threatening Butte Fire: August 27–29' **47**, 1–40. http://www.fs.usda.gov/sites/default/files/legacy_files/fire-management-today/63-4.pdf.

Safdari MS, Amini E, Weise DR, Fletcher TH (2019) Heating rate and temperature effects on pyrolysis products from live wildland fuels. *Fuel* **242**, 295–304. doi:10.1016/j.fuel.2019.01.040.

San-Miguel-Ayanz J, Oom D, Artès T, Viegas DX, Fernandes P, Faivre N, Freire S, Moore P, Rego F, Castellnou M (2021) Forest fires in Portugal in 2017. *Science for Disaster Risk Management 2020: Acting Today, Protecting Tomorrow*.

Sardoy N, Consalvi JL, Porterie B, Fernandez-Pello AC (2007) Modeling transport and combustion of firebrands from burning trees. *Combustion and Flame* **150**, 151–169. doi:10.1016/j.combustflame.2007.04.008.

Schemel CF, Simeoni A, Biteau H, Rivera JD, Torero JL (2008) A calorimetric study of wildland fuels. *Experimental Thermal and Fluid Science* **32**, 1381–1389. doi:10.1016/j.expthermflusci.2007.11.011.

Scott JH (2012) Introduction to Wildfire Behavior Modeling. *National Interagency Fuels, Fire, & Vegetation Technology Transfer*. www.niftt.gov.

Scott JH, Burgan RE (2005) Standard fire behavior fuel models: a comprehensive set for use with Rothermel's surface fire spread model. doi:10.2737/RMRS-GTR-153.

Sharples JJ (2009) An overview of mountain meteorological effects relevant to fire behaviour and bushfire risk. *International Journal of Wildland Fire* **18**, 737. doi:10.1071/WF08041.

Sharples JJ, McRae RHD, Weber RO (2010) Wind characteristics over complex terrain with implications for bushfire risk management. *Environmental Modelling and Software* **25**, 1099–1120. doi:10.1016/j.envsoft.2010.03.016.

Sharples JJ, McRae RHD, Wilkes SR (2012) Wind-terrain effects on the propagation of wildfires in rugged terrain: Fire channelling. *International Journal of Wildland Fire* **21**, 282–296. doi:10.1071/WF10055.

Sharples JJ, Towers IN, Wheeler G, Wheeler V-M, Mccoy JA (2013) Modelling fire line merging using plane curvature flow. In 'Piantadosi, J., Anderssen, R.S. and Boland J. (eds) MODSIM2013, 20th International Congress on Modelling and Simulation', 1–6. (Modelling and Simulation Society of Australia and New Zealand) doi:10.36334/modsim.2013.A3.sharples2.

Shavit T, Shahrabani S, Benzion U, Rosenboim M (2013) The effect of a forest fire disaster on emotions and perceptions of risk: A field study after the Carmel fire. *Journal of Environmental Psychology* **36**, 129–135. doi:10.1016/j.jenvp.2013.07.018.

Shi M, Kim J, Sawada JA, Lam J, Sarabadan S, Kuznicki TM, Kuznicki SM (2013) Production of argon free oxygen by adsorptive air separation on Ag-ETS-10. *AIChE Journal* **59**, 982–987. doi:10.1002/aic.13879.

Silvani X, Morandini F, Dupuy JL (2012) Effects of slope on fire spread observed through video images and multiple-point thermal measurements. *Experimental Thermal and Fluid Science* **41**, 99–111. doi:10.1016/j.expthermflusci.2012.03.021.

Silvani X, Morandini F, Dupuy JL, Susset A, Vernet R, Lambert O (2018) Measuring velocity field and heat transfer during natural fire spread over large inclinable bench. *Experimental Thermal and Fluid Science* **92**, 184–201. doi:10.1016/j.expthermflusci.2017.11.020.

Simard A, Haines D, Blank R, Frost J (1983) The Mack Lake Fire. USDA Forest Service, North Central Forest Experiment Station, General Technical Report NC-83 (St Paul, MN). doi:https://doi.org/10.2737/NC-GTR-83.

Skulska I, Montiel-Molina C, Germano A, Castro Rego F (2021) Evolution of Portuguese community forests and their governance based on new institutional economics. *European Journal of Forest Research* **140**, 913–930. doi:10.1007/s10342-021-01375-y.

Soares PMM, Lima DCA (2022) Water scarcity down to earth surface in a Mediterranean climate: The extreme future of soil moisture in Portugal. *Journal of Hydrology* **615**, 128731. doi:10.1016/j.jhydrol.2022.128731.

Storey MA, Price OF, Almeida M, Ribeiro C, Bradstock RA, Sharples JJ (2021) Experiments on the influence of spot fire and topography interaction on fire rate of spread. *PLoS ONE* **16**,. doi:10.1371/journal.pone.0245132.

Sullivan AL (2007) Convective Froude number and Byram's energy criterion of Australian experimental grassland fires. *Proceedings of the Combustion Institute* **31 II**, 2557–2564. doi:10.1016/j.proci.2006.07.053.

Sullivan AL (2009) Wildland surface fire spread modelling, 1990 - 2007. 1: Physical and quasi-physical models. *International Journal of Wildland Fire* **18**, 349. doi:10.1071/wf06143.

Sullivan AL, Ball R (2012) Thermal decomposition and combustion chemistry of cellulosic biomass. *Atmospheric Environment* **47**, 133–141. doi:10.1016/j.atmosenv.2011.11.022.

Sullivan AL, Gould JS (2019) Wildland Fire Rate of Spread. 'Encyclopedia of Wildfires and Wildland-Urban Interface (WUI) Fires'. pp. 1–4. (Springer International Publishing) doi:10.1007/978-3-319-51727-8_55-1.

Tarifa CS, Perez P, Notario D, Moreno FG (1965) ON THE FLIGHT PATHS AND LIFETIMES OF BURNING PARTICLES OF WOOD. The Combustion Institute,

Tedim F, Leone V, Amraoui M, Bouillon C, Coughlan M, Delogu G, Fernandes P, Ferreira C, McCaffrey S, McGee T, Parente J, Paton D, Pereira M, Ribeiro L, Viegas D, Xanthopoulos G (2018) Defining Extreme Wildfire Events: Difficulties, Challenges, and Impacts. *Fire* **1**, 9. doi:10.3390/fire1010009.

Tedim F, Remelgado R, Borges C, Carvalho S, Martins J (2013) Exploring the occurrence of mega-fires in Portugal. *Forest Ecology and Management* **294**, 86–96. doi:10.1016/j.foreco.2012.07.031.

Thomas CM, Sharples JJ, Evans JP (2015) Pyroconvective interaction of two merged fire lines: curvature effects and dynamic fire spread. In 'Weber, T., McPhee, M.J. and Anderssen, R.S. (eds) MODSIM2015, 21st International Congress on Modelling and Simulation', Gold Coast, Australia. 312–318. (Modelling and Simulation Society of Australia and New Zealand: Gold Coast, Australia) doi:10.36334/MODSIM.2015.A4.Thomas.

Thomas CM, Sharples JJ, Evans JP (2017) Modelling the dynamic behaviour of junction fires with a coupled atmosphere-fire model. *International Journal of Wildland Fire* **26**, 331–344. doi:10.1071/WF16079.

Valente S, Coelho C, Ribeiro C, Liniger H, Schwilch G, Figueiredo E, Bachmann F (2015) How much management is enough? Stakeholder views on forest management in fire-prone areas in central Portugal. *Forest Policy and Economics* **53**, 1–11. doi:10.1016/j.forpol.2015.01.003.

Vaz GC, André JCS, Viegas DX (2004) Fire spread model for a linear front in a horizontal solid porous fuel bed in still air. *Combustion Science and Technology* **176**, 135–182. doi:10.1080/00102200490255343.

Viegas DX (2002) Fire line rotation as a mechanism for fire spread on a uniform slope. *International Journal of Wildland Fire* **11**, 11–23. doi:10.1071/WF01049.

Viegas DX (2004) On the existence of a steady state regime for slope and wind driven fires. *International Journal of Wildland Fire* **13**, 101–117. doi:10.1071/WF03008.

Viegas DX (2005) A mathematical model for forest fires blowup. *Combustion Science and Technology* **177**, 27–51. doi:10.1080/00102200590883624.

Viegas DX (2006) Parametric study of an eruptive fire behaviour model. *International Journal of Wildland Fire* **15**, 169–177. doi:10.1071/WF05050.

Viegas DX, Almeida MA, Ribeiro LM, Raposo J, Viegas MT, Oliveira R, Alves D, Pinto C, Rodrigues A, Ribeiro C, Lopes S, Jorge H, Viegas CX (2019) Análise dos Incêndios Florestais Ocorridos a 15 de outubro de 2017. (Centro de Estudos sobre Incêndios Florestais (CEIF/ADAI/LAETA))

Viegas DX, Pita LP (2004) Fire spread in canyons. *International Journal of Wildland Fire* **13**, 253–274. doi:10.1071/WF03050.

Viegas DX, Raposo JR, Davim DA, Rossa CG (2012) Study of the jump fire produced by the interaction of two oblique fire fronts. Part 1. Analytical model and validation with no-slope laboratory experiments. *International Journal of Wildland Fire* **21**, 843–856. doi:10.1071/WF10155.

Viegas D, Raposo J, Figueiredo A (2013) Preliminary analysis of slope and fuel bed effect on jump behavior in forest fires. In 'Procedia Eng', 1032–1039. (Elsevier Ltd) doi:10.1016/j.proeng.2013.08.158.

Viegas DXFC, Raposo JRN, Ribeiro CFM, Reis L, Abouali A, Ribeiro LM, Viegas CXP (2022) On the intermittent nature of forest fire spread – Part 2. *International Journal of Wildland Fire* **31**, 967–981. doi:10.1071/WF21098.

Viegas DXFC, Raposo JRN, Ribeiro CFM, Reis LCD, Abouali A, Viegas CXP (2021) On the non-monotonic behaviour of fire spread. *International Journal of Wildland Fire* **30**, 702–719. doi:10.1071/WF21016.

Viegas DX, Ribeiro C, Almeida M, Pinto P, Ribeiro LM, Silva Á (2023) Field and laboratory analysis of the junction fire process in the catastrophic fire of Pedrógão Grande in June 2017. *International Journal of Wildland Fire*. doi:10.1071/WF22161.

Viegas DX, Rossa C (2009) Fireline rotation analysis. *Combustion Science and Technology* **181**, 1495–1525. doi:10.1080/00102200903228891.

Viegas D, Rossa C, Ribeiro L (2011) 'Incêndios Florestais.' (verlag dashöfer, Ed.). (Portugal)

Viegas DX, Simeoni A (2011) Eruptive Behaviour of Forest Fires. *Fire Technology* **47**, 303–320. doi:10.1007/s10694-010-0193-6.

Viegas DX, Soares J, Almeida M (2013) Combustibility of a mixture of live and dead fuel components. *International Journal of Wildland Fire* **22**, 992. doi:10.1071/WF12031.

Viegas DX, Viegas DX (2010) The Carmel Fire Initial Spread Preliminary Report.

Wade DD, Ward DE (1973) An Analysis of the Air Force Bomb Range Fire. *Res Pap SE-105 Asheville, NC: US Department of Agriculture, Forest Service, Southeastern Forest Experiment Station 41 p*. https://www.srs.fs.usda.gov/pubs/rp/rp_se105.pdf.

Van Wagner CE (1968) Fire behaviour mechanisms in a Red Pine plantation: field and laboratory evidence. (Ottawa, Canada) http://cfs.nrcan.gc.ca/publications/?id=24753%5Cnhttp://cfs.nrcan.gc.ca/publications/download-pdf/24753.

Weber RO (1989) Analytical Models for Fire Spread Due to Radiation.

Weise D, Biging G (1994) Effects Of Wind Velocity And Slope On Fire Behavior. *Fire Safety Science* **4**, 1041–1051. doi:10.3801/iafss.fss.4-1041.

Weise DR, Fletcher TH, Safdari MS, Amini E, Palarea-Albaladejo J (2022) Application of compositional data analysis to determine the effects of heating mode, moisture status and plant species on pyrolysates. In 'Int J Wildland Fire', 24–45. (CSIRO) doi:10.1071/WF20126.

Viegas D, Almeida M, Ribeiro M, Raposo J, Viegas M, Oliveira R, Alves D, Pinto C, Jorge H, Rodrigues A, Lucas D, Lopes S, Silva F (2017) O Complexo de Incêndios de Pedrógão Grande e Concelhos Limítrofes, Iniciado a 17 de Junho de 2017. https://www.portugal.gov.pt/pt/gc21/comunicacao/documento?i=o-complexo-de-incendios-de-pedrogao-grande-e-concelhos-limitrofes-iniciado-a-17-de-junho-de-2017.

Xiaodong X, Naian L, Viegas DX, Raposo JR (2014) Experimental research on upslope fire and jump fire. In 'Fire Safety Science', 1430–1442. (International Association for Fire Safety Science) doi:10.3801/IAFSS.FSS.11-1430.

Xie X, Liu N, Raposo JR, Viegas DX, Yuan X, Tu R (2020) An experimental and analytical investigation of canyon fire spread. *Combustion and Flame* **212**, 367–376. doi:10.1016/j.combustflame.2019.11.004.

Xie X, Liu N, Viegas DX, Raposo JR (2014) Experimental Research on Upslope Fire and Jump Fire. *Fire Safety Science* **11**, 1430–1442. doi:10.3801/IAFSS.FSS.11-1430.

Yang Z, Chen HX (2018) Experimental Study on Flame Geometry along the Inclined Surface with and without Sidewalls by Using a Gas Burner. In 'Procedia Eng', 925–933. (Elsevier Ltd) doi:10.1016/j.proeng.2017.12.094.

Yang H, Yan R, Chen H, Lee DH, Zheng C (2007) Characteristics of hemicellulose, cellulose and lignin pyrolysis. *Fuel* **86**, 1781–1788. doi:10.1016/j.fuel.2006.12.013.

Appendix

Appendix A1 – Wind Velocity Measured Inside of the Combustion Tunnel

Laboratory experiments were carried out at the Forest Fire Research Laboratory of the University of Coimbra using an indoor Combustion Tunnel (CT). The fuel used in all tests was composed of dry particles of straw (*Avena sativa*) with a constant load of 600g.m^{-2} (dry basis). Inside of the Combustion Tunnel, the wind velocity was measured for wind velocities 1, 3 and 5m.s^{-1} in the OX axis at the points $P_{x,y}$ where x and y are the coordinates relatively the referential OXY, with a KimoAMI 300 hot-wire probe (Kimo Instruments, Montpon-Ménestérol, France) 22cm above the CT ground (OZ axis). Figure A1 a) shown the positions where flow velocity was measured. Table A1, Table A2 and Table A3 shown the data recorded during the three replications for wind velocities 1, 3 and 5m.s^{-1}, respectively.

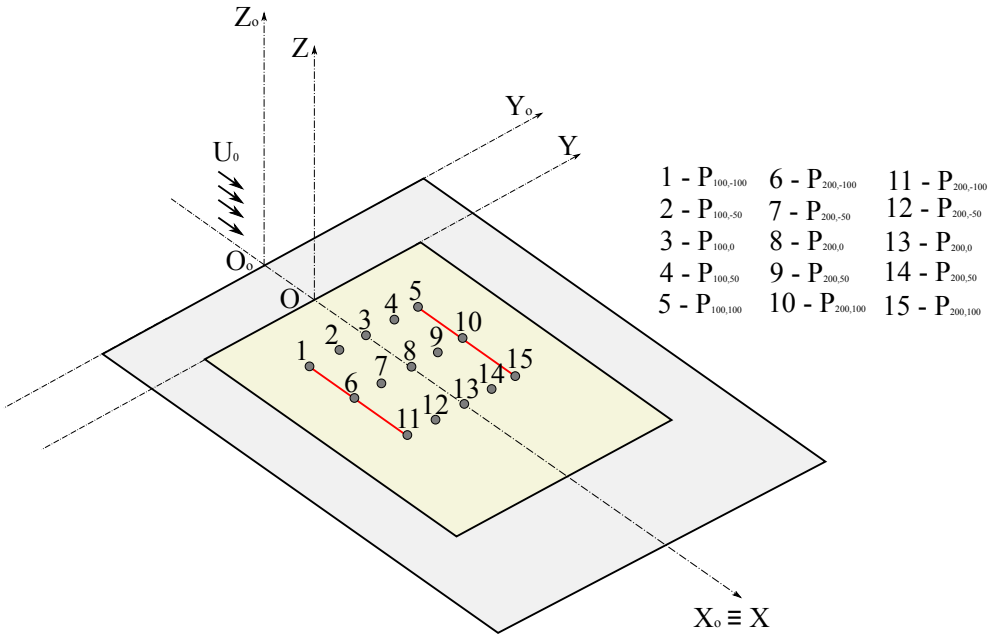

a)

b)

Figure A1: a) Distribution points Px,y,z where wind velocity was measured for wind velocities 1, 3 and 5m.s-1 in the OX axis. b) KimoAMI 300 hot-wire probe (Kimo Instruments, Montpon-Ménestérol, France), 22cm above the CT ground (OZ axis)

Table A1: Wind velocity for $U_0=1m.s^{-1}$.

x	*y*	T1				T2				T3			
		Min	**Max**	**AVG**	**DEV**	**Min**	**Max**	**AVG**	**DEV**	**Min**	**Max**	**AVG**	**DEV**
100	-100	0.98	1.12	1.04	0.05	0.79	1.10	1.01	0.08	0.82	0.95	0.89	0.04
100	-50	1.22	1.46	1.34	0.09	1.18	1.52	1.37	0.10	1.24	1.51	1.35	0.11
100	0	1.07	1.48	1.29	0.12	1.19	1.38	1.29	0.06	1.22	1.43	1.30	0.07
100	50	0.86	1.31	1.09	0.14	1.01	1.68	1.34	0.19	1.15	1.47	1.32	0.11
100	100	0.96	1.41	1.16	0.14	1.06	1.47	1.26	0.13	0.83	1.20	1.01	0.11
200	-100	1.05	1.23	1.13	0.06	0.92	1.25	1.10	0.10	0.95	1.32	1.10	0.13
200	-50	0.90	1.37	1.10	0.15	1.15	1.35	1.24	0.07	0.86	1.50	1.14	0.27
200	0	0.80	1.80	1.90	0.21	1.19	1.65	1.37	0.18	0.98	1.29	1.10	0.09
200	50	1.20	1.39	1.24	0.06	0.95	1.30	1.11	0.14	1.16	1.41	1.24	0.08
200	100	0.97	1.50	1.18	0.25	0.96	0.96	0.91	0.04	0.73	0.98	0.81	0.06
300	-100	0.84	1.15	0.97	0.09	0.88	1.00	0.93	0.03	0.89	1.22	1.06	0.11
300	-50	1.04	1.61	1.23	0.16	0.97	1.75	1.26	0.27	0.93	1.22	1.00	0.08
300	0	1.11	1.46	1.23	0.09	0.96	1.51	1.19	0.15	1.00	1.21	1.01	0.06
300	50	0.75	1.09	0.92	0.11	0.76	0.98	0.88	0.07	0.85	1.09	0.96	0.08
300	100	0.88	1.30	1.04	0.11	0.69	1.05	0.85	0.09	0.88	1.08	0.96	0.06

Table A2: Wind velocity for U_0=3m.s^{-1}.

x	y	T1				T2				T3			
		Min	**Max**	**AVG**	**DEV**	**Min**	**Max**	**AVG**	**DEV**	**Min**	**Max**	**AVG**	**DEV**
100	-100	2.60	3.87	3.279	0.40	2.67	3.46	3.12	0.28	2.7	4.32	3.50	0.52
100	-50	3.10	4.60	3.57	0.48	2.84	4.15	3.66	0.49	3.4	3.80	3.63	0.15
100	0	3.30	4.90	4.00	0.48	3.10	4.20	3.91	0.27	3.4	4.80	4.09	0.50
100	50	2.67	4.11	3.28	0.52	2.25	4.16	3.26	0.54	3.1	3.90	3.41	0.28
100	100	2.51	3.60	3.01	0.30	2.62	4.05	3.15	0.43	2.06	3.23	2.70	0.36
200	-100	3.10	4.50	3.75	0.43	3.10	3.70	3.28	0.18	2.73	3.62	3.29	0.32
200	-50	3.00	4.60	3.20	0.46	2.77	4.76	3.63	0.55	4.00	5.00	4.49	0.34
200	0	3.20	4.20	3.64	0.32	3.30	4.30	3.94	0.33	3.40	4.40	3.83	0.28
200	50	2.88	3.49	3.24	0.16	2.59	3.64	3.01	0.37	2.76	4.30	3.39	0.46
200	100	2.86	3.31	3.07	0.15	2.63	3.99	3.23	0.47	2.75	3.93	3.21	0.35
300	-100	2.70	3.35	3.02	0.22	2.70	4.09	3.49	0.36	3.00	3.80	3.54	0.20
300	-50	3.40	5.00	4.27	0.57	3.40	4.80	4.02	0.41	3.40	5.30	4.28	0.66
300	0	3.50	4.30	3.96	0.29	3.00	4.10	3.54	0.29	2.79	4.03	3.54	0.41
300	0.5	2.25	3.92	3.19	0.52	2.70	4.00	3.40	0.45	2.50	3.60	3.17	0.29
300	1	2.22	3.62	2.92	0.37	2.70	3.19	3.01	0.12	2.65	3.57	3.00	0.27

Table A3: Wind velocity for U_0=5m.s^{-1}.

x	*y*	T1				T2				T3			
		Min	**Max**	**AVG**	**DEV**	**Min**	**Max**	**AVG**	**DEV**	**Min**	**Max**	**AVG**	**DEV**
100	-100	4.6	5.7	5.14	0.38	4.99	5.21	5.10	0.43	4.99	5.21	5.10	0.70
100	-50	5.0	7.4	6.26	0.81	4.93	6.72	5.82	0.44	4.93	6.72	5.82	1.56
100	0	5.1	6.7	6.04	0.40	5.48	6.98	6.23	0.33	5.48	6.98	6.23	0.36
100	50	3.5	6.2	4.86	0.99	3.89	6.09	4.99	0.51	3.89	6.09	4.99	0.64
100	100	4.2	5.8	4.89	0.58	4.05	6.58	5.32	0.27	4.05	6.58	5.32	0.27
200	-100	4.3	5.9	5.18	0.44	4.38	5.63	5.00	0.70	4.38	5.63	5.00	0.43
200	-50	4.3	8.0	5.78	1.05	4.98	7.44	6.21	1.56	4.98	7.44	6.21	0.44
200	0	4.8	6.0	5.38	0.37	4.26	5.51	4.89	0.36	4.26	5.51	4.89	0.33
200	50	4.4	6.4	5.4	0.49	4.68	6.38	5.53	0.64	4.68	6.38	5.53	0.51
200	100	4.0	4.9	4.51	0.27	4.09	5.58	4.84	0.27	4.09	5.58	4.84	0.27
300	-100	4.8	6.3	5.51	0.43	4.99	6.28	5.63	0.38	4.99	6.28	5.63	0.38
300	-50	5.7	7.1	6.27	0.44	5.60	7.16	6.38	0.81	5.60	7.16	6.38	0.81
300	0	5.5	6.7	5.98	0.33	5.43	7.22	6.33	0.40	5.43	7.22	6.33	0.40
300	50	3.8	5.5	4.96	0.51	4.42	5.64	5.03	0.99	4.42	5.64	5.03	0.99
300	100	3.9	4.7	4.46	0.27	3.68	4.10	3.89	0.58	3.68	4.10	3.89	0.58

Appendix A2 – Calibration of Pitot Tubes

The TCO tunnel's calibration constant, the relationship between the frequency value (Hz) of the fan rotation speed and the flow speed in the rectangular section where the tests to calibrate the Pitot tubes, were determined with a hot film anemometer (KIMO AMI 300). Three replications were performed, and the hot film anemometer recorded the flow velocity during the 60s and calculated the average flow velocity. Table A4 shows the values recorded during 60s for each set of Frequency considered and Figure A2 shows the linear regression of the plot of the frequency value as function of the wind flow velocity.

Table A4: The relationship between the frequency value (Hz) of the fan rotation speed and the wind flow speed measured with a hot film anemometer (KIMO AMI 300) with three replications (T1, T2 and T3).

$Freq$ (Hz)	U_0 ($m.s^{-1}$) T1	T2	T3	sd	T_a (^oC)
0	0	0	0	0	0
1	0.59	0.57	0.69	0.03	28.24
2	1.20	1.30	1.30	0.02	28.21
3	1.83	1.84	1.53	0.03	28.25
5	3.17	3.15	3.97	0.03	28.48
10	6.47	6.40	6.17	0.22	28.64
15	9.40	9.41	9.90	0.12	28.94
20	12.05	12.09	11.85	0.37	28.96
30	18.85	18.95	17.85	0.81	28.92
40	24.96	24.86	25.36	0.39	28.22
50	29.83	30.73	29.53	0.20	28.46

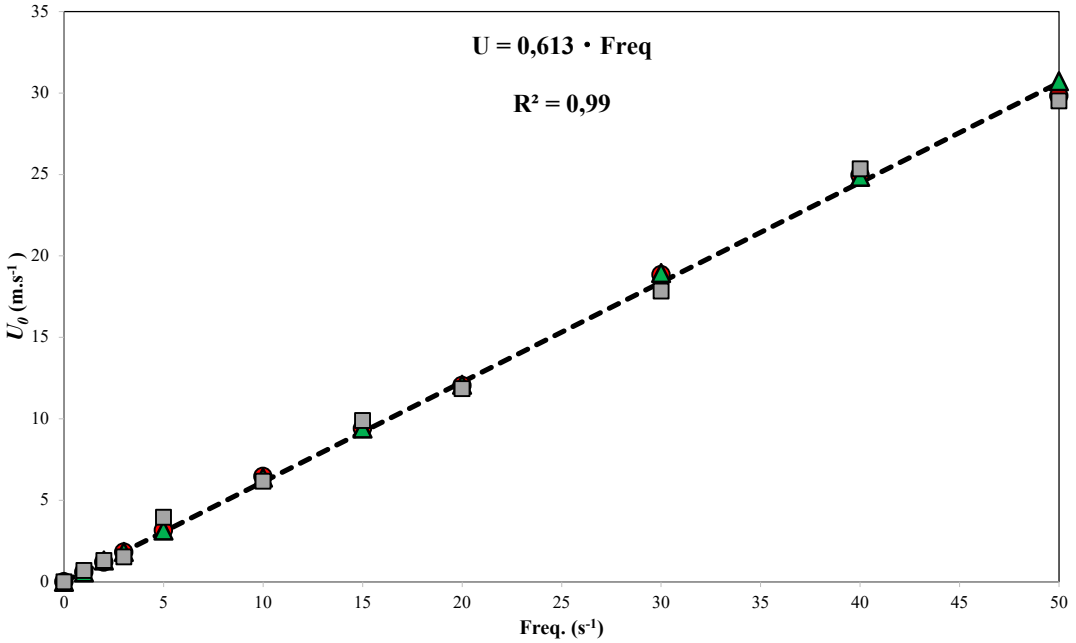

Figure A2: Linear regression of the plot of the frequency value as function of the wind flow velocity.

However, during this calibration if the misalignment is in the range between 0 to 30°, the error is less than 2%. In Figure A3 the measured velocity $U(\alpha_{TCO})$ is normalized with $U_0 = U(0°)$. The calibration curve is practically symmetrical and independent of the value of the reference velocity U_0. The tests were measure for the wind velocity $U_0 = 5$, 10 and 15 m.s^{-1} and the fitting curve corresponds to:

$$U = -7\mathrm{E}^{-9}.{\alpha_{TCO}}^4 + 2\mathrm{E}^{-7}.{\alpha_{TCO}}^3 - 0{,}0001.{\alpha_{TCO}}^2 - 0{,}0002.\alpha_{TCO} + 1{,}0999$$

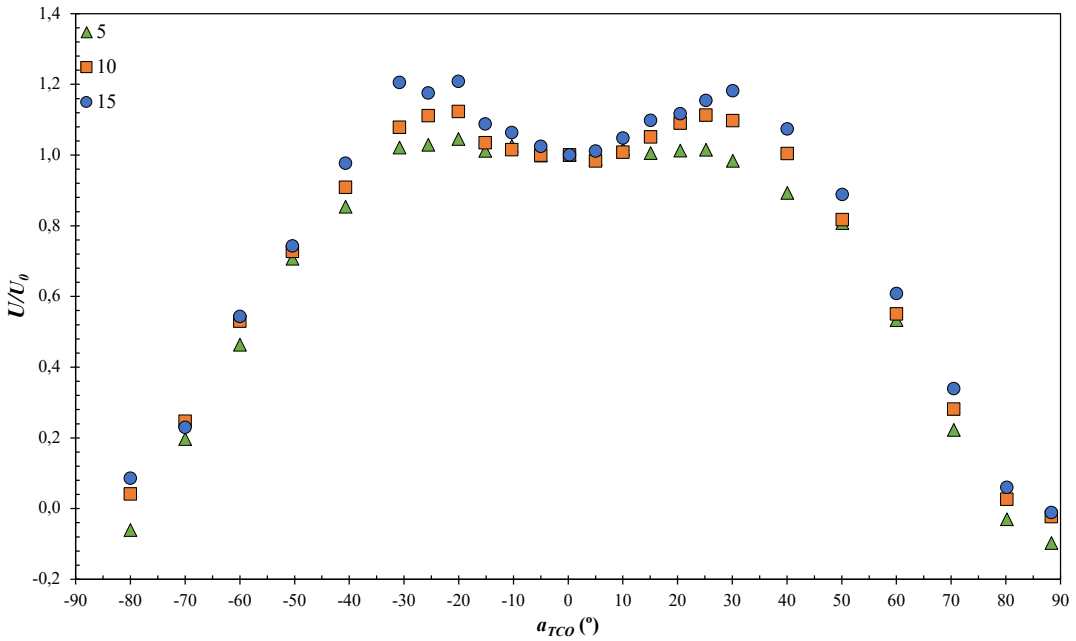

Figure A3: Effect of pitch angle α misalignment on the measurement of the S-type Pitot tube for flow velocities U_0 = 5, 10 and 15 m.s^{-1}.

During the calibration tests it is performed hysteresis test to analyse the response time. The response time is on average around 1s, thus being in the same order of magnitude as the signal acquisition.

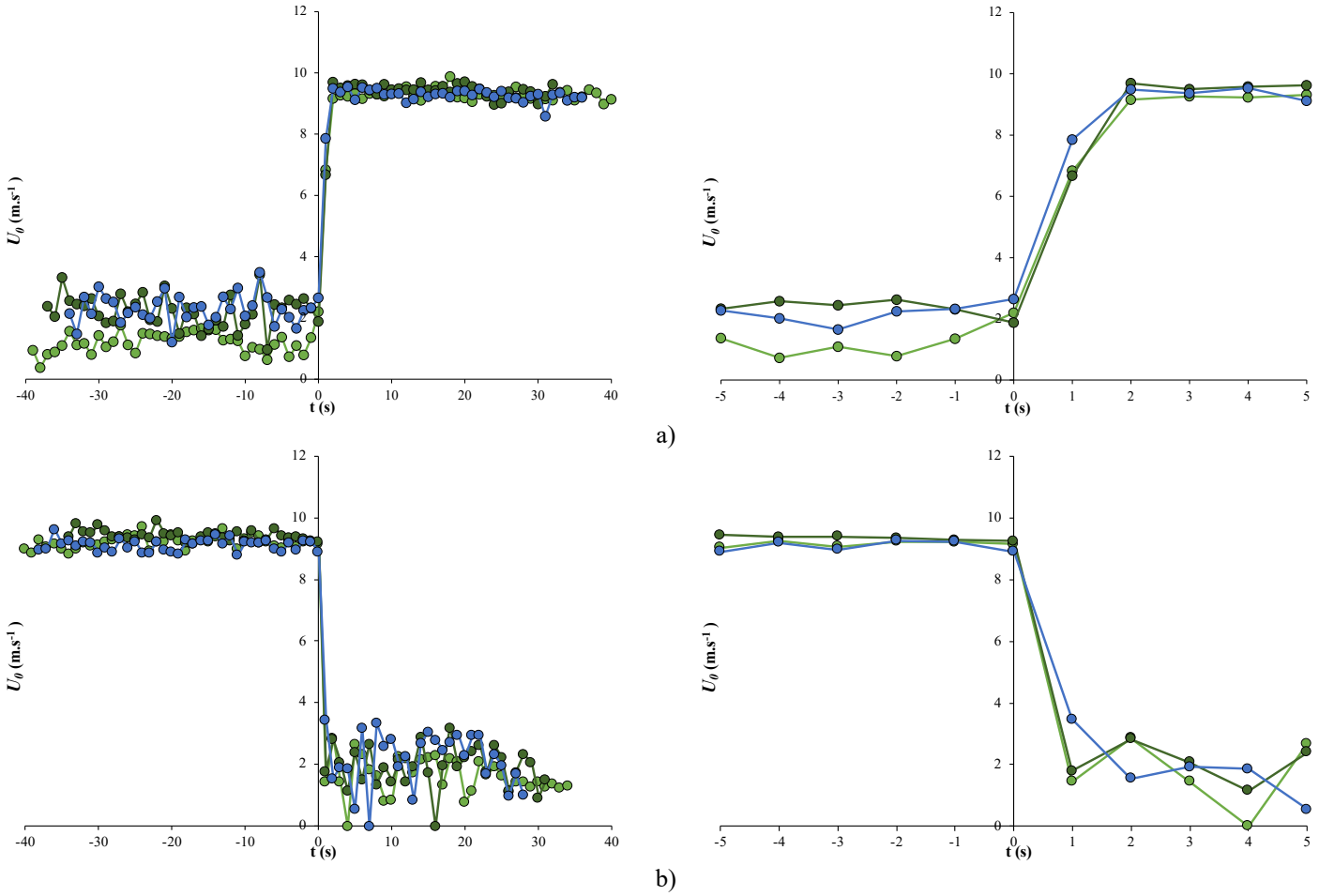

Figure A4: Hysteresis response test. a) acceleration; b) deceleration